COMPLEX TRANSITION METAL CHALCOGENIDE FERROMAGNETIC SEMICONDUCTOR WITH GENERAL FORMULA MSb_2Se_4 (M=Mn, Fe): SYNTHESIS AND CHARACTERIZATION

by

Honore Djieutedjeu

A dissertation submitted in partial fulfillment
of the requirements for the degree of
Doctor of Philosophy
(Materials Science and Engineering)
in The University of Michigan
2013

Doctoral Committee:

Assistant Professor Pierre Ferdinand Poudeu-Poudeu, Chair
Assistant Professor Emmanouil Kioupakis
Professor Joanna M. Millunchick
Professor Xiaoqing Pan
Professor Ctirad Uher

© Honore Djieutedjeu 2013

DEDICATION

To my parents, my wife and my twins Julie and Jesse

ACKNOWLEDGEMENTS

This work has constantly received diverse support from my committee members, friends, family and collaborators. Here I would like to acknowledge all of you for giving me hope through this long process.

First and foremost I would like to thank my advisor, Prof. Pierre Ferdinand Poudeu Poudeu for welcoming me in his group and for supporting me during my time the in USA. Beyond our sometimes late discussions about this work and science in general, you and your entire family were part of my dedication toward my PhD. May you and your entire family find here my entire infinite acknowledgement.

To my committee members and particularly to Prof. Joanna M. Milluchick, I have received a wealth of wisdom even though we have only had a few encounters. I would like to thank you for helping me form my committee. I always leave our meetings with something constructive.

To you Professor Ctirad Uher especially, I would like to say thanks for promptly accepting to be part of this committee and for providing space in your lab for my transport property measurements, magnetic measurements and your invaluable comments each time we have published together.

I would also like to thank Professors Emmanouil Kioupakis and Xiaoqing Pan for promptly and happily accepting to be part of this committee and for helping me complete my work.

Special thanks to Professor Emmanuel Ngameni, former Chair of inorganic chemistry department and Chair of the analytical chemistry laboratory at University of Yaoundé I, for suggesting and convincing me to join Prof. Poudeu's group.

To all my current group members, particularly Pranati Sahoo and Yuanfeng Liu for what we shared together for these past four years. I would like thank Erica Chen and Juan Lopez for your help editing my documents; I really appreciate your patience when trying to improve my communication.

To my former group members, particularly Dr. Kulugammana G. S. Ranmohotti, Dr. Julien P. A. Makongo, and Dr. Nathan J. Takas for all you have provided as scientists

To Professor Uher's students: Alexander Page and Chi Hang for all your collaboration and scientific discussions. .

To Professor David P. Young and Neel Haldolaarachchige for your collaboration. Professor Barth Bartlett and his group, Professor Leonard Spinu, Professor Aurelian Rotaru for SQUID MPMS training, and your time to fix the high temperature system.

To Professor Jean Fotie for your permanent support and your time to go through this thesis, for your suggestion and correction.

To my entire family, my dad and mom who trust me although my disability and constantly support me whenever I need them. May you find here my deepest gratitude and love!

To my lovely wife, for your patience, care, understanding and devotion to a bright future for us. To you Jesse and Julie for being part of our joy.

Finally, I would like to thank the Jesuit Society of Cameroon and over the world and particularly Martin Birba and Ludovic Lado for your assistance as priest and teaching me the meaning of my mission as a future scientist and my responsibility wherever I go.

Table of Contents

LIST OF FIGURES

LIST OF TABLES

ABSTRACT

This work presents two new magnetic semiconducting compounds ($FeSb_2Se_4$ and $MnSb_2Se_4$), which are subsequently used as template for the investigation of the effect of electronic structure engineering of low band gap magnetic semiconductor in the magnetic behavior and the Curie ferromagnetic to paramagnetic transition temperature (T_c). The compounds were synthesized by solid-state reaction of the elements at moderate temperature. Both compounds are isostructural and crystallize in the monoclinic crystal system with space group *C*2/*m* (#12). Their crystal structure can be viewed as consisting of two types of building units, denoted A and B alternate along [001]. The unit A is built of paired rods of face-sharing monocapped trigonal prisms around Sb atoms alternating along the *a*-axis with a single chain of edge-sharing octahedra around the magnetic M (Fe, Mn) atoms. The unit B is a NaCl-type block separating adjacent units A, within which chains of edge-sharing octahedral around Sb atoms alternate along the a-axis with a single chain of edge-sharing octahedra around the magnetic M (Fe, Mn). Temperature dependent measurements of the magnetic susceptibility and electrical conductivity revealed that $FeSb_2Se_4$ is a high temperature *p*-type ferromagnetic semiconductor with an electrical conductivity of ~ 2 S/cm and the Curie transition temperature T_c ~ 450K, whereas a dominant antiferromagnetic ordering was observed in the $MnSb_2Se_4$ compound. To probe the effect of changes in the electronic transport properties in $FeSb_2Se_4$ and $MnSb_2Se_4$ on their magnetic behavior, the solid-solution series, $Fe_{1-x}Sb_2Sn_xSe_4$, $FeSb_{2-x}Sn_xSe_4$, $MnSb_{2-x}Sn_xSe_4$, and $FeSb_2Se_{4-x}Te_x$ were investigated. All Fe containing compositions (except the $FeSb_2Se_{4-x}Te_x$ series (x= 1, 2, 3 and 4) were found to be isostructural with $FeSb_2Se_4$ and showed a ferromagnetic ordering up to 600K with magnetic and electronic transitions at 130K,321K, 400K and 440K. These transitions were found also to be related to structural changes upon heating or cooling from 300K. The transitions at 130K, 400K and 440K disappear with increasing concentration of Sn indicating the structural effect is annealed with increasing Sn content. The

materials exhibit large positive values of the thermopower and optical measurements revealed an optical band gap of 0.32eV, suggesting that the substituted $FeSb_2Se_4$ families of compounds are p-type narrows band gap semiconductors. Neutron diffraction data, Arrott`s plot of the magnetic data and magnetoresistance indicate that the long range ferromagnetic ordering present in these solid-solutions at low temperatures originate from interactions between localized charge carriers and active magnetic centers via the formation of bound magnetic polarons (BMPs). At high temperature, the long-range ferromagnetism in the Fe containing compounds is believed to be mediated by spin-polarized carriers (holes). X-ray photoelectron spectroscopy(XPS) studies of various $FeSb_{2-x}Sn_xSe_4$ samples revealed that a fraction Fe and Sb, which are initially in the Fe^{2+} and Sb^{3+} oxidation states gradually oxidize to Fe^{3+} and Sb^{5+} when a sufficient amount of Sb is substituted by Sn in $FeSb_{2-x}Sn_xSe_4$. This XPS result is consistent with the increasing change of the electronic transport in $FeSb_{2-x}Sn_xSe_4$ from the semiconductor to metallic behavior upon addition of Sn at Sb sites. The $Fe_{1-X}Sb_2Sn_xSe_4$ and $FeSb_{2-x}Sn_xSe_4$ phases displayed very low thermal conductivity suggesting that the compounds are promising thermoelectric materials. To optimize the thermoelectric behavior, we performed Te doping at Se sites in the $FeSb_2Se_4$ structure. The resulting $FeSb_2Se_{4-x}Te_x$ ($0 \leq x \leq 0.1$) series l maintains unchanged crystal structure of the parent compound. However, the change in the chemical composition resulted in a slight decrease of the electrical conductivity upon increasing Te concentration. A full substitution between Se and Te in $FeSb_2Se_{4-x}Te_x$ (x = 1, 2, 3, 4) results to a striking change in the crystal structure from the monoclinic layered structure of $FeSb_2Se_4$ to the rhombohedral structure of $FeSb_2Se_{4-x}Te_x$. Interestingly, this change in the crystal structure resulted in a sharp increase of the electrical conductivity, and the magnetic behaviors were similar to that observed in the $Fe_{1-X}Sb_2Sn_xSe_4$ and $FeSb_{2-x}Sn_xSe_4$. Calculation of the thermoelectric figure of merit using thermopower, electrical conductivity and thermal conductivity data suggest a thermoelectric figure of merit ZT ~0.15 was observed in $FeSb_2Te_4$ at 300K.

The $MnSb_{2-x}Sn_xSe_4$, phases are isostructural with $FeSb_2Se_4$ and we found the parent compound ($MnSb_2Se_4$) to be antiferromagnetic semiconductors with Curie-Weiss constant of -76K. Upon partial doping of Sn at Sb sites, ferromagnetic ordering with a very low Curie transition temperature of 56K was observed. This change from antiferromagnetic to ferromagnetic ordering in $MnSb_{2-x}Sn_xSe_4$ ($0 \leq x \leq 0.25$) was observed for x values in the range $0.05 \leq x \leq 0.25$ and a reversal to a dominant antiferromagnetic ordering was observed for higher Sn content.

Both $FeSb_2Se_4$ and $MnSb_2Se_4$ were found to exhibit spin dependent transport phenomena, making them potential candidates for spintronics applications.

Chapter I

Introduction

Magnetic semiconductors have regained great interest over the last two decades.[1-4] This renewed interest has been motivated by the opportunities for a new generation of devices, which should arise from the combination of standard microelectronics with spin-dependent effects.[5,6] Future information technology for instance, requires devices capable of processing and storing information simultaneously. Currently, these two functionalities are provided by two independent devices with semiconducting or magnetic properties.[4] The denomination of magnetic semiconductor assumes presumably that magnetism and electronic properties are used simultaneously. This results to magnetoelectronic or spin electronic. This new field of condensed matter physics exploits the quantum properties of electron such as charge and spin.[7,8] In spintronics (short name of spin electronic), electron charge and spin are both used to store and process a piece of information. The discovery and explanations of the spin-dependent transport in metallic ferromagnetic multilayered structures initiated the spintronics research leading to the first generation of spintronics devices in the form of a spin valve.[1,10] It was known a longtime ago that under an applied magnetic field, the resistivity of the metal decreases. However, the magnitude of the drop was insignificant until the recent discovery of giant magnetoresistance (GMR) by Peter Grünberg and Albert Fert.[12,13] They were able to observe a resistivity drop of about 80%, when the magnetization is saturated at 4.2 K.[13] Since then, interest in spin-based electronics has been deeply investigated in terms of relationship between spin and charge, structure and simultaneous spin, and electronic transport properties. However, the ability to control charge transport has made possible to form functional devices such as transistors and diodes particularly in semiconductors.[7]

I-Overview of Semiconductor-based electronic materials

In semiconductor-based electronics, only the electron-charge transport is of relevance. Electron-spins are ignored. This is due to the fact that electron-spin in semiconductors does not have a specific direction and even when detected, has low magnitude. In ferromagnetic metals, electron-charge is ignored, while electron-spins are easily modulated.[7] However, the first generation of spintronics was constructed from alternating layers of ferromagnetic metal and normal metal (Figure 1).[1,10,12-14] This type of material has an advantage of providing high Curie ferromagnetic temperature (T_c).[14,15] In addition, the magnetic anisotropy of these types of materials are easily modulated by alloying, and the synthesis route is well-established.[15] However, the integration of metallic multilayer in conventional semiconductor materials is difficult because of the large conductance mismatch between the semiconductor and the metal.[15]

The theory of spin current proposed to explain the change of the resistivity of metal under applied field also stands for materials tailored by doping a semiconductor with a magnetic atom such as Mn. For a semiconductor, spin current is expected to improve the magnetic properties.[15] In addition the new materials resulting from successful integration of magnetism into semiconductors will greatly improve the semiconductor technology by allowing it to perform functionalities such as high data storage density, high processing speed, increased longevity of memory chips, and even lower power consumption.[6]

I-1-Magnetic semiconductor

The magnetic semiconducting property is not a new concept, since it was discovered in the 1960's, in materials such as EuSe, EuO, $CdCr_2Se_4$, $CdCr_2S_4$.[16,17] These materials exhibited interesting exchange interactions between the itinerant electrons and localized magnetic moment. Since the discovery of GMR, the idea that new materials suitable for spintronic applications could come from magnetic semiconductors became fascinating again. However, the concept of spin injection in semiconductors has attracted much attention. In diluted magnetic semiconductors, a sizable fraction of magnetic atom (Mn, Co, Cr) are used to substitute equal amount of cation in conventional III-V (GaAs, InSb, GaN, InN, GaP, InP), II-VI (ZnTe, ZnO, ZnTe), and IV-VI based semiconductors.[3,16,18,19] These materials exhibit a spin dependent coupling between localized magnetic moments and electrons in both the valence and conduction bands. Owing to these interexchange interactions, charge carriers (electrons or holes) can easily mediate ferromagnetism between the localized spin and electronic band population. This makes

the control of the magnetization by the electric field possible, which is an important requirement for spin-based devices to operate and also for prospect bright future in electronic with multifunctional materials enable fabrication of easily portable and efficient devices. The integration of the magnetic elements into commercial semiconductor used in most electronics today is a new approach to simultaneously make use of both charge and spin of electrons. GaAs and Si are the most commercialized semiconductor materials and several III-V, II-VI and IV-IV semiconductor have been doped with transition metals as Mn and Cr to synthesize such target materials. Magnetic semiconductors could be subdivided into magnetic semiconductors (MS), diluted magnetic semiconductors and non magnetic semiconductors.

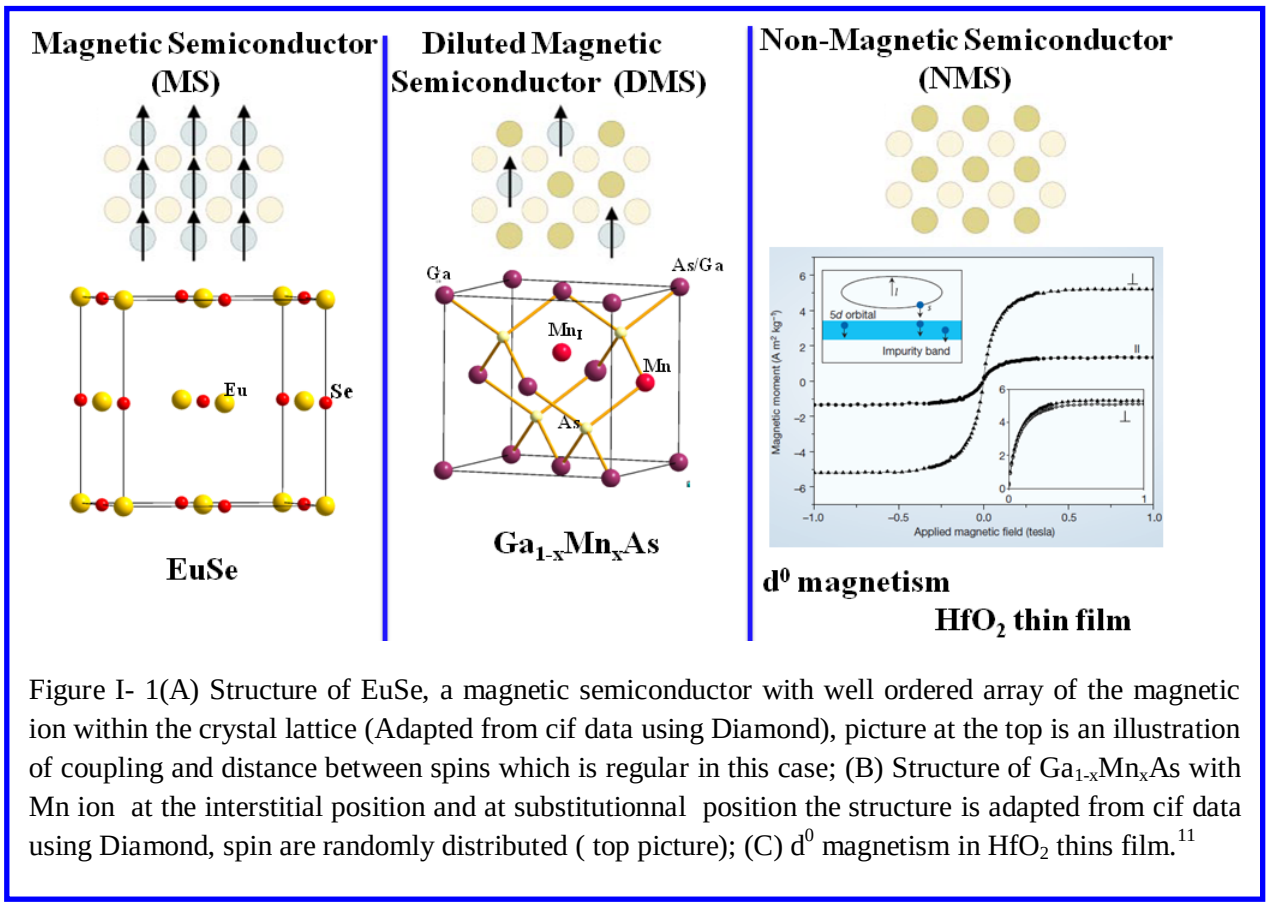

Figure I- 1(A) Structure of EuSe, a magnetic semiconductor with well ordered array of the magnetic ion within the crystal lattice (Adapted from cif data using Diamond), picture at the top is an illustration of coupling and distance between spins which is regular in this case; (B) Structure of $Ga_{1-x}Mn_xAs$ with Mn ion at the interstitial position and at substitutionnal position the structure is adapted from cif data using Diamond, spin are randomly distributed (top picture); (C) d^0 magnetism in HfO_2 thins film.[11]

I-1-1-Magnetic semiconductor

In magnetic semiconductors such as EuSe, $CrCd_2Se_4$ and $ZnCr_2Se_4$, magnetic ions have a between the free electrons or holes in the semiconducting band and the localized electrons of the magnetic ions provide interesting properties. For instance, from photo-luminescence spectroscopy, a red shift of the band gap is observed in most of them when the ferromagnetism sets in.[8] The red shift of the photo luminescence spectra is a shift of band structure from the wide band to the lower band. This shrinking of the band is attributed to the sp-d interaction between the free charge carrier in the semiconductor band and the localized magnetic moments.[8,20] Exchange interactions between the magnetic ions' spins are known to be dominated by the long range ordering through spin polarized holes or electrons from the impurity band of the semiconductor[3,21-26] Therefore, we can predict the manipulation of magnetic properties using optical stimuli in the devices made from magnetic semiconductors.[4,10,27] Figure I-1A is an illustration of the EuSe structure, with well ordered Eu ion embedded into semiconducting network. The magnetic semiconductors listed above received intensive attention between 1960s and 1970s because of the intriguing phenomena due to the exchange interaction between the electron in the semiconductor band and the localized electrons at the magnetic sites.[16,17] However, it is a challenge to grow large crystals. Furthermore, the low Curie temperature displayed by these compounds, which was far below 100 K, cause to abandon interest attached by researchers in these materials.

I-1-2-Diluted magnetic semiconductor (DMS)

This is the most widely investigated class of magnetic semiconductors. Here, transition or rare earth metals atoms randomly replace a fraction of atoms in the host semiconductor.[8,28-34,35] Diluted magnetic semiconductors are based on doping of the most commercialized semiconducting materials such as Si, III-V, II-VI and IV-IV with magnetic impurities such as Mn, Cr, Fe and rare earth elements carrying unpaired spins. This in turn, transforms non-magnetic semiconductors into a magnetic material. The magnetic interaction between isolated

spins in such materials are mediated by free carriers, which can be controlled by the external

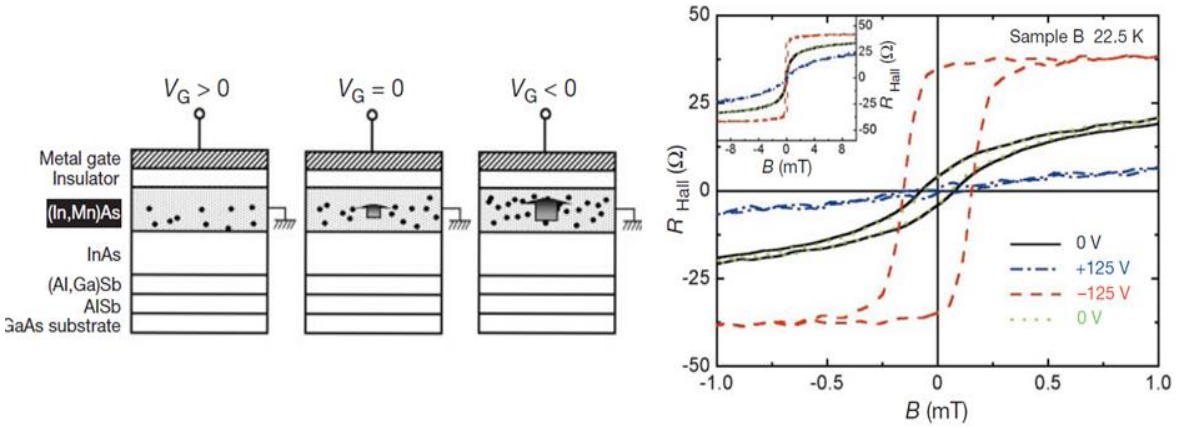

Figure I- 2: Magnetic ordering induced from voltage switch, for $V_G > 0$ no FM ferromagnetism, for $V_G \leq 0$, FM ordering observed, this is a manifestation of carrier induced or mediated ferromagnetism.

parameters or stimuli such as light, electric or magnetic fields. For instance, in (InMn)As, ferromagnetism is suppressed when a positive voltage is applied across the sample.[11] As depicted in Figure I-2, different voltages across the sample induce different magnetic behaviors. This is explained by the change of the carrier concentration under the applied voltage. The control of the magnetization direction with an applied electric field and photo-induced ferromagnetism have been verified, proved and featured in DMS such as (InMn)As, (GaMn)Sb and (GaMn)As.[36,11] This suggests that semiconductor spintronics can play a crucial role in next the generation of electronics, since several functionalities such as light controlled information can be developed within the fabricated magnetic semiconductor devices. However, because of the concentration dependence of magnetization, the spin dependent transport in the DMS is not systematic. Several parameters such as material preparation, band structure and the position of magnetic impurities compared to the Fermi level account for the ferromagnetism in DMS's. The effect of materials processing and synthesis on Curie temperature and on ferromagnetism is proved to be very complex and has made accurate modeling on the origins of ferromagnetic phenomena in most diluted magnetic semiconductors difficult.

I-1-3- Non magnetic semiconductor

Magnetism in most materials is determined by the number of unpaired electrons in the transition metals or rare earths electronic shell d^n or f^n with $1 \leq n \leq 7$. The strange find of magnetism in HfO_2 thin film with d^0 has objected this old belief of the origin of magnetism in oxides and materials in general. Magnetism in HfO_2 and other oxides is contingent on upon sample preparation. In the case of HfO_2,[11] reported preparation shows that oxygen vacancies are created during the thin film growth of HfO_2 leading to n-type doping of the material. The extra electrons from the vacancy have large dielectric constants and occupy large Bohr orbitals, and tend to form an impurity band with d orbitals from Hf ions. This mixture of *5d* orbitals of Hf with extra electrons from defects lead to polarization of the impurity band and provide ferromagnetic coupling with large orbital contributions coming from the *5d* moment electrons in a spin-orbit coupled $j = 3/2$ state (Figure I-1C).[11]

I-2-Origin of ferromagnetism in Magnetic semiconductor

Classical theory of magnetism is focused on the understanding of magnetic behavior in DMS and MS. The classic dipole-dipole exchange interactions between magnetic moments are weaker than exchange coupling in DMS. The direct exchange interactions between *d-d* or *f-f* are less important in DMS. These direct exchange interactions are more or less indirect via the spin polarization of bands.[28,37-39] The spin polarization is produced from exchange interactions between the free carriers and band edge or impurity band with the magnetic ions. It is called the spin dependent hybridization of the magnetic impurity.[38,40,41] If the magnetic orbitals are involved in the polarization process, the mechanism is known as superexchange, with dominant antiferromagnetic behavior (AFM).[41] However, in the case of p-type diluted magnetic semiconductors the situation is quite different and ferromagnetic ordering (FM) is expected.[38] In this case several mechanisms have been proposed to explain the origin of ferromagnetism in the p-type magnetic semiconductors.

I-2-1- Zener's Model

Zener's model also known as double exchange model proposed by Zener[42] in 1960s occurs in two magnetic ions separated by non magnetic atom. The magnetic ions involved in this interaction usually have different oxidation states.[38] The electron can be transferred from a magnetic ion through non magnetic ion to the nearest neighboring magnetic ion. The mechanism of this exchange interaction is the hopping of electron from one magnetic ion to the adjacent ion.

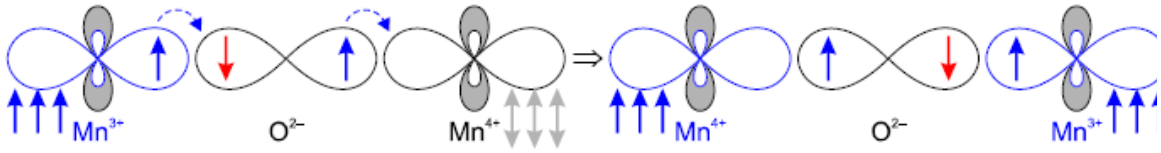

Figure I- 3**:** Double exchange mechanism via O^{2-} in $La_{0.67}Ba_{0.33}MnO_3$; Mn^{4+} and Mn^{3+} are exchanging spin via p orbital of the oxygen atom.[9]

Spin in magnetic ions that are involved in such exchange interactions need to be in the same state (spin up or spin down) in order to favor or increase the hopping probability. This state corresponds to the more favorable and stable in term of kinetic energy of the system. An illustration of double exchange interaction of Mn^{3+}-O-Mn^{4+} in $La_{0.67}Ba_{0.33}MnO_3$[9] is presented in the figure above. The Zener's model was developed to explain the magnetism in the metal. This model was proposed for manganite, where ferromagnetism and metallicity usually come together. The ferromagnetic critical temperature in double exchange model is proportional to the density of the carriers and bandwidth, with very small values in the low density limit appropriate to diluted magnetic oxides. This model failed to explain the high Curie temperature of diluted magnetic oxides and other diluted magnetic semiconductors.[43]

I-2-2-RKKY interaction

Two magnetic moments embedded in a metal induce spin polarization of the conduction electron gas.[44,45] This leads to indirect exchange coupling between the moments which can be extended over a long distance. This coupling is known as the RKKY[46-50] (Ruderman-Kittel-Kasuya-Yosida) interaction. The RKKY exchange interaction could be either FM or AFM, depending on the separation between the magnetic moments.[49,50] In the metal, the competing exchange interactions between the FM and AFM ordering leads to the formation of a spin-glass. In the

semiconductors, the mean distance between the carriers is usually much greater than that of the spins.[51]. In such situations, the exchange interaction mediated by the carriers is ferromagnetic for most of the spin pairs.[3,43,51] This will reduce the tendency toward the spin-glass freezing.[51]. Conversely to the Zener's model, which is dominant in the metallic systems and used in the short range interaction, the RKKY model integrates the metallic and non metallic system as semiconductor. It also includes the effect of the spin-orbit interaction and the details of the electronic structure on the magnetic behavior.

I-2-3- The p-d Zener's Model

The most recent model developed by Dietl et al[5] based on the Zener's[44,45] model to explain the magnetism in III-V and II-VI magnetic semiconductors takes into considerations the presence of the delocalized band carriers mediating ferromagnetic ordering between the localized spins via the *p-d* exchange coupling. This produces the splitting of the valence band, therefore lowering the carriers energy. This approach is known as the mean-field approximation. In this approach, the interaction of few localized spins occurs for certain minimum of delocalization length and carriers density. As these minimum are available, carriers and spins can mediate magnetic order. Generally speaking, the magnetization *M* in the Mn doped III-V and II-VI in absence of carriers is given by[5,51]:

$$M = g x_{eff} \mu_B N_0 S B_s \left[\frac{g \mu_B H}{K_B (T - T_{AF})}\right]$$

Where g is the Lande factor, x_{eff} represents the effective Mn concentration contributing to the magnetization, T_{AF} is the empirical parameter accounting for the short range antiferromagnetic superexchange between the Mn ion mediated by the *p-d* exchange coupling with occupied electron bands. This parameter can be neglected in some compounds with dominant long-range FM ordering.

The mean-field approach is based on the minimization of total free energy of the magnetization and is given by:

$$M = g x_{eff} \mu_B N_0 S B_s \left[\frac{g \mu_B (-\frac{\partial F_C[M]}{\partial M} + H)}{K_B (T - T_{AF})}\right]$$

Where $F_c[M]$ holes dependent contribution to the free energy and can be related to the carrier magnetic susceptibility $\chi_s = A_F(g\mu_B)^2\rho_s$ where ρ_s is the spin density of states and A_F accounts for carrier-carrier interaction.

$$F_C(M) = F_C(0) - \frac{A_F\rho_s M^2\beta^2}{8(g\mu_b)^2}$$

β is the coupling constant due the indirect exchange coupling.

The Curie temperature from the mean-field with account of the free carriers is given by:

$$T_c = \frac{x_{eff}S(S+1)\beta^2 A_F\rho_s(T_c)}{12N_0K_B} - T_{AF}$$ [5,51]

This formula shows that, the Curie temperature is proportional both to the concentration and spin of the magnetic ions, the density of states of the mediating holes and the square of the coupling constant. Also, the Curie temperature increases infinitely with the concentration of the effective magnetic ions, the coupling constant and the spin density of states. However, the spin frustration at high concentrations of the effective magnetic ions and the localization due to the strong exchange interaction should in reality hamper this limitless increase of the T_C value from the mean-filed approximation. Furthermore, a large density of states at Fermi level may also result in a variation of the sign of the RKKY interaction. However, this theory predicts the requirement toward room temperature ferromagnetic semiconductors.[6,25,38,52,53]

I-2-4- Bound magnetic polarons

Models currently prescribed work and explain the interaction in the system perfectly where carriers are delocalized, but fail to predict the magnetism in the insulating regime. In this regime, the bound magnetic polaron concept has been used to properly describe the magnetic behavior.[3,5,24,54-56] This concept speculates that, localized carriers (holes or electrons) are coupled by the AFM exchange mechanism with a number of impurities within its localization radius, which leads to the creation of the so called bound magnetic polarons (BMP) resulting from the interaction between spins of the magnetic ion with quasiparticles called polarons. In fact, an electron in the crystal lattice for instance interacts through its electrical charge with the ions or atoms of the lattice and creates a local deformation of the lattice. The deformation further follows the electron as it moves through the lattice. The electron coupled with this strain field is

called a polaron. The BMP interacts ferromagnetically with each other in contrast with AFM interaction which leads to their formation. The effective radius of the polaron increases with the ratio of the exchange interaction and the thermal energy causing BMP to overlap at sufficiently low temperatures to give the FM exchange interaction between the percolated polarons (Figure I-4).

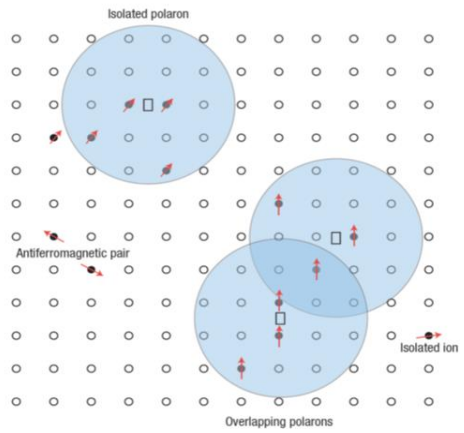

Figure I- 4: Representation of magnetic polaron in the semiconductor lattices.

I-3-Requirements for efficient magnetic semiconductor materials

For efficient use as spintronic materials, magnetic semiconducting materials should first be ferromagnetic with low carrier density.[2,53] This will allow the magnetic properties to be modulated through doping. The ferromagnetic transition temperature should be above room temperature, which will allow the materials to be used for practical applications at room temperature and above. The materials should be insensitive to small magnetic impurity,[53] in order to allow reproducibility. The materials should have strong magneto-optical effect to allow manipulation of the stored information using light or other optical stimuli.[5] For efficient energy consumption, the materials ideally should have low band gap as required for many semiconductor technologies.[53,57,58] Several other criteria are known, but are beyond the scope of this work. However, the DMS and magnetic materials obtained from spin injection are known to have very low Curie temperature. The actual highest Curie temperature (T_c) for Mn-doped III-V DMS of ~173 K is still far from the targeted room temperature value.[53,2] In order to achieve room temperature T_c, Dielt et al. predicted that high T_c can be achieved in large band gap

semiconductors.[5] This prediction was derived from theoretical calculation using modified Zener's model of ferromagnetism, which is controlled by the exchange interaction between the localized spin and itinerant carriers-spin. In this calculation authors assumed the ferromagnetism to originate from mediating shallow hole-doping.[5,51] This theory also predicts as described earlier in this work, the T_c in the $Ga_{1-x}Mn_xAs$ for instance to be dependent on the Mn concentration. However, recent experimental data have shown that the T_c is mostly dependent on the location of the Fermi level within the impurity band instead of the hole concentration.[21,59] Moreover, since ferromagnetic materials with high Curie temperature were only reported for the n-type semiconductors[15] according to the theory predicted by Dielt et al., this leads to the assumption that the nature of the magnetism in the materials is not only controlled by the location of the Fermi level but also by other parameters. For instance, experimental data from Debrowolska et al. has shown that material preparation affects the Mn distribution in GaAs,[21]which is a parameter that was not taken into account in the calculation by Dielt et al. during theoretical investigation.[5,51] Another controversy is about the origin of the ferromagnetism in these materials.[2,52] It is not clear if the ferromagnetism between localizes spin is mediated by the delocalized carriers(Intrinsic) with long range ordering to satisfying the term "dilute" in diluted magnetic semiconductors or is originated from magnetic cluster. Because of these controversies and challenges to find the suitable ferromagnetic semiconductors, it is important to search for new materials, which encompass the magnetism and semiconductivity as their intrinsic properties.

I-4-The Approach in this thesis

In the previous section, various theories and models explaining ferromagnetism in magnetic semiconductors were elaborated. This discussion highlights the significant disparity in the models for ferromagnetism in magnetic semiconductors. As such, new directions for spintronic research must be developed in order to quell the model enigma. We approach this by suggesting different pathways toward spintronic research:

- Indentify new materials with both high Curie temperature and low band gap semiconducting properties.

- Use these new materials as template to understand the correlation between the ferromagnetism and semiconductivity, and requirement for both properties to co-exist with high Curie temperature.

- Use these materials to understand the band structure required for ferromagnetism and semiconductivity to co-exist with high Curie temperature. This will enable the band gap engineering of most commercialized semiconducting materials when doping them with transition metal.

We approach this from the bottom-up method by intentionally selecting transition metals such as Mn, Fe, Co or Ni which are the active magnetic centers in the final material. These elements are then combined with Sb, Bi, Pb, Sn or In with semiconducting character using S, Se and Te which are arranged in order of increasing semiconducting behavior. In this way we are able to create well odered magnetic semiconducting system with properties tunable from chemical manipulation of the sublattices.

I-5 -Complex transition metal chalcogenide and chemistry of the chalcogenide

The chemistry of main group of metal chalcogenide elements offers flexibility on building up solid state materials based on the concept of homologous series.[60,61] This concept allows the prediction of crystal structure, structural dimensionality and modular classification of the resulting structures.[60] Several properties on compounds obtained from this concept of homologous series have been investigated, and it turned out that they are good materials for thermoelectric, nonlinear optics, photoelectronics and solid-state electrolytes.[62-64] In addition, these properties can be tuned by manipulating the modular segments describing the homologous series.[65] Using these advantages of the combination of chemical and structural flexibility and the resulting interesting properties, the design and the investigation of multifunctional materials with ferromagnetism or charge carrier-induced ferromagnetism is now gaining tremendous attention. As a consequence, transport properties in main group metal chalcogenides are predictable, which is a great step towards the understanding and improvement of correlations between localized spin and spin-current in ferromagnetic semiconductors.

The ternary families of complex transition metal chalcogenides with general formula MPn_2Q_4 (M = Mn, Fe; Pn = Sb, Bi; Q = S, Se) are of great interest because of their physical properties and

structural flexibility and connectivity, which can vary from 1D to 3D depending on the composition and the synthesis method. Taking advantage of these structural and compositional flexibilities, we have designed a new family of ternary and quaternary materials based on 3d transition metal elements (Mn, Fe, Co, Ni), elements from group IV (Pb, Sn), group V (Sb, Bi) and the chalcogenide elements such as Se and Te. Owing to this flexibility in building up solid state materials, the chalcogenide chemistry offers the possibility to selectively insert magnetic atoms into the semiconducting framework with a well ordered arrangement and systematic control of the interatomic distances between magnetic ions. The transport properties of the chalcogenide materials are very sensitive to the applied field (magnetic and electric field) and to the impurities as dopants. In these structures, the semiconducting unit can be isolated easily from the magnetic unit. Complex transition metal chalcogenides can be generated from the homologous series of chalcogenide compounds by either replacing a metal in the framework in the host material with a transition metal with the same oxidation state as the metal in the host material.

We were able to synthesize and characterize several compounds exhibiting *p*-type semiconducting behavior and ferromagnetic properties with high Curie temperature. In this thesis we focus our attention to two ternary compounds, $MnSb_2Se_4$ and $FeSb_2Se_4$. We showed how to induce carrier mediated ferromagnetism in the $MnSb_2Se_4$ *p*-type antiferromagnetic semiconductor. $FeSb_2Se_4$ was found to be an intrinsic p-type ferromagnetic semiconductor with Curie temperature far above the room temperature. Magnetism in this compound could be altered upon substitutions at antimony or selenium sites.

I-6-Thesis Motivation and outline

My motivation in this work is to explore new magnetic semiconductor materials with spin dependent transport which could be used for next generation microelectronic devices. We have been motivated by the current challenge to understand the mechanism of ferromagnetism in diluted magnetic semiconductors and the current low Curie temperature (173 K) which hampers any application at room temperature based on the semiconducting host materials used for spin injection in semiconductor. We are exploring simple systems with low band gap and high Curie temperature with spin dependent transport in order to enable the understanding of the magnetic ordering mechanism and spin-dependent transport in FM semiconductor. The flexible

chalcogenide chemistry enables the integration of magnetic chains into its semiconducting framework. This could generate well-ordered magnetic sublattices within the semiconducting framework, which enables flexible control of the carrier density through chemical processing and applied fields (magnetic and electrical).

This thesis is organized as follows:

Chapters I and II provide background in spintronics, magnetic semiconductors and different theories used to understand the mechanism of magnetic ordering in semiconductors. We provide also the current challenges in the field of magnetic semiconductors and the most recent and probably the most accurate models. We clarified our choice of multinary complex transition metal chalcongenides as potential materials for next generation of spin-based electronic or as template for band gap engineering of new magnetic and diluted magnetic semiconductors.

The chapter III to VII is a journey within different structural aspects, neutron diffraction, electrical transport properties, magnetic and magnetotransport properties of new ferromagnetic semiconductor identified as $FeSb_2Se_4$ with Curie temperature of about 440K. We report in these chapters the effect of temperature on the structure and magnetic properties of $FeSb_2Se_4$ and $Fe_{1-x}Sb_2Sn_xSe4$(chapter IV), the effect of Sn and Te doping on properties of this new materials (Chapter V and VI) and the last chapter of this section reports the effect of the substitution of Se with Te on $FeSb_2Se_4$ properties.

Chapters VIII and IX report the new antiferromagnetic system which can be easily switched into a ferromagnetic system through small fraction of Sn doping in the specimen of $MnSb_2Se_4$. We demonstrate that this is possible only through spin-dependent transport (Spin-polarized electron or hole or magnetic polaron).

References

(1) Fert, A. *Thin Solid Films* 2008, *517*, 2.

(2) Dietl, T. *Nature Material*, 2010, *9*, 965.

(3) Coey, J. M. D.; Venkatesan, M.; Fitzgerald, C. B. *Nat Mater* 2005, *4*, 173.

(4) Wolf, S. A.; Awschalom, D. D.; Buhrman, R. A.; Daughton, J. M.; von Molnar, S.; Roukes, M. L.; Chtchelkanova, A. Y.; Treger, D. M. *Science* 2001, *294*, 1488.

(5) Dietl, T.; Ohno, H.; Matsukura, F.; Cibert, J.; Ferrand, D. *Science* 2000, *287*, 1019.

(6) Awschalom, D. D.; Flatte, M. E. *Nature Physique* 2007, *3*, 153.

(7) Y. Wu In *in Encyclopedia of Nanoscience and Nanotechnology*; Ed.; American Scientific publishers,: 2003; Vol. Vol. X, p 1.

(8) Ohno, H. *Science* 1998, *281*, 951.

(9) Matthias, O. *Journal of Physics D: Applied Physics* 2012, *45*, 033001.

(10) Fert, A.; George, J.-M.; Jaffres, H.; Mattana, R. *Europhysics news* 2003, 227.

(11) Venkatesan, M.; Fitzgerald, C. B.; Coey, J. M. D. *Nature* 2004, *430*, 630.

(12) Grünberg, P.; Schreiber, R.; Pang, Y.; Brodsky, M. B.; Sowers, H. *Physical Review Letter* 1986, *57*, 2442.

(13) Baibich, M. N.; Broto, J. M.; Fert, A.; Van Dau, F. N.; Petroff, F.; Etienne, P.; Creuzet, G.; Friederich, A.; Chazelas, J. *Physical Review Letter* 1988, *61*, 2472.

(14) Jiles, D. C. *Acta Materialia* 2003, *51*, 5907.

(15) *Spintronic and Material Technology*; Xu, Y.; Thompson, S., Eds.; Taylor and Francis group: Boca Raton, 2010.

(16) Lehmann, H. W. *Phys Rev* 1967, *163*, 488.

(17) Baltzer, P. K.; Robbins, M.; Wojtowic.P. *Journal of Applyied Physics* 1967, *38*, 953.

(18) Coey, M. *Nat Mater* 2005, *4*, 9.

(19) Sharma, P.; Gupta, A.; Owens, F. J.; Inoue, A.; Rao, K. V. *Journal of Magnetism and Magnetic Material* 2004, *282*, 115.

(20) Wang, X. L.; Luan, C. Y.; Shao, Q.; Pruna, A.; Leung, C. W.; Lortz, R.; Zapien, J. A.; Ruotolo, A. *Applied Physics Letter*, 2013, *102*.

(21) Dobrowolska, M.; Tivakornsasithorn, K.; Liu, X.; Furdyna, J. K.; Berciu, M.; Yu, K. M.; Walukiewicz, W. *Nature Material*, 2012, *11*, 444.

(22) Akai, H. *Phys Rev Lett* 1998, *81*, 3002.

(23) Bader, S. D.; Parkin, S. S. P. *Annual Review of Condensed Matter, P* 2010, *1*, 71.

(24) Calderon, M. J.; Sarma, S. D. *Annal of Physics New York* 2007, *322*, 2618.

(25) Dietl, T. *Nature Material*, 2003, *2*, 646.

(26) Dietl, T.; Cibert, J.; Ferrand, D.; d'Aubigne, Y. M. *Mat Sci Eng B-Solid* 1999, *63*, 103.

(27) Žutić, I.; Fabian, J.; Das Sarma, S. *Reviews of Modern Physics* 2004, *76*, 323.

(28) Jungwirth, T.; Sinova, J.; Mašek, J.; Kučera, J.; MacDonald, A. H. *Reviews of Modern Physics* 2006, *78*, 809.

(29) Kossacki, P.; Ferrand, D.; Arnoult, A.; Cibert, J.; D'Aubigne, Y. M.; Wasiela, A.; Tatarenko, S.; Staehli, J. L.; Dietl, T. *NATO Workshop on Optical Properties of Semiconductor Nanostructures, edited by M.L. Sadowski, M. Potemski, and M. Grynberg (Kluwer, Dordrecht, 2000) p. 211*. 2000, *81*, 225.

(30) Okabayashi, J.; Kimura, A.; Mizokawa, T.; Fujimori, A.; Hayashi, T.; Tanaka, M. *Physical Review B* 1999, *59*, R2486.

(31) Prinz, A.; Brunthaler, G.; Ueta, Y.; Springholz, G.; Bauer, G.; Grabecki, G.; Dietl, T. *Physical Review B*, 1999, *59*, 12983.

(32) Sadowski, J.; Mariette, H.; Wasiela, A.; Andre, R.; dAubigne, Y. M.; Dietl, T. *Physical Review B* 1997, *56*, R1664.

(33) terHaar, E.; Bindilatti, V.; Oliveira, N. F.; McCabe, G. H.; Shapira, Y.; Golacki, Z.; Charar, S.; Averous, M.; McNiff, E. J. *Physical Review B*, 1997, *56*, 8912.

(34) Wang, K. Y.; Sawicki, M.; Edmonds, K. W.; Campion, R. P.; Rushforth, A. W.; Freeman, A. A.; Foxon, C. T.; Gallagher, B. L.; Dietl, T. *Applied Physics Letter*, 2006, *88*.

(35) Krstajić, P. M.; Peeters, F. M.; Ivanov, V. A.; Fleurov, V.; Kikoin, K. *Physical Review B* 2004, *70*, 195215.

(36) Koshihara, S.; Oiwa, A.; Hirasawa, M.; Katsumoto, S.; Iye, Y.; Urano, C.; Takagi, H.; Munekata, H. *Physical Review Letter*, 1997, *78*, 4617.

(37) Story, T.; Gałązka, R. R.; Frankel, R. B.; Wolff, P. A. *Physical Review Letter* 1986, *56*, 777.

(38) *Semiconductor spintronics*; Dietl, T., Ed.; Springer: Berlin Heidelberg, 2007; Vol. 712.

(39) Jungwirth, T.; Niu, Q.; MacDonald, A. H. *Physical Review Letter,* 2002, *88*, 207208.

(40) Litvinov, V. I.; Dugaev, V. K. *Physical Review Letter,* 2001, *86*, 5593.

(41) Dietl, T.; Ohno, H.; Matsukura, F. *Phys Rev B* 2001, *63*.

(42) Zener, C. *Physical Review,* 1951, *82*, 403.

(43) Calderón, M. J.; Das Sarma, S. *Annal of Physics -New York* 2007, *322*, 2618.

(44) Zener, C. *Physical Review,* 1951, *82*, 403.

(45) Zener, C. *Physical Review,* 1951, *81*, 440.

(46) Yosida, K. *Physical Review;* 1957, *106*, 893.

(47) Yosida, K. *Physical Review,* 1957, *107*, 396.

(48) Ruderman, M. A.; Kittel, C. *Phys Rev* 1954, *96*, 99.

(49) Kasuya, T. *Progess of Theoretical Physics,* 1956, *16*, 45.

(50) Kasuya, T. *Prog. Theor. Phys.* 1956, *16*, 58.

(51) Dietl, T.; Ohno, H.; Matsukura, F. *Physical Review B,* 2001, *63*, 195205.

(52) Dietl, T.; Ohno, H. *Mater Today* 2006, *9*, 18.

(53) Macdonald, A. H.; Schiffer, P.; Samarth, N. *Nature Materials,* 2005, *4*, 195.

(54) Durst, A. C.; Bhatt, R. N.; Wolff, P. A. *Physical Review B*, 2002, *65*.

(55) Dyck, J. S.; Drašar, Č.; Lošťák, P.; Uher, C. *Physical Review B,* 2005, *71*, 115214.

(56) Fries, T.; Shapira, Y.; Palacio, F.; Moron, M. C.; McIntyre, G. J.; Kershaw, R.; Wold, A.; McNiff, E. J. *Physical Review B* , 1997, *56*, 5424.

(57) Jansen, R. *Nature Material* 2012, *11*, 400.

(58) Bauer, G. E. W.; Saitoh, E.; van Wees, B. J. *Nat Mater* 2012, *11*, 391.

(59) Ohya, S.; Takata, K.; Tanaka, M. *Nature Physics,* 2011, *7*, 342.

(60) Kanatzidis, M. G. *Accounts of Chemistry Research,* 2004, *38*, 359.

(61) Mrotzek, A.; Kanatzidis, M. G. *Accounts of Chemistry Research,* 2003, *36*, 111.

(62) Kanatzidis, M. G. *Semiconductors and Semimetals*, 2001, *69*, 51.

(63) Anglin, C.; Takas, N.; Callejas, J.; Poudeu, P. F. P. *Journal of Solid State Chemistry*, 2010, *183*, 1529.

(64) Poudeu, P. F. P.; Takas, N.; Anglin, C.; Eastwood, J.; Rivera, A. *Journal of American Chemical Society*, 2010, *132*, 5751.

(65) Kanatzidis, M. G. In *Semiconductors and Semimetals*; Terry, M. T., Ed.; Elsevier: 2001; Vol. Volume 69, p 5

Chapter II

Experimental Techniques

Synthesis methods, characterization and details of the instruments are discussed in this chapter. Most materials were obtained via solid state method within temperature range from 750 K to 875 K, and were black (dark gray) polycrystalline materials, very stable in air also very stable upon thermal processing.

II-1-Synthesis techniques

II-1-1-Solid state synthesis

Single phase polycrystalline powders of $MnSb_2Se_4$, $Fe_{1-x}Sb_2Sn_xSe_4$, $MnSb_{2-x}Sn_xSe_4$ and $MnSb_2Se_{4-x}Te_x$ were obtained through solid-state reactions of the elements at moderate temperatures. Stoichiometric mixtures of high purity elements (99.999%, from Cerac), were roughly mixed under argon atmosphere in a dry glove box using an agate mortar with pestle and sealed in an evacuated quartz tube with a residual pressure of ~10^{-3} Torr. The sealed tubes were then placed in a furnace and the temperature was ramped to 573 K, at a rate of 48 K/h, and dwelled for 24 h. This first step is required to allow elements with low melting temperatures (Se, Sn) to react completely with other elements and to avoid any explosive reactions. The temperature was then ramped up to 773 K over 12 h and dwelled there for 72 h, and finally cooled slowly to room temperature over 48 hours. The resulting products were dark gray polycrystalline powders. In some cases suitable single crystals were obtained for structural and phase identification. Several doped samples with similar structure as $MnSb_2Se_4$ and $FeSb_2Se_4$ were obtained when samples were doped with Sn, and new compounds with different structures compared with the $FeSb_2Se_4$ were obtained when Se was substituted with Te.

II-1-2-Induction Melting

This is a non-contact heating process, which uses a high frequency changing magnetic field to heat electrically conductive materials by induction. As shown in Figure II.1, a high frequency AC power source is used to drive a large alternating current through the induction coil. The

sample is placed inside the work coil. When current passes through the work coil, a very intense and rapidly changing magnetic field is generated within the coil. Since the sample is placed in this magnetic field, there are several things to consider. The alternating magnetic field induces a current flow in the conductive sample, which can be explained by considering the work coil and sample as an electrical transformer. The work coil can be considered as the primary coil where energy is given, and the sample is a single turn secondary coil that is short-circuited, causing

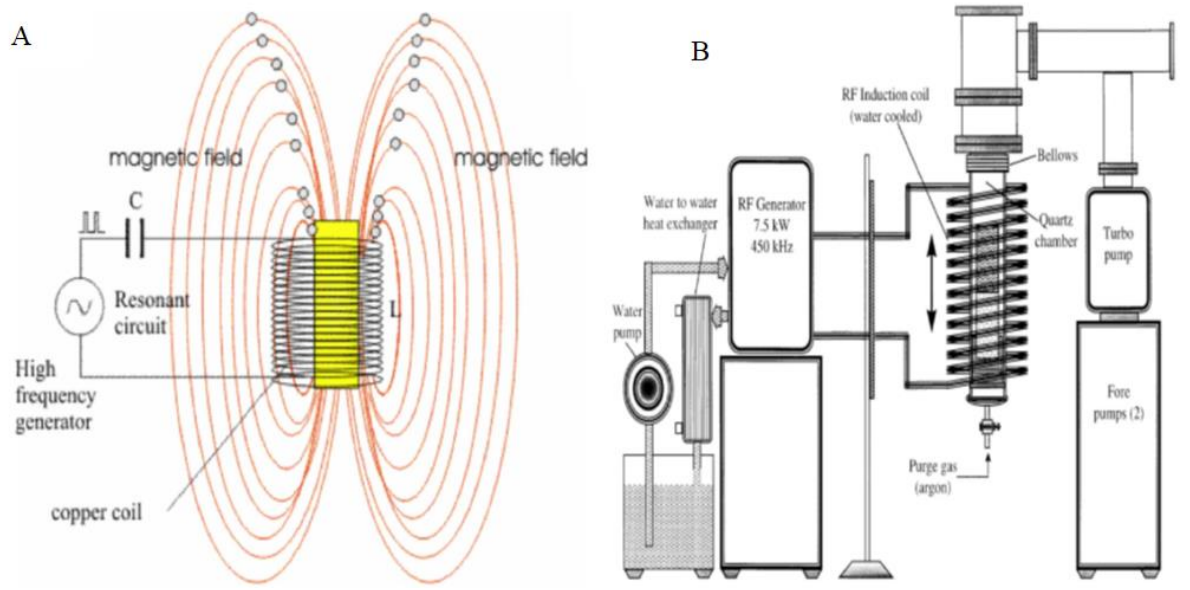

Figure II- 1) (A) High frequency alternating current induces an intense and rapidly changing magnetic field through sample, (B) Simplified picture of induction furnace.[1,2]

tremendous currents to flow through the sample, which are known as eddy currents. For each synthesis, 5g of a stoichiometric mixture of starting materials in graphite crucible container properly sealed in the quartz tube are placed in a high temperature glass container inside the induction coil, and then RF power is supplied. The sample can be melted under a partial pressure under ultra-high vacuum of -0.1MPa. The operating frequency of our RF supply can be varied 0 - 100 kHz, which provides the freedom to increase the heating temperature of the sample at a very slow rate.

II-2- Characterization techniques

Structural identification, phase purity, transport properties and magnetic properties in this work were measured using techniques listed in this section.

II-2-1-Structural, Phase Identification and Elemental Analysis

The focus of this thesis is the design, synthesis, crystal structure and structure properties relationship in multinary complex transition metal chalcogenide. Because of the critical requirement in term of phase purity for these properties, structural identification is a crucial step in this work.

II-2-1-1 X-ray diffraction (XRD)

II-2-1-1-a-Powder X-ray diffraction (PXRD)

To assess the phase purity of the synthesized polycrystalline powder, PXRD data were collected using curved graphite crystal monochromatized CuK_α radiation (λ = 1.54056 Å) in reflection geometry on a Philips X-ray powder diffractometer equipped with a position sensitive scintillation counter and operating at 45 kV and 40 mA. The experimental X-ray diffraction pattern was subsequently matched with the theoretical pattern simulated using single crystal structure data.

II-2-1-1-1-Single crystal structure refinement

II-2-1-1-2-a-Structure refinement of $MnSb_2Se_4$

A black needle-shape single crystal of $MnSb_2Se_4$ with approximate dimensions of 0.04 × 0.09 × 0.25 mm^3 was used for X-ray data collection. Intensity data were recorded at 300 K on a STOE Imaging Plate Diffraction System (IPDS-2T) presented in the Figure II-2 using a graphite-monochromated MoK_α radiation (λ = 0.71073 Å) and were indexed in the monoclinic crystal system with cell parameters a =13.076(6) Å; b =3.9651(8) Å; c =15.236(4) Å; β =115.1(1)°, which are similar to the unit cell parameters of $FeSb_2Se_4$. Therefore, atomic positions of $FeSb_2Se_4$ were used as starting model for the structure refinement in the space group $C2/m$ (#12) using the SHELTXL package.[3] Initially, Sb atoms were assigned to the general positions M1(4*i*) and M2(4*i*) located respectively in a distorted octahedral and square pyramidal coordination, while Mn atoms were located in special positions M3(2*d*) and M4(2*a*) with octahedral coordination. The refinement of this model using full-matrix least-squares techniques resulted in R_1 = 5% with reasonable thermal parameters for all atoms except Mn4 which displayed smaller thermal parameters compared to those of Sb atoms. This suggested a Mn/Sb mixed occupancy at the M4 position. To allow for a charge balanced final composition, Sb/Mn mixed occupancy at

M1, M2 and M3 positions were also considered. The refinement of this model resulted in more uniform thermal parameters for all atoms and an almost neutral composition with ~5% Mn in each of the Sb1 and Sb2 sites, while the M3 position remained fully occupied by Mn. In the final refinement cycles, an electroneutrality restraint was included along with a secondary extinction correction and anisotropic displacement parameters for all atoms. The occupancy factors at M1, M2 and M4 positions were refined to the final values of M1 = 95%Sb + 5%Mn, M2 = 96%Sb + 4%Mn, and Mn4 = 81%Mn $^{+}$ 19%Sb leading to the final charge balanced composition $Mn_{0.995(3)}Sb_{2.005(3)}Se_4$ assuming 2^+, 3^+, and 2^- oxidation states for Mn, Sb and Se, respectively. The final assignment of Sb and Mn atoms at metal positions and the suggested oxidation state for Sb and Mn atoms in $MnSb_2Se_4$ are consistent with the results of bond valence sum (BVS) calculations (Sb1: 2.8; Sb2: 2.8; Mn3: 2.3; Mn4: 2.2). Summary of crystallographic data for $MnSb_2Se_4$ are given in the Table VIII-1. The atomic coordinates and isotropic displacement parameters of all atoms are given in Table VIII-2. Selected inter-atomic distances are gathered in Table VIII-3 (details on geometrical information are reported in the annex table VIII). The software Diamond was utilized to create the graphic representation of the crystal structure with an ellipsoid representation (98% probability level) for all atoms. Further details of the crystal structure investigation can be obtained from the Fachinformationszentrum Karlsruhe, 76344 Eggenstein- Leopoldshafen, Germany, (fax: +49 7247 808 666; e-mail: crysdata@fiz.karlsruhe.de) on quoting the depository numbers CSD_421940.

II-2-1-1-2-b-Structure refinement of $FeSb_2Se_4$

A black needle-shape single crystal of $FeSb_2Se_4$ and $Fe_{0.87}Sb_2Sn_{0.13}Se_4$ with approximate dimensions of 0.04 × 0.09 × 0.25 mm^3 was used for X-ray data collection. Intensity data were recorded at from 120 K to 400 K and indexed in the monoclinic crystal system with cell parameters a = 13.076(6)/13.069(3) Å; b = 3.9651(8)/3.9671(8) Å; c = 15.236(4)/15.192(4) Å; β = 115.1(1)/114.99(3)º at 120K/300K; and a = 38.2254(76) Å b = 3.9708(8) Å c = 15.1907(30) Å β = 111.272(30)° at 350K. The high temperature data were collected using an OXFORD CRYOSYSTEMS, Cryostream 700 Series as heat supplier. The structures were solved by the direct methods in the space group $C2/m$ (#12) with the SHELTXL package. Initially, Sb atoms were assigned to the general positions M1 (4*i*) and M2 (4*i*) located respectively in a distorted octahedral and square pyramidal coordination, while Fe atoms were located in special positions

M3 (2*d*) and M4 (2*a*) with octahedral coordination. The refinement of this model using full-matrix least-squares technique resulted in *R*1 = 5% with reasonable thermal parameters for all atoms except Fe4 which displayed smaller thermal parameter compared to those of Sb atoms. This suggested a Fe/Sb mixed occupancy at the M4 position. To allow for a charge balanced final composition, Sb/Fe mixed occupancy at M1, M2 and M3 positions were also considered. The refinement of this model resulted in more uniform thermal parameters for all atoms and an almost neutral composition with ~4% Fe in each of the Sb1 and Sb2 sites while the M3 position remained fully occupied by Fe. In the final refinement cycles, an electroneutrality restraint was included along with a secondary extinction correction and anisotropic displacement parameters for all atoms. The occupancy factors at M1, M2 and M4 positions were refined to the final values of M1 = 96% Sb + 4% Fe, M2 = 96% Sb + 4% Fe and M4 = 86% Fe + 14% Sb, with a charge balanced formula of Fe0.999(1)Sb2.001(1)Se4 assuming 2+, 3+, and 2- oxidation states for Fe, Sb and Se respectively. The low-temperature intensity data of $FeSb_2Se_4$ were also indexed in the monoclinic crystal system with unit cell parameters a = 13.020(1) Å, b = 3.955(1) Å, c = 15.180(4) Å and β = 114.90(1)^o. At 120 K, $FeSb_2Se_4$ was refined using atomic positions of the structure at 300 K as the starting model. The same procedure used to refine $FeSb_2Se_4$ at room temperature was also used to achieve the R-factor R1 = 1.75 % and *wR2* = 4.51 % in the case of $FeSb_2Se_4$ at 120 K. The details for high temperature data is reported in Section IV-3. Further details on the crystal structure investigation at low temperature can be obtained from the Fachinformationszentrum Karlsruhe, 76344 Eggenstein- Leopoldshafen, Germany, (fax: +49 7247 808 666; e-mail:5 crysdata@fiz.karlsruhe.de) on quoting the depository numbers CSD_421938 ($FeSb_2Se_4$ at 300K) and CSD_421939 ($FeSb_2Se_4$ at 120K).

II-3-Transport Properties Measurement

II-3-1- Low Temperature Resistivity, Seebeck, Thermal conductivity and Hall Effect

A rectangular-shape specimen with dimensions of 2.4 mm × 2.6 mm × 11 mm cut from a 96% dense hot pressed pellet of specimen were used for low temperature measurements of electrical conductivity, Seebeck coefficient and thermal conductivity. These experiments were carried out in our collaborator research group (Prof. Ctirad Uher's group). Electrical resistivity (ρ) and thermopower (*S*) were measured simultaneously from 300 K to 140 K using (1) the standard four-probe method in a Quantum Design Physical Property Measurement System (PPMS) and

(2) the four-probe longitudinal steady-state technique using a liquid ^{4}He cryostat. In the latter method, samples were mounted on the cryostat and protected from excessive radiation loss by two radiation shields. One end of the sample was attached to a heat sink by indium solder. The heat sink was the cold tip of the liquid helium cryostat, and the temperature was adjusted using a Lakeshore 340 temperature controller. Heat input to the sample was made via a small 350 Ω strain gauge heater attached to the free end of the sample using varnish. The heat flow injected by the heater developed a temperature difference ΔT between the two points along the length of the sample. Fine copper (Cu) wires were selected as Seebeck / resistive probes due to their small resistivity and thermopower

II-3-2- High Temperature Resistivity, Seebeck, Thermal Conductivity and Hall Effect

Sample for high temperature thermal conductivity, electrical resistivity and thermopower measurements were obtained by consolidating polycrystalline materials under a dynamic vacuum of ~10^{-4} Torr. Pellets were fabricated using a uniaxial hot press by simultaneously applying a maximum pressure of 100 MPa and a maximum temperature of 500 ^{o}C. The samples were placed into a graphite die with an inner diameter of 10 mm and then sintered under vacuum (10^{-5} Torr). The final working set point of pressure (100 MPa) was first reached with a ramp of 2 MPa/min, followed by a hold of 4 h while the temperature was still rising to 500 ^{o}C. The maximum temperature and pressure were kept for 1 h to achieve higher strengthening and good compaction of the pellet. The sample was then cooled to room temperature. The density of the resulting pellet was determined by measuring the dimensions and mass. Usually a final density of about 95% was obtained in most of the samples

Thermal diffusivity data were measured using a Netzsch LFA 457 laser flash system. A pyroceram reference material was measured alongside each sample. Measurements were made under flowing N_2 gas (>30 mL/min) from 300 K to 775 K at increments of 25 K. C_p values for thermal conductivity calculations were extracted from the laser flash data. The instrument precision for the thermal diffusivity data is ± 6%. Seebeck coefficient and electrical resistivity were measured simultaneously from 375 to 775 K under a low pressure of He atmosphere using a commercial ZEM-3 system from ULVAC-RIKO which uses the standard four probe method..

II-3-3-Magnetoresistance

One of the main purposes of this work is to prove the presence of polarized electron in the multinary complex transition metal chalcogenide. This has already been highlighted in other chalcogenide magnetic semiconductors.[4,5] This is the change of the resistivity when a magnetic field is applied across the sample. The magnetoresistance was measured in our collaborator laboratories (Ctirad Uher's group at University of Michigan and David P. Young at Louisiana State University). In both laboratories, the magnetoresistance were measured using the MPMS on hot pressed shaped with 1 mm x 1 mm x 6 mm. An applied field between of -90 KOe to 90 KOe was used.

II-3-4-The Hall Effect

The normal hall effect of different samples has been measured using the Quantum Design MPMS system from low to high temperature. The Hall Effect refers to the potential difference (Hall voltage) on the opposite sides of an electrical conductor through which an electric current is flowing, created by a magnetic field applied perpendicular to the current. Bulk rectangular shaped specimen is mounted, and indium solder contacts are made in a hall bar configuration. The hall resistance is measured through a resistance bridge with 6 digit accuracy for a given range. From Hall Effect we have more information about the mobility (μ), the carrier concentration p (hole) and n (electron). In most of the samples presented we are dealing with hole concentration (p).

II-4 -The Magnetic Properties

The direct current (DC) magnetic susceptibilities of all specimens were investigated from 2 K to 300 K using a Quantum Design MPMS-XL SQUID magnetometer. Approximately 50 mg of the as synthesized polycrystalline specimen powder materials was mounted inside a clear plastic straw sample holder, the magnetic moment contribution of which was subtracted from the combined (sample + sample holder) measurement. DC magnetic susceptibility data were collected using applied magnetic fields of 100 Oe and 1000 Oe. Field-dependent magnetization measurements were performed from 2 K to 600 K using up to 50 kOe applied magnetic field. AC

susceptibility data for $FeSb_2Se_4$ were recorded on cooling and heating (between 90 K and 150 K), at 10 kHz and applying an AC field of 10 Oe. Isothermal magnetization measurements were carried out at temperatures between 2 K and 300 K in DC magnetic fields varying from 0 to 20 kOe. AC magnetic susceptibility measurements were performed on about 40 mg – 70 mg of polycrystalline $MnSb_{2-x}Sn_xSe_4$. The AC susceptibility at different frequencies was collected on the same sample used for the DC measurements. The applied magnetic field used for the AC magnetic susceptibility was 0.1 Oe, and data were collected within the temperature range between 5 K and 100 K. Field-dependent magnetization measurements were performed at 4 K on the samples with x = 0.05, 0.1 and 0.15 in applied magnetic fields up to 5 kOe. Detailed for high temperature measurement is reported in the section IV-3.

References

(1) http://www.gpgyjr.com.cn/ In *Induction melting* 2013.
(2) http://nvlpubs.nist.gov/nistpubs/jres/104/3/html/j43nav.htm In *Induction melting block diagram* 2013.
(3) Sheldrick, G. M. In *Bruker Analitical X-ray Intruments, Inc*; V6.12 ed.; v6.12, Ed.; Bruker Analitical X-ray Intruments, Inc: Madison, WI, 2000.
(4) Menyuk, N.; Dwight, K.; Arnott, R. J.; Wold, A. *Journal of Applied Physics* **1966**, *37*, 1387.
(5) Prinz, A.; Brunthaler, G.; Ueta, Y.; Springholz, G.; Bauer, G.; Grabecki, G.; Dietl, T. *Physical Review B,* **1999**, *59*, 12983.

Chapter III
Structural-Distortion-Driven Cooperative Magnetic and Semiconductor-to-Insulator Transitions in Ferromagnetic $FeSb_2Se_4$.

Introduction

Transition metal compounds exhibiting spontaneous drops in magnetization are being investigated for use as molecular switches, sensors, and data storage devices. This phenomenon of magnetization change is generally associated with spin transition or spin crossover (high spin to low spin) induced by temperature, pressure, or irradiation, and is generally found in insulating antiferromagnetic oxides[1-5] and in transition metal complexes containing $3d^n$ ($4 \leq n \leq 7$) ions, such as iron(II), iron(III), or cobalt(III)[3,6-12], in octahedral or square planar coordination[2,5,9]. Spontaneous loss of magnetization can also be induced by other mechanisms, such as the spin dimerization observed in $CuIr_2S_4$,[13] the so-called spin-Peierls transition[14-17] observed in $CuGeO_3$, and the Verwey transition[18-20], which is commonly observed in mixed-valence transition metal oxides with the AB_2X_4 spinel or inverse spinel structures such as magnetite (Fe_3O_4)[21]. The loss of magnetization in Verwey compounds is accompanied by a metal-to-insulator transition, which is interpreted as resulting from long-range ordering of the mixed-valence ions within the B sites of the spinel structure[22].Herein we present the observation of room-temperature ferromagnetism, semiconductivity, and reversible, cooperative magnetic and semiconductor-to-insulator (SI) transitions in $FeSb_2Se_4$. To the best of our knowledge, the coexistence of these phenomena in a single transition metal chalcogenide compound has not been reported to date. Despite the analogy of stoichiometry between $FeSb_2Se_4$ and $CuIr_2S_4$[13] and the similarity in the formal distribution of charges between $Fe^{2+}(Sb^{3+})_2(Se^{2-})_4$ and $Fe^{2+}(Fe^{3+})_2(O^{2-})_4$ (magnetite), the crystal structures of these compounds are profoundly different and none of the mechanisms mentioned

above is suitable for the interpretation of the phase transitions observed in the three-dimensional monoclinic structure of $FeSb_2Se_4$. Therefore, alternative mechanisms to explain the observed transitions must be explored. Because the nature of the phase transitions in $FeSb_2Se_4$ can be rather complex, we have tackled the problem by performing systematic investigations of 1) the crystal structure above and below the transition temperature, 2) the thermal evolution of unit cell parameters using X-ray diffraction on powder and on single-crystal samples, 3) the electrical resistivity, and 4) the magnetic properties across the transition temperature.

III-1-Crystal Structure of $FeSb_2Se_4$ at 120K and 300K

$FeSb_2Se_4$ (Experimental details is reported on section **II-2-1-1-2-b**) crystallizes in the monoclinic space group *C* 2*m* (No.12) with lattice parameters a = 13.069(3)Å, b = 3.9671(8)Å, c = 15.192(4)Å, and β = 114.99(3)°, and it is isostructural with $MnSb_2S_4$[23]. The structure contains four crystallographically independent metal positions and four Se positions. All metal sites located at special positions (Fe(3) at (0,1/2,1/2) and Fe(4) at (0, 0, 0)) showed strong preference for the iron atom. The Fe(3) position is fully occupied by Fe, whereas the Fe(4) position contains

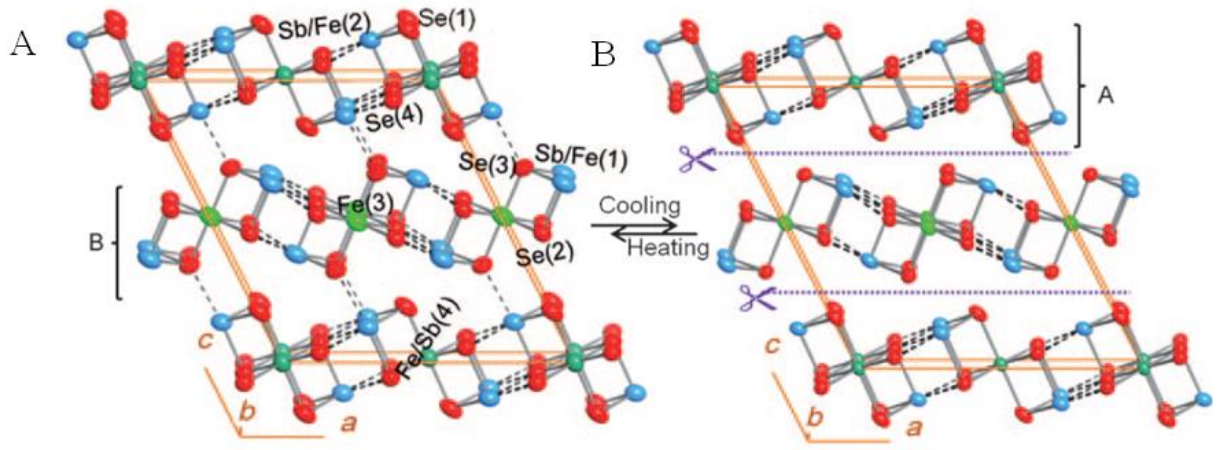

Figure III - 1 Representations of the crystal structures of $FeSb_2Se_4$ at 300K (A) and 120K (B); ellipsoids set at 98% probability for all atoms. To highlight the difference between the structures, a bond threshold of 3.12Å was used. The structure reversibly distorts from a three dimensional (3D) network to a two-dimensional (2D) layered structure upon cooling to 120K due to the expansion (weakening) of the Sb(2)−Se(3) bond connecting adjacent layers A and B.

some Sb in the ratio 85 %(Fe) to 15 %(Sb). Both Fe positions are coordinated by six selenium atoms with Fe(3) located in a distorted [2 + 4] octahedral geometry with two short axial bonds

and four long equatorial bonds, whilst Fe(4) is found in an almost regular octahedral geometry with interatomic distances ranging between 2.680(2) and 2.704(1)Å as reported in the Table III-1. In the structure, $\{M\}Se_6$ octahedra (M = Fe or Fe/Sb) share edges to form one-dimensional chains running along the *b*-axis.$[\{Fe(4)\}Se_6]_\infty$ chains are interconnected by the Sb(2) atom in a distorted [1 + 2 + 2 + 1] octahedral coordination of Se atoms to build a layer denoted A (Figure III-1-A). Likewise,$[\{Fe(3)\}Se_6]_\infty$ chains are linked by the Sb(1) atom in a distorted [1 + 2 + 2] square pyramid of Se atoms to form layer B, which alternates with layer A along the c axis. Because of the partial Sb substitution at the Fe(4) position (0, 0, 0), the remaining Fe atoms (ca. 15 %) are distributed almost equally in both Sb positions with the ratio of 96 %(Sb) to 4 %(Fe) (Table III-2). The refined formula of the compound (Table III-3) and bond valence sum calculations[24] (Table III-4) indicate + 2, + 3, and − 2 oxidation states for Fe, Sb, and Se, respectively.

Table III-1 : Selected inter-atomic distances (Å) in $FeSb_2Se_4$ at 300K and 120K and relative contraction of individual bonds. * indicates bonds showing expansion upon cooling.

Bond	300K	120K	$\Delta d/d_0$
Sb1|Fe1—Se2	2.603(2)	2.600(1)	-0.12
Sb1|Fe1—Se3(x2)	2.731(2)	2.720(1)	-0.40
Sb1|Fe1—Se2(x2)	3.114(2)	3.109(1)	-0.16
Sb1|Fe1—Se1(x2)	3.620(2)	3.614(1)	-0.17
Sb2|Fe2—Se4	2.682(2)	2.669(1)	-0.48
Sb2|Fe2—Se1(x3)	2.718(2)	2.711(1)	-0.26
Sb2|Fe2—Se4(x2)	3.087(2)	3.082(1)	-0.16
Sb2|Fe2—Se3	3.118(2)	3.123(1)*	0.16
Fe3—Se3(x2)	2.548(2)	2.546(1)	-0.08
Fe3—Se3(x2)	2.721(1)	2.7096(1)	-0.42

Fe4|Sb4—Se1(x2)	2.680(2)	2.671(1)	-0.34
Fe4|Sb4—Se1(x2)	2.704(1)	2.692(1)	-0.44

Table III-2. Atomic coordinates, Wyckoff positions (W.P.), site occupancy factors (*k*), and equivalent isotropic displacement parameters $U_{eq}/10^{-4}$Å^2) for all atoms in the asymmetric unit of $FeSb_2Se_4$ (300K/*120K*)

Atom	W.P	k	x	y	z	U_{eq}
Sb1	4i	0.96(1)/ 0.96(1)	0.2735(8)/ 0.2736(8)	0	0.6334(9)/ 0.6336(3)	214(2)/ 126(1)
Fe1	4i	0.04(1)/ 0.04(1)	0.2735(8)/ 0.2736(8)	0	0.6334(9)/ 0.6336(3)	214(2)/ 126(1)
Sb2	4i	0.96(1)/ 0.96(1)	0.3547(7)/ 0.3548(1)	0	0.1259(6)/ 0.1259(6)	181(2)/ 112(1)
Fe2	4i	0.04(1)/ 0.04(1)	0.3547(7)/ 0.3548(1)	0	0.1259(6)/ 0.1259(6)	181(2)/ 112(1)
Fe3	2d		0	1/2	1/2	227(5)/ 122(2)
Sb4	2a	0.16(1)/ 0.14(1)	0	0	0	170(6)/ 92(2)
Fe4	2a	0.84(1)/ 0.86(1)	0	0	0	170(6)/ 92(1)
Se1	4i		0.0116(5)/ 0.0118(5)	0	0.1803(8)/ 0.1800(2)	207(3)/ 129(1)
Se2	4i		0.1144(6)/	0	0.4574(6)/	165(3)/

		0.1144(6)		0.4578(8)	99(1)
Se3	4i	0.3448(8)/	0	0.3274(7)/	182(3)/
		0.3447(7)		0.3275(9)	106(1)
Se4	4i	0.6551(2)/	0	0.0539(7)/	182(3)/
		0.6546(7)		0.0534(6)	115(1)

U_{eq} is defined as one-third of the trace of the orthogonalized U_{ij} tensor

Table III-3. Selected crystallographic data for $FeSb_2Se_4$ at 300K and 120K

Temperature	300K	120K
Crystal system ; space group	Monoclinic ; *C* 2/*m*(#12)	Monoclinic ; *C* 2/*m*(#12)
Formula weight(g/mol)	615.19	615.19
Density ($\rho_{cal.}$)(g/cm^3)	5.72	5.76
Lattice parameters/Å		
a =	13.069(3) Å	13.020(1) Å
b =	3.967(1) Å	3.955(1) Å
c =	15.192(3) Å	15.180(4) Å
β =	114.99(3) °	114.90(1) °
Volume(Å^3) ; Z	714(1) Å^3 ; 4	709(1) Å^3 ; 4
Crystal size (mm)	0.02x0.03x0.15	0.02x0.03x0.15
Crystal shape, color	Needle-shape ; Black	Needle-shape ; Black
Radiation/Å	$\lambda(MoK_\alpha)$ = 0.71073	$\lambda(MoK_\alpha)$ = 0.71073
μ/cm^{-1}	298	300

Diff.elect.density(e/Å^3)	+1.09 to − 0.99	+ 2.10 to – 2.17
R_1(Fo>4σ(Fo))[a]	0.020	0.017
wR_2 (all)[b]	0.054	0.45
GooF	1.242	1.060

[a] $R_1 = \sum||F_0|-|F_c||/\sum|F_0|$ [b] $wR_2 = [\sum w(F_0^2 - F_c^2)^2/\sum w(F_0^2)^2]^{1/}$

Table III-4: Bond valence sums (BVS)* for $FeSb_2Se_4$ at 300K and 120K

Atom	BVS-300K	BVS-120K	Expected BVS	Oxidation state
Sb1	2.8	2.9	3	3+
Sb2	2.8	2.9	3	3+
Fe3	2.2	2.3	2	2+
Fe4	1.9	2.0	2	2+

* BVS = Σνi; νi =Exp[(R0-d*i*)/0.37], R0(Sb-Se) = 2.57 Å; R0(Fe-Se) = 2.28Å.

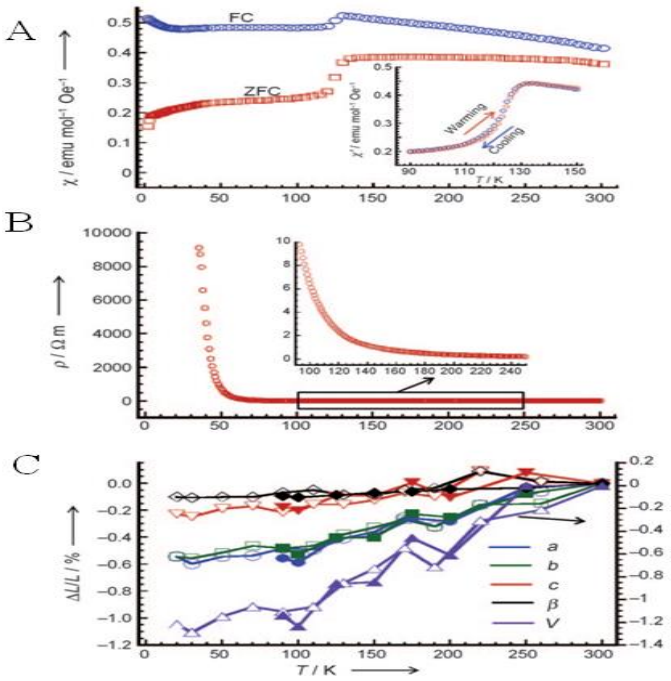

Figure III - 2 Manifestation of anisotropic lattice-distortion-driven magnetic and semiconductor–insulator transitions in $FeSb_2Se_4$. A) Field cooled (FC) and zero-field-cooled (ZFC) magnetic susceptibility, showing a magnetic transition at about 130K. The observed drop in magnetization is reversible as indicated by the AC magnetic susceptibility on cooling and warming (see inset in (A)). B) Temperature dependent electrical resistivity, showing spontaneous jumps at 130K and 50K. C) Thermal behavior of the unit cell parameters between 300 K and 20 K, showing preferential lattice contraction within the *ab* plane. $\Delta L/L$ represents the relative contraction of unit cell parameters a, b, c, and b as well as the unit cell volume *V* upon cooling. Open symbols: from X-ray powder patterns; filled symbols: from single crystal X-ray analysis.

III-2-Magnetic Properties of $FeSb_2Se_4$

As shown in Figure III-2A, $FeSb_2Se_4$ remains ferromagnetic over the entire measured temperature range from 2K to 300K. The susceptibility increases slowly with decreasing temperature down to about 130 K, at which point a spontaneous drop on the susceptibility is observed. From 130 K to about 10K, the susceptibility remains almost constant, and slightly increases below 10 K (FC curve). Interestingly, AC magnetic susceptibility data revealed that the

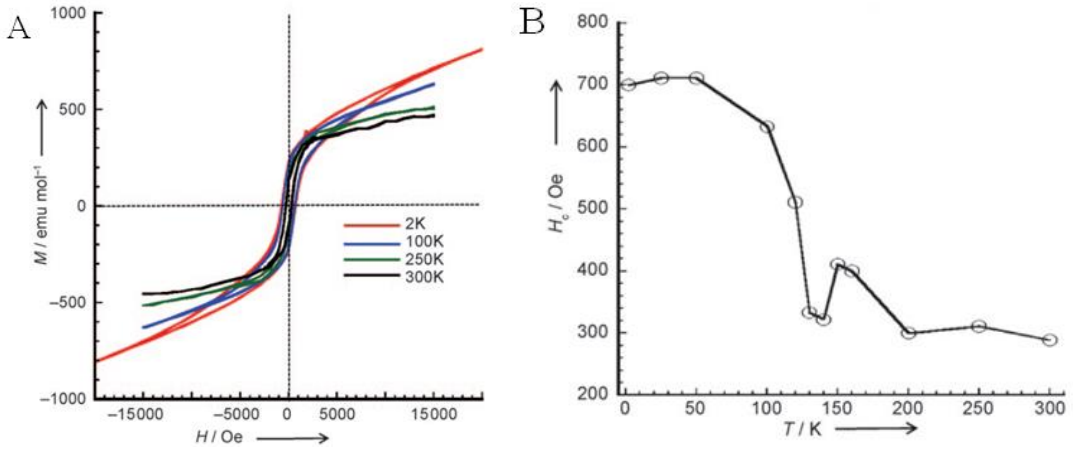

Figure III - 3 Ferromagnetic behavior of $FeSb_2Se_4$ between 2K and 300K.A) Field-dependent isothermal magnetization of $FeSb_2Se_4$ measured at 2K, 100K, 250K, and 300K with applied fields of up to 15kOe. The ferromagnetic behavior of compound is maintained above and below the transition temperature (130K). b) Temperature dependence of the coercivity of $FeSb_2Se_4$, showing a spontaneous drop at about 150 K.

drop in the magnetization is recovered almost without hysteresis upon warming the sample through the transition temperature (Figure III-2A, inset), indicating the reversible character of the magnetic transition at 130K in $FeSb_2Se_4$. To further investigate the nature of the transition around 130K, we have carried out isothermal magnetization at various temperatures between 2K and 300K (Figure III-3A ; Supporting Information, Figure S1). Magnetization data at 2K shows a mild hysteresis with coercivity of about 700Oe, which is typical for a soft ferromagnet. The magnetization curve at room temperature still showed a hysteresis with a sizable coercivity of about 300Oe and a saturation magnetization value of about 500 $emu.mol^{-1}$ at an applied field of 15kOe, thus confirming the ferromagnetic behavior of $FeSb_2Se_4$ at room temperature. The sizable values of the magnetic susceptibility (Figure III-2A) and coercivity at 300K suggest a fairly high ferromagnetic ordering temperature for $FeSb_2Se_4$. Careful examination of isothermal

magnetization curves around the transition temperature (Figure III-4) revealed that the hysteresis shape is conserved above and below the transition. Furthermore, the coercivity of $FeSb_2Se_4$ slowly increases with decreasing temperature, drops spontaneously around 150K, and increases rapidly thereafter with further cooling (Figure III-3B). The above findings suggest that the ferromagnetism of the compound is maintained after the transition.

III-3-Relation Structure-Magnetic Properties

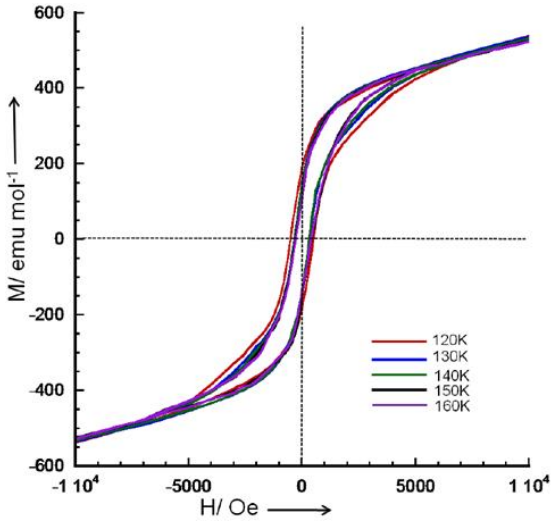

Figure III - 4 Field dependent isothermal magnetization of $FeSb_2Se_4$ measured at temperatures between 120 and 160K with applied fields of up to 15kOe. The ferromagnetic behavior of compound is maintained throughout the magnetic transition around 130K

To understand the magnetic behavior of $FeSb_2Se_4$, we have examined the coupling between spins located on adjacent Fe atoms using the Goodenough–Kanamori rules[25-27]. As described above, the geometry of the Fe(3) and Fe(4) coordination polyhedron and also the length of Fe-Se bonds are very different. These parameters can influence the crystal field splitting energy (*Δo*) and thus the ordering of the iron $3d^6$ orbitals, as well as the spin distribution within the orbitals. Along this line, the [$FeSe_{2+4}$] geometry of the octahedral coordination around Fe(3) suggests a Jahn–Teller distortion of $3d^6$ orbitals with spin distribution of $(d_{xy})^2(d_{xz}, d_{yz})^1(d_{x^2-y^2})^1(d_{z^2})^1$, leading to a total spin value of S = 2 (high spin),whilst the almost-perfect [$FeSe_6$] configuration of the octahedral coordination of Fe(4) suggests an octahedral splitting of $3d^6$ orbitals with a spin distribution of $(d_{xz}, d_{yz}, d_{xy})^2$ $(d_{z^2}, d_{x^2-y^2})^0$ corresponding to a total spin value of S = 0 (low spin). Therefore, the structure can be viewed as a bistable system consisting of diamagnetic layers A of Fe(4) atoms in a low-spin state (S =0) alternating along the *c*-axis with the magnetic layers B of Fe(3) atoms in a high-spin state (S = 2). Adjacent magnetic layers B are isolated magnetically from each other by the large distance of 15.192(3)Å between them. Therefore, the magnetic properties of $FeSb_2Se_4$ are controlled by exchange interactions between magnetic ions within layer B (intralayer interactions). However, $[\{Fe(3)\}Se_6]_\infty$ chains building layer B are about 6.829(2)Å apart suggesting weak interchain interactions. The magnetic properties of $FeSb_2Se_4$ therefore depend on the nature and magnitude of intrachain exchange interactions between adjacent magnetic ions. Along the chain (b axis), the Fe(3)−Fe(3) distance of 3.967(2)Å is too long for direct magnetic exchange interactions between the magnetic moments on neighboring Fe atoms. Therefore, adjacent Fe(3) atoms are magnetically coupled via indirect exchange interactions through the bridging Se(2) atom. The observed Fe(3)−Se(2)−Fe(3) angle of 93.6(1)8 suggests weak ferromagnetic coupling of spins located on adjacent Fe atoms in an individual chain. This analysis

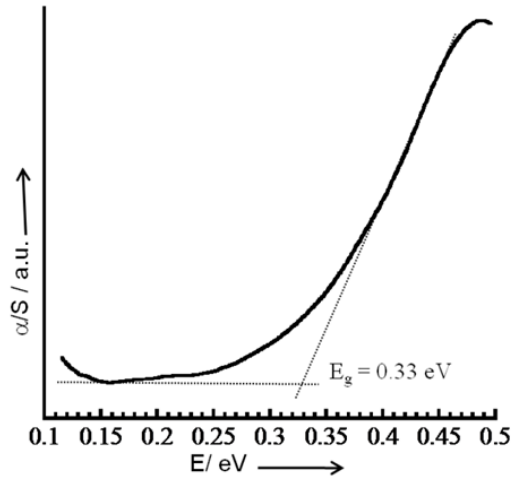

Figure III - 5 Optical absorption spectrum of FeSb2Se4 measured at 300K showing a narrow energy band gap of ~ 0.33 eV. The observed band gap is consistent with the dark gray color of the polycrystalline powder of $FeSb_2Se_4$

is consistent with the small values of magnetic susceptibility and magnetization measured around 300K.

The drop in magnetic susceptibility observed around 130K in $FeSb_2Se_4$ is accompanied by a sharp increase of the electrical resistivity (semiconductor–insulator transition) at about the same temperature. As shown in Figure III-2B and Figure III-5, $FeSb_2Se_4$ at room temperature is a narrow band gap semiconductor with electrical resistivity of 0.16 Ω.m and an optical band gap of 0.33 eV. The electrical resistivity initially increases slowly with decreasing temperature down to about 130 K, after which a rapid increase by an order of magnitude is observed. As the temperature decreases further, a sharper jump by four orders of magnitude in the resistivity occurs around 50 K and an out of- range resistivity (> 10kΩ.m) is reached below 35K (Figure III-2B). The sharp increase in the electrical resistivity of $FeSb_2Se_4$ suggests a semiconductor-to-insulator (SI) transition. The observed simultaneous change in the magnetic susceptibility and electrical resistivity around 130K suggests that both transition processes in $FeSb_2Se_4$ are induced by the same driving force.

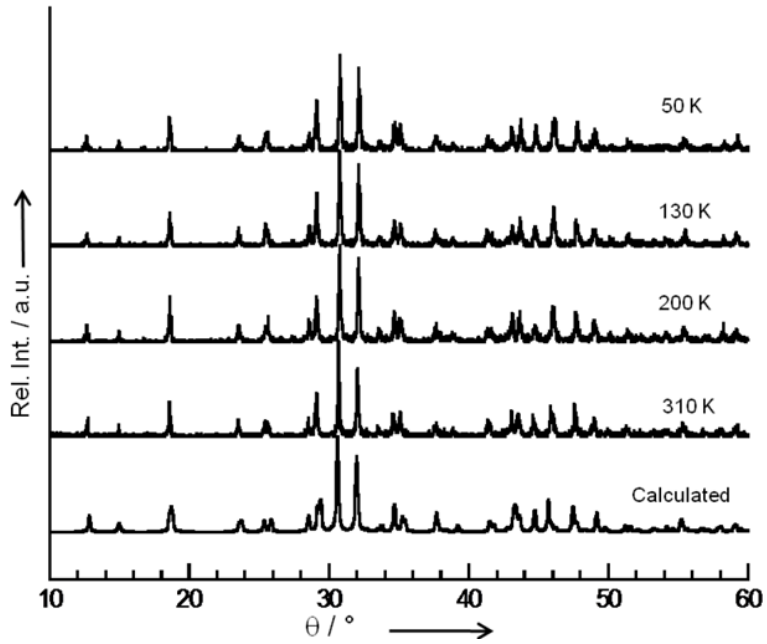

Figure III - 6 Selected X-ray diffraction patterns of polycrystalline FeSb2Se4 powder measured at various temperatures between 20 and 300K, compared with the theoretical pattern calculated from single crystal structure data at 300K. No appearance/disappearance of small peaks or peak splitting which would suggest breaking of symmetry could be detected above the XRD background.

To understand the nature and the origin of the transitions in the magnetic susceptibility and electrical resistivity data and to examine the possibility of a structural phase change that may be responsible for these transitions, we carried out X-ray diffraction experiments on powder (XRPD) and on a single crystal at temperatures between 20K and 300K and have determined the thermal

evolution of the lattice parameters. Furthermore, we have also performed the structure determination of $FeSb_2Se_4$ at 120K (below the transition at 130K). The powder diffraction patterns were recorded on heating and on cooling and all peaks were indexed with the monoclinic structure of $FeSb_2Se_4$. No appearance disappearance of small peaks or peak splitting that would suggest breaking of symmetry could be detected above the XRD background (Figure III-6). The refinement of the unit cell parameters at various temperatures reveals fast contraction of the a and b parameters upon cooling (Figure III-2C), whilst the c parameter and b angle first expand and then contract slowly with decreasing temperature. This effect suggests an increase in the strength of anisotropic distortion of the unit cell parameters with decreasing temperature. Similar thermal evolution of the unit cell parameters was also observed on single-crystal data (Figure III-2C). The observed anisotropic lattice distortion in $FeSb_2Se_4$ is reversible without hysteresis upon heating. The absence of symmetry breaking upon cooling suggests that the transition observed around 130 K in the magnetic and resistivity data of $FeSb_2Se_4$ does not induce major structural changes.

The structure of $FeSb_2Se_4$ at 120K was determined using the same single crystal employed for the structure determination at 300K. Analysis of diffraction data indicated no change in the crystal symmetry (monoclinic space group *C*2*m*), and the contraction of unit cell parameters is consistent with XRPD results (Table III-3). The structure at 120K was refined using structural parameters of $FeSb_2Se_4$ obtained at 300K as the starting model. The overall quality of the fit was excellent (Table III-3), and indicates that no major structural changes occur upon cooling through the transition temperature. The refined structure of $FeSb_2Se_4$ at 120K and 300K drawn using a M−Se (M = Fe, Sb) bond threshold of 3.12Å (longest Sb-Se bond at 300K) are compared in Figure I. To detect structural differences that might provide some insights on the origin and the underlying mechanism of the observed magnetic and SI transitions, we have carefully analyzed the variation of chemical bonding within the structure of $FeSb_2Se_4$ upon cooling below the transition temperature at 130K (Table III-1). The direct consequence of the strong preferential contraction of the *a* and *b* parameters upon cooling through the transition temperature is the sharp decrease in the length of all interatomic bonds parallel to the ab plane, whilst interatomic bonds parallel to the c axis only showed marginal contraction. The strong preferential contraction within the *ab* plane induces an anomalous expansion of the equatorial Sb(2)−Se(3) bond bridging layers A and B, from 3.118(2)Å at 300K to 3.123(1)Å at 120K.

In heavy main group metal chalcogenides with a high degree of covalency, such as the $FeSb_2Se_4$ phase, the balance of short- and long-range interactions is strongly related to the electronic subsystem. Therefore, a small change in the lattice parameters could disturb the electronic subsystem, inducing the spontaneous changes in the electrical resistivity observed in $FeSb_2Se_4$. For instance, careful examination of the structures of $FeSb_2Se_4$ above and below the transition temperature of 130K showed that the preferential contraction within the *ab* plane causes the weakening (electronically) of the connectivity between layers A and B (Sb(2)-Se(3)) leading to a distortion of the structure from the three-dimensional (3D) network (Figure III-1A) to a two-dimensional (2D) layered structure (Figure III-1B). This reduction of dimensionality from 3D to 2D is believed to be responsible for the fast increase in the electrical resistivity observed around 130K (Figure III-2B). The weakening of the Sb(2)-Se(3) bond presumably increases the band gap of the material, which translates into an increase in the electrical resistivity. As the structure continues to distort upon cooling (increasing the $\Delta c/c$ to $\Delta a/a$ ratio; Figure III-2C), we anticipate further increases in the length of the Sb(2) − Se(3) bond, leading to a larger gap between layers A and B. This mechanism is consistent with the sharp increase in electrical resistivity observed below 50K.

As discussed above, the magnetic behavior of $FeSb_2Se_4$ is controlled by indirect exchange interactions between adjacent Fe(3) atoms within individual chains building layer B. The nature and magnitude of the indirect magnetic exchange interactions strongly depend on the Fe(3)-Se(2) − Fe(3) angle[25-27]. In $FeSb_2Se_4$, the observed preferential contraction within the ab plane causes the Fe(3)-Se(2)−Fe(3) angle to increase slightly (from 93.6(1)Å at 300K to 93.8(1)Å at 120K). This increase of angle favors antiferromagnetic coupling of spins located on adjacent Fe atoms in an individual chain at the expense of weak ferromagnetic interactions, resulting in the observed drop in the magnitude of the magnetic susceptibility below 130K. The driving force behind the anisotropic lattice contraction (Figure III-2C) in $FeSb_2Se_4$ upon cooling, which leads to the observed complex and reversible ordering pattern is yet to be understood. However, by looking carefully at the geometry of the $\{Sb(2)\}Se_6$ octahedron bridging layers A and B, we can see that the Sb(2) − Se(3) bond expands (rather than contracting) on cooling below the transition at 130K. Therefore, we can speculate that the stereoactivity of the Sb $5S^2$ lone pair, which is manifested by the expansion of the Sb(2) − Se(3) axial bond (parallel to the *c* axis) is a possible "force" resisting the fast contraction of the c parameter and b angle upon cooling. Presumably

the volume of the {Sb(2)}Se_6 octahedron near 300K is the critical size for the stability of Sb $5S^2$ lone pair and further contraction upon cooling is opposed by an increased stereoactivity of the lone pair. This mechanism is consistent with the observed increase in the degree of lattice distortion in $FeSb_2Se_4$ at temperatures below the transition.

Conclusion

In summary, we have found that the most interesting feature of the $FeSb_2Se_4$ phase is the coexistence of room temperature ferromagnetism and semiconductivity, with a remarkable interplay between reversible magnetic ordering phenomena and semiconductor-to-insulator (SI) transition upon cooling. The observed cooperative magnetic and SI transitions in $FeSb_2Se_4$ are driven by local isostructural distortions arising from the preferential lattice contraction within the ab plane. Such a cooperative transition, to our knowledge, has no precedent in pure inorganic materials and represents a significant increase in the level of complexity with respect to known phase transitions. The sizable difference between the magnetic susceptibility and electrical resistivity of $FeSb_2Se_4$ above and below the transition of 130K shows great promise for application as highly sensitive temperature sensors through the detection of change in the intensity of magnetic and/or electrical responses. Furthermore, the high chemical and thermal stability of $FeSb_2Se_4$ are favorable for processing into molecular-based devices. It is also interesting to note the stability of the monoclinic structure throughout the anisotropic contraction, which points to the exciting prospect of inducing similar magnetic and SI transitions around room temperature by stretching the material along the c axis or through application of weak pressure perpendicular to ac and/ or *bc* planes. It would be interesting to investigate these points experimentally. Another important feature of the $FeSb_2Se_4$ phase is the bistability of Fe atoms in the structure where layers of Fe(3) atoms (layer B) in high-spin state (S = 2) and Fe(4) atoms (layer A) in low-spin state (S = 0) alternate along the c axis. This unique feature could provide a new degree of flexibility and control to the design of next generation molecular memory[7,8,12,28] and data storage devices[12].

References

(1) Kawakami,T.; Tsujimoto,Y.; Kageyama, H.; Chen, X.-Q.; Fu, C. L.; Tassel, C.; Kitada, A.; Suto, S.; Hirama, K.; Sekiya, Y.; Makino, Y.; Okada, T.; Yagi, T.; Hayashi, N.; Yoshimura, K.; Nasu, S.; Podloucky, R.; Takano, M. *Nature Chemistry*, **2009**, *1*, 371.

(2) Badro, J.; Fiquet, G.; Guyot, F.; Rueff, J.-P.; Struzhkin, V. V.; Vankó, G.; Monaco, G. *Science*, **2003**, *300*, 789.

(3) Gutlich, P.; Garcia, Y.; Goodwin, H. A. *Chemical Society Reviews*, **2000**, *29*, 419.

(4) Li, J.; Struzhkin, V. V.; Mao, H.-k.; Shu, J.; Hemley, R. J.; Fei, Y.; Mysen, B.; Dera, P.; Prakapenka, V.; Shen, G. *Proceedings of the National Academy of Sciences of the United States of America*, **2004**, *101*, 14027.

(5) Lin, J.-F.; Struzhkin, V. V.; Jacobsen, S. D.; Hu, M. Y.; Chow, P.; Kung, J.; Liu, H.; Mao, H.-k.; Hemley, R. J. *Nature*, **2005**, *436*, 377.

(6) Gütlich, P.; Hauser, A.; Spiering, H. *Angewandte Chemie International Edition in English*, **1994**, *33*, 2024.

(7) Kahn, O.; Kröber, J.; Jay, C. *Advanced Materials*, **1992**, *4*, 718.

(8) Konig, E.; Ritter, G.; Kulshreshtha, S. K. *Chemical Reviews*, **1985**, *85*, 219.

(9) Real, J. A.; Andrés, E.; Muñoz, M. C.; Julve, M.; Granier, T.; Bousseksou, A.; Varret, F. *Science*, **1995**, *268*, 265.

(10) Real, J. A.; Gaspar, A. B.; Niel, V.; Muñoz, M. C. *Coordination Chemistry Reviews*, **2003**, *236*, 121.

(11) Boukheddaden, K.; Shteto, I.; Hôo, B.; Varret, F. *Physical Review B*, **2000**, *62*, 14796.

(12) Létard, J.-F.; Guionneau, P.; Codjovi, E.; Lavastre, O.; Bravic, G.; Chasseau, D.; Kahn, O. *Journal of the American Chemical Society* , **1997**, *119*, 10861.

(13) Radaelli, P. G.; Horibe, Y.; Gutmann, M. J.; Ishibashi, H.; Chen, C. H.; Ibberson, R. M.; Koyama, Y.; Hor, Y.-S.; Kiryukhin, V.; Cheong, S.-W. *Nature*, **2002**, *416*, 155.

(14) Bray, J. W.; Hart, H. R., Jr.; Interrante, L. V.; Jacobs, I. S.; Kasper, J. S.; Watkins, G. D.; Wee, S. H.; Bonner, J. C. *Physical Review Letters*, **1975**, *35*, 744.

(15) Hase, M.; Terasaki, I.; Uchinokura, K. *Physical Review Letters* , **1993**, *70*, 3651.

(16) Hirota, K.; Cox, D. E.; Lorenzo, J. E.; Shirane, G.; Tranquada, J. M.; Hase, M.; Uchinokura, K.; Kojima, H.; Shibuya, Y.; Tanaka, I. *Physical Review Letters*, **1994**, *73*, 736.

(17) Jacobs, I. S.; Bray, J. W.; Hart, H. R., Jr.; Interrante, L. V.; Kasper, J. S.; Watkins, G. D.; Prober, D. E.; Bonner, J. C. *Physical Review B* , **1976**, *14*, 3036.

(18) García, J.; Subías, G. *Journal of Physics: Condensed Matter*, **2004**, *16*, R145.

(19) Walz, F. *Journal of Physics: Condensed Matter*, **2002**, *14*, R285.

(20) J.E.W.Verwey *Nature* **1939**, *144*, 327.

(21) W.H.Bragg *Nature* **1915**, *95*, 516.

(22) Imada, M.; Fujimori, A.; Tokura, Y. *Reviews of Modern Physics*, **1998**, *70*, 1039.

(23) Pfitzner, A.; Zabel, M.; Rau, F. *Monatshefte für Chemie*,**2005**, *136*, 1977.

(24) Okeeffe, M.; Brese, N. E. *Journal of Amican Chemical Society*, **1991**, *113*, 3226.

(25) Goodenough, J. B. *Physical Review* **1955**, *100*, 564.

(26) Goodenough, J. B. *Journal of Physics and Chemistry of Solids*, **1958**, *6*, 287.

(27) Kanamori, J. *Journal of Physics and Chemistry of Solids*, **1959**, *10*, 87.

(28) Kahn, O.; Martinez, C. J. *Science*, **1998**, *279*, 44.

Chapter IV

On the nature of high temperature ferromagnetism in the p-type $FeSb_2Se_4$ narrow band gap semiconductor

Introduction

The prospect of magnetic semiconductors with a high Curie temperature for new spin-based electronic devices reactivated research interest on these materials.[1,2] Materials in which spins and charge properties coexist provide tremendous features from both fundamental and technological perspective.[3-5] This fundamental aspect, viewed as the cornerstone to boost the search for ideal magnetic semiconductors with tunable ferromagnetic behavior, has revealed interestingly strong correlation between the charge from the semiconductor and the spin of the local magnetic moment.[2,6-17] However, the low Curie temperature exhibited by the early members of magnetic semiconductors (for example, $HgCr_2Se_4$, $HgCr_2S_4$, $CdCr_2S_4$, EuSe and EuS) has restricted applications and investigations in these compounds.[18-20] Recently, the possibility of controlling the ferromagnetic interactions between localized spins by the carriers through spin injection into a normal semiconductor revived the interest in magnetic semiconductors.[5,8,21-24] The literature in the last two decades is well-furnished with interesting properties from diluted magnetic semiconductors (DMSs) and diluted magnetic oxides (DMOs) such as Mn-doped IV-VI, III-V, II-VI and n-type oxides with general formula $A_{1-x}M_x\ O_{n-\delta}$(n = 1or 2).[4,21,25] In this formula, A, M and delta represent the non-magnetic cation, the magnetic cation and the defect concentration respectively. Investigations on these DMSs and DMOs have raised several questions on the origin of ferromagnetism and the mechanism of magnetic exchange interaction. One of the most debated questions is related to the origin of ferromagnetism in the MSs which is can either originate from direct exchange interactions between the local magnetic moments of the magnetic impurity or be related to the indirect exchange coupling between the charge carriers and the local magnetic moments. The latter case has been found to be very important for spin-based

electronics because of the spin-polarized transport expected in some materials with this type of correlation (spin of the carrier and spin of local magnetic moment). In addition, the explanation of high Curie temperatures observed in several magnetic semiconductors materials use theories such as the Zener's model of ferromagnetic metal, p-d Zener[26,27] or Ruderman-Kittel-Kasuya-Yosida (RKKY)[16,28-31] model and Dilet's[32] model, which all consider the contribution of free carriers' spins on the magnetic exchange coupling within the magnetic semiconductor. However, the Zener model was found to be incompatible in the case of magnetic semiconductors but suitable to describe well the magnetism in the metal.[26,27] Therefore, Zener's model was revised according to the two last models to explain the exchange interaction in magnetic semiconductors and DMS's where free carriers can mediate or induce ferromagnetism. The most recent assumption to understand the plausible high Curie temperature in MSs considers carriers to be either localized or delocalized depending on the temperature. In the case of the localized carrier, a collective magnetic ordering is observed at low temperature and the ferromagnetism result from the coupling of the 3d magnetic moment of the transition metal with the donors (electrons) or acceptors (holes) forming bound magnetic polaron (BMP).[9,10,12,33,34] Because of the thermal activation of the acceptors or donors impurities, delocalized charges interact with the spin of the magnetic ion through the spin polarized electrons or holes and this is also possible at high temperature. Therefore, the spin polarized electron or hole and the BMP could be two complementary mechanisms to explain and anticipate the behavior of particular MS with high Curie temperature as recently reported by Calderón et al.*[21]*

Multinary chalcogenide compounds have been reported as potential multifunctional materials able to provide several physical properties such as thermoelectrics, nonlinear optics, photoelectronics, and solid-state electrolytes.[35-37] This is mainly because of the structure flexibility of this class of compounds. This structural flexibility can allow sizable integration of magnetic elements into specific homologous series, therefore turning nonmagnetic materials into magnetic materials with low symmetry.[37,38] Consequently, the chalcogenide compounds can also be used as basic materials for spin-based electronics or to understand the origin of complex and interesting physical properties observed in MSs.[24] The advantages of this new family of compounds as compared to classical DMSs and DMOs range from their low dimensionality to their low symmetry, in addition to the well-ordered solid structure and well-defined site occupancy of the magnetic center over their entire lattice. We have reported several new

ferromagnetic semiconductors based on metal complex chalcogenide with interesting magnetic and transport properties.[37-40] So far, the origin of ferromagnetism at high temperature exhibited in most of these materials was not gaining attention and it turns out to be relevant to understand fundamentally the electronic structure of the ideal ferromagnetic semiconductor with high T_c.

Here, we report the nature and the origin of the ferromagnetic ordering in $Fe_{1-x}Sb_2Sn_xSe4$(x = 0 and 0.13), a narrow band gap magnetic semiconductor. We demonstrate that in $Fe_{1-x}Sb_2Sn_xSe_4$, despite the dominant AFM ordering from superexchange along the *b*-axis and spin frustration from magnetic sub-lattice in their structures, the manifestation of ferromagnetic behavior observed above room temperature could originate from complementary collective magnetic ordering of bound magnetic polarons at low temperatures and mediation by spin-polarized hole at high temperatures.

IV-1-Experimental

IV-1-1-Synthesis of $Fe_{1-x}Sn_xSb_2Se_4$ (x = 0, 0.13)

The compounds were obtained from solid-state reaction of a mixture of high purity elements (Fe, Sb, Se and Sn 99.999%, from Cerac) that were used as purchased. The elements were thoroughly mixed under argon atmosphere using mortar and pestle and sealed in evacuated quartz tube under residual pressure of ~10^{-3} Torr. All sample mixtures were then placed in the furnace with temperature heating rate of 48K/h to 573K. The reaction was kept at this temperature for 24h. This first step is required to allow low melting elements (Se) to react completely with other elements and to avoid any explosive reactions. The temperature was then ramped up to 773K over 12h, dwelled for 72h, and finally cooled slowly to room temperature over 48h.

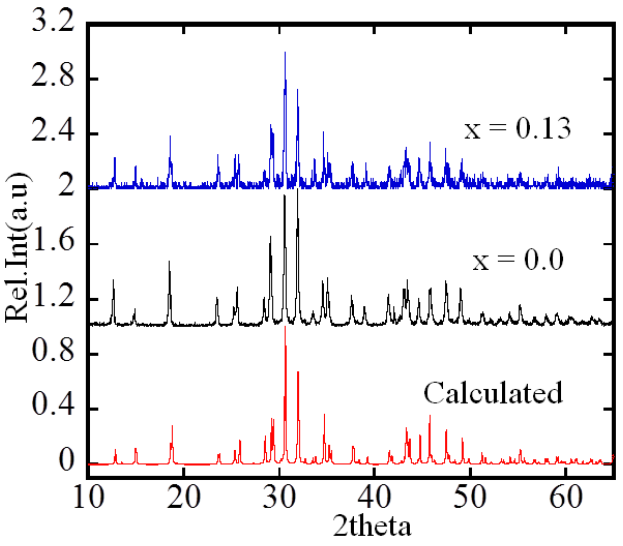

Figure IV- 1: X-ray powder diffraction calculated (red) and experimental (x = 0, 0.13) of $Fe_{1-x}Sb_2Sn_xSe_4$ at 300K. Perfect matching is observed between the experimental pattern and calculated, validating the structure of $FeSb_2Se_4$ and $Fe_{1-x}Sb_2Sn_xSe_4$.

IV-1-2-X-ray diffraction, neutron diffraction, phase identification of $Fe_{1-x}Sn_xSb_2Se_4$ (x= 0, 0.13)

IV-1-2-1- X-ray powder diffraction

X-ray powder diffraction (XRD) data were recorded on a Philips X'Pert system equipped with a curved graphite monochromator and Cu Kα radiation (λ = 1.5418 Å). Standard X-ray data were collected in a step-scanning mode with a 0.02° step width and 10s count time in the 2θ range of 15-75° (Figure IV-1).

IV-1-2-2-Single crystal X-ray diffraction of $Fe_{0.87}Sb_2Sn_{0.13}Se_4$

A black needle-shaped crystal of $Fe_{0.87}Sb_2Sn_{0.13}Se_4$ was mounted on glass fibers with epoxy and intensity data were collected at 120K, 300K, 350K and 400K on STOE IPDS-2T diffractometer. Intensity data were recorded using graphite monochromatized CuKα radiation (λ = 1.5418Å).Temperatures were controlled using an OXFORD CRYOSYSTEMS, Cryostream 700 Series as heat supplier with temperature ramping rate of 50K/h. Intensity data at low and high temperatures were indexed in monoclinic crystal system with unit cell parameters: a = 13.037(3)/13.083(3)/38.243(8)/27.543(6)Å, b = 3.9599(8)/3.9723(8)/3.9727(8)/3.980(8)Å, c = 15.171(3)/15.171(3)/15.174(3)/26.22(5)Å and β = 114.67(3)/114.78(3)/111.21(3)°/90.72(3) for the structures at 120K, 300K, 350K and 400K, respectively. These structures were refined using the SHELTXL package [41]

Intensity data at 120K, 300K and 350K were indexed in the space group *C* 2/*m* (No.12); while at 400K the space group changes to *C* 2/*c* (No.15). The structures at 120K and 300K were refined using the structure model of $FeSb_2Se_4$.[40] The structure solution at 350K (space group *C* 2/*m*) revealed 10 metal positions and 12 selenium atom positions. The first refinement cycle revealed that, Sb1, Sb2 and Sb3 atoms were located in the distorted octahedral positions while the Sb4, Sb5 and Sb6 were located in the distorted square pyramidal positions. All Fe positions identified as Fe1(*2d*), Fe2(*4i*), Fe3(*2a*) and Fe4(*4i*) were located in the octahedral distorted environment. The refinement of this model gave an unweighted residual factor R1~14%. In the model obtained from this first refinement with the starting composition $FeSb_{1.80}Sn_{0.2}Se_4$, the thermal parameters of Fe1 and Fe2 was slightly lower compared to the average value in all other positions. This suggests a mixed occupancy of the Fe atom in these positions with heavy atoms. These positions were then mixed with Sn to respect the charge balance in the final composition. Refinement of all mixed occupancy sites with appropriate constraints yielded acceptable thermal parameters for

all atoms and the value of R1 dropped to 6.55%. The refinement of this model with a secondary extinction correction and anisotropy displacement for all atoms gave the final composition $Fe_{0.866}Sb_2Sn_{0.134}Se_4$ with R1~4.40%. Similarly, the structure refinement at 400K revealed 7 metal positions where Sb1(*8f*) and Sb2(*8f*) were all in distorted octahedral positions; Sb3(*8f*) and Sb4(*8f*) were in the square pyramidal positions; Fe atoms Fe5(*8f*), Fe6(*4e*) and Fe7(*4b*) were in the distorted octahedral positions. The same procedure as described above for the structure at 350K resulted with the final R1~3.25% and final composition $Fe_{0.866}Sb_2Sn_{0.134}Se_4$ as observed in the structure refined in all other temperatures. The atomic coordinates of the magnetic atoms at different temperatures (between 120K-400K) are given in the Table IV-1 and the interatomic distances around magnetic atoms are presented in Table IV-2. All other information on the geometrical and atomic thermal parameters can be found in the annex Tables IV. The graphical representations of the structures were created using Diamond software [42] are depicted in Figure IV-4.

IV-1-3-Magnetic Properties Measurements

Direct current (DC) magnetic susceptibility measurements were performed on 40mg of polycrystalline $Fe_{1-x}Sn_xSb_2Se_4$ powder using a Superconducting Quantum Interference Device (SQUID). DC susceptibility data in field-cooled (FC) and zero-field-cooled (ZFC) modes were recorded from 2K to 300K with an applied magnetic field of 100Oe for low temperature measurement, and from 300K to 600K for high temperature measurements. For the high temperature data, the polycrystalline sample was carefully enclosed in a pure aluminum foil (99.999% from Alfa Aesar). This sample as prepared was attached on the regular SQUID rod and introduce in the furnace installed in the system for the purpose.

Table IV-1: Atomic coordinates, Wyckoff positions (W.P), site occupancy factors (*k*) and equivalent isotropic displacement parameters ($U_{eq}/10^{-4}$ x $Å^2$) for all magnetic atoms in the asymmetric unit of $Fe_{0.87}Sb_2Sn_{0.13}Se_4$ (120K-400K).(All other informations are reported in Annex)

Temperature(K)	Atom	*k*	W.P	*x*	*y*	*z*	U_{eq}
120K	Fe1/Sn1	0.74/0.26	2d	0	1/2	1/2	88(8)
	Fe2	1	2a	1/2	1/2	0	79(9)
300K	Fe1/Sn1	0.74/0.266	2a	0	0	0	185(6)
	Fe2	1	2d	0	1/2	1/2	186(6)
350K	Fe1/Sn1	0.7/0.3	2c	1/2	-1/2	1/2	226(8)
	Fe2/Sn2	0.72/0.28	4i	0.3334(2)	0	0.1666(4)	218(1)
	Fe3	1	2b	1/2	0	0	229(2)
	Fe4	1	4i	0.3332(2)	-1/2	0.6669(5)	214(1)
	Fe/Sn1	0.72/0.28	8f	0.2504(9)	0	0.3752(9)	258(8)
	Fe2	1	4e	0	0.599(2)	1/4	265(5)

400K	Fe3	1	4a	0	0	1/2	252(7)

U_{eq} is defined as one-third of the trace of the orthogonalized U_{ij} tensor

Table IV-2: Selected inter-atomic distances (Å) around the magnetic Fe atom in $Fe_{0.87}Sb_2Sn_{0.13}Se_4$ at 120K, 300K, 350K and 400K.

Bond	120K	Bond	300K
Fe1|Sn1−Se2(x 2)	2.6768(7)	Fe1|Sn1−Se2(x 2)	2.6831(8)
Fe1|Sn1−Se3(x 4)	2.6913(3)	Fe1|Sn1−Se1(x 4)	2.7033(6)
Fe2−Se1(x 4)	2.7043(5)	Fe2−Se1(x 4)	2.7169(5)
Fe2−Se4(x 2)	2.5633(1)	Fe2−Se3(x 2)	2.5631(1)
Bond	350K	Bond	350K
Fe1|Sn1−Se9(x 2)	2.680(5)	Fe2|Sn2−Se8	2.698(8)
Fe1|Sn1−Se6(x 4)	2.701(3)	Fe2|Sn2−Se7(x 2)	2.708(5)
Fe2|Sn2−Se4(x 2)	2.707(5)	Fe3−Se10(x 2)	2.553(4)
Fe2|Sn2−Se5	2.673(8)	Fe3−Se2(x 4)	2.716(3)
Fe4 −Se12	2.565(8)	Fe4−Se1 (x 2)	2.718(6)
Fe4 –Se11	2.568(9)	Fe4−Se3(x 3)	2.723(3)
Bond	400K	Bond	400K
Fe1|Sn1−Se6	2.677(5)	Fe3−Se1^{i,vi}	2.717(4)
Fe1|Sn1−Se5	2.696(5)	Fe3–Se1(x 2)	2.728(4)
Fe1|Sn1−Se4^{ii}	2.703(6)	Fe3−Se7(x 2)	2.561(2)

Fe1|Sn1−Se3	2.709(6)	Fe2−Se8(x 2)	2.564(2)
Fe1|Sn1−Se4	2.713(6)	Fe2−Se2 (x 2)	2.715(8)
Fe2−Se2[iii]	2.734(8)	Fe2−Se2	2.734(8)

IV-1-4-Transport Properties Measurements

The electrical resistivity and magneto-resistance were measured from 300K down to 50K, using the standard four-probe method on a Quantum Design Physical Property Measurement System (PPMS) and using high density (97%) hot pressed bar shape samples with average sizes 1 x 1 x 2mm.

IV-2-Results and Discussion

IV-2-1 Phase Purity and Structural Identification

All samples with nominal composition $FeSb_2Se_4$ and $Fe_{0.87}Sb_2Sn_{0.13}Se_4$ synthesized in several batches under identical conditions using the method described above resulted in single phase product. Further annealing was always required to improve the crystallinity of the phases. Obtaining large crystals for anisotropy studies and understanding of quantum phenomena responsible for the observed properties is in progress. The Figure IV-1 shows experimental and the simulated X-ray powder diffraction pattern of $FeSb_2Se_4$ and $Fe_{0.87}Sb_2Sn_{0.13}Se_4$ obtained from the crystal structure refinement at 300K. The neutron powder diffraction patterns of $FeSb_2Se_4$ at different temperatures are presented in Figure IV-2. Each experimental pattern at a specific temperature is associated with the corresponding nuclear structure model used for refinement. Perfect match is observed between the experimental and the calculated pattern confirming the phase purity of at least 95%, of the material. An attempt to refine the neutron diffraction data of $FeSb_2Se_4$ collected above 300K using the structural model at 300K turned out to be unsuccessful, suggesting a possible structural change upon heating the material. This change in the structure of $FeSb_2Se_4$ was observed on the temperature dependent magnetization as depicted on the Figure IV-5 and is consistent with magnetic phase transitions observed at different temperature range. An extra peak was observed at $2\theta \sim 85°$ on neutron diffraction pattern in all selected experimental temperatures. This peak was absent in the experiment powder diffraction and calculated patterns of the nuclear phases presented in the Figure IV-1. The origin of that peak in not clear. However, the perfect matching of the nuclear structure with the neutron experimental

powder diffraction suggests that ferromagnetic ordering is dominant at all measured temperature ranges in this compound. X-ray diffraction experiments were performed on single-crystal specimens of $FeSb_2Se_4$ and $Fe_{0.87}Sb_2Sn_{0.13}Se_4$ at temperatures between 120K and 400 K to understand the relationships between the change in the magnetic behavior and the crystal structure. The temperatures were selected within the different magnetic phase transition segments observed at high temperature.

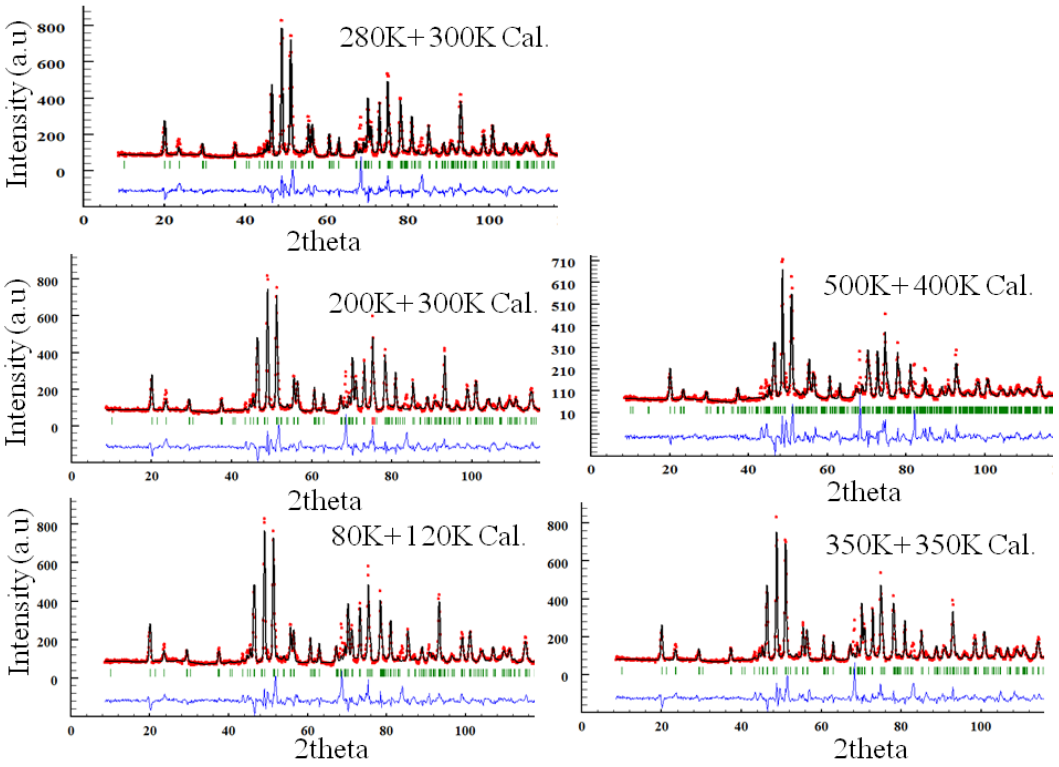

Figure IV- 2: Neutron diffraction of $FeSb_2Se_4$ at different temperatures refined using the nuclear structure of $FeSb_2Se_4$ solved at 120K, 300K, 350K and 400K. Perfect agreement is observed between the calculated pattern of the nuclear phase and the neutron experimental pattern. Each experimental pattern is associated with the corresponding nuclear pattern at the selected temperature.

IV-2-2-Crystal structure of $Fe_{0.87}Sb_2Sn_{0.13}Se_4$ (120K-400K)

$Fe_{0.87}Sb_2Sn_{0.13}Se_4$ is isostructural with $FeSb_2Se_4$ at low temperatures (120K to 300K) and adopts the monoclinic space group *C* 2*m* (No.12) with lattice parameter *a* = 13.037(3)/13.083(3)Å *b* = 3.959(9)/3.972(3)Å *c* = 15.171(3)/15.171(3)Å β = 114.67(3)^o/114.78(3)^o at 120K and 300K respectively. At a constant temperature, the lattice parameters of $Fe_{0.87}Sb_2Sn_{0.13}Se_4$ are slightly larger along the *a*- and *b*-axis compared to that of $FeSb_2Se_4$. However, the structural distortion of $Fe_{0.87}Sb_2Sn_{0.13}Se_4$ upon cooling keeps the *c*-axis constant while all other cell parameters decrease with decreasing temperature, leading to the overall volume contraction of 0.57% (711.72(9)Å^3 at 120K and 715.84(9)Å^3 at 300K). Four crystallographically independent metal positions and four Se are identified for each temperature. The Sb(1) and Sb(2) sites are fully occupied by Sb. The special position Fe(1) located at (0, ½, ½) contains 25.95% Sn while the Fe(2) at (0,0,0) is fully occupied by the Fe. Fe(1) and Fe(2) are coordinated with six Se atoms in a distorted [2+4] octahedral geometry with two axial bonds and four long equatorial bonds. The interatomic distances around the magnetic atoms are ranging between 2.5631(1) and 2.7169(5)Å. The shape of the octahedron around Fe(2) is almost regular compared to the more distorted shape of the octahedron around Fe(1). The difference in the shape of octahedra around Fe(1) and Fe(2) plays a key role in the magnetic behavior of $Fe_{0.87}Sb_2Sn_{0.13}Se_4$. $[\{Fe\}Se_6]_\infty$ chains along the *b*-axis are similarly connected as in $FeSb_2Se_4$ to build a one dimensional magnetic chain, which are interconnected along the *a*-axis through Sb atoms in a [1+2+2+1] distorted octahedral coordination. Upon heating the crystal up to 350K, the structure of $Fe_{0.87}Sb_2Sn_{0.13}Se_4$ undergoes a drastic expansion of about $\Delta a/a$ = 192% along the *a*-axis resulting in overall volume expansion of ~200%. This corresponds to the tripling of the unit cell volume when compared to the structure at 300K. This increase in the *a*-axis and unit cell volume is followed by a 3% contraction of β (111.21) ^{o} when compared to the value at room temperature (114.78^o). The intensity data at 350K was indexed in the monoclinic crystal system with space group *C2/m* (No.12). The unit cell parameters were *a* = 38.243(8) Å; *b* = 3.9727(8) Å; *c* = 15.174(3) Å; β = 111.21 ^{o}. The structure at 350K shows four independent magnetic atomic positions. The two general positions *4i* are occupied by Fe2/Sn2 and Fe4, while the remaining two special positions *2b* and *2c* are occupied by Fe3 and Fe1/Sn1, respectively. Fe1/Sn1 and Fe3 atoms are located in a [2+4] distorted octahedral coordination with bond length ranging between 2.553(4)Å and 2.716(3)Å. The octahedral around Fe2/Sn2 and Fe4 are distorted in [1+2+2+1] geometry with

bond length ranging between 2.564(8)Å and 2.729(7)Å. Infinite chains of octahedra that are built around the Fe1/Sn1 and Fe2/Sn2 are connected with face-sharing distorted [1+2+2+1] octahedra around Sb2 and Sb4, to form an infinite 2D magnetic layer denoted with A running parallel to the (201) plane. The distance between magnetic chains within layer A was found to be about 6.8450(6)Å, which is close enough to induce exchange coupling between these magnetic centers. Similarly, the 2D layer, denoted B, is formed from the infinite chains of octahedra around Fe3 and Fe4 , which are 6.8391(8) Å apart, and interconnected by face-sharing [1+2+2] distorted square pyramid around Sb4, Sb5 and Sb6 with Sb-Se bond distances ranging from 2.6113(8)Å to 2.7433(4)Å. Both layers (A and B) are separated by 7.66(1)Å.

Further increase of the temperature to 400K resulted in additional change in the crystal structure of $Fe_{0.87}Sb_2Sn_{0.13}Se_4$. Intensity data at 400K was indexed in the monoclinic crystal system and can be described as a 2*a* x *b* x 2*c* superstructure of the structure at 300K. The expansion observed along *a* and *c*-axis with $\Delta a/a$ = 53% and $\Delta c/c$ = 42% leads to approximately $\Delta V/V$ = 300% expansion of the unit cell volume. The value of β drastically decreased from 114.78(3)^o down to 90.72(3)^o representing a relative change of 21% compared to the value at room temperature. The intensity data was indexed in the monoclinic crystal system with space group *C2/c* (#15) and unit cell parameters *a* = 27.543(6) Å; *b* = 3.9800(8) Å; *c* = 26.220(5)Å. The observed increase in the crystal symmetry led to a reduction in the number of crystallographically independent magnetic atoms in the structure of $Fe_{0.87}Sb_2Sn_{0.13}Se_4$ at 400K. Three independent positions were identified (see Table IV-1), with the special position *4a* occupied by the Fe3 atom, whereas the general positions *4e* and *8f* are occupied by Fe2 and Fe1/Sn1, respectively. The octahedron around Fe1/Sn1 is distorted in a [1+2+2+1] geometry with bonds length ranging from 2.677(5)Å to 2.713(6)Å, while Fe2 and Fe3 are located in a distorted [2+2+2] octahedral with bond length between 2.564(2)Å and 2.734(8)Å. This suggests that the slight change on the susceptibility might originate from special distortion of the coordination polyhedra around the magnetic atoms. In fact, Fe1/Sn1 and Fe3 at 350K showed a Jahn-Teller type distortion, which may be enough to induce difference in magnetic ordering at high temperatures. As observed in the structure at

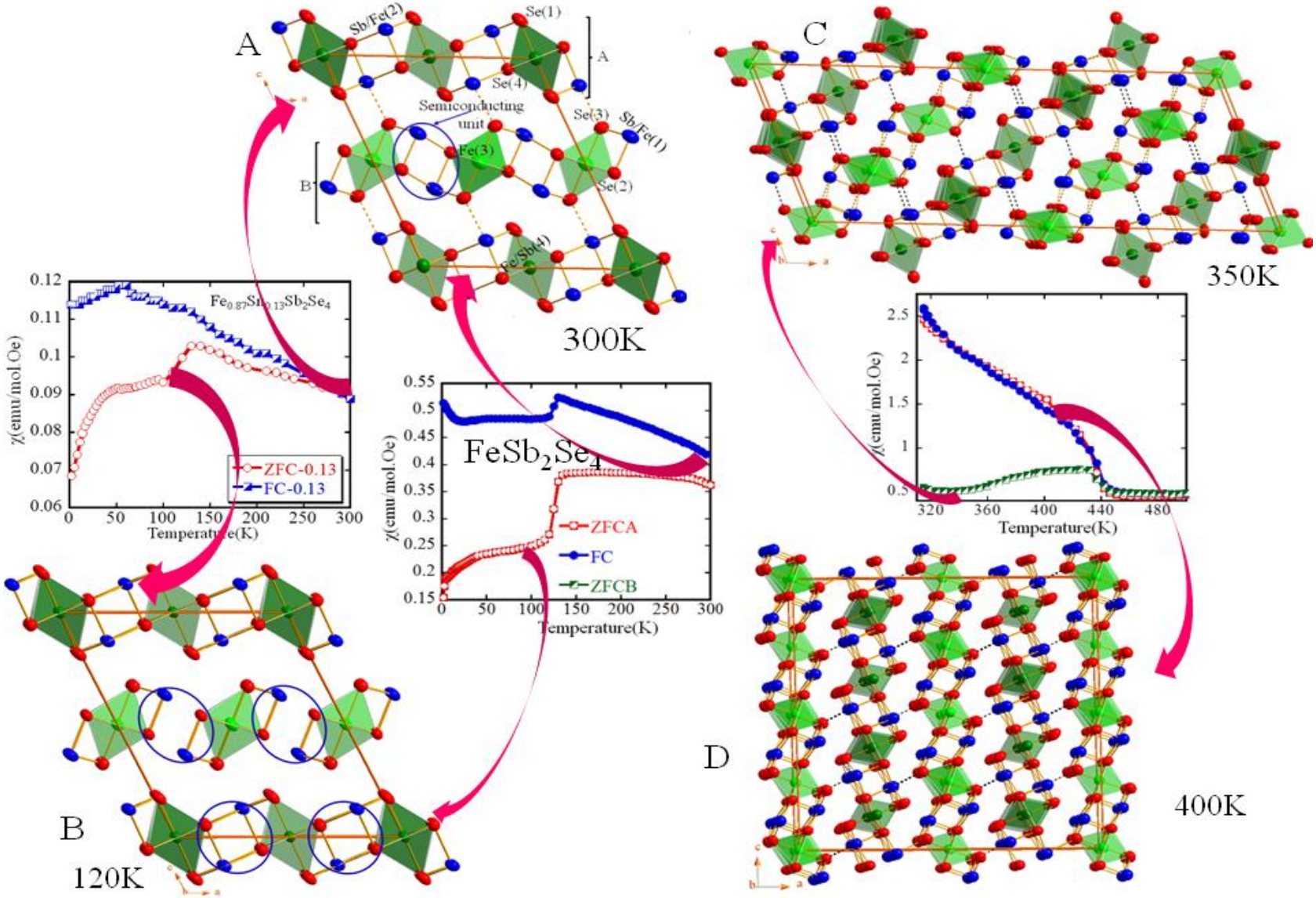

Figure IV- 3: Effect of temperature on structure and magnetic properties of $Fe_{1-x}Sn_xSb_2Se_4$, (A) the structure at 300K, (B) the structure at 120K, (C) the structure at 350K, (D) the structure at 400K. Changes in the crystal structure can be correlated to magnetic phase change as observed at 120K, 300K, 321K and 400K, on temperature dependent magnetization.

Such magnetic sub-lattices are expected to impact the magnetic behavior of $FeSb_2Se_4$ and $Fe_{0.87}Sb_2Sn_{0.13}Se_4$

IV-2-3- Electronic Transport and Optical Properties of $Fe_{1-x}Sn_xSb_2Se_4$ (x= 0, 0.13)

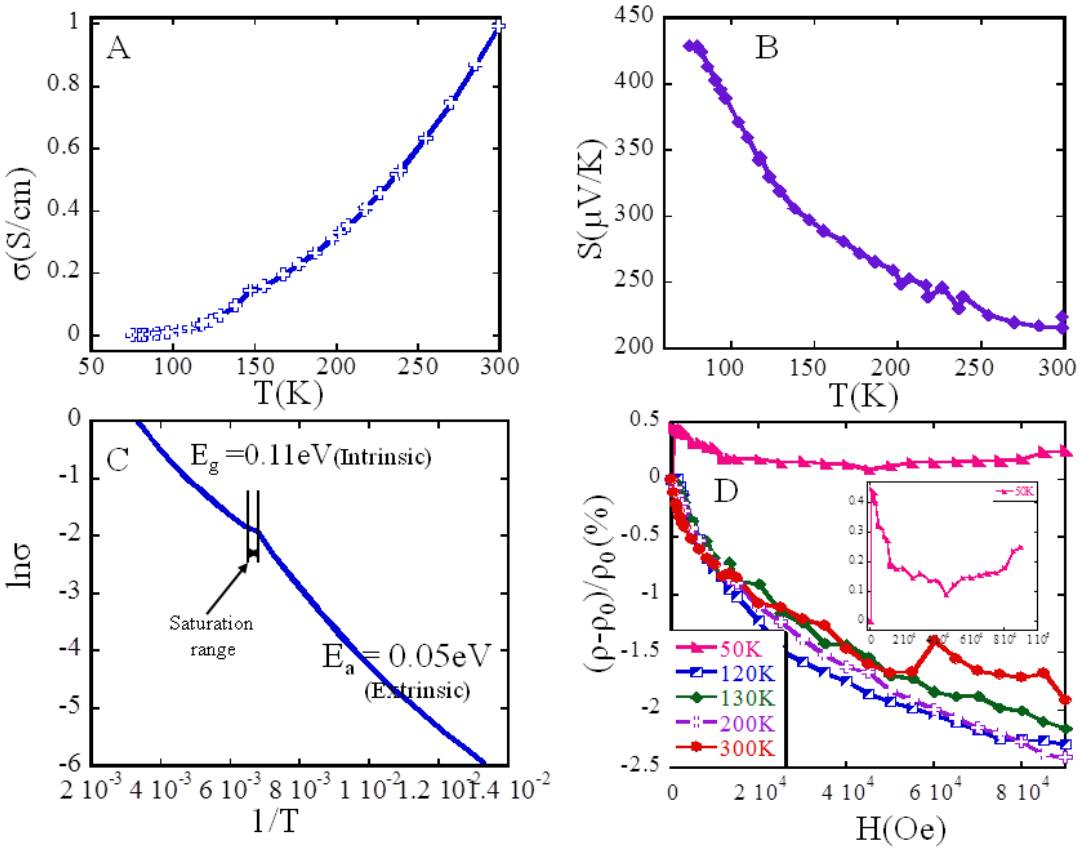

Figure IV- 4: Conductivity as function of temperature of $FeSb_2Se_4$ showing the conductivity increasing with temperature, (B) temperature dependent Seebeck coefficient with large positive value of Seebeck coefficient,(C) Arrhenius plot of the logarithmic conductivity versus inverse temperature showing activation energy, E_a = 0.05eV; (D) The magnetoresitance of $FeSb_2Se_4$ at different temperatures.

Figure IV-5 shows the temperature dependent electrical conductivity of $FeSb_2Se_4$. The conductivity increases with increasing temperature over the entire temperature range, which is characteristic of a semiconducting behavior. The electronic behavior of this compound is dominated by the thermally activated charge carriers across the band gap and shows (Figure IV-

5C) two regions depicting different regimes of the transport properties. The low temperature regime follows the Arrhenius equation $\rho = \rho_0 \exp(E_a/kT)$, where E_a is the binding or activation energy and was found to be about 0.05eV. The high temperature region corresponding to the intrinsic regime gave the electronic energy gap of 0.11eV from the relation $\rho = \rho_0 \exp(E_g/2kT)$, where Eg is the energy band gap. This value is twice the activation energy of the extrinsic regime (low temperature region). The temperature dependent Seebeck coefficient depicts in Figure IV-5B shows decreasing values of the Seebeck with increasing temperature from 430µV/K at 50K to 225µV/K at 300K. These positive values indicate that holes are the majority charge carrier in this material. The ferromagnetic behavior of this material in addition to the high resistivity observed make the Hall Effect measurement complicated. However, the change on carrier concentration could be accessed qualitatively from temperature dependent Seebeck measurement. The Seebeck coefficient is given by the relation $S = 8\pi^2 k_B m^* T/ (3eh^2) \times (\pi/3p)^{2/3}$ where k_B is the Boltzmann's constant, m* the effective mass, p the carrier concentration and h the Planck's constant. This expression shows that as we increase the carrier concentration, the Seebeck coefficient will decrease. The observed change on the Seebeck coefficient is consistent with the behavior of intrinsic semiconductor, since the carrier concentration increases with increasing temperature.

Figure IV-5D represents the resistivity change under applied field or magnetoresistance (MR) for $FeSb_2Se_4$ at different temperatures. Regardless of the temperature, the MR is field dependent with a maximum relative change of 2.5% at 200 K under applied field of 90 KOe. However, a positive MR was observed at 50 K in all range of magnetic field, while at temperature greater than 50 K, a negative MR is observed and monotonically increases with the increasing field. This difference on the sign of the MR might be helpful in the understanding of the origin of ferromagnetic behavior in this compound at different temperature range. Indeed, $FeSb_2Se_4$ undergoes an electronic transition below 120K going from semiconductive to a highly insulative behavior. Below this temperature the charge carriers are frozen and trapped Shallow energy levels from impurities which leads to the very low carrier concentration.[44] This is consistent with the simultaneous increase of the resistivity and the thermopower which is more pronounced at 75K. The consequence of this scenario is the formation of the magnetic clusters from spin of trapped free-carriers which are bounded by the local magnetic moment of Fe^{2+}.[44,45] All these spins form the collective ferromagnetic ordering state. Therefore, one can anticipate the existence of polarons in $FeSb_2Se_4$, which

started forming before the electronic transition temperature as suggested by the field dependent magnetization (Figure IV-6). From 120K, the magnetoresistance is negative. These negative values observed at high temperature, confirm the correlation between the carriers (holes) and the spins of local magnetic moment in this compound. One can anticipate that, the magnetic exchange coupling in $FeSb_2Se_4$ and $Fe_{0.87}Sb_2Sn_{0.13}Se_4$ is regulated by the p-d exchange mechanism. The change on magnetoresistance might also suggest the existence of spin-polarized current which is of relevance for spin based devices and particularly those based on ferromagnetic semiconductors.

IV-2-4-Magnetic properties

The temperature dependent magnetization (FC and ZFC) of $FeSb_2Se_4$ and $Fe_{0.87}Sb_2Sn_{0.13}Se_4$ in the range of 2K-600K are shown in the Figure III-4. The structural changes in this material at different temperatures are also depicted with the corresponding magnetic phase transition. The ZFC and FC regimes of low and high temperature zones show mismatch at the intercept temperature (300K). The discrepancy observed at that particular temperature might come from the difference on the instrument configuration and experimental process. During the DC measurement of ZFC, the temperature dependent susceptibility showed different behavior depending on the heating process and condition. We observed different behaviors when the materials are initially heated up and cooled down in absence of applied field and when we started the measurement from room temperature without any prior heating and cooling. The ZFC temperature dependence magnetization obtained without any prior heating shows the increasing magnetization with increasing temperature; while upon

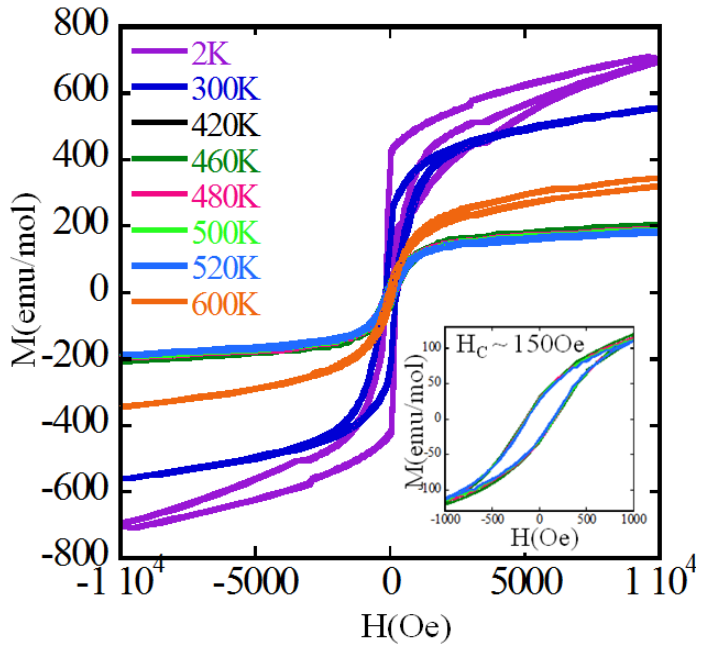

Figure IV- 5: Field dependent magnetization with hysteresis up to 600K and the inset showing almost temperature independent magnetization and coercivity between 460K-520K.

heating and cooling without any applied field, we observed that the magnetization decreases with increasing temperature. This ZFC data was almost similar to the FC temperature dependence magnetization above the room temperature. For clarity, FC prior to heating will be denoted ZFCB and ZFC after heating, ZFCA in the following sections. The ZFCA data was collected under 1000 Oe applied field after the FC regime and the system was cooled down in absence of applied field. We allowed a waiting time of about 180 s before starting the measurement of the ZFCA. Despite this long time, we observed that ZFCA and FC are almost superimposed. We suspect spin polarized electron to induce this irregular behavior. This means that the spins of the local magnetic moments which are coupled through long range ordering from itinerant carriers (hole) needed long relaxation time to return to the their ground state. The magnetization at ZFCB increases with increasing temperature up to 434K and decreases drastically thereafter to 446K from where it remains almost constant up to 500K. The increased value of the magnetization with increasing temperature of ZFCB corroborates the correlation between the free carriers and the spin of the local magnetic ions. In fact, the conduction in $Fe_{1-x}Sb_xSe_4$ is through the activation process, therefore the number of carrier at the edge of the valence band increases with increasing temperature. Those carriers turn out to contribute to the magnetization of the itinerant electrons' spins. The FC and both ZFC show magnetic transition starting from 425K up to 446K in the case FC and ZFCA; in case of the ZFCB, the transition is observed within 425K and 446K. Within this range of temperature, all magnetizations were superimposed. From 446K, the magnetization is almost constant in both regimes. One can anticipate paramagnetic behavior from this temperature. This is inconsistent with the FM ordering observed at this temperature as suggested by the field dependent magnetization. In addition, ZFCA and FC are completely distinguishable as highlighted in the inset of the Figure 3D. This divergence up to 500K suggests the persistence of ferromagnetic ordering at high temperature. This is corroborated by the hysteresis loop observed in the field dependent magnetization at 600K (Figure III-5). The coercivity field of about 55 Oe observed at that temperature is large enough to assign the observed hysteresis to the superparamagnetic behavior. However, the field dependence magnetization within 420K and 520K is independent of the temperature with coercivity force of 150Oe (inset Figure III-6). The magnetization increases above these temperatures while the coercivity force decreases to 55Oe. All these values confirm the persistence of the FM at high temperature.

To probe the origin of the ferromagnetic ordering, we assume that, as in several magnetic semiconductors, $Fe_{1-x}Sb_2Sn_xSe_4$ is subjected to other unusual magnetic phenomena such as spin glass, spin-polarization of free-carriers and formation of bound magnetic polaron (BMP), which could induce long-range magnetic ordering. However, no evidence of spin-glass was observed. To probe the two latter cases, we measured the field-dependent magnetization of $FeSb_2Se_4$ in the temperature range from 2K to 600K. The Figure IV-6A shows the experimental magnetization as function of applied field at different temperatures. The plots of magnetization (M) versus applied field (H) can be fitted to the equation $M = M_0L(x) + \chi_m H$,

where $L(x) = cothx - 1/x$ is the Langevin term and represent the contribution of the BMP to the magnetization and the $\chi_m H$ term is the contribution of the matrix. $M_0 = Nm_s$ and $x = m_{eff}H/k_BT$ where N is the number of BMPs involved, m_s and m_{eff} represent the true and effective spontaneous moment per BMPs. Fig.IV-6A shows the fitting of experimental data for the temperatures between 100K and 300K using the Langevin function (this range of temperature is chosen for visual clarity, but the fitting is also perfect down to 2K). All data were perfectly fitted at temperatures below 300K with slightly deviation observed at 280K and 300K for field above 10 KOe. Table IV-7 shows calculated parameters obtained from fitting of M-H data with the Langevin function. For each temperature, the total BMP moment Nm_s can be estimated by the linear extrapolation of the high-field to H = 0. The average value of the total BMP moment Nm_s was about 1.19 emu/g. Since the temperature range was sufficiently high, we assume m_{eff} and m_s to be the same. From this insight, we estimated the number of BMP at each temperature which is also roughly the same number of occupied acceptors. A quantitative analysis of the magnetization data allowed us to estimate the number of BMPs (N) to be about $1.17x10^{19}/cm^3$ at high temperatures. Using this value N and the Nm_s, the values of m_s as function of temperature was calculated and are reported on the Table IV-3. These values increase with increasing temperature from 60K to 150K. The saturation of these moments appears to occur within 150-200K. This optimal value decreases thereafter for temperature above 200K. The maximum value of $68.5\mu_B$ was observed at 150K close to the values of effective magnetic moments calculated from susceptibility data. This suggests that most of the contributions into the magnetic moment are related to the free-carriers, which can act through different mechanism depending to the temperature. The fast increase of the magnetization at low field is believed to originating from BPMs associated with trapped carriers (holes), while the slight increase of the magnetization

above ~ 3000 Oe might be arising from the spins of the *d*-orbital outside the BMPs. It is well known that in the collective regime particularly in the diluted magnetic semiconductor, the BMP is favorable to the *p*-type semiconductor compared to the *n*-type because of the p-d exchange constant coupling β term that is larger in *p*-type compared to the s-d exchange coupling α term of *n*-type.[12] This allows us to anticipate that strong p-d exchange coupling is the main mechanism of the magnetic interaction in $Fe_{1-x}Sb_2Sn_xSe_4$. The BMPs in magnetic semiconductors are mostly reported at low temperature[46,47]. However, we observed here a possible situation where BMPs persist up to 300K. Further investigations are needed to understand the magnetism of these compounds and the source of FM at low and high temperatures. In the following section we will attempt to clarify the mechanism of ferromagnetism in the $Fe_{1-x}Sn_xSb_2Se_4$ (x= 0, 0.13) compounds.

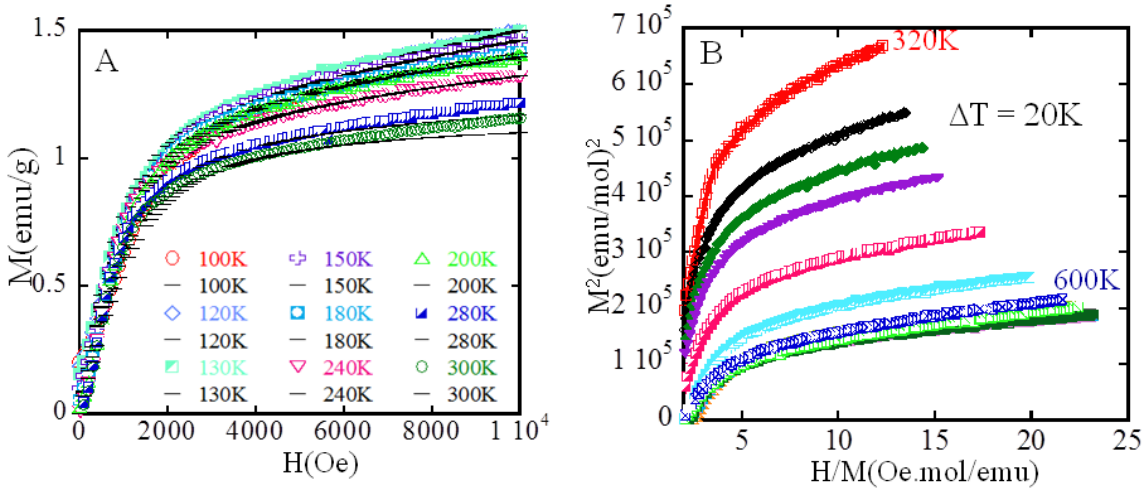

Figure IV- 6(A) Field dependent magnetization at different temperatures fitted with the Langevin function, suggesting the existence of bound magnetic polarons (BMPs in the compounds); (B) The Arrott's plot of $FeSb_2Se_4$ suggesting that the Curie temperature should be above 600K.

As discussed earlier, there is a strong correlation between the changes in the crystal structure with the magnetic transition observed on the temperature dependence magnetic susceptibility. From Figure IV-3, we can anticipate that each magnetic transition is coincides with the structural phase transition, since we can easily assign the observed structural change at 120K, 350K and 400K to different magnetic phase transition observed at 130K, 300K, 340K and 460K respectively.

At 130K, a sharp drop was observed in the magnitude of the FC and ZFC magnetic susceptibility and was already ascribed to the structural change induced by stereoactivity of Sb lone pair upon cooling and heating of the system.[40] This stereoactivity of the Sb lone-pair depends on the thermal agitation affecting the material structure (chemical bonds) upon heating and cooling. Below 130K, the temperature dependent magnetization remains almost constant on FC down to 17K and then increases with decreasing temperature. In the meantime, the ZFC regime drastically decreases after 130K with perceptible changes from 60K down to 2K which are observable in the FC with pronounced slope magnitude from 17K. This divergence between the FC and ZFC at low temperatures might be due to the anisotropy in the BMP.[12,48] Interestingly, this effect is observed up to 435K, corroborating the current prediction that the BMP could favor the ferromagnetism with high Curie temperature [32,49] and might persists in this material up to room temperature. However, this theory was developed in the case of the wide band gap semiconductor doped with magnetic impurities[32]. Therefore, $Fe_{1-x}Sb_2Sn_xSe_4$ becomes a particular and interesting system to understand the correlation between localized spin from magnetic ion and carriers in magnetic semiconductors.

To understand the effect of this structural change on magnetism at high temperatures, we analyzed the magnetic structural subunit in this material. Along the *a*-axis, the separation between two adjacent Fe atoms is 19.215(4) Å and 13.925(3) Å, respectively in the crystal structure at 350K and 400K. This separation is too long for direct or indirect magnetic interaction between adjacent magnetic chains. However, a separation of 7.851(1)Å and 7.081(3)Å is observed between adjacent magnetic chains along the *c*-axis at 350K and 400K,respectively . The structural expansion of the unit cell observed at 350K and 400K generated the rearrangement of magnetic structural subunit compared to the structure at 120K and 300K depicted as the diamond sublattice in Figure IV-3. The Fe-Se-Fe average distances along the *b*-axis are presented in the annex Table IV-1. These distances increase with increasing temperature and ranged from 3.9599(8)Å (120K) to 3.9800(8)Å (450K). These distances suggest that an indirect exchange interaction is expected between adjacent Fe atoms along the [010] through the Fe-Se-Fe bridge. The increasing distance with increasing temperature is expected to affect the Fe-Se-Fe angle, which is increasing with increasing temperature as can be observed in the Table IV-2. Therefore, AFM ordering is expected to increase with increasing temperature as a result of indirect exchange coupling according to the Goodenough-Kanamori rules [50-53].

The Figure IV-5 shows the field dependence magnetization at different temperatures up to 600K. The hysteresis loop was observed with coercivity fields between 240Oe to 55Oe. The material shows large coercivity field at 300K. The minimum coercivity field observed at 600K suggests that the materials exhibit ferromagnetic ordering up to 600K. This is consistent with the neutron diffraction data at different temperatures as shown in Figure IV-2, where the calculated patterns of the nuclear phases perfectly match with the experimental patterns of neutron powder diffraction. No AFM phase in the system was detected although we do observe some extra peaks at high angle ($2\theta = 85$) on the neutron diffraction which do not exist in the experimental powder pattern and calculated pattern of the nuclear phase. In addition, by converting magnetization into Bohr magneton per unit formula at maximum field yielded a very low value at all temperatures (0.13, 0.1, 0.04, and $0.063\mu_B$/unit formula), suggesting that canting AFM or other mechanism might be competing with the observed ferromagnetism up to 600K. The above description of the correlation structure-magnetism relationship suggests the presence of anti-ferromagnetic ordering competing with ferromagnetic ordering in our materials. This scenario is not strange in a magnetic semiconductor. However, no report of undoped magnetic semiconductor with ferromagnetism at high temperature exists in the literature as of yet. One might expect the FM ordering to vanish with increasing temperature owing to the frustration and thermal agitation, which will favor the paramagnetism in the system. Interestingly we do observe ferromagnetism up to 600K (Figure IV-5).

One should better consider a different mechanism ruling the magnetic behavior in the magnetic semiconductor and diluted magnetic semiconductor in order to clearly understand the FM ordering observed at high temperature in this material. As we mentioned above, $FeSb_2Se_4$ exhibit spontaneous magnetization up to 600K. This is supported by the Figure IV-6B showing the Arrott's plot, which is commonly used to accurately determine the Curie temperature. From Figure IV-6B, the hysteresis loops at different temperatures might suggest that the Curie temperature of $Fe_{1-x}Sb_2Sn_xSe_4$ will be above 600K although we do observe a confusing transition around 450K from where the magnetization of this compound change almost linearly with temperature(Figure IV-4). We assume that the ferromagnetism in this material originates from the interaction between the spin of free carriers and the spin of the local magnetic atoms. In fact, the $FeSb_2Se_4$ structure shows two magnetic layers denoted A and B [39,40]connected through Sb-Se weak interaction. Within these layers, intermixing of Sb and Fe in the same atomic site

was observed in all Sb sites where a fraction of Sb is replaced by 4% of Fe.[40] Since Fe^{2+} in this site has fewer electrons than Sb^{3+}, holes are generated. Simultaneously, a fraction of Sb^{3+} (15%) also substitutes Fe^{2+} in all Fe sites within the layer A. With an extra electron from Sb^{3+} more electrons are expected in the Fe sites. This means that both free holes and electrons are present in the crystal lattice of $FeSb_2Se_4$. However, thermopower measurements indicated that the compound is a p-type semiconductor suggesting that free-holes are the dominant charge carriers. The holes from the impurity band have activation energy of 0.05eV and behave like the hydrogenic holes, which tend to form the BMPs, coupling the 3*d* moments of Fe^{2+} within their Bohr radius orbit ferromagnetically by preventing any manifestation of the AFM. This is pronounced when cooling down the materials under an applied field to low temperatures. In addition, the B layers are mainly FM and are also trapped within the Bohr radius of the BMP created from Sb^{3+}/Fe^{2+} surrounding all Fe^{2+} ion in these layers. As a result, all local magnetic atoms (Fe, Fe/Sb, Fe/Sn) are surrounded by free carriers, mainly holes, which are then able to induce long-range FM ordering. In the classical system mostly studied where BMP are found, the impurities and local magnetic atoms are randomly distributed within the lattices. This situation required suitable size of the polaron to exhibit ferromagnetism. However, the $FeSb_2Se_4$ and $Fe_{0.87}Sb_2Sn_{0.13}Se_4$ compounds show sizable impurities distributed within the lattices that either come from local magnetic moment or surround the local magnetic moment. This reduces drastically the percolation threshold of the polaron and favors the onset of the ferromagnetism from the high temperature since the size of the polaron growth with decreasing temperature. The small value of the activation energy (Figure IV-3C) observed in the extrinsic regime suggests the large localization radius and also means larger number of spins are bounded together. The actual magnetic behavior of $FeSb_2Se_4$ could raise debate in the correlation between the energy gap and T_c, since $Fe_{1-x}Sb_2Sn_xSe_4$ is definitely a narrow band gap semiconductor, while FM above room temperature is mainly predicted to be possible only in wide band gap semiconductors.

At high temperature, the localized carriers become delocalized and induce long-range ordering between Fe atoms through the spin-polarized hole. In fact, the activation energy of 0.05eV in $FeSb_2Se_4$ is really small compared to those reported in other systems with Curie temperature above room temperature.[21,54] This means that large fractions of electrons are activated and move above the mobility edge of the impurity band as the temperature increases. This induces the coupling of the local magnetic moment of the Fe^{2+} ion with the itinerant free-carriers through the

Ruderman-Kittel-Kasuya-Yosida (RKKY) mechanism. The minimum distance between Fe in (101) plane is about 6.845(1)/6.8493(6)Å and the maximum distance between Fe in the same plane within the same atoms is about 7.6677(8)/7.8582(4)Å respectively at 350K and 400K. These distances are large enough to preclude direct exchange coupling between adjacent Fe. Therefore, only the indirect exchange coupling could explain the exchange interaction between Fe in this plane. The magnetic centers in $FeSb_2Se_4$ are connected via the Se-Sb-Se in the (101) plane. This bridge will mediate the exchange interaction ferromagnetically owing to the spin polarized hole and electron resulting from the mixed occupancy at Fe^{2+}/Sb^{3+}. Furthermore, the increasing magnetization in ZFCB with increasing temperature up to 436K is an indication that the free-carrier should mediate the exchange interaction above 300K as the result of the activation process increasing defect in the system, therefore increasing the spin density of states. Above 450K, the persistence of FM ordering will be the result of the residual spin polarized hole/electron competing with the thermal effect on the local magnetic moment. Despite the thermal effect on Fe^{2+} spins, the long-range exchange still dominates probably because of the strong p-d exchange interaction, which could maintain the band splitting resulting in the imbalance of spin ups and downs.

Conclusion

We have successfully synthesized high quality bulk polycrystalline single phase of $Fe_{1-x}Sb_2Sn_xSe_4$ by solid state reaction at 500°C. The temperature dependent X-ray diffraction study on $Fe_{1-x}Sb_2Sn_xSe_4$ single crystal revealed a sequence of 4 phase transformations at 120K, 300K, 350K and 400K. These structural changes at high temperature are perceptible on the temperature dependence of the magnetic susceptibility. Each transition is consistently associated with a structural transition. However, the AFM behavior suggested from structural analysis was inhibited by the dominant FM up to 600K. The ferromagnetism observed in this compound from low to the high temperatures is assigned to the strong coupling between the spin of localized magnetic ions and the free carriers which act through the BMP at low temperatures and through the spin-polarized hole at high temperatures. In addition, $FeSb_2Se_4$ was found to be narrow gap p-type semiconductor. This makes it an ideal material for the study of the physical phenomena behind the magnetic semiconductor properties.

References

(1) Dietl, T. *Nature Material*, **2003**, *2*, 646.
(2) Tian, Y. F.; Li, Y. F.; He, M.; Putra, I. A.; Peng, H. Y.; Yao, B.; Cheong, S. A.; Wu, T, *Applied Physics Letters* **2011**, *98*.
(3) Chattopadhyay, A.; Das Sarma, S.; Millis, A. J. *Physical Review Letter*, **2001**, *87*.
(4) Dietl, T. *Nature Material*, **2010**, *9*, 965.
(5) Quilty, J. W.; Shibata, A.; Son, J. Y.; Takubo, K.; Mizokawa, T.; Toyosaki, H.; Fukumura, T.; Kawasaki, M. *Physical Review Letter,* **2006**, *96*.
(6) Ferrand, D.; Cibert, J.; Bourgognon, C.; Tatarenko, S.; Wasiela, A.; Fishman, G.; Bonanni, A.; Sitter, H.; Kolesnik, S.; Jaroszyski, J.; Barcz, A.; Dietl, T. *J Cryst Growth* **2000**, *214*, 387.
(7) Ferrand, D.; Cibert, J.; Wasiela, A.; Bourgognon, C.; Tatarenko, S.; Fishman, G.; Kolesnik, S.; Jaroszynski, J.; Dietl, T.; Barbara, B.; Dufeu, D. *Journal of Applied Physics,* **2000**, *87*, 6451.
(8) Fukuma, Y.; Arifuku, M.; Asada, H.; Koyanagi, T. *Journal of Applied Physics,* **2002**, *91*, 7502.
(9) He, M.; Tian, Y. F.; Springer, D.; Putra, I. A.; Xing, G. Z.; Chia, E. E. M.; Cheong, S. A.; Wu, T. *Applied Physics Letter,* **2011**, *99*.
(10) Kaminski, A.; Das Sarma, S. *Physical Review Letter,* **2002**, *88*.
(11) Kaminski, A.; Das Sarma, S. *Physical Review B,* **2003**, *68*.
(12) McCabe, G. H.; Fries, T.; Liu, M. T.; Shapira, Y.; RamMohan, L. R.; Kershaw, R.; Wold, A.; Fau, C.; Averous, M.; McNiff, E. J. *Physical Review B,* **1997**, *56*, 6673.
(13) Prinz, A.; Brunthaler, G.; Ueta, Y.; Springholz, G.; Bauer, G.; Grabecki, G.; Dietl, T. *Physical Review B,* **1999**, *59*, 12983.
(14) Quintero, E.; Quintero, M.; Morocoima, M.; Bocaranda, P. *Journal of Applied Physics,* **2007**, *102*.
(15) Quintero, E.; Tovar, R.; Quintero, M.; Gonzalez, J.; Broto, J. M.; Rakoto, H.; Barbaste, R.; Woolley, J. C.; Lamarche, G.; Lamarche, A. M. *Journal of Magnetism and Magnetic Materials,* **2000**, *210*, 208.
(16) Ruderman, M. A.; Kittel, C. *Physical Review,* **1954**, *96*, 99.
(17) Umehara, M. *Phys Rev B* **1996**, *54*, 5523.
(18) Baltzer, P. K.; Lehmann, H. W.; Robbins, M. *Physical Review Letter,* **1965**, *15*, 493.
(19) Baltzer, P. K.; Robbins, M.; Wojtowic.P. *Journal of Applied Physics,* **1967**, *38*, 953.
(20) Robbins, M.; Baltzer, P. K. *Journal of Applied Physics,* **1965**, *36*, 1039.
(21) Calderon, M. J.; Sarma, S. D. *Ann Phys-New York* **2007**, *322*, 2618.
(22) Dietl, T.; Haury, A.; dAubigne, Y. M. *Physical Review B,* **1997**, *55*, R3347.
(23) Philip, J.; Punnoose, A.; Kim, B. I.; Reddy, K. M.; Layne, S.; Holmes, J. O.; Satpati, B.; Leclair, P. R.; Santos, T. S.; Moodera, J. S. *Nature Material*, **2006**, *5*, 298.
(24) Pappas, S. D.; Poulopoulos, P.; Lewitz, B.; Straub, A.; Goschew, A.; Kapaklis, V.; Wilhelm, F.; Rogalev, A.; Fumagalli, P. *Sci. Rep.* **2013**, *3*.
(25) Macdonald, A. H.; Schiffer, P.; Samarth, N. *Nature Material,* **2005**, *4*, 195.
(26) Zener, C. *Physical Review,* **1951**, *81*, 440.
(27) Zener, C. *Physical Review,* **1951**, *82*, 403.
(28) Kasuya, T. *Progress of Theoretical Physics,* **1956**, *16*, 45.
(29) Kasuya, T. *Progress of Theoretical Physics,* **1956**, *16*, 58.

(30) Yosida, K. *Physical Review*, **1957**, *106*, 893.
(31) Yosida, K. *Physical Review*, **1957**, *107*, 396.
(32) Dietl, T.; Ohno, H.; Matsukura, F.; Cibert, J.; Ferrand, D. *Science*, **2000**, *287*, 1019.
(33) Bednarski, H.; Spalek, J. *Journal of Physics:Condensed Matter*, **2012**, *24*.
(34) Coey, J. M. D.; Venkatesan, M.; Fitzgerald, C. B. *Nature Material*, **2005**, *4*, 173.
(35) Anglin, C.; Takas, N.; Callejas, J.; Poudeu, P. F. P. *Journal of Solid State Chemistry*, **2010**, *183*, 1529.
(36) Mrotzek, A.; Kanatzidis, M. G. *Accounts of Chemical Research*, **2003**, *36*, 111.
(37) Poudeu, P. F. P.; Takas, N.; Anglin, C.; Eastwood, J.; Rivera, A. *Journal of American Chemical Society*, **2010**, *132*, 5751.
(38) Poudeu, P. F. P.; Djieutedjeu, H.; Sahoo, P. *Zeitschrift für anorganische und allgemeine Chemie*, **2012**, *638*, 2549.
(39) Djieutedjeu, H.; Makongo, J. P. A.; Rotaru, A.; Palasyuk, A.; Takas, N. J.; Zhou, X. Y.; Ranmohotti, K. G. S.; Spinu, L.; Uher, C.; Poudeu, P. F. P. *European Journal of Inorganic Chemistry*, **2011**, 3969.
(40) Djieutedjeu, H.; Poudeu, P. F. P.; Takas, N. J.; Makongo, J. P. A.; Rotaru, A.; Ranmohotti, K. G. S.; Anglin, C. J.; Spinu, L.; Wiley, J. B. *Angewendte Chemie International Edition*, **2010**, *49*, 9977.
(41) Sheldrick, G. M. In *Bruker Analitical X-ray Intruments, Inc*; V6.12 ed.; v6.12, Ed.; Bruker Analitical X-ray Intruments, Inc: Madison, WI, 2000.
(42) Brandenburg, K. In *Crystal Impact GbR, ;* v3.1a ed.; v3.1a, Ed. Bonn, Germany, 2005.
(43) Pfitzner, A.; Kurowski, D. *Z Kristallogr* **2000**, *215*, 373.
(44) Ogale, S. B.; Choudhary, R. J.; Buban, J. P.; Lofland, S. E.; Shinde, S. R.; Kale, S. N.; Kulkarni, V. N.; Higgins, J.; Lanci, C.; Simpson, J. R.; Browning, N. D.; Das Sarma, S.; Drew, H. D.; Greene, R. L.; Venkatesan, T. *Physical Review Letter*, **2003**, *91*.
(45) Nagaev, E. L. *Journal of Magnetism and Magnetic Material*, **1992**, *110*, 39.
(46) Calderón, M. J.; Das Sarma, S. *Ann Phys-New York* **2007**, *322*, 2618.
(47) Durst, A. C.; Bhatt, R. N.; Wolff, P. A. *Physical Review B*, **2002**, *65*.
(48) Fries, T.; Shapira, Y.; Palacio, F.; Moron, M. C.; McIntyre, G. J.; Kershaw, R.; Wold, A.; McNiff, E. J. *Physical Review B*, **1997**, *56*, 5424.
(49) von Molnár, S. *Sensors and Actuators A: Physical* **2001**, *91*, 161.
(50) Goodenough, J. B. *Physical Review* **1955**, *100*, 564.
(51) Goodenough, J. B. *Journal of Physics and Chemtry Solids*, **1958**, *6*, 287.
(52) Goodenough, J. B.; Loeb, A. L. *Physical Review* **1955**, *98*, 391.
(53) Kanamori, J. *J Phys Chem Solids* **1959**, *10*, 87.
(54) Yakunin, A. M.; Silov, A. Y.; Koenraad, P. M.; Wolter, J. H.; Van Roy, W.; De Boeck, J.; Tang, J. M.; Flatte, M. E. *Physical Review Letter*, **2004**, *92*.

Chapter V

Carrier-Mediated Ferromagnetism in $FeSb_{2-x}Sn_xSe_4$ *p*-type Semiconductor

Introduction

Chemical manipulation of the magnetic substructure in magnetic semiconductors and particularly in ferromagnetic semiconductors[1,2] is very important when looking for new materials for spin based electronics. This has as advantage to reduce the energy required to induce ferromagnetic ordering in magnetic semiconductors upon application of electric or magnetic fields. [3,4] In addition, nonmagnetic semiconductor can be turned into magnetic semiconductors (MS) by introducing sizable concentration of magnetic ions such as Mn, Fe, Ni and Co into the semiconductor. Since electronic properties of most conventional semiconducting materials can be modulated using impurities, it has been proposed that magnetic impurities such as Mn^{2+}, may be helpful in order to provide more functionalities in the doped material. This approach has been used for a decade on III-V, II-VI and IV-IV semiconductor.[5-8] Semiconductor materials such as III-V(GaAs) are already being used in a large number of electronic devices and equipment where, magnetic materials are also in needed. However, the integration of the as doped materials into practical devices is actually restricted by the low magnetic transition temperature of 173K and low solubility of the magnetic ion into the host semiconductor.[8,9] Various magnetic semiconductor from this approach revealed that, the exchange interactions between the free electrons or holes in the semiconducting band and localized spin of the magnetic ions are bounded.[10-18] This makes the fabricated MS a multifunctional materials combining classical properties of semiconductors and magnetic materials. Therefore, a feature application could be for instance the control of magnetic properties through charge carriers in an optically active

medium.[13,19-22] Understanding the mechanism of the interaction between the spin of the charge carriers and the spin of the local magnetic moment remain controversial.[9,23,24] In addition, the origin of ferromagnetism assigned by different authors to the exchange interaction between the spin of the carriers and the spins of the local magnetic moment, is suspected to come from magnetic impurities precipitating in the sample. Therefore, this question could be handled by manipulating a ferromagnetic semiconductor with nonmagnetic ion.

To address this situation, we used our recently reported $FeSb_2Se_4$[25] compound as a template. This compound showed interesting magnetic properties at low and high temperature. We report here the effect of Sn substitution at Sb sites on the magnetic properties of this material. We found that, different compositions obtained from substitution of Sb with Sn show strong correlation between the concentration of Sn and magnetic properties.

V-1- X-ray powder diffraction and Differential Scanning Calorimetry (DSC) of $FeSb_{2-x}Sn_xSe_4$ ($0 \leq x \leq 0.25$)

The Figure V-1shows (A) the powder X-ray diffraction and (B) the differential scanning

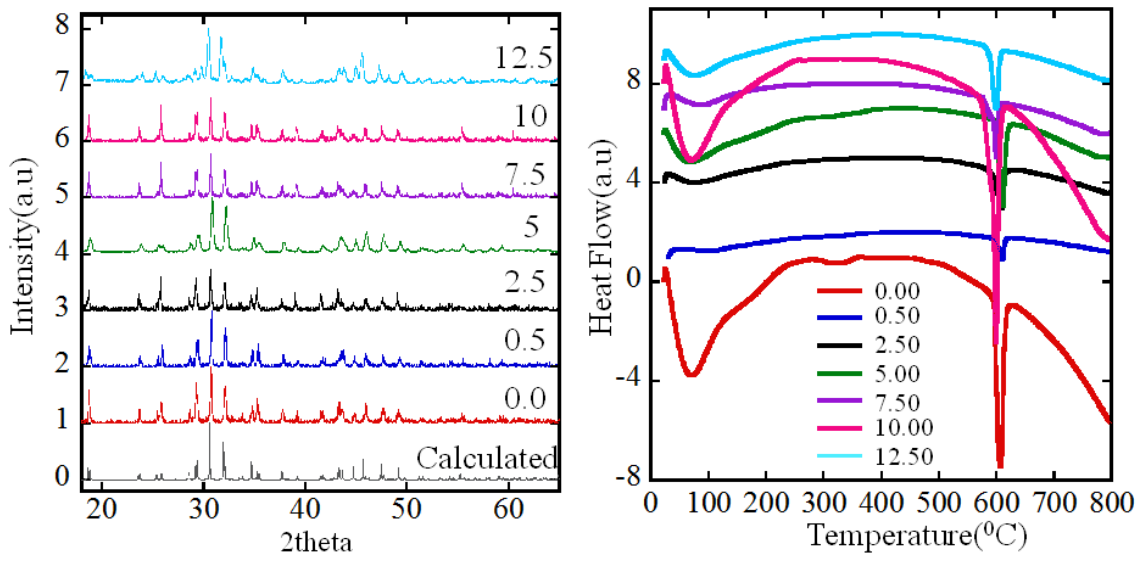

Figure V- 1: (A) Powder X-ray diffraction of various $FeSb_{2-x}Sn_xSe_4$ compositions compared with the simulated pattern of $FeSb_2Se_4$; experimental patterns are in perfect agreement with the simulated pattern. (B) Differential Scanning Calorimetric graph of different compositions with melting point between 862K-873K, the doping does not affect the melting point of $FeSb_2Se_4$.

calorimetric (DSC) graph at different concentrations of $FeSb_{2-x}Sn_xSe_4$ ($0 \leq x \leq 0.25$). The

composition (x values) were converted into the percentage fraction of Sb (y = x/2) substituted in $FeSb_2Se_4$. Compositions with y values 0.5%, 2.5%, 5%, 7.5%, 10%, and 12.5% are used in our study. All compositions of $FeSb_{2-x}Sn_xSe_4$ are isostructural with $FeSb_2Se_4$ as suggested by the X-ray powder diffraction patterns (Figure V-1A). The endothermic plots show the onset of the melting temperature between 862K to 873K for various samples. For compositions with small fractions of Sn, the melting point is below the value observed for the undoped compound. The difference between the lowest and the highest value of the melting point in different concentrations compared to undoped materials was about 10K. This indicates that the melting point of $FeSb_2Se_4$ is not significantly affected by Sn doping at Sb sites for up to y = 12.5%.

V-2-Electrical properties and thermopower of $FeSb_{2-x}Sn_xe_4$

V-2-1-Low temperature electrical properties, thermopower of $FeSb_{2-x}Sn_xSe_4$

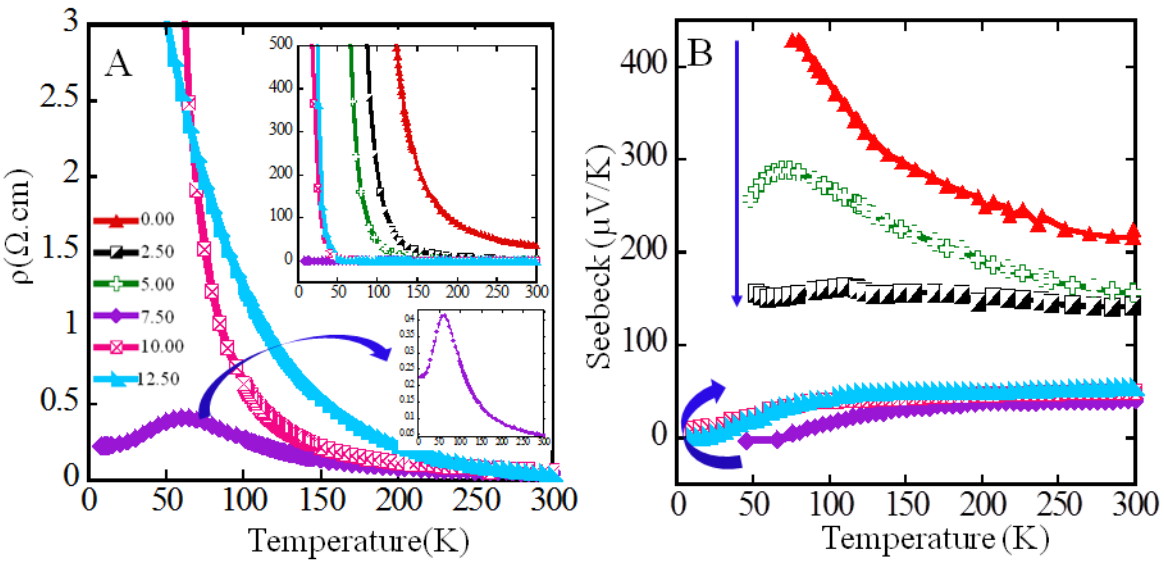

Figure V- 2:(A) The temperature dependent electrical conductivity of different $FeSb_{2-x}Sn_xSe_4$ compositions; the insets highlight the general trend of the electrical conductivity change with Sn concentration, and the transition from semiconductor to metallic behavior in $FeSb_{1.85}Sn_{0.15}Se_4$; (B) is the temperature dependent thermopower of different compositions of $FeSb_{2-x}Sn_xSe_4$.

The temperature dependence of the electrical resistivity and thermopower are presented in the Figures V-2(A) and (B). The striking sharp increase in the value of electrical resistivity observed on $FeSb_2Se_4$ at 130K is also replicated on the doped samples. However, the transition temperature decreases down to 40K with increasing Sn concentration. However, the

sample with 7.5% of Sb substituted by Sn shows semiconductor-to-metallic like phase transition. In fact, for this particular composition, the resistivity initially increases with decreasing temperature, reaches a peak at 62K with a maximum resistivity of 0.42Ω.cm, and continues to decrease with further cooling down to 0.23Ω.cm at 6.6K. This behavior suggests that the $FeSb_2Se_4$ system might be subjected to quantum critical physics phenomena (QCP). This is consistent with the metal to insulator transition (MIT) like curve observed on composition with Sn amount lesser than 7.5%. For compositions y = 7.5% and above, the electrical resistivity values were below 0.5 Ω.cm when the temperature is above 50K. This is consistent with the overall observed trend in the series where the electrical conductivity increases with increasing concentration of Sn. Furthermore, the strong alteration of the magnetic properties (as will be discussed later) with the manipulation of the carrier density through Sb substitution with Sn is an additional reason supporting the presence of QCP phenomena, which is also contingent to the charge carrier change in the materials.

The thermopower decreases with increasing temperature from 426μV/K at 75K to 218μV/K at 300K for the sample containing y = 0% of Sn. These values drop down to -3.37μV/K for the lowest temperature in the case of sample with 7.5% Sn concentration. In addition the thermopower in that same composition is the lowest in the whole series with observable value of 38μV/K at 300K. Although, the Seebeck coefficient irregularly decreases with increasing amount of Sn up to 7.5% doping level, the situation is reversed when further Sn is added in $FeSb_2Se_4$. As observed for the 7.5% Sn doping level, the thermopower of compositions with 10% and 12.5% increases with increasing temperature up to 120K from where it becomes almost constant. The large positive values observed for composition between y = 0% and 5% suggest that these compositions are p-type semiconductors.

V-2-2-High temperature electrical conductivity and thermopower of $FeSb_{2-x}Sn_xSe_4$

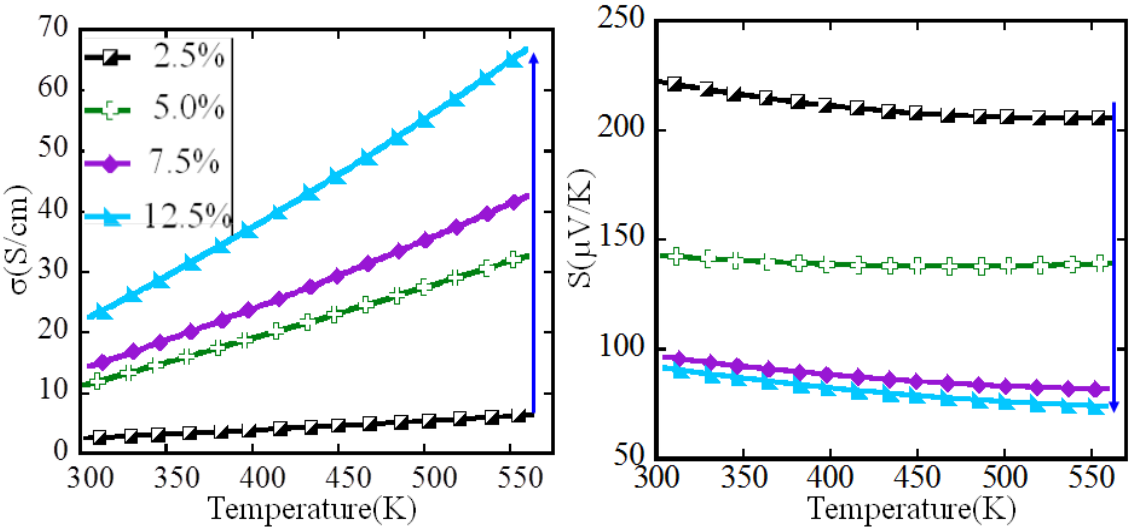

Figure V- 3: (A) High temperature electrical conductivity and (B) thermopower for different concentrations of $FeSb_{2-x}Sn_xSe_4$ with x spanning from 0.05 to 0.25.

Figure V-3 displays the electrical conductivity (A) and thermopower (B) curves of $FeSb_{2-x}Sn_xSe_4$ with x spanning from 0.05 to 0.25 at temperatures range from 300K to 570K. Regardless of the temperature, the conductivity increases with increasing concentration of Sn with the highest values in the whole temperature range observed for the sample with 12.5% of Sn. The $FeSb_{1.75}Sn_{0.25}Se_4$ sample displayed an electrical conductivity value of 23 S/cm at 300K, which represents a relative enhancement of 2200% compared to the pristine compound. In the meantime, the Seebeck coefficient decreases with increasing concentration of Sn. The sample with 12.5% of Sn displays the lowest Seebeck coefficient, which slightly decreases with increasing temperature going from 90µV/K at 300K to 74µV/K at 560K. The variation on both Seebeck and electrical conductivity suggest that, the carrier concentration of $FeSb_2Se_4$ increases by increasing the amount of Sn. This is change in the carrier density with increasing Sn content is believed to be driving force leading to the observed alteration in the magnitude of the magnetic susceptibility despite the constant concentration of the magnetic ions in all $FeSb_{2-x}Sn_xSe_4$ samples.

V-3-Low Temperature Magnetic Properties of $FeSb_{2-x}Sn_xSe_4$

V-3-1-Low Temperature Magnetic Susceptibility

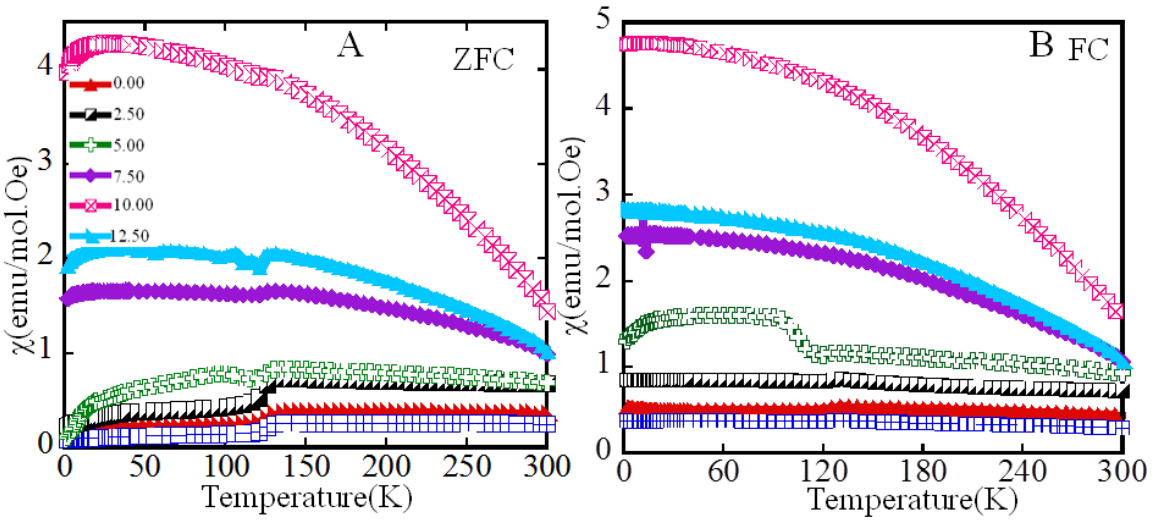

Figure V- 4: temperature dependent magnetic susceptibility under ZFC (A) and FC (B) for samples with different concentration of Sn. Both figures suggest that the magnetic properties are strongly altered with the amount of Sn in $FeSb_2Se_4$.

The Figure V-4 shows the temperature dependence of the magnetic susceptibility under zero field cooled (ZFC) (A) and under field cooled (FC) (B) of different $FeSb_{2-x}Sn_xSe_4$ compositions prepared. The supplementary document in the annex (V-1) shows field dependent magnetization for each composition. ZFC and FC curves are completely divergent for each composition, suggesting a strong anisotropy effect on the bound magnetic polarons[26] for compositions between y = 0.0% to y = 5%, the temperature dependent magnetic susceptibility plots show decreasing values of the susceptibility with decreasing temperature. A striking drop is observed at 130K and is followed by the plateau between 112K and 45K for compositions between y = 0.0% and y = 2.5%. After 45 K, the susceptibility decreases drastically but never reaches zero. Below 100K, the susceptibility of $FeSb_{1.90}Sn_{0.10}Se_4$ (5% Sn doping level) monotonically drops down to 0.097 emu/mol.Oe when the temperature decreases. Furthermore, the compound with Sn composition within y = 7.5% and y = 12.5% showed increasing values of the susceptibility with decreasing temperature. The susceptibility monotonically increases for the $FeSb_{1.85}Sn_{0.15}Se_4$ (7.5%) sample between 300 K and 130 K. For samples with Sn content above 5%, the magnetic

susceptibility decreases below 26 K. Looking closely at these three samples (y = 7.5%, 10%, 12.5%), one can realize that the onset temperature of this downturn of the magnetic susceptibility change depends on the composition with the lowest transition temperature of 19 K observed for the sample with 10% of Sn. However, the FC temperature dependent susceptibility shows increasing values of the susceptibility with decreasing temperature for all samples. But, samples with Sn concentration within y = 0% and 5% showed irregular changes on the magnetic susceptibility. In fact, a magnetic transition is observed at 130K for samples with y = 0% to 2.5% of Sn. This change ends around 120K, below which, the magnetic susceptibility continues to increase with further cooling. All the above observed changes suggest that the spin frustration around 130K could be switched to well ordered magnetic structure with non-magnetic impurities from Sn.

We found that the magnetization and its temperature dependence are strongly altered by the variation of Sn concentration. Indeed, upon substitution of 0.5% Sb by Sn in $FeSb_2Se_4$, the susceptibility drops in all range of temperature. Further addition of Sn results to increasing value of the susceptibility in all range of the temperature for composition between y = 2.5% and 10% of Sn. The maximum susceptibility is obtained on composition with y = 10% Sn in all range of temperature under ZFC and FC conditions. Above y = 10% of Sn, the magnetic susceptibility starts decreasing with further addition of Sn. This change on the magnetic susceptibility suggests that, the magnetic property of $FeSb_2Se_4$ is really sensitive to the concentration of non-magnetic impurities added into the sample.

V-3-2 Low temperature isothermal field dependent magnetization of $FeSb_{2-x}Sn_xSe_4$

The Figure V-4 shows the field dependent magnetization for different compositions (y = 0.0%-12.5%). The applied field varied between -10000Oe to and +10000Oe. Figure V-4A is the field dependent magnetization at 2K while Figure V-4B is collected at 300K. The field dependent magnetization for all samples shows hysteresis up to 300K, suggesting ferromagnetism in all samples up to room temperature and above. As observed on the temperature dependent magnetization, the magnetic saturation initially decreases upon addition of 0.5% Sn in $FeSb_2Se_4$. The values of magnetic saturation at 2K and 300K are 670 emu/mol and 410emu/mol, respectively, representing 7% and 25% magnetization loss at 2K and 300K respectively when compared to the pristine sample. When adding more Sn, the magnetic saturation continuously

increases up to y = 7.5% Sn sample at 2 K and 300 K (except for the sample with y = 5% at 2 K). The value of the magnetic saturation observed at 2 K for that particular sample is 1432 emu/mol and represent 99% increasing value of the magnetic saturation when compared to the Sn free $FeSb_2Se_4$ sample. However at 300 K, the magnetic saturation for y = 7.5% Sn doping level was comparable with the undoped parent compound. Above y = 7.5% the magnetic saturation consistently decreases as we observed on the temperature dependent susceptibility curves. The coercivity fields at different temperatures are presented in the Table V-1. From that table, one can see that the coercivity initially increases, going from 205 Oe for undoped composition to 1000 Oe upon addition of 0.5% Sn. For Sn concentration equal y = 2.5% and above, the coercivity decreases continuously down to 62 Oe at 2 K with increasing amount of Sn. However, at 300 K the coercivity changes irregularly with increasing amount of Sn, but decreases continuously from compositions with y = 2.5%, which exhibit the maximum coercivity for all samples at 300 K.

V-3-3-High temperature magnetic properties of $FeSb_{2-x}Sn_xSe_4$

The magnetic properties of $MnSb_2Se_4$, $Mn_xBi_{2-x}Se_4$ and $FeSb_2Se_4$ have shown correlations with the transport properties in these compounds. Such correlation is one of the important

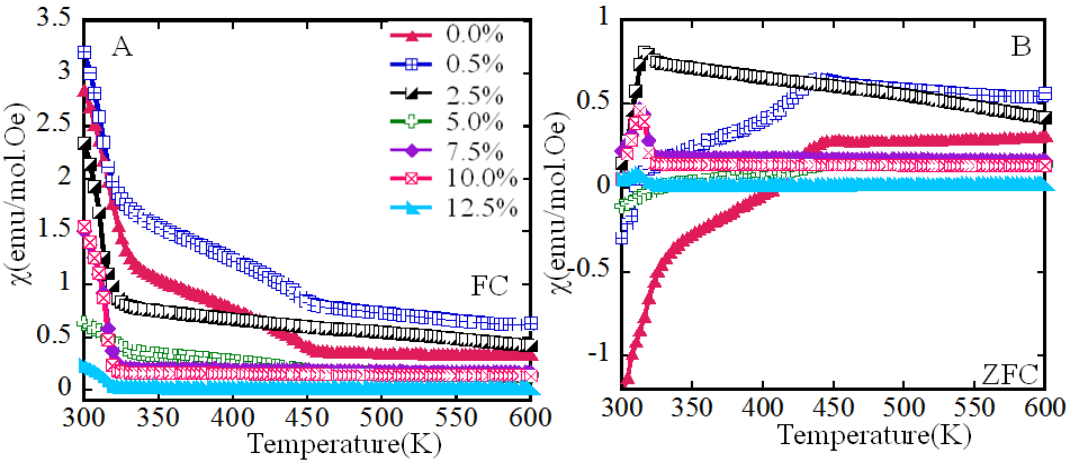

Figure V- 5: (A) FC magnetic susceptibility and (B) ZFC magnetic susceptibility for different compositions within 300K-600K temperature range.

requirements expected for ideal system for promising spin based electronics[26]. Ferromagnetism must be induced in this case via low carrier density. This will presumably allow the control of

magnetic properties from carrier density modulation through doping or applied magnetic/electric fields. To test the effect of impurities on the magnetic properties of $FeSb_2Se_4$, we decided to dope this material with different dopants. In the case Sb to Sn substitution, changes on the magnetic properties at high temperatures are reported here. The Figure V-5 displays the FC and ZFC magnetic susceptibility curves of the $FeSb_{2-x}Sn_xSe_4$ solid solution. Throughout, the susceptibility is altered upon addition of a small fraction of Sn in the material. Contrary to the trend displayed at low temperatures, where both ZFC and FC show similarly changes with increasing concentration on Sn, the situation is rather complex at high temperatures. The concentration dependence of the susceptibility under FC and ZFC shows that, the susceptibility increases when 0.5% Sn is added in $FeSb_2Se_4$ and decreases thereafter up to y = 2.5% where the whole value remains greater than the susceptibility of the pristine compound above 450K. Further doping results in continuously diminution of the magnetization with increasing concentration of Sn with the magnitude of the susceptibility below that of $FeSb_2Se_4$.

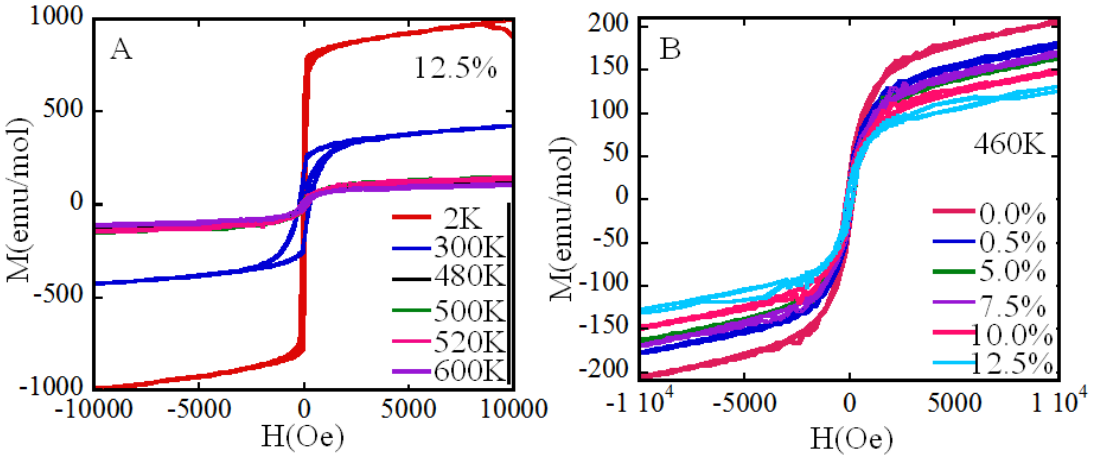

Figure V- 6: (A) Field dependent magnetization of $FeSb_{1.75}Sn_{0.25}Se_4$ for temperature between 2K-600K, this is the highest doped composition and still exhibits ferromagnetism; (B) isothermal field dependent magnetization at 460K for different concentration of Sn.

However, below 450 K and under FC conditions, only the susceptibility of $FeSb_{1.99}Sn_{0.01}Se_4$ is above the value displayed by the undoped composition. All other compositions exhibit susceptibility values below that of the undoped material. The ZFC regime however, shows that

the susceptibility increases with increasing concentration of Sn up to y = 2.5% with magnetic transition around 450 K as observed on the FC curves. Above 2.5% Sn, the susceptibility continuously decreases with further addition of Sn. However, irregularity on the trend is observed on the sample with 5% Sn, which shows the increase in susceptibility with increasing temperature up to 450 K. In the case of compositions with y between 2.5% and 12.5% the susceptibility increases with increasing temperature up to 315 K where they display the maximum values. Thereafter, a sharp drop in the susceptibility is observed on further heating the sample up to 322 K for compositions with Sn amount between y = 7.5% and 12.5%. Above this temperature the susceptibility is almost constant with increasing temperature. Two critical transition temperatures at 330 K and 450 K are observed for samples with 0.0%, 0.5% and 5% amount of Sn, while all other samples show transition temperature at 332 K under FC and ZFC conditions. To understand the origin of such transitions, we must consider the effect of thermal processing on the $FeSb_2Se_4$ structure. As reported earlier, the $FeSb_2Se_4$ compound undergoes structural phase change when it is heated. Upon heating this material from 300 K to 350 K, a striking change along the *a*-axis of the crystal structure was observed. The *a*-axis drastically expand from 13.083(3) Å at 300 K to 38.243(8) Å at 350 K, while the β angle slightly drop from 114.78^o(300 K) to $111.21(3)^o$ (350 K). Further heating the material up to 400 K results to change of *a*-axis to 27.543(6) Å and *c*-axis to 26.22(5) Å while β sharply decreases to $90.72(3)^o$. In addition the space group switches from *C* 2 /*m* at 350K to *C* 1/*c* 1. These structural phase - change are associated with the magnetic phase transitions observed at 323 K and 450 K, respectively. One can anticipate that, the structural phase transition at 350 K started below 323 K, where transition from 300 K to 350K induced the rearrangement of the magnetic subunit. The second magnetic transition temperature at 450K corresponds to the simultaneous change in the structure and the electronic structure of this material, which strongly alters the magnetic behavior of $FeSb_2Se_4$.

The ferromagnetism persists at high temperatures when we increase the amount of Sn in $FeSb_2Se_4$. This could be observed on the field dependent magnetization for different compositions at 460 K and the hysteresis loop of the highest concentration of Sn for temperatures between 2 K-600 K. The Figure V-6A shows the field dependent magnetization at different temperatures for $FeSb_{1.75}Sn_{0.25}Se_4$ which is the composition with highest amount of Sn. The figure highlights the coercivities for all temperatures that range from 62 Oe to 277 Oe with

the highest value observed at 300 K. As the temperature increases, the coercivity initially increases from 62 Oe to 277 Oe and decreases afterward down to 100 Oe with further increase of the temperature. Meanwhile, the magnetization saturation evaluated from 10000 Oe applied field decreases monotonically, going from 1000 emu/mol at 2K to 111emu/mol at 600 K. Each composition of $FeSb_{2-x}Sn_xSe_4$ at high temperature show similar behavior of field dependent magnetization. The Figure V-6B is the field dependent magnetization at 460 K for different compositions of $FeSb_{2-x}Sn_xSe_4$ prepared in this work. As we increase the concentration of Sn the magnetization decreases. This is in contradiction with the trend observed at low temperatures where the magnetization initially decreases for the composition with y = 0.5% and then increases up to 10% from where it drops down under further addition of Sn. This variation in the magnetization of $FeSb_{2-x}Sn_xSe_4$ could be clarified from the correlation between the d orbital of the local magnetic moment and the free carriers available near the valence band of the semiconductor in these materials. This happens as the magnetic ordering, which is correlated to free carrier in this case is also affected by the temperature. Presumably, because of the activation processes that allow free carrier at band edge to be promoted to the conduction band. As we reported at low temperatures, the doping of $FeSb_2Se_4$ with Sn leads to the increasing electron concentration in the material. This reduces the $N\beta$ term which is define in chapter I of the exchange coupling, which favors the strong p-d exchange coupling .

V-4-Correlations between charge transport magnetic properties in $FeSb_{2-x}Sn_xSe_4$

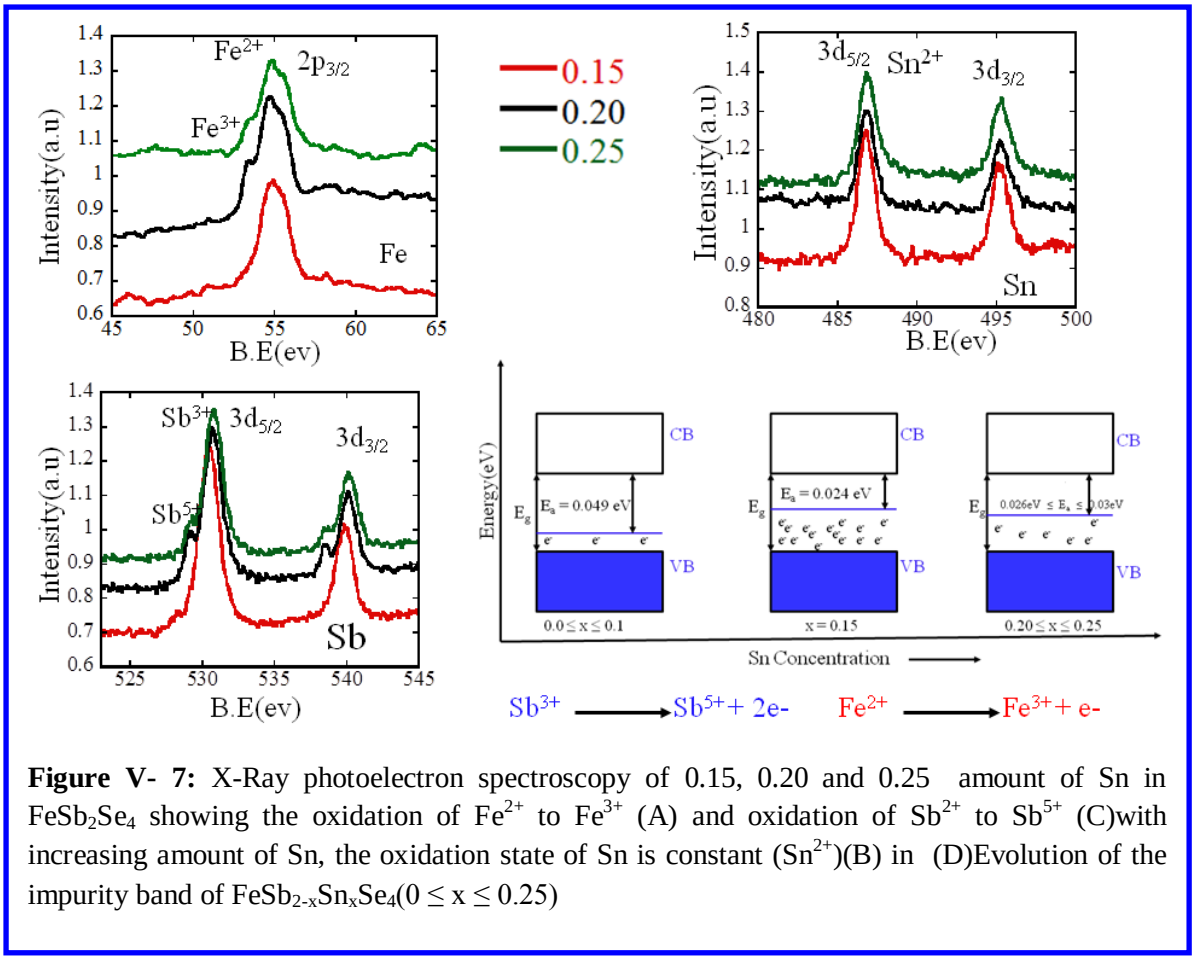

Figure V- 7: X-Ray photoelectron spectroscopy of 0.15, 0.20 and 0.25 amount of Sn in $FeSb_2Se_4$ showing the oxidation of Fe^{2+} to Fe^{3+} (A) and oxidation of Sb^{2+} to Sb^{5+} (C)with increasing amount of Sn, the oxidation state of Sn is constant (Sn^{2+})(B) in (D)Evolution of the impurity band of $FeSb_{2-x}Sn_xSe_4(0 \leq x \leq 0.25)$

The magnetic and electrical properties of $FeSb_{2-x}Sn_xSe_4$ ($0 \leq x \leq 0.25$) consistently change with increasing concentration of Sn. Our recent work showed that, the magnetic properties of $FeSb_2Se_4$ can be altered by change in the electronic behavior.[1] The chemical manipulation of this material through substitution of small fraction of Sn indicates alteration of its electrical behavior, suggesting that this material is sensitive to the impurities. Activation energy for different compositions were calculated from the Arrhenius's relation $\rho = \rho_0 \exp(E_a/k_BT)$, where E_a is the activation energy and k_B is the Boltzmann constant. The electrical resistivity for all samples shows an activation behavior from 100 K to 300 K. Effort to have the resistivity of the $FeSb_{1.99}Sn_{0.01}Se_4$ sample failed. We suspect this scenario to be related to the high resistivity of this particular sample. This might also explain the drop on the magnetic susceptibility of $FeSb_{1.99}Sn_{0.01}Se_4$ compared to the parent compound.

As reported in the Figure V7, the oxidation state of Fe^{2+} change to Fe^{3+} and Sb^{3+} to Sb^{5+} with increasing concentration of Sn is observed on XPS spectra. We expected the observed behavior to affect the magnetization of different samples. In fact, two main mechanisms of interaction govern the magnetic exchange interaction here. (1) The long range exchange interaction from extra electron added at the band edge polarizing spin of the Fe^{2+} that are on the impurities band. In this case adding more electron (presumably adding more Sn) results into increasing the density of spin-polarized carriers, leading to increasing magnetization as observed from 2.5% to 10%. The increasing magnetization from 2.5% suggests that, the oxidation of Fe^{2+} and Sb^{3+} may start when sufficient slightly amount of Sn is added. That is consistent with the decreasing value of the activation energy with increasing amount of Sn. (2) The double exchange mechanism between $Fe^{3+} - Se - Fe^{2+}$ which is mainly AFM in the case $Fe^{3+} - O - Fe^{2+}$. This could explain the diminution of the magnetization when further Sn is added in FeSb2Se4 above 10% doping.

The increasing value of the susceptibility and the magnetization for sample with 2.5% Sn ($FeSb_{1.95}Sn_{0.05}Se_4$) was followed by the drop of the electrical conductivity and the Seebeck. However, the Seebeck coefficient for the composition with 5% Sn was larger in all range of the temperature compared to the values observed for the sample with 2.5% Sn. In addition, the values of the Seebeck for the sample with y = 2.5% change from 150µV/K at 50K to 142µV/K at 300K are almost constant in the whole range of the temperature (Figure V-2B), since only 1.33% deviation is observed at 300K compared to the value at 50K. This suggests a slight change in the carrier concentration of the sample.

For $FeSb_{2-x}Sn_xSe_4$ compositions with Sn concentration above 5%, all samples showed low electrical resistivity with maximum value of 0.45Ω.cm for temperature between 50K and 300K. Interestingly, the Seebeck coefficient drop from 142µV/K for 2.5% doping level to 40µV/K for composition with 7.5% amount of Sn at 300K. Furthermore the Seebeck coefficient of this composition ranged between 60µV/K at 300K and -2µV/K at 43K (7.5%). This means that, increasing the fraction of Sn in the $FeSb_2Se_4$ changes its electrical behavior from almost insulating to metallic-like behavior. This switch from insulator to metallic behavior observed around 62K for the sample with y = 7.5% is also observed in the magnetic behavior of this composition. In fact, the maximum magnetic susceptibility at all temperatures was observed for $FeSb_{2-x}Sn_xSe_4$ composition with about 7.5%Sn. In addition the inset of the Figure V-2A showed

that the resistivity of the $FeSb_{1.85}Sn_{0.15}Se_4$ composition (y = 7.5%) increases with decreasing temperature going from 0.048Ω.cm at 300K to a maximum of 0.42Ω.cm at 62K and decreases thereafter down to 0.22Ω.cm for further decrease of the temperature. This particular sample shows the highest magnetization on the field dependent magnetization data at 2K and at 300K. The Seebeck coefficient of $FeSb_{1.85}Sn_{0.15}Se_4$ composition (y = 7.5%) and compositions with high Sn content, initially increases sharply with increasing temperatures up to 200K (for y = 7.5%), 91K (for y = 10%), and 123K(for y = 12.5%). After that, the Seebeck was constant with further increase in the temperature. We suspect this change on Seebeck to originate from the thermal activation of carriers from the intermediate impurity band to the conduction band of the $FeSb_{2-x}Sn_xSe_4$ compounds.

The $FeSb_2Se_4$ structure is subjected to defects from the mix occupancies of Fe^{2+}/Sb^{3+} either at Fe^{2+} or Sb^{3+} crystallographic sites. We anticipated that, the Sb to Sn substitution will initially take place at these mixed positions. Therefore the electronic band structure of this compound would be mainly dominated by the impurity band form by the mixture of Fe^{2+}/Sb^{3+}. The activation energy for the $FeSb_{1.85}Sn_{0.15}Se_4$ composition (y = 7.5%) was calculated considering the dominant activation process in this material at low temperature, and the value of 0.049eV allows concluding that the impurity band is confined within the band gap and is mainly populated by electrons. Upon substitution of Sb with Sn, the system change from p-type narrow band gap semiconductor to metallic like as suggested by the low Seebeck coefficient for $FeSb_{2-x}Sn_xSe_4$ composition with y =7.5% to 12.5% and the transition from positive to negative Seebeck at low temperatures. This situation suggests that, the substitution of Sb^{3+} with Sn, leads to an increase in the density of electrons in the p-type $FeSb_{2-x}Sn_xSe_4$ semiconductor, instead of the anticipated increase in hole concentration. Indeed, X-ray photoelectron spectroscopy (XPS) (Figure V-7) of samples with y = 7.5% , 10% and 12.5 %, indicated that a small fraction of Fe^{2+} oxidize in to Fe^{3+} and Sb^{3+} to Sb^{5+} upon substitution of Sb^{3+} with Sn^{2+}. This oxidation of Fe^{2+} and Sb^{3+} results in the contribution of extra electrons to the impurity band. These free electrons dominate electronic conductions at sufficiently low temperatures. Upon increasing the temperature, electron-hole compensation processes result in lowing Seebeck coefficient for these samples. The activation energies for all $FeSb_{2-x}Sn_xSe_4$ compositions reported in the Table V-2, showed a marginal decrease with increasing concentration of Sn.

The change of impurity band with Sn concentration is illustrated on the Figure V-7D, where one can see the decreasing gap of the band with increasing amount of Sn. The decreasing value of the activation energy with increasing Sn is consistent with our assumption that as more Sn is added in the sample, more electrons are provided leading to a decrease in the hole concentrations. From the samples with y = 7.5% and above, the hole concentration become small and conduction is now dominated by electrons. This explained the metallic like behavior exhibited in the samples with y = 7.5% and above. In addition, the electrical conductivity consistently increases with increasing concentration of Sn. This suggests that adding Sn in $FeSb_2Se_4$ mainly increase the concentration of charge carriers of the resulting materials.

From the variation of the Seebeck coefficient, we anticipate that the carrier concentration change with temperature is less pronounced for samples with Sn content above 2.5%. Therefore, the most important factor leading to the observed increase in the magnetic susceptibility of samples with Sn content above 2.5% is the density of spin polarized electron at the impurity band. Since the mean field theory predicts the susceptibility in magnetic semiconductor to be dependent on both density localized spin magnetic atoms and the density of spin polarized electron (hole), the maximum susceptibility observed for the sample with y = 7.5% corresponds to a situation of maximum concentration of added electrons to the impurity band. The susceptibility of $FeSb_{2-x}Sn_xSe_4$ samples with Sn concentration of 10% and above decreases with increasing Sn concentration. This is consistent with the change on the electrical conductivity and the increasing value of the activation energy. In contrary to the $MnSb_{2-x}Sn_xSe_4$ system, the $FeSb_{2-x}Sn_xSe_4$ compounds exhibit a monotonic increase in the resistivity with increasing concentration of Sn. This situation could be assigned to an increase in the density of electrons and/or a decrease of the spin disorder scattering due to the preferential alignment of spin polarized carriers in ferromagnetic materials[27].

Table V- 1 : Coercivity of $FeSb_{2-x}Sn_xSe_4$ ($0 \leq x \leq 0.25$) giving at 2K and 300K

Sn Concentration (%)	Coercivity at 2K(Oe)	Coercivity at 300K(Oe)
0.0	205	238
0.5	1000	327
2.5	316	377
5	122	327
7.5	183	300
10	95	140
12.5	62	250

Table V- 2: Activation energies of $FeSb_{2-x}Sn_xSe_4$ for different concentration of Sn.

Sn Concentration (%)	Activation Energy Ea(eV)
0.00	0.049
2.50	0.048
5.00	0.046
7.50	0.024
10.00	0.030
12.50	0.026

Conclusion

The $FeSb_{2-x}Sn_xSe_4$ ($0 \leq x \leq 0.25$) phases show a strong dependence of the magnetic behavior on the carrier density. We found that, the mechanism of magnetic coupling is related to the modification of the band structure of $FeSb_2Se_4$ upon doping with Sn. The impurity band edge decreases with increasing amount of Sn in the sample. Coercivity and magnetic saturation were altered when Sb is substituted with Sn. The most interesting finding is the magnetic and electrical behavior of the sample with 7.5% Sn doped. This particular sample shows the highest magnetic susceptibility in the whole series and exhibits a switch from semiconductor to metallic like behavior at low temperatures. This particular sample suggests a possibility of quantum critical phenomena in $FeSb_2Se_4$, making this material a suitable template for various studies of electron-correlated phenomena, particularly to understand the effect of the manipulation of the band edge on magnetic ordering.

References

(1) Ranmohotti, K. G. S.; Djieutedjeu, H.; Poudeu, P. F. P. *J Am Chem Soc* **2012**, *134*, 14033.
(2) Story, T.; Gałązka, R. R.; Frankel, R. B.; Wolff, P. A. *Physical Review Letters* **1986**, *56*, 777.
(3) Chiba, D.; Fukami, S.; K., S.; N., I.; K., K.; T., O. *Nature Materials* **2011**, *10*, 853.
(4) Chiba, D.; Werpachowska, A.; Endo, M.; Nishitani, Y.; Matsukura, F.; Dietl, T.; Ohno, H. *Phys Rev Lett* **2010**, *104*.
(5) Akai, H. *Physical Review Letters* **1998**, *81*, 3002.
(6) Ando, K. *Science* **2006**, *312*, 1883.
(7) Chattopadhyay, A.; Das Sarma, S.; Millis, A. J. *Physical Review Letters* **2001**, *87*, 227202.
(8) Dietl, T.; Ohno, H.; Matsukura, F.; Cibert, J.; Ferrand, D. *Science* **2000**, *287*, 1019.
(9) Dietl, T. *Nat Mater* **2010**, *9*, 965.
(10) Cibert, J.; Kossacki, P.; Haury, A.; Ferrand, D.; Wasiela, A.; d'Aubigne, Y. M.; Arnoult, A.; Tatarenko, S.; Dietl, T. *J Cryst Growth* **1999**, *201*, 670.
(11) Coey, J. M. D.; Venkatesan, M.; Fitzgerald, C. B. *Nat Mater* **2005**, *4*, 173.
(12) Dietl, T.; Haury, A.; dAubigne, Y. M. *Phys Rev B* 1997, *55*, R3347.
(13) Dietl, T.; Ohno, H. *Mater Today* **2006**, *9*, 18.
(14) Dietl, T.; Ohno, H.; Matsukura, F. *Phys Rev B* **2001**, *63*.
(15) Durst, A. C.; Bhatt, R. N.; Wolff, P. A. *Phys Rev B* **2002**, *65*.
(16) Ferrand, D.; Cibert, J.; Bourgognon, C.; Tatarenko, S.; Wasiela, A.; Fishman, G.; Bonanni, A.; Sitter, H.; Kolesnik, S.; Jaroszyski, J.; Barcz, A.; Dietl, T. *J Cryst Growth* **2000**, *214*, 387.
(17) Kaminski, A.; Das Sarma, S. *Phys Rev Lett* **2002**, *88*.
(18) Kundaliya, D. C.; Ogale, S. B.; Lofland, S. E.; Dhar, S.; Metting, C. J.; Shinde, S. R.; Ma, Z.; Varughese, B.; Ramanujachary, K. V.; Salamanca-Riba, L.; Venkatesan, T. *Nat Mater* **2004**, *3*, 709.
(19) Bader, S. D.; Parkin, S. S. P. *Annu Rev Conden Ma P* **2010**, *1*, 71.
(20) Fert, A.; George, J.-M.; Jaffres, H.; Mattana, R. *europhysics news* **2003**, 227.
(21) Jansen, R. *Nat Mater* **2012**, *11*, 400.
(22) *Concepts in Spin Electronics*; Sadamichi; Maekawa, Eds.; Oxford Science Publication: Oxford, 2006.
(23) Dobrowolska, M.; Tivakornsasithorn, K.; Liu, X.; Furdyna, J. K.; Berciu, M.; Yu, K. M.; Walukiewicz, W. *Nat Mater* **2012**, *11*, 444.
(24) Jungwirth, T.; Wang, K. Y.; Masek, J.; Edmonds, K. W.; Konig, J.; Sinova, J.; Polini, M.; Goncharuk, N. A.; MacDonald, A. H.; Sawicki, M.; Rushforth, A. W.; Campion, R. P.; Zhao, L. X.; Foxon, C. T.; Gallagher, B. L. *Phys Rev B* **2005**, *72*.
(25) Djieutedjeu, H.; Poudeu, P. F. P.; Takas, N. J.; Makongo, J. P. A.; Rotaru, A.; Ranmohotti, K. G. S.; Anglin, C. J.; Spinu, L.; Wiley, J. B. *Angew Chem Int Edit* **2010**, *49*, 9977.
(26) Macdonald, A. H.; Schiffer, P.; Samarth, N. *Nat Mater* **2005**, *4*, 195.
(27) Lee, S.; Hwang, S. J.; Lee, H. S.; Shon, Y.; U.Yuldashev, S.; Kim, D. Y. *Journal of Applied Physics* **2005**, *98*, 123905.

Chapter VI

Effect of Te Doping on Transport and Magnetic Properties of $FeSb_2Se_4$

Introduction

The previous two chapters have shown interesting correlations between the transport properties and the magnetic properties in $FeSb_2Se_4$. However, $FeSb_2Se_4$ has very low conductivity at low and high temperatures. The effort so far to increase the conductivity by replacing fractions of Sb with Sn did not give significant enhancement of the transport properties. We proposed to improve the conductivity of the parent composition by replacing a fraction of Se with Te. We expect to improve the conductivity by increasing the carrier mobility, while keeping the crystal structure and carrier density unchanged. In this chapter, we report the transport and magnetic properties of $FeSb_2Se_{4-x}Te_x$ with x spanning from 0 to 0.1. We found that the magnetic properties upon doping of $FeSb_2Se_4$ with Te were altered by the variation of the transport properties.

VI-1- X-ray diffraction on polycrystalline sample of $FeSb_2Se_{4-x}Te_x$ ($0.01 \leq x \leq 0.1$)

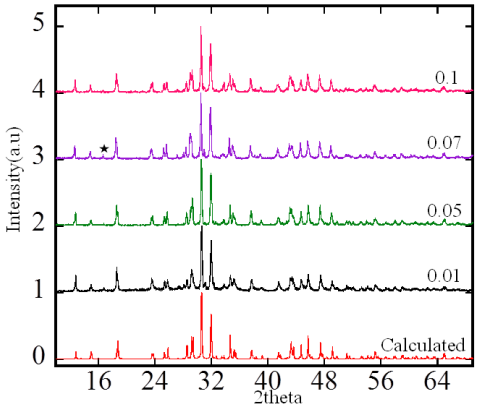

Figure VI- 1: X-ray powder diffraction of $FeSb_2Se_{4-x}Te_x$ ($0.01 \leq x \leq 0.1$). All compositions are isostructural with $FeSb_2Se_4$ parent phase.

A series of $FeSb_2Se_{4-x}Te_x$ with x values ranging from 0.0 to 0.1 has been prepared. Figure VI-1 shows the X-ray diffraction pattern of the synthesized compounds. The experimental X-ray powder diffraction patterns are compared with the calculated pattern from the structure of $FeSb_2Se_4$ at 300K. All experimental X-ray powder diffractions show perfect match with the calculated pattern. Therefore, all compositions are believed to adopt the monoclinic crystal system.

V-2-Electronic transport properties

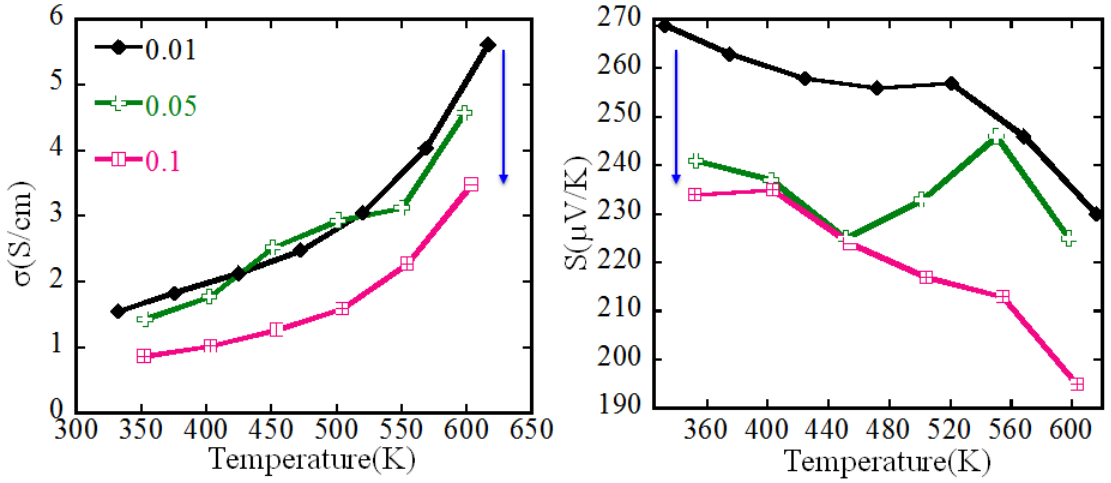

Figure VI- 2: High temperatures Electrical conductivity (A) and Seebeck coefficient (B) of $FeSb_2Se_{4-x}Te_x$ samples showing diminution of both the electrical conductivity and the Seebeck coefficient with increasing amount of Te.

Figure VI-2(A) shows the temperature dependent electrical conductivity of three samples within the temperature range from 300K to 600K. Despite the low value of the conductivity observed in these samples, the conductivity increases with increasing temperature with the highest value of 1.54 S/cm and 5.61S/cm observed at 334K and 615K respectively for the composition with x = 0.01. The lowest value of the electrical conductivity, 0.86 S/cm at 300K and 3.47S/cm at 600K, was observed for the compound containing about 0.1 Te. However, the room temperature value is slightly higher compared to 0.99 S/cm for the undoped composition at that temperature. Therefore, adding a small fraction of Te into $FeSb_2Se_4$ results in a decrease in the electrical conductivity, which is opposite to the initially anticipated trend. Regardless of Te concentration (x value), the electrical conductivity increases with increasing temperatures, which is consistent with the semiconducting behavior of the samples.

Figure VI-2 (B) shows the thermopower of different compositions as a function of temperature. For all compositions, the thermopower decreases with increasing temperature. The highest thermopower value of 269 μV/K is obtained at 330 K for x = 0.01. The thermopower decreases with increasing temperature to 229 μV/K at 615 K. The lowest values are obtained for the

composition with x = 0.1, with a thermopower value of 233 µV/K at 300 K and 195 µV/K at 602 K. These values are lower compared to the Seebeck coefficient of the undoped $FeSb_2Se_4$ at the same temperatures. All samples are *p*-type semiconductors. The low values of the electrical conductivity and thermopower upon Te doping at Se sites in $FeSb_2Se_4$ indicates that the carriers mobility drastically decreases, while the carrier density increases despite the fact that Te to Se substitution is expected to be isoelectronic. One possible explanation of this surprising behavior is that the Te to Se substitution largely decreases the electronic band gap of the material leading to the thermal excitation of a large fraction of electrons from the valence band to the conduction band at a given temperature.

VI-3-Effect of Te doping on the magnetic properties of $FeSb_2Se_{4-x}Te_x$

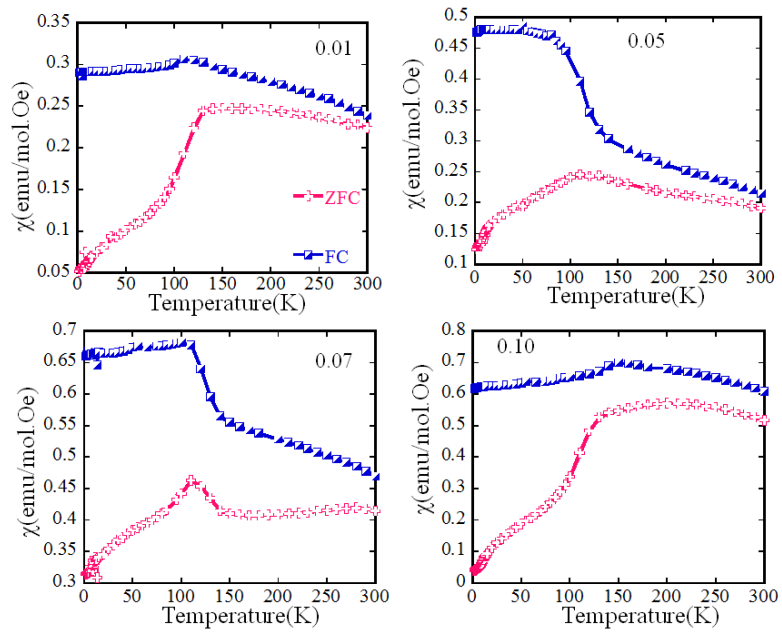

Figure VI- 3: ZFC and FC of different samples at low temperature showing field dependent magnetization, the large gap between ZFC and FC is also observed.

Figure VI-3 depicts the temperature dependent of the magnetic susceptibility under zero field cooled (ZFC) and field cooled (FC) for samples with different concentrations of Te. For each concentration, the susceptibility increases with decreasing temperature up to 130K. Below this temperature, a sharp discrepancy is observed between the ZFC and FC. From 130K, a significant

change on the ZFC susceptibility is observed as depicted by the downturn on Figure VI-3 and continuously decreasing value of the magnetization with decreasing temperature. In the meantime, the magnetization under the FC increases with decreasing temperature.

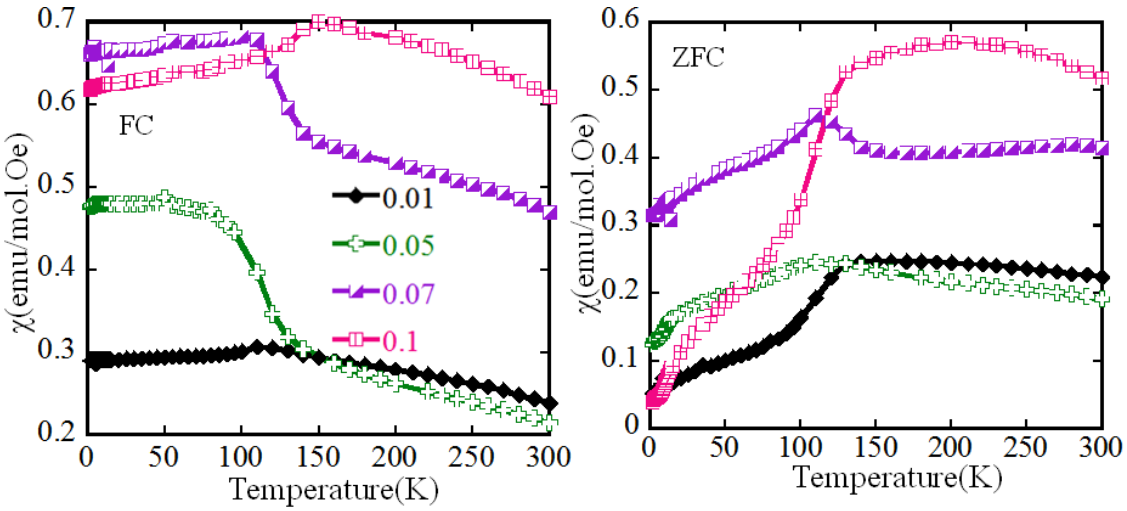

Figure VI- 4: FC and ZFC of different composition generated from the synthesis of $FeSb_2Se_{4-x}Te_x$

The FC magnetic susceptibility for the samples with x = 0.05 and 0.07 is almost constant below 100K. Regardless of the temperature, the magnitude of the magnetic susceptibility generally increases with increasing Te concentration. Below 130 K, an irregular trend on susceptibility is observed on both FC and ZFC regime with the maximum susceptibility observed for the sample with x = 0.07. However, for temperatures above 130 K, the susceptibility initially decreases in both FC and ZFC upon addition of x = 0.01 Te atom. Above the concentration with x = 0.01, the susceptibility increases with increasing Te content and the maximum susceptibility is observed for the sample with x = 0.1(Figure VI-4). The divergence between the FC and ZFC (Figure VI-3) susceptibility curves from 2K up to 300K allows us to anticipate ferromagnetic ordering in these compounds at room temperature and above. This is consistent with the magnetic behavior of the parent compound $FeSb_2Se_4$, which is ferromagnetic with a transition temperature far above 300K. The doping with Te aims to increase the very low conductivity observed in the parent compound. We also doped the Sb site with Sn for the same purpose, but the various solid-solutions obtained via this manipulation of the chemical composition displayed very low carrier

mobility, and therefore a very low conductivity. As we observed from the temperature dependent conductivity discussed above, the electrical conductivity of the various $FeSb_2Se_{4-x}Te_x$ phases increases compared to that of the $FeSb_2Se_4$ compound. The change in the electrical conductivity did not inhibit the FM ordering in the system. However, it turns out that the magnitude of the magnetic susceptibility is altered when the electrical conductivity increases.

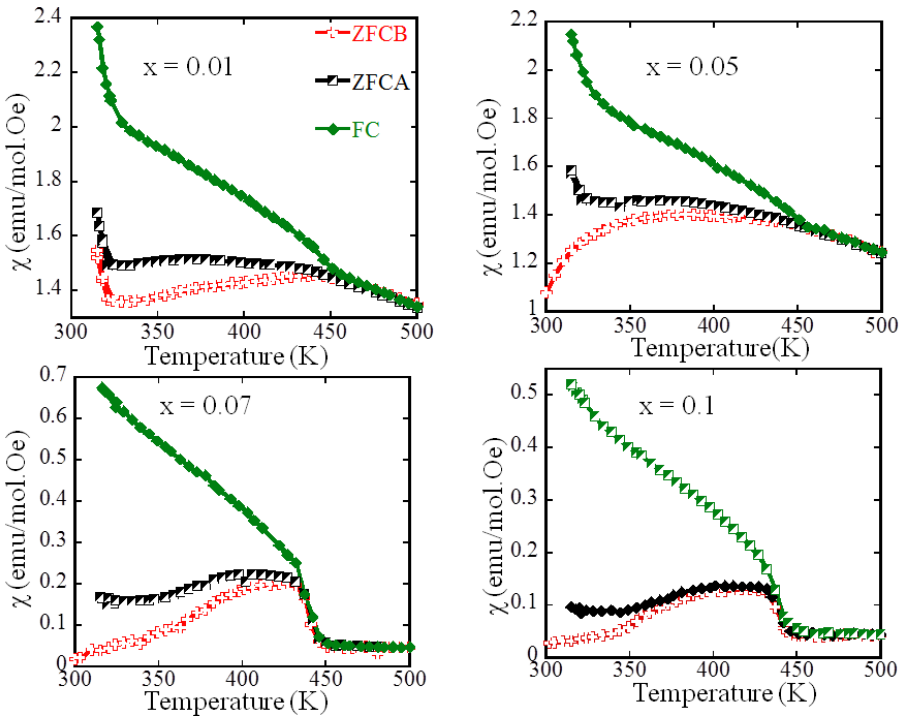

Figure VI- 5: High temperatures dependence of the magnetic susceptibility for different various $FeSb_2Se_{4-x}Te_x$ compositions. The ZFCA and ZFCB curves for all samples are distinguishable below 440K, with the gap between them.

The high temperature (300K-500K) dependence of the magnetic susceptibilities of the $FeSb_2Se_{4-x}Te_x$ samples are displayed in Figure VI-5. Because of the mismatch between the low and high temperature susceptibility data and the gap between the FC and ZFC curves observed for the high temperature dependent susceptibility, we have collected the temperature dependent susceptibility data as followed:

-We initially measured the susceptibility data under ZFC on the ZFC regime when heating up sample from 300K to 600K under applied field of 100Oe. This data is denoted by ZFCB on Figure VI-5.

-After the first step, we cooled the system down to 300K under applied field and then collected data when heating up the system under the same applied field. This data is denoted by FC on Figure VI-5.

-The sample was now cooled down to 300K without any applied field and finally heat is applied from 300K to 600K when collecting data under 100Oe applied field. We denoted this step as ZFCA on Figure VI-5.

From Figure VI-5, one can see that the FC susceptibility of each $FeSb_2Se_{4-x}Te_x$ composition decreases with increasing temperature and shows a sharp drop in the susceptibility around 450K. Interestingly, the ZFCB and ZFCA curves for the samples with x = 0.07 and x = 0.1 increase

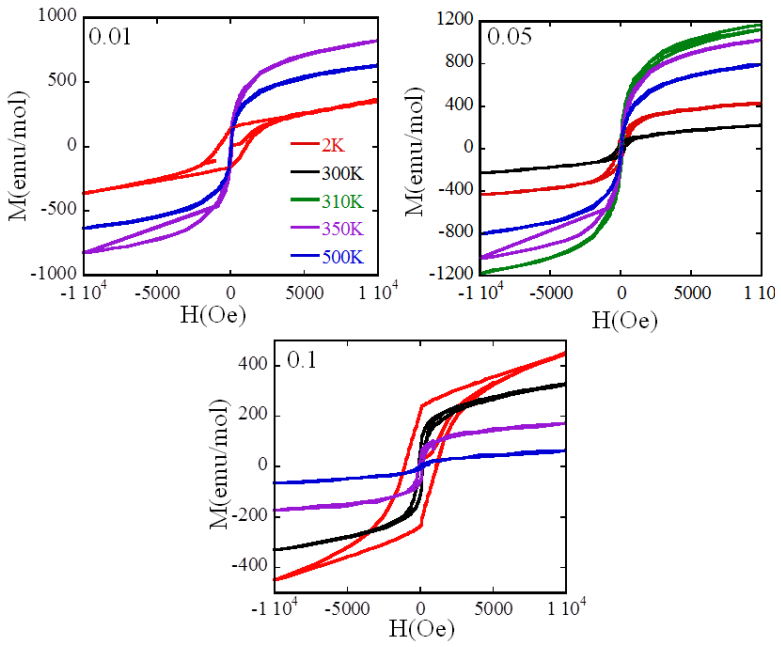

Figure VI- 6: Field dependent magnetization of different $FeSb_2Se_{4-x}Te_x$ compositions at temperatures range between 2K and 500K. All samples showed ferromagnetic ordering up to 500K.

with increasing temperature up to 431K where the maximum susceptibility is observed under ZFC and FC conditions. The susceptibility decreases at temperatures above 431 K and becomes almost constant above 450K. However, in the case of samples with x = 0.01 and 0.05, the ZFCA and ZFCB susceptibilities initially decrease from 300K to 320K and subsequently increase with

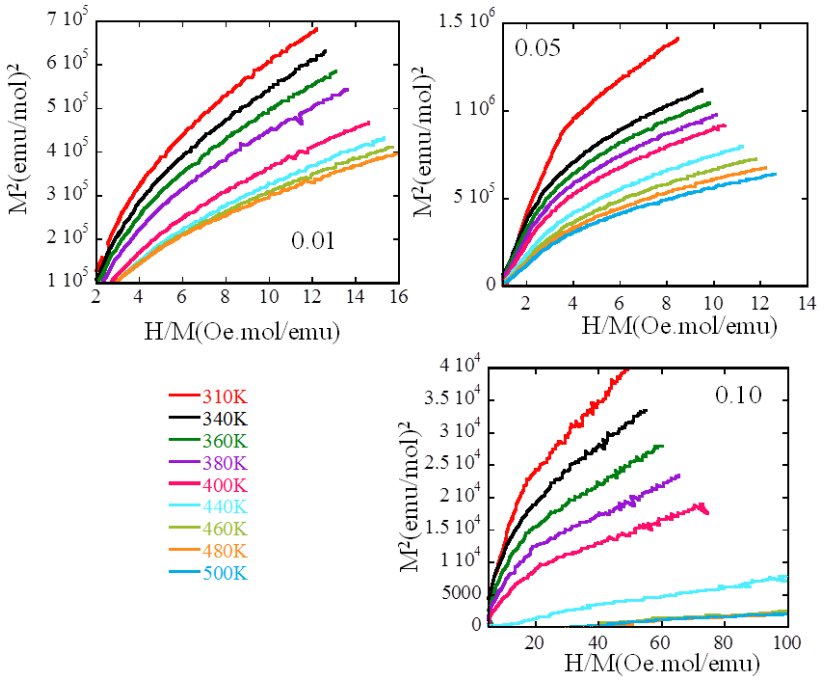

Figure VI- 7: Arrott`s plot of various $FeSb_2Se_{4-x}Te_x$ composition at temperatures between 310K-500K. The composition with x = 0.10 shows extrapolation to zero at 440K, suggesting a Currie temperature T_c of 440K. The hysteresis loop in field dependent magnetization above 450K might be an expression of superparamagnetism.

further increase in the temperature up to 450K. Both ZFCB and ZFCA curves are divergent at temperatures below 450K, but converge at 450K along with the FC curve. The increasing values of the susceptibility from 300K to 450K under ZFC condition is similar to the temperature dependence of the susceptibility for the parent compound. This is assigned to the effect of spin-polarized free-carriers induced by the external applied magnetic field (100 Oe). Such spin-polarized carriers presumably mediate long range ordering between the localized magnetic moment from pure magnetic ions, which is the Fe^{2+} in this case. The increasing value of the ZFC

susceptibility observed when we increase the temperature of the system suggests an increase in the density of spin-polarized carriers in the materials due to thermal activation of additional electrons from the valence band to the conduction band. This is consistent with the increasing values of the electrical conductivity. However, the susceptibility reaches the maximum value at 431K, where all FC and ZFC curves converge, and a sharp drop of the susceptibility to the lowest value is observed at 450K. We suspect that the drop in the susceptibility originates from the dominant effect of thermal spin fluctuation over the magnetic coupling between the spin of free carriers and the external applied magnetic field.

The Figure VI-6 is the field dependent magnetization of $FeSb_2Se_{4-x}Te_x$ ($0.01 \leq x \leq 0.1$) at various temperatures. The samples with x = 0.01 and 0.05 fraction showed temperature dependent magnetization, with maximum magnetization of 826 emu/mol for x =0.01 at 350K and 1161 emu/mol for x = 0.05 at 310K. Interestingly, the magnetization increases with temperature from 300K to these maximum values. Normally, one should expect the magnetization to decrease with increasing temperature as a result of thermal vibration inducing spin disorder. However, the magnetization for the samples with x = 0.01 and 0.05 decreases from 2K to 300K and increases thereafter. This change is consistent with the increasing magnetic susceptibility observed under ZFC conditions. This could confirm our current hypothesis, which assumes that the thermal activation of electrons from the valence band to the conduction band and the subsequent polarization of these carriers by the external applied magnetic field govern the magnetic behavior at high temperatures through the mediation of long-range ordering of localized magnetic moments on Fe ions.

The unusual increase in the magnetization with increasing temperature observed on samples with x = 0.01 and 0.05 is absent in the sample with x = 0.1 where the saturation magnetization monotonically decreases with increasing temperature going from 452 emu/mol at 2K to 63 emu/mol at 500 K. This means that for this sample (x = 0.1), the effect of spin-polarized free carriers on the mediation of long-range magnetic ordering might be less pronounced compared to other samples. The coercivity field changes from 111 6Oe to 0 Oe with the largest coercivity field observed at 2 K for the sample with x= 0.10. For each sample, the coercivity field decreases with increasing temperature. Samples with Te concentration x = 0.01 and 0.05 showed coercivities between 1000 Oe and 45 Oe for temperatures below 350 K, while at 500 K, the

coercivity was found to be 0 Oe. Therefore, one can anticipate the ferromagnetism in of $FeSb_2Se_{4-x}Te_x$ ($0.01 \leq x \leq 0.1$) compounds to vanish above 450 K, which is the onset temperature of the convergence of the ZFC and FC susceptibility curves. The "snake" shape of the field dependent magnetization observed at 500 K is an indication of superparamagnetism in the samples. For sample with x = 0.1, the coercivity of 92 Oe was observed at 500 K. This suggests that the sample does not show any superparamagnetic behavior above 450 K. However, the Arrott's plots for different compositions presented in Figure V-7 suggest that ferromagnetic behavior can exist up to 500 K in samples with $x < 0.1$, while the sample with x = 0.1 shows transition from ferromagnetism to superparamagnetism at 440 K as indicated by the linear extrapolation of the M^2 versus H/M curve to 0 at T = 440 K.

Conclusion

$FeSb_2Se_{4-x}Te_x$ ($0 \leq x \leq 0.1$) solid-solutions prepared by adding small fractions of Te into Se sites in the structure of $FeSb_2Se_4$ showed ferromagnetic ordering up 500 K for composition below x = 0.1 and a transition from ferromagnetic ordering to superparamagnetism at 450 K for the sample with x = 0.1. The carrier concentration increases with increasing amount of Te as indicated by the decreasing value of the Seebeck coefficient. However, the mobility was found to be less affected by the amount of Te. Therefore, the electrical conductivity is still quite small, although slightly higher than that of the $FeSb_2Se_4$ composition. The magnetic behavior of $FeSb_2Se_{4-x}Te_x$ samples was found to be correlated to the transport properties of each sample, which is an important requirement for spin-based electronic applications.

Chapter VII

Effect Se Substitution by Te on Transport and Magnetic Properties of $FeSbSe_{4-x}Te_x$ ($0 \leq x \leq 4$)

Introduction

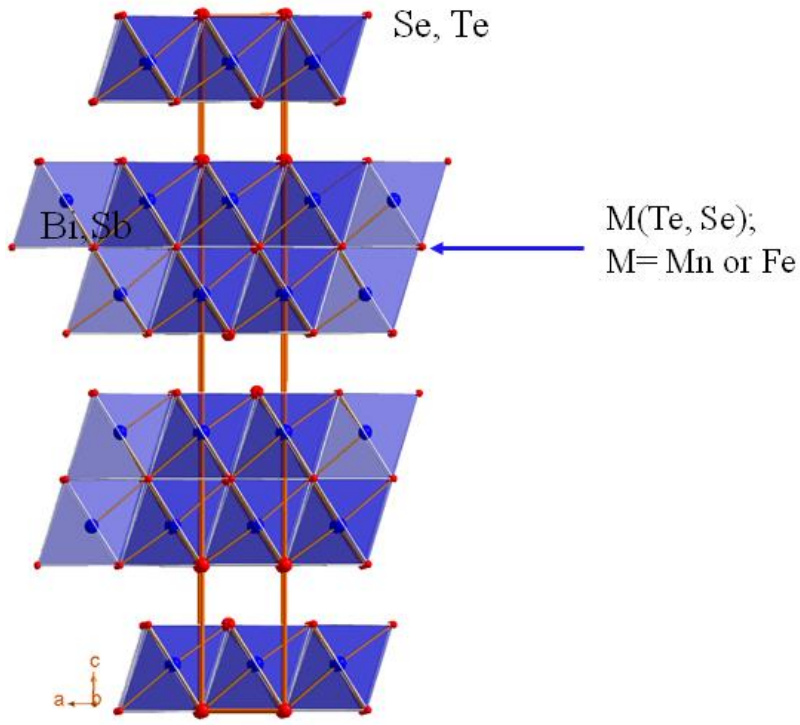

Figure VII- 1: Structure of $(Sb/Bi)_2(Se/Te)_3$ showing stacking sequences along the *c*-axis where M(Te/Se) can be inserted between two blocks to create Te-Sb-Te-Fe-Te-Sb-Te.

In chapter V, we have reported the effect of Te doping at Se sites in the structure of $FeSb_2Se_4$ on the magnetic behavior and electronic transports. It was found that adding a small fraction of Te (0.01, 0.05, 0.07, 0.1) in $FeSb_2Se_4$ results in a small enhancement of the transport properties. For instance the electrical conductivity of the Te-doped samples was slightly higher than that of the pristine sample. However, a decrease in both the

thermopower and electrical conductivity was observed upon increasing the Te content. Interestingly, the magnetic behavior and the crystal structure of the Te-doped samples were similar with that of $FeSb_2Se_4$. In an attempt to further increase the electrical conductivity of the p-type ferromagnetic semiconductor, $FeSb_2Se_4$, we have operated gradual isoelectronic substitutions of Se by Te atoms accordingly with the general formula $FeSb_2Se_{4-x}Te_x$ ($1 \leq x \leq 4$). Since, Se and Te were found to substitute each other in binary compounds such as $Sb_2Se_{3-x}Te_x$ and $Bi_2Se_{3-x}Te_x$ to form Sb_2Te_3 layered structure, we anticipate that similar substitutions in the $FeSb_2Se_{4-x}Te_x$ ($1 \leq x \leq 4$) series can lead to a layered crystal structure that can be derived from that of Sb_2Te_3. In the rhombohedral (*R*-3*m*) structure of Sb_2Te_3 adjacent building blocks formed by three atomic layers of Te atoms and two atomic layers of Sb (Te-Sb-Te-Sb-Te) alternated along the c-axis and are linked by weak van der Waals interactions between adjacent Te atomic layers[28-31]. Since the chemical formula $FeSb_2Te_4$ ($x = 4$) can be rewritten as (FeTe)-(Sb_2Te_3), we anticipate that the crystal structure of $FeSb_2Se_{4-x}Te_x$ ($1 \leq x \leq 4$) can be obtained by insertion of one atomic layer of Fe and one additional atomic layer of Te within the (Te-Sb-Te-Sb-Te) building block of the structure of Sb_2Te_3 in such as way that the crystal symmetry (*R*-3*m*) is preserved. Therefore, the rhombohedral hypothetical structure of $FeSb_2Se_{4-x}Te_x$ ($1 \leq x \leq 4$) should consist of three blocks with atomic stacking sequence Te-Sb-Te-Fe-Te-Sb-Te alternating along the *c*-axis (Figure VII-1). A similar structure refined from powder recently reported for $MnBi_2Te_4$[32]. In this hypothetical structure of $FeSb_2Se_{4-x}Te_x$ ($1 \leq x \leq 4$) the octahedral environment of the Fe atoms by Se/Te atoms as well as the $[Fe(Se/Te)_6]$ one-dimensional chain of edge-sharing octahedra building the layer of magnetic atoms is similar to the ones observed in the parent compound $FeSb_2Se_4$. Therefore, no drastic change in the magnetic behavior is anticipated, while a significant alteration in the thermal and electronic transports is anticipated due to the changes in the crystal packing of the semiconducting lattice built by Sb-(Se,Te). $Sb_2Se_{3-x}Te_x$ and $Bi_2Se_{3-x}Te_x$ have been investigated as room temperature thermoelectric materials with dimensionless figure of merit more or less close to 1.[33] Transition metal doped Sb_2Te_3 and Bi_2Te_3 have also been reported and showed very interesting magnetic properties, which can be altered by tuning the transport properties in the host system.[34-36] However, the thermoelectric properties and the effect of the manipulation of the electronic properties of the Sb_2Te_3 block on the magnetic ordering in the $FeSb_2Se_{4-x}Te_x$ ($1 \leq x \leq 4$) series have not been investigated. Therefore, this materials system provide a unique opportunity to study new multifunctional

materials suitable for both thermoelectric and spintronic application on a single device. Here, we report on the structure, magnetic and thermoelectric properties of $FeSb_2Se_{4-x}Te_x$

VII-1. Synthesis and characterization

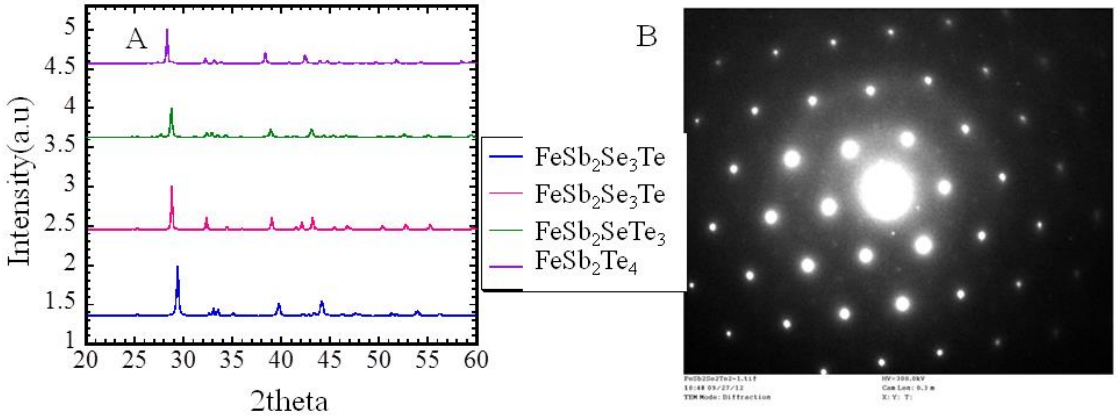

Figure VII- 2: X-ray powder diffraction showing different structure when compared with $FeSb_2Se_4$ (A) and HTEM diffraction image (B) of $FeSb_2Se_{4-x}Te_x(1 \leq x \leq 4)$ indicating high symmetry crystal structure when compared to FeS_2Se_4.

Polycrystalline $FeSb_2Se_{4-x}Te_x$ ($0 \leq x \leq 4$) samples were obtained from combination of pure elements in stoichiometry ratio. Elements were thoroughly mixed and sealed under vacuum atmosphere in the cleaned quartz tube. The temperature profile was the same as mentioned earlier in this work (See Chapter II for more detailed). All $FeSb_2Se_{4-x}Te_x$ samples revealed different X-ray powder pattern when compared to $FeSb_2Se_4$ (Figure VII-2A), indicating a drastic change in the crystal symmetry upon Te substitutions at Se sites. Crystal structure refinement on selected single crystal from different compositions did not provide a good structure model. However, Indexing on the HTEM diffraction suggests that the structure might be tetragonal (see Figure VII-1B).

VII-2-Magnetic properties of $FeSb_2S_{4-x}Te_x$ ($0 \leq x \leq 4$)

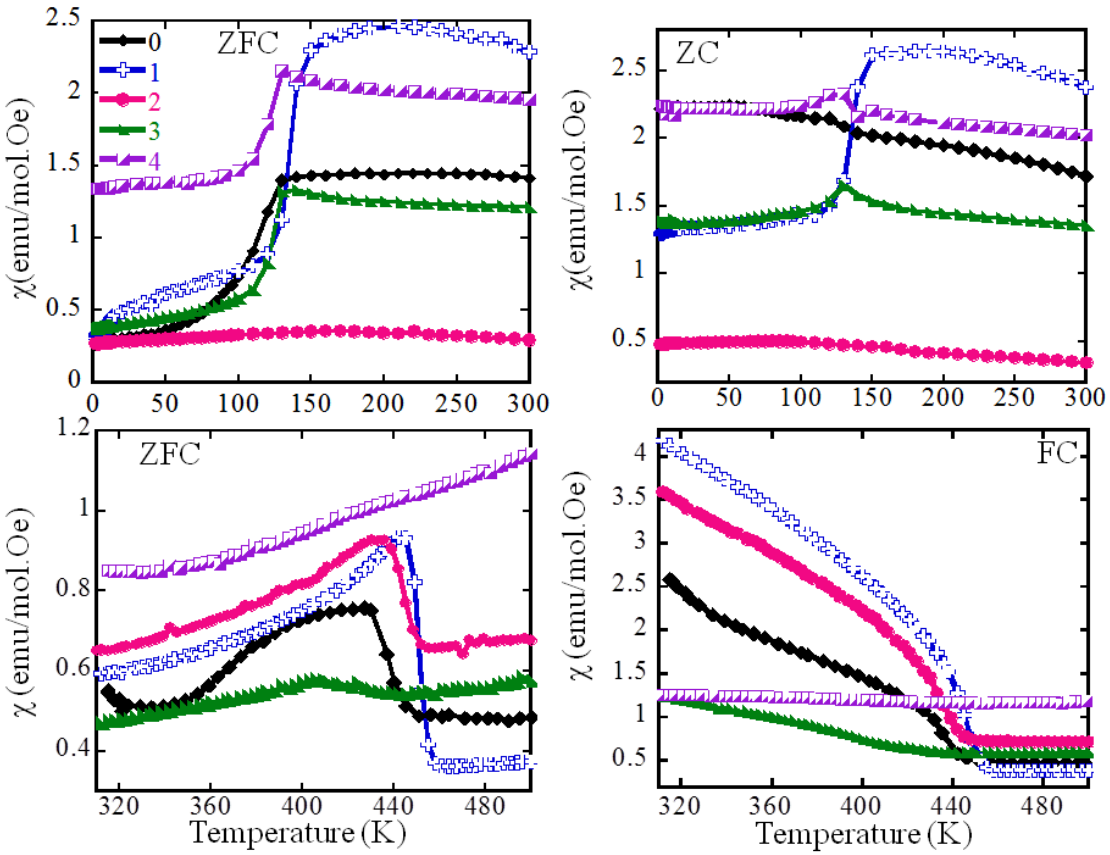

Figure VII- 3: Temperature dependent FC and ZFC magnetic susceptibility from 2K to 500K showing the variation of the susceptibility; and the Curie transition temperatures with Te concentration. The low temperature part of the plots shows magnetic comparable behavior comparable with that of $FeSb_2Se_4$.

The Figures VII-3 and Figure VII-4, respectively show the temperature dependent susceptibility and field dependent magnetization at different temperatures for $FeSb_2Se_{4-x}Te_x$ with various Te concentrations. Regardless of the amount of Te in the particular composition, the temperature

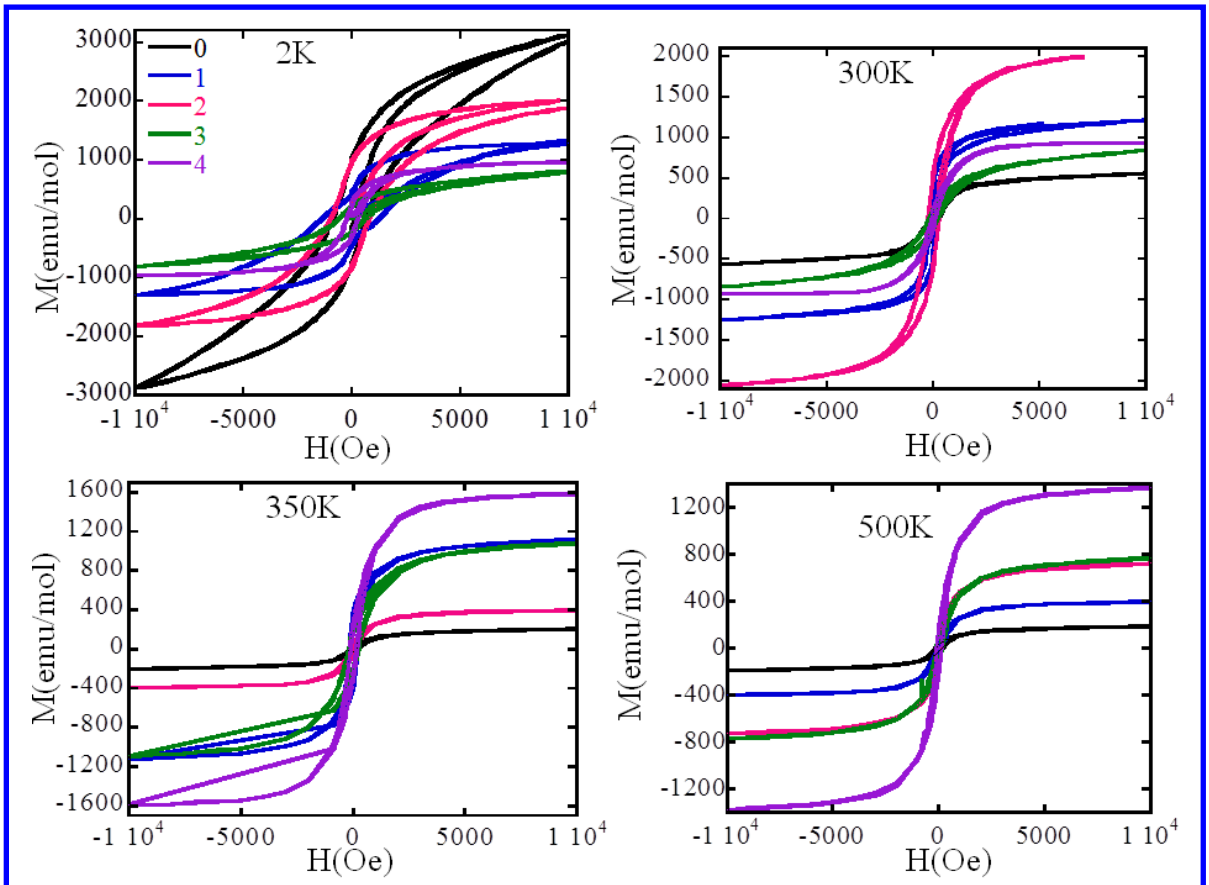

Figure VII- 4: Field dependent magnetization for various $FeSb_2Se_{4-x}Te_x$ compositions at different temperatures. All compositions show hysteresis loop.

dependent susceptibility curves for various $FeSb_2Se_{4-x}Te_x$ compounds are comparable with that of $FeSb_2Se_4$ under FC and ZFC at low temperatures. The susceptibility of all samples sharply drops around 130K, which is reminiscent of the behavior observed in $FeSb_2Se_4$ around the same temperature. The ferromagnetic to paramagnetic (FM-PM) like transition is observed on FC data for compositions with x = 1, 2, and 3, with the transition temperatures of 455K, 445K and 436K (Figure VII-3), respectively. The ZFC high temperatures susceptibility curves for all compositions increase with increasing temperature, and are consistent with the behavior reported

for the $FeSb_{2-x}Sn_xSe_4$ ($0 \leq x \leq 0.25$) and $FeSb_2Se_{4-x}Te_x$ ($0 \leq x \leq 0.1$) series. This behavior is believed to be induced by the exchange interaction between the spin-polarized free carriers and spin of the local magnetic moments. However, for the $FeSb_2Te_4$ composition, the temperature dependent ZFC susceptibility curve continuously increases with increasing temperature. Similar behavior was observed on samples with x = 1, 2 and 3.

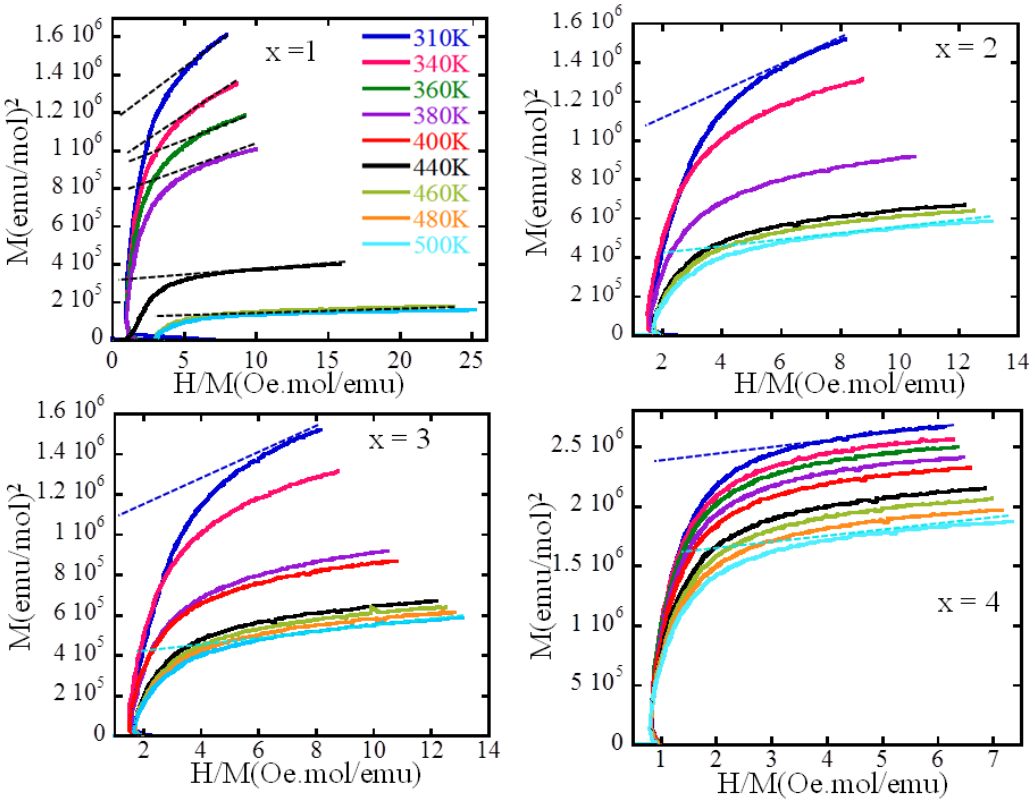

Figure VII- 5: Arrott's plots of $FeSb_2Se_{4-x}Te_x$($0 \leq x \leq 4$) samples suggesting ferromagnetism above 500K for all compositions.

The FC and ZFC curves of different compositions reported on the same graphs for low and high temperatures measurements (Figure VII-3) suggest that the susceptibility depends on the Te concentration. This is supported by the field dependent magnetization at different temperatures reported on the Figure VII-4. All magnetic parameters such as the coercivity and saturation magnetization are altered with increasing amount of Te. The variations of magnetic parameters with compositions are summarized in Table VII-1.With the exception of the composition with x = 1, where the coercivity are constant within 2K and 500K with the

observable value of 125Oe, all other compositions show decreasing value of the coercivity with increasing temperature. Interestingly, the coercivities for all compositions are found between 700Oe and 80Oe, with the highest values in each composition observed at 2K. The lowest coercivity were observed at 300K for the sample with x = 4. One can conclude that the $FeSb_2Se_{4-x}Te_x$ ($0 \leq x \leq 4$) is a soft magnet. For each composition with $x \leq 3$ the magnetic saturation decreases with increasing temperature. However, for x = 4, the magnetic saturation increases and reaches the optimum value of 1580 emu/mol at 350 K and decreases afterward with further increase in temperature. For each temperature, it was difficult to find correlations between the magnetization and the composition change, since no consistent trends were observed upon alteration of the magnetic properties with increasing amount of Te. However, at 500 K we observed an increasing value of the magnetic saturation with increasing concentration of Te. We suspect the irregular change of the magnetization to originate from the electronic structure of the prepared materials. Although we could not find the perfect crystal to explore the single crystal structure in order to discuss the structure-magnetic property relationship, some degrees of disorder at the Sb and Fe sites can be anticipated in the ideal model structure described in the introduction, given the disorder between Sb and Fe at various metal sites in the parent compound. Such p-d hybridization (Sb/Fe intermixing) could presumably facilitate the formation of spin-polarized electron leading to ferromagnetic ordering both at low and high temperatures. Figure VII-5 shows the Arrott`s plots for different $FeSb_2Se_{4-x}Te_x$ compositions. From these plots, we observed that the Curie temperature might be above 500 K for all compositions. This is supported by the field dependent magnetization curves that show hysteresis on all samples at 500 K. The constant values of the susceptibility above 450 K observed in all compounds in this work is believed to be the signature of superparamagnetism due to the strong thermal agitation affecting the coupling of spin-polarized carriers to the external applied magnetic field and local magnetic moments. However, the hysteresis loop exhibited on the field dependent magnetization is presumably a manifestation of the FM ordering. This is consistent with the coercivity values observed in all samples, which were found to be greater than 100 Oe.

Table VI-1: Values of coercivities and saturation magnetization as function of temperature and Te concentration in the $FeSb_2Se_{4-x}Te_x (0 \leq x \leq 4$ samples

Magnetic Parameters	Temperature(K)	x=0	x=1	x=2	x=3	x= 4
	2	700	125	763	611	261
	300	250	125	258	191	80
Coercivity	350	157	158	117	217	142
(Oe)	500	150	125	108	133	108
	2	3140	1326	2000	1000	807
Saturation	300	560	1195	1990	817	938
Magnetization	350	191	1109	400	1065	1580
(emu/mol)	500	184	400	715	751	1366

To probe the possible p-d exchange coupling, and therefore the existence of spin-polarized carriers (electrons, holes) in the compounds, we performed magnetoresistance (MR) measurements on various compositions between 10K and 300K (FigureVII-6). The experimental data shows a positive magnetoresistance for all samples. However, the magneto-resistance

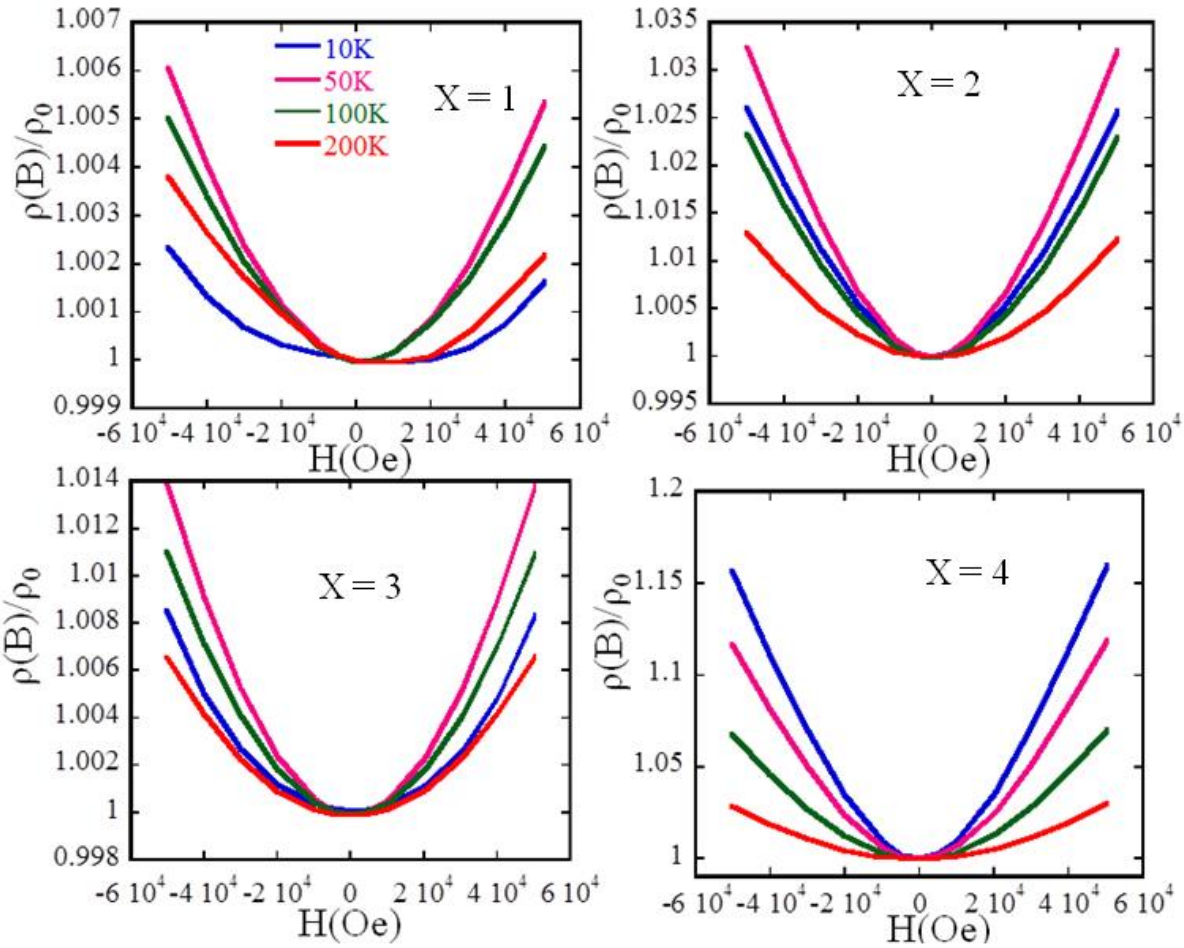

Figure VII- 6 : Field dependent magnetoresistance of $FeSb_2Se_{4-x}Te_x$ at different temperatures, showing decreasing change on magnetoresistance with increasing temperature.

curves at maximum applied field did not show saturation. The magnitudes of the magneto-resistance were very small and decreased with increasing temperature for composition with $x \leq 3$. A number of physical phenomena have been listed to induce the magneto-resistance. (1)

Weak localization phenomena and (2) the strong sp-d exchange coupling. In the case of weak localization phenomenon saturation is expected with large applied field[37,38]. In our case the MR did not show any saturation. The positive values observed on MR here might be connected to p-d exchange coupling. This is consistent with our assertion on the origin of FM ordering above room temperature, which mainly originate from the delocalized spin-polarized electrons due to the hybridization of p-d orbital. At low temperatures, holes are localized and generated FM ordering from bound magnetic polarons (BMPs). The correlation between the density of free carriers and the susceptibility is highlighted in the Figure VII-7, where one can clearly see that

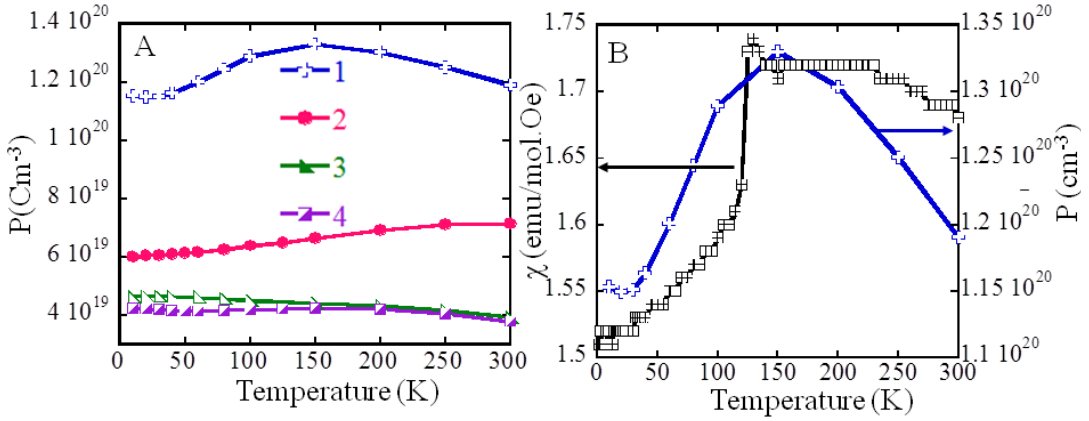

Figure VII- 7: (A) Carrier concentration as a function of temperature. The carrier concentration decreases with increasing amount of Te; (B) The temperature dependent carrier concentration and temperature dependent susceptibility suggesting correlation between the carrier concentration and magnetization.

both the susceptibility and the carrier concentration for instance in the $FeSb_2Se_3Te$ compound increase with increasing temperature. The drastic increase of the ZFC susceptibility with temperature from 27K is followed by increasing concentration of free carriers and both curves reach the maximum nearly at the same temperature (131K for the susceptibility and 149K for the carrier concentration). Above 130K both the susceptibility and carrier density decrease with prominent drop observed on the carrier density. This consistent change of both the susceptibility and the carrier concentration are the results of correlated electron phenomena involving free carriers, mainly holes in $FeSb_2S_{4-x}Te_x$ system and spin of the local magnetic moment of the Fe^{2+}.

VII-3-Transport properties of $FeSb_2Se_{4-x}Te_x$

Figure VII-8 shows the thermoelectric properties of $FeSb_2Se_{4-x}Te_x$ at low temperature. The temperature dependence electrical conductivity is presented in Figure VII-8A (low temperature) Regardless of the composition the electrical conductivity decreases with increasing temperature with maximum values observed in sample with x = 4 in the whole range of temperature. This particular sample exhibits an electrical conductivity of 6572 S/cm at 2K and 735S/cm at 575K. The lowest value of the electrical conductivity, 630S/cm at 2K, was observed for the sample with x = 3. At 300K, the electrical conductivity value of 540S/cm for the sample with x = 1 is lower than that of the composition with x = 3 suggesting that the electrical conductivity of $FeSb_2SeTe_3$ decrease slowly with increasing temperature, while that of the sample with x = 1 decreases faster. Regardless of the temperature, the electrical conductivity increases with increasing amount of Te except for the composition with x = 3, which shows lower values of electrical conductivity between 2K and 575K. This change in the electrical conductivity was inconsistent with the gradual change of Te concentration in the pristine compound. To explain this inconsistent trend, we measure the carrier concentration, which is displayed in Figure VII-7. Regardless of the temperature, the carrier concentration decreases with increasing amount of Te. Since the electrical conductivity is proportional to the carrier concentration and the mobility, we think that both parameters are altered simultaneously with increasing amount of Te. The increasing value of the electrical conductivity upon substitution of two atoms of Se might be due to the slightl difference in the carrier mobility between sample with x = 1 and x = 2. For the composition with x = 3 both the carrier mobility and carrier density were reduced, leading to the observed low conductivity in this sample compare to the other compositions. Therefore, increasing the Te concentration in $FeSb_2Se_{4-x}Te_x$ tends to affect the electronic structure of the parent compound.

Generally speaking the Seebeck coefficient of this series increases with increasing concentration of Te. This is consistent with the change observed on the carrier concentration plots (Figure VII-7), since the thermopower is inversely proportional to the carrier concentration. As the temperature increases, the thermopower increases almost linearly for the first three samples of the series, and take a parabolic shape for the sample with x = 4. The increasing value of the

Seebeck with increasing temperature is consistent with the degenerate semiconducting behavior of these compounds as suggested by the conductivity plots (Figures VII-8A). The very small values of the Seebeck coefficient below 50K are also consistent with large conductivity observed in this range of temperature, particularly for the sample with x = 4. However, all samples show positive values of the thermopower suggesting that the $FeSb_2Se_{4-x}Te_x$ phases maintain the p-type semiconducting behavior observed in the parent compound.

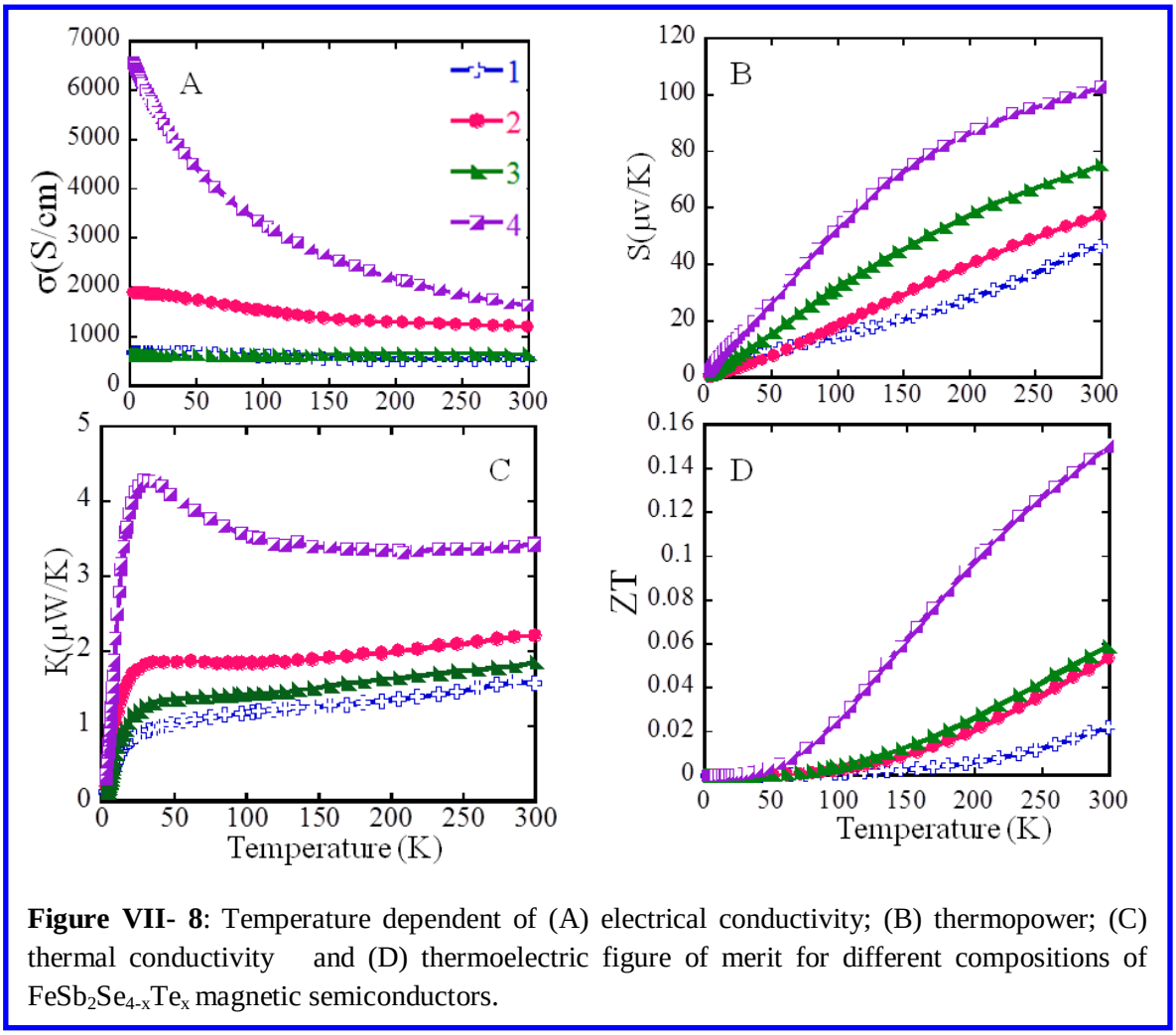

Figure VII- 8: Temperature dependent of (A) electrical conductivity; (B) thermopower; (C) thermal conductivity and (D) thermoelectric figure of merit for different compositions of $FeSb_2Se_{4-x}Te_x$ magnetic semiconductors.

The temperature dependence of the thermal conductivity is reported in the Figure VII-8C and the dimensionless thermoelectric figure of merit ZT is shown in Figure VII-8D. The thermal conductivity increases with increasing concentration of Te. The thermal conductivity at 50K range from 1.05μW/m.K to 4.08μW/m.K when the amount of Te goes from 1 to 4. These values

are larger than the values observed for the parent phase. At room temperature, the thermal conductivity increases with increasing Te content from 1.57μW/m.K to 3.42μW/m.K. This means that the thermal conductivity decreases with increasing temperature. In the series of $FeSb_2Q_4$ (Q = Se, Te) system studied in this thesis, the thermal conductivity was found to be mainly dominated by the lattice thermal conductivity. However, in the $FeSb_2Se_{4-x}Te_x$ series, although we do have a strong contribution of lattice thermal conductivity, the large values of the electrical conductivity suggest a strong contribution of the electronic thermal conductivity to the total thermal conductivity. This could explain the large difference of about 50% between the thermal conductivity of the composition with x =3 and x = 4. The thermoelectric figure of merit in the whole series increases with increasing temperature, and show the maximum value of 0.15 at 300K for $FeSb_2Te_4$. The figure of merite of the $FeSb_2Se_{4-x}Te_x$ materials can be further enhanced through optimization of the synthesis method, nanostructuring or any other processing method used to improve the thermoelectric properties of thermoelectric materials such as Bi_2Te_3 and Sb_2Te_3. This will make the $FeSb_2Se_{4-x}Te_x$ series new multifunctional materials with applications encompassing both thermoelectrics and spintronics.

References

(1) Kanatzidis, M. G. *Semiconduct Semimet* 2001, *69*, 51.

(2) Mrotzek, A.; Iordanidis, L.; Kanatzidis, M. G. *Inorg Chem* 2001, *40*, 6204.

(3) Mrotzek, A.; Kanatzidis, M. G. *Accounts Chem Res* 2003, *36*, 111.

(4) Tritt, T. M.; Subramanian, M. A. *MRS Bulletin* 2006, *31*, 188.

(5) Lee, D. S.; Kim, T.-H.; Park, C.-H.; Chung, C.-Y.; Lim, Y. S.; Seo, W.-S.; Park, H.-H. *CrystEngComm* 2013, *15*, 5532.

(6) Wright, D. A. *Nature* 1958, *181*, 834.

(7) Dyck, J. S.; Hájek, P.; Lošťák, P.; Uher, C. *Physical Review B* 2002, *65*, 115212.

(8) Zhou, Z.; Chien, Y.-J.; Uher, C. *Phys Rev B* 2006, *74*, 224418.

(9) Dyck, J. S.; Drašar, Č.; Lošťák, P.; Uher, C. *Phys Rev B* 2005, *71*, 115214.

(10) Kilanski, L.; Szymczak, R.; Dobrowolski, W.; Podgorni, A.; Avdonin, A.; Slynko, V. E.; Slynko, E. I. *Journal of Applied Physics* 2013, *113*, 063702.

(11) Fukuma, Y.; Asada, H.; Arifuku, M.; Koyanagi, T. *Applied Physics Letters* 2002, *80*, 1013.

(12) Bente, E. A. J. M.; Hogervorst, W. *Z Phys D Atom Mol Cl* 1989, *14*, 119.

(13) Bente, K.; Edenharter, A. *Z.Kristallogr.* 1989, *31*, 186.

(14) Buerger, M. J.; Hahn, T. *Am Mineral* 1955, *40*, 226.

(15) Djieutedjeu, H.; Poudeu, P. F. P.; Takas, N. J.; Makongo, J. P. A.; Rotaru, A.; Ranmohotti, K. G. S.; Anglin, C. J.; Spinu, L.; Wiley, J. B. *Angew Chem Int Edit* 2010, *49*, 9977.

(16) Kurowski, D., University of Regensburg, Germany, 2003.

(17) Leone, P.; Doussier-Brochard, C.; Andre, G.; Moelo, Y. *Phys Chem Miner* 2008, *35*, 201.

(18) Matar, S. F.; Weihrich, R.; Kurowski, D.; Pfitzner, A.; Eyert, V. *Phys Rev B* 2005, *71*.

(19) Pfitzner, A.; Kurowski, D. *Z Kristallogr* 2000, *215*, 373.

(20) Mumme, W. G.; Watts, J. A. *Acta Crystallogr B* 1980, *36*, 1300.

(21) Leone, P.; Andre, G.; Doussier, C.; Moelo, Y. *J Magn Magn Mater* 2004, *284*, 92.

(22) Matsushita, Y.; Ueda, Y. *Inorg Chem* 2003, *42*, 7830.

(23) Matsushita, Y.; Ueda, Y. *Inorg Chem* 2006, *45*, 2022.

(24) Leone, P.; Le Leuch, L. M.; Palvadeau, P.; Molinie, P.; Moelo, Y. *Solid State Sci* 2003, *5*, 771.

(25) Lecker, A.; Kurowski, D.; Pfitzner, A. *Z Anorg Allg Chem* 2006, *632*, 2144.

(26) Shannon, R. D. *Acta Crystallogr A* 1976, *32*, 751.

(27) Mydosh, J. A. *Spin glasses: an experimental introduction*; Taylor & Franacis: London ; Washington, DC, 1993.

(28) Binder, K.; Young, A. P. *Rev Mod Phys* 1986, *58*, 801.

(29) Fischer, K. H.; Hertz, J. A. *Spin glasses*; Cambridge University Press: Cambridge ; New York, NY, USA, 1991.

(30) Gingras, M. J. P.; Stager, C. V.; Gaulin, B. D.; Raju, N. P.; Greedan, J. E. *J Appl Phys* 1996, *79*, 6170.

(31) Wang, P.; Stadnik, Z. M.; Zukrowski, J.; Cho, B. K.; Kim, J. Y. *Phys Rev B* 2010, *82*.(32) Goodenough, J. B. *Phys Rev* 1955, *100*, 564.
(33) Goodenough, J. B. *J Phys Chem Solids* 1958, *6*, 287.
(34) Goodenough, J. B.; Loeb, A. L. *Phys Rev* 1955, *98*, 391.
(35) Kanamori, J. *J Phys Chem Solids* 1959, *10*, 87.
(36) Dronskowski, R.; Blochl, P. E. *J Phys Chem-Us* 1993, *97*, 8617.

Chapter VIII

Crystal Structure, Charge Transport, and Magnetic Properties of $MnSb_2Se_4$

Introduction

Among known complex transition-metal chalcogenides is the fascinating family of ternary MPn_2Q_4 (M = Fe, Mn; Pn = Sb, Bi; and Q = S, Se) compounds with crystal structures that show 1D to 3D connectivity (depending on composition and synthetic method) as well as interesting physical properties.[25,39-45] For instance, $MnSb_2S_4$ synthesized by solid-state reaction crystallizes in the monoclinic lattice (*mC*28)[45] and is isotypic with $HgBi_2S_4$,[46] whereas an orthorhombic modification (*oP*28),[39,42] isostructural with $FeSb_2S_4$,[41] was obtained from crystals of the same composition isolated from a hydrothermal preparation method. In the crystal structure of the orthorhombic and the monoclinic $MnSb_2S_4$, MnS_6 octahedra share edges to form single chains separated by the Sb_2S_3-type substructure. These isolated chains of MnS_6 octahedra represent the substructure that controls the magnetic properties,[47-50] whereas the electronic properties of the compound are controlled by the Sb_2S_3-type network that connects adjacent magnetic chains. Because of the unique spatial arrangement of atoms in the MPn_2Q_4 structure, we have been very interested in how magnetism and electronic transport respond to modifications of the structure by altering M, Pn, and/or Q. For instance, electrical-conductivity and magnetic susceptibility measurements revealed that $MnSb_2S_4$ is a semiconducting antiferromagnet with a Néel temperature (T_N) of 26.5K and an energy band gap (Eg) of 0.77eV.[42-44] By modifying the nature of the Sb–S bonds that connect the magnetic and semiconducting subunits in $MnSb_2S_4$ through isoelectronic substitution of S by Se, we anticipate a significant alteration in electronic charge transport as well as the nature of coupling between adjacent magnetic chains. For instance, an

energy band gap smaller than that of $MnSb_2S_4$ (Eg = 0.77eV) and high electrical conductivity are expected for $MnSb_2Se_4$ due to an increase in the degree of covalency of the Sb–Se bond. $MnSb_2Se_4$ was first investigated by Kurowski and reported in his doctoral thesis.[42] Based on this work, four different crystal structure models were proposed. The first model obtained from single-crystal structure refinement in the space group *C* 2/m revealed the Mn(2a) site to be randomly occupied by Mn and Sb atoms with nearly equal statistical probability, thus leading to a charge-unbalanced final composition, $Mn_{0.75}Sb_{2.25}Se_4$. The other three models have been obtained from Rietveld refinement using neutron diffraction data. Two of them considered Mn/Sb mixed occupancies at all the Mn and Sb positions and featured very large atomic displacement parameters for both Mn(2a) and Mn(2d) sites. The last model, which was similar to the ordered structure of $HgBi_2S_4$, also showed large atomic displacement parameters for Mn atoms. Therefore, a conclusive structure model for $MnSb_2Se_4$ could not be obtained from this early study. Another investigation (from the same research group) of the $MnSb_{2-x}Bi_xSe_4$ solid solution also revealed large discrepancies in the unit-cell parameters and atomic distribution in $MnSb_2Se_4$.[51] Here, we report an accurate determination of the crystal structure of $MnSb_2Se_4$ by using high-quality single crystals grown from a solid-state reaction of high-purity elements at 500 °C and discuss results of electronic and thermal transport, electronic structure, as well as direct current (DC) and alternating current (AC) magnetic-susceptibility data.

VIII-1-Experiments

VIII-1-1-Differential Scanning Calorimetry (DSC)

Differential scanning calorimetry data were recorded on a 404-F1 DSC apparatus (NETZSCH) using approximately 15mg of the synthesized compound sealed in a small quartz tube under a residual pressure of ~10^{-3} Torr. An equivalent mass of Alumina (Al_2O_3) was used as the reference. The sample and reference were simultaneously heated to 1073 K at a rate of 20 K/min, isothermed for 2 min and then cooled to 423 K at a rate of 20 K/min. DSC data were recorded during two heating and cooling cycles. The endothermic onset temperature is reported as the melting point and the exothermic onset temperature is the crystallization point.

VIII-1-2-Infrared Spectroscopy

To probe the optical band gap of $MnSb_2Se_4$, room temperature diffuse reflectance infrared spectroscopy was performed in the 4000 – 400 cm^{-1} region using a Thermo Nicolet NEXUS 670 FT-IR spectrometer. The reflectance data were converted into absorption data using the Kulbelka-Munk function $\alpha/S = (1-R)^2/2R$ [38] (where R is the reflectance at a given wavelength, α is the absorption coefficient, and S is the scattering coefficient) and the optical band gap was estimated from an absorption (α/S) [38-39] versus energy plot.

VIII-1-3-Electronic Structure Calculations

The electronic structure of $MnSb_2Se_4$ was calculated with the linear muffin-tin orbital (LMTO) method in the atomic sphere approximation (ASA) using the tight-binding program TB-LMTO-ASA [40]. A charge balanced model was constructed by assigning Sb atoms at M1 and M2 positions whilst Mn atoms were located at the M3 and M4 sites. The radii of the Wigner-Seitz (WS) spheres were assigned automatically so that the overlapping potentials would be the best possible approximations to the full potentials, and an interstitial sphere was necessary with thedefault 16% overlap restriction [40]. Since the structure of $MnSb_2Se_4$ is rather open, special care was taken in filling the interatomic space. Using only atom-centered spheres resulted in errors because of too large overlaps. Therefore, the empty interstitial spheres (ES) were added to the crystal potential and the basis set. The sphere radii and their positions were chosen so that space filling was achieved without exceeding a sphere overlap of 16%. All sphere positions and radii were calculated automatically; the WS radii [Å] were Mn, 1.47 – 1.57; Sb, 1.57 – 1.61; Se, 1.45 – 1.53; and ES, 0.74 – 1.33. The calculations used a basis set of Mn-4*s*/4*p*/3*d*, Sb-5*s*/5*p* and Se-4*s*/4*p* orbitals and the reciprocal space integrations were performed on 12 × 12 ×12 grids of irreducible *k*-points using the tetrahedron method [41-42].

VIII-2-Characterization of $MnSb_2Se_4$ Powder

A single-phase polycrystalline powder of $MnSb_2Se_4$ was obtained through combination of elemental Mn, Sb, and Se at 773K. Slow heating of the starting mixture to the reaction temperature with intermediate annealing at 573K was necessary to produce a high-purity phase. Attempts to speed up the reaction by either eliminating the intermediate dwelling step or by slow cooling the starting mixture from the molten state resulted in polycrystalline samples with unreacted selenium as the main impurity phase. Rapid increase of the furnace temperature presumably results in high vapor pressure of the low-melting Se inside the sealed tube, thus leading to a reaction mixture with lower Se content. Upon cooling the furnace to room temperature, the Se vapor ultimately condenses and mixes with the reaction product. X-ray diffraction on polycrystalline powders of the synthesized compound (Figure VIII-1A) showed an excellent match with the theoretical pattern simulated from the single-crystal structure refinement. This indicates successful formation of nearly a single phase of $MnSb_2Se_4$ and also attests to the accuracy of the proposed structural model. The accuracy of the structural model, as well as the successful synthesis of $MnSb_2Se_4$, is also supported by the experimental density of 5.65(2) $g.cm^{-3}$ (measured using helium gas

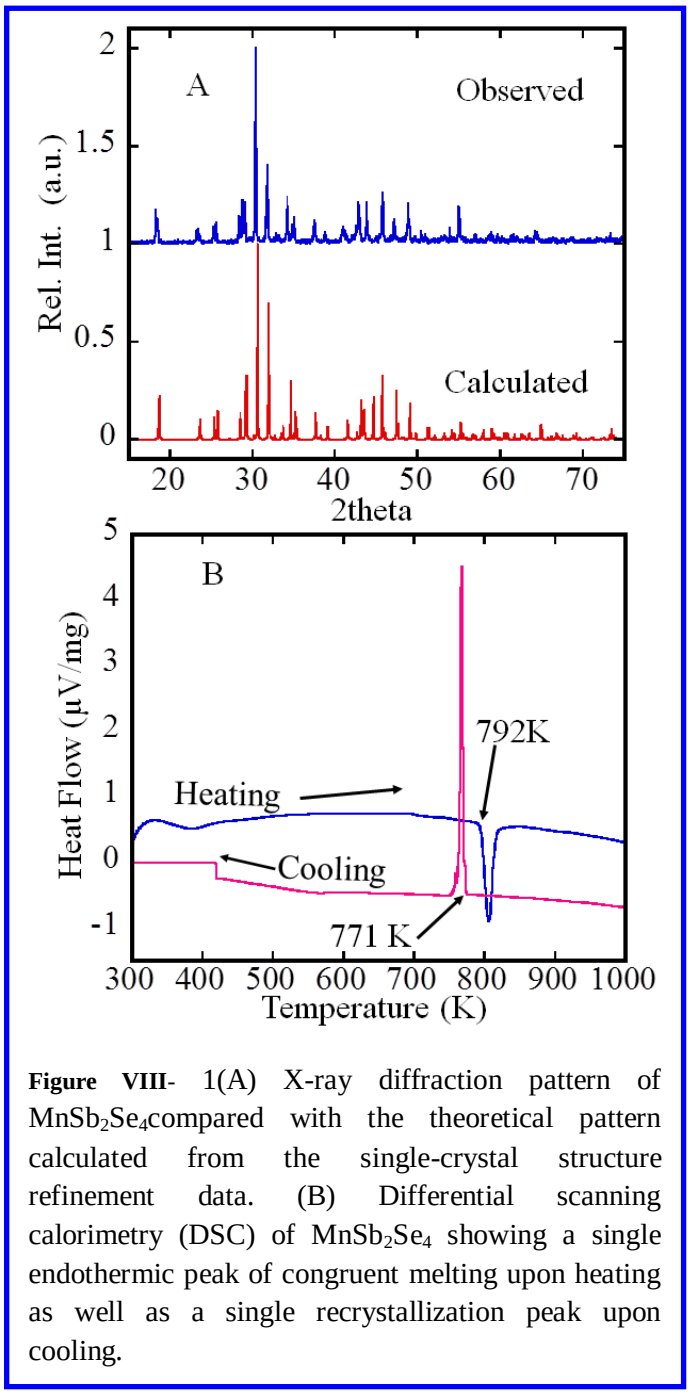

Figure VIII- 1(A) X-ray diffraction pattern of $MnSb_2Se_4$compared with the theoretical pattern calculated from the single-crystal structure refinement data. (B) Differential scanning calorimetry (DSC) of $MnSb_2Se_4$ showing a single endothermic peak of congruent melting upon heating as well as a single recrystallization peak upon cooling.

pycnometry), which represents approximately 99 % of theoretical density calculated from single-crystal structure data (Table VIII-1). $MnSb_2Se_4$ melts congruently at 790K and shows no sign of decomposition after heating up to 1000K (Figure VIII-1B). Upon cooling, $MnSb_2Se_4$ fully recrystallizes at 771K, thereby suggesting its high thermal stability. The absence of additional endothermic peaks on heating again suggests the successful synthesis of $MnSb_2Se_4$ as a single phase.

VIII-3-Crystal Structure of $MnSb_2Se_4$

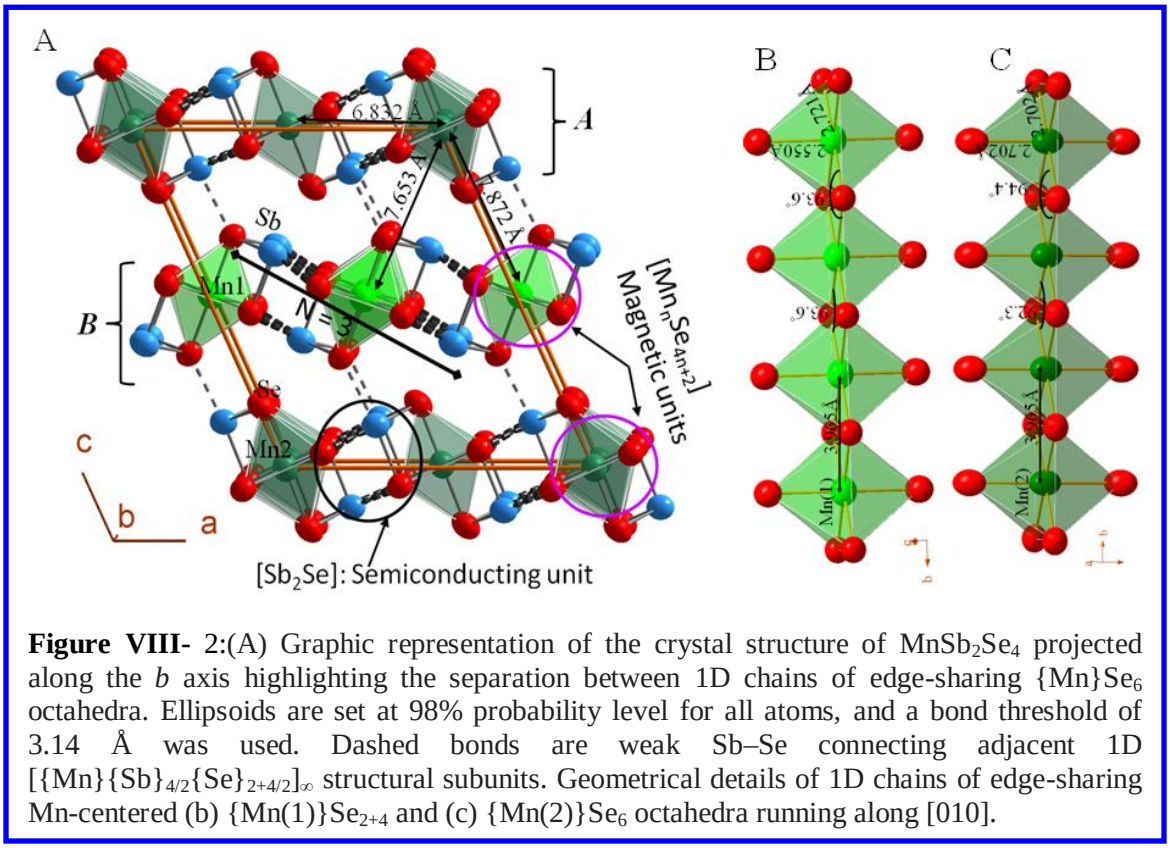

Figure VIII- 2:(A) Graphic representation of the crystal structure of $MnSb_2Se_4$ projected along the *b* axis highlighting the separation between 1D chains of edge-sharing $\{Mn\}Se_6$ octahedra. Ellipsoids are set at 98% probability level for all atoms, and a bond threshold of 3.14 Å was used. Dashed bonds are weak Sb–Se connecting adjacent 1D $[\{Mn\}\{Sb\}_{4/2}\{Se\}_{2+4/2}]_\infty$ structural subunits. Geometrical details of 1D chains of edge-sharing Mn-centered (b) $\{Mn(1)\}Se_{2+4}$ and (c) $\{Mn(2)\}Se_6$ octahedra running along [010].

$MnSb_2Se_4$ is isostructural with $FeSb_2Se_4$ [25] crystallizing in the monoclinic space group C2/m (no. 12) with lattice parameters, a = 13.076(3)Å, b = 3.965(1)Å, c = 15.236(3)Å, β = 115.1(3)° (Table VIII-1). The observed slight increase in the unit-cell parameters of $MnSb_2Se_4$ relative to those of $FeSb_2Se_4$ is consistent with the difference in the effective ionic radii of Mn(0.83Å) and Fe (0.78Å) in six fold coordination.[52] The structure (Figure VII-2) contains two crystallographically independent Mn atoms located at special positions Mn(1) (2d) and Mn(2) (2a) (Table VIII-2).

The Mn(1) position is fully occupied by Mn, whereas the Mn(2) position contains 19 % Sb. Both Mn positions are coordinated by six selenium atoms with Mn(1) located in a distorted [2+4] octahedral geometry with two short axial bonds at 2.550(2)Å and four long equatorial bonds at 2.721(2)Å, whereas Mn(2) is found in an almost regular octahedral geometry with bond lengths that range between 2.676(2)Å and 2.702(2) Å. Along [010], adjacent $\{Mn(1)\}Se_{2+4}$ octahedra share edges to form one-dimensional (1D) $[\{Mn(1)\}Se_{2+4}]$ chains (Figure VIII-2B), which are weakly linked [through an Sb(1)–Se(2) bond of 3.116(2) Å] along the *a* axis by the Sb(1) atom in a distorted [1+2+2] square pyramid of Se atoms (Table VIII-3) to build a slab denoted B parallel to the *ab* plane. A similar type of slab denoted A is formed by interconnecting [through the Sb(2)–Se(4) bond of 3.093(2) Å] 1D $[\{Mn(4)\}Se_6]$ chains (Figure VIII-2C) parallel to [010] with Sb(2) atoms in a distorted [1+2+2+1] octahedral coordination (Figure VIII-2A). Both A and B slabs are linked along the *c* axis by a rather long Sb(2)–Se(3) bond [3.138(2) Å] to build the three-dimensional (3D) structure. Alternatively, the structure of $MnSb_2Se_4$ can be better described as a one-dimensional arrangement of $[\{Mn\}\{Sb\}_2\{Se\}_4]$. chains of edge-sharing octahedra parallel to [010], thus giving the rather long Sb–Se bonds (dashed bonds in Figure VII-2A) interconnecting individual chains.

Table VIII-1 Selected crystallographic data for $MnSb_2Se_4$ at 300 K.

Crystal system; space group	Monoclinic; *C*2/*m*(no.12)
Formula weight [g.mol^{-1}]	614.28
Density ($\rho_{calc.}$) [g.cm^{-3}]	5.70
Density ($\rho_{meas.}$) [g.cm^{-3}]	5.65(2)
Lattice parameters [Å]	
a[Å]	13.076(3)
b[Å]	3.965(1)
c[Å]	15.236(6)

β[Å]	115.1(3)
V[Å^3]	716(2)
Z	4
Crystal size [mm]	0.04 x 0.09 x 0.25
Crystal shape, color	needle, black
Radiation [Å]	λ(Mo-K_α) = 0.71073
μ[cm^{-1}]	295
Diff.elec.density[e Å]	+1.36 to -1.35
$R_1[F_o.4\sigma(F_o)]$[a]	0.027
wR_2 (all)[b]	0.072
GoF	1.124

[a] $R_1 = \sum||F_o| - |F_c||/\sum|F_o|$. [b] $wR_2 = [\sum w(F_o^2 - F_c^2)^2/\sum w(F_o^2)^2]^{1/2}$.

Table VIII-2: Atomic coordinates, Wyckoff positions (W.P.), site-occupancy factors (*k*), and equivalent isotropic displacement parameters $U_{eq}/10^{-4}$ Å^2 for all atoms in the asymmetric unit of $MnSb_2Se_4$.

Atom	W.P	*k*	*x*	*y*	*z*	U_{eq}[a]
Sb(1)	4*i*	0.95	0.2738(2)	0	0.6334(2)	267(3)
Mn(1)	4*i*	0.05	0.2738(2)	0	0.6334(2)	267(3)
Sb(2)	4*i*	0.96	0.3554(2)	0	0.1260(2)	242(3)
Mn(2)	4*i*	0.04	0.3554(2)	0	0.1260(2)	242(3)

Mn(3)	3*d*		0	1/2	1/2	265(7)
Sb(4)	2*a*	0.19	0	0	0	252(9)
Mn(4)	2*a*	0.81	0	0	0	252(9)
Se(1)	4*i*		0.0123(2)	0	0.1799(2)	269(4)
Se(2)	4*i*		0.1143(2)	0	0.4575(2)	228(4)
Se(3)	4*i*		0.3446(2)	0	0.3277(2)	243(4)
Se(4)	4*i*		0.6549(2)	0	0.0533(2)	246(4)

[a] U_{eq} is defined as one-third of the trace of the orthogonalized U_{ij} tensor.

Table VIII-3. Selected interatomic distances [Å] in $MnSb_2Se_4$ at 300 K.

Sb(1)|Mn(1)–Se(2)	2.607(2)	Mn(3)–Se(3) [ii]	2.550(2)
Sb(1)|Mn(1)–Se(3) [i]	2.731(2)	Mn(3)–Se(3) [vii]	2.550(2)
Sb(1)|Mn(1)–Se(3) [ii]	2.731(2)	Mn(3)–Se(2) [viii]	2.721(2)
Sb(1)|Mn(1)–Se(2) [ii]	3.116(2)	Mn(3)–Se(2) [ix]	2.721(2)
Sb(1)|Mn(1)–Se(2) [i]	3.116(2)	Mn(3)–Se(2)	2.721(2)
Sb(1)|Mn(1)–Se(1) [ii]	3.620(2)	Mn(1)–Se(2) [x]	2.721(2)
Sb(1)|Mn(1)–Se(1) [i]	3.620(2)		
		Mn(4)|Sb(4)–Se(1)	2.676(2)
Sb(2)|Mn(2)–Se(4) [iii]	2.674(2)	Mn(4)|Sb(4)–Se(1) [xi]	2.676(2)
Sb(2)|Mn(2)–Se(1) [iv]	2.718(2)	Mn(4)|Sb(4)–Se(4) [xii]	2.702(2)

Sb(2)|Mn(2)–Se(1)[v]	2.718(2)	Mn(4)|Sb(4)–Se(4)[vii]	2.702(2)
Sb(2)|Mn(2)–Se(4)[vi]	3.093(2)	Mn(4)|Sb(4)–Se(4)[xiii]	2.702(2)
Sb(2)|Mn(2)–Se(4)[vii]	3.093(2)	Mn(4)|Sb(4)–Se(4)[vi]	2.702(2)
Sb(2)|Mn(2)–Se(3)	3.138(2)		

[a] Operators for generating equivalent atoms: (i) 1/2 – *x*, –1/2 – *y*, 1 – *z*; (ii) 1/2 – *x*, 1/2 – *y*, 1 – *z*; (iii) 1 – *x*, –*y*, –*z*; (iv) 1/2 + *x*, 1/2 + *y*, *z*; (v) 1/2 + *x*, –1/2 + *y*, *z*; (vi) –1/2 + *x*, –1/2 + *y*, *z*; (vii) –1/2 + *x*, 1/2 + *y*, *z*; (viii) *x*, 1 + *y*, *z*; (ix) –*x*, –*y*, 1 – *z*; (x) –*x*, 1 – *y*, 1 – *z*; (xi) –*x*, –*y*, –*z*; (xii) 1/2 – *x*, –1/2 – *y*, –*z*; (xiii) 1/2 – *x*, 1/2 – *y*, –*z*.

VIII-3-Magnetic Properties $MnSb_2Se_4$

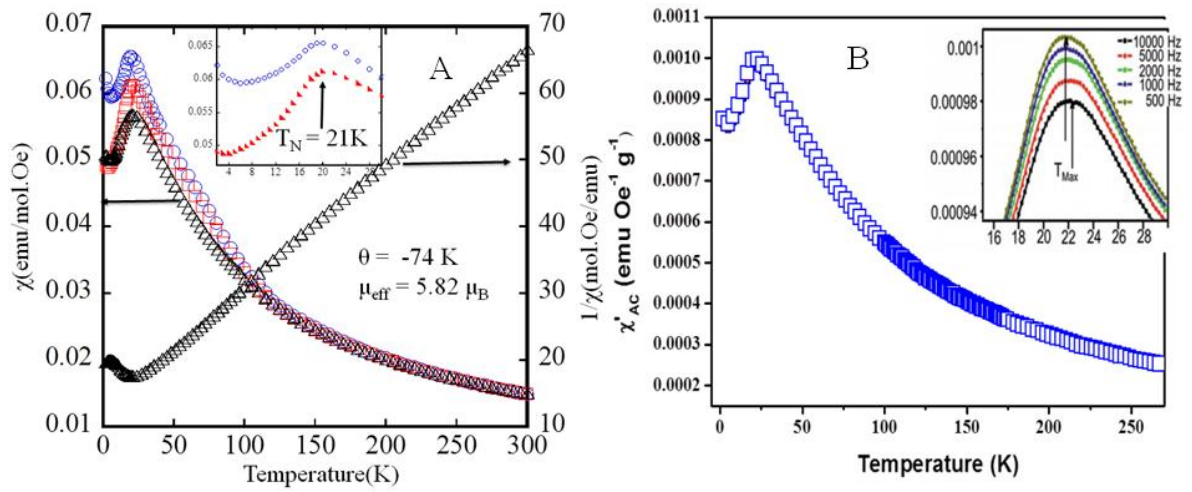

Figure VIII- 3(A) Temperature dependence of the field-cooled (FC) and zero-field-cooled (ZFC) molar magnetic susceptibility and inverse susceptibility of $MnSb_2Se_4$ measured under applied field of 100 and 1000Oe. Blue circle: FC at 100Oe; red square: ZFC at 100Oe; black triangle: ZFC at 1000Oe. The inset is the magnification of the susceptibility around $T_N \approx 20$K. (B) Temperature dependence of the in-phase component of the AC susceptibility measured for various applied frequencies from 500 Hz to 10 kHz under an applied field of 10Oe. The inset is a magnification of the portion of the curves around the maximum χ'.

Figure VIII-3A shows the magnetic susceptibility and the inverse susceptibility of the synthesized polycrystalline powders of $MnSb_2Se_4$ measured at 100 and 1000Oe. The susceptibility exhibits a broad peak at 20 K, which suggests an ordering of Mn magnetic moments at low temperatures. The susceptibility data above 120 K could be fitted to the Curie–Weiss law with a Curie constant of 5.48emu.K.mol^{-1} and a Weiss constant of –74K. The corresponding effective magnetic moment is μ_{eff} = 5.82(2)μ_B per Mn atom. This value is relatively close to the expected theoretical value of μ_{eff} ~5.92μ_B for Mn^{2+} ($3d^5$) in the high-spin configuration, thereby confirming our assignment of the oxidation state of Mn ions (2+) in the crystal structure. The large negative value of the Weiss constant indicates that the interaction between the Mn^{2+} magnetic moments is predominantly antiferromagnetic (AFM). However, the slight increase in the susceptibility observed below 5K (Figure VIII-3A inset) also suggests the existence of a small ferromagnetic (FM) ordering in the sample at very low temperatures. In addition, the observed strong dependence of the magnetic susceptibility below 20K on the applied magnetic field, the shift of the blocking temperature to lower values with the increase in the applied magnetic field, as well as the difference between the ZFC and FC data suggests competing magnetic ordering similar to spin-glass behavior within the sample[53]. To better assess this magnetic behavior, AC susceptibility measurements at various frequencies and different amplitudes of the excitation field were performed. Figure VIII-3B shows the in-phase part, χ of the AC susceptibility of $MnSb_2Se_4$ for selected frequencies between 500Hz and 10000Hz. The amplitudes and positions of the peak maxima (T_{max}) depend on the frequency of the applied AC magnetic field (Figure VIII-3B, inset). T_{max} gradually shifts to higher temperatures, and the peak intensity decreases with increasing frequency, which indicates that the peaks are associated with the onset of spin freezing. These features are typical for classical spin-glass systems such as $Cu_{1-x}Mn_x$ and $Au_{1-x}Mn_x$ alloys[53-56] A quantitative measure of the change in the freezing temperature with frequency in spin glass materials is obtained by calculating the Mydosh parameter (K) defined as the relative shift of the maximum temperature (T_{max}) per decade of frequency.[53]The estimated $K = \Delta T_m/[T_m \log(\omega)] = 0.013$ is about three times higher than K values found in spin-glass systems such as $Cu_{1-x}Mn_x$ (K = 0.005) and $Au_{1-x}Mn_x$ (K=0.0045) and suggests that the relaxation behavior is consistent with a spin-glass-like behavior. However, in most spin-glass systems, the magnitude of the AC susceptibility below T_{max} is frequency-dependent and becomes independent of the frequency above T_{max}.[57] Therefore, the observed dependence of the

magnitude of the AC susceptibility above and below T_{max} upon frequencies (Figure VII-3B, inset) suggests that the downturn on the magnetic-susceptibility curves (ZFC and FC) of $MnSb_2Se_4$is more complicated in nature. A tentative explanation of this behavior is provided below. To understand the magnetic behavior of $MnSb_2Se_4$, we have carefully analyzed geometrical details of the [$MnSe_6$] magnetic chains, their arrangement in the 3D structure, and the coupling (intrachain and interchain) between localized spins on adjacent Mn atoms by using the Goodenough– Kanamori rules.[58-61] As described above, the Mn3 atom is located in a distorted octahedral geometry, [{Mn(1)}Se_{2+4}] with two apical short bonds [2.550(2) Å] and four equatorial long bonds [2.721(2) Å]. Despite the fact that $Mn^{2+}(3d^5)$ is not a Jahn–Teller ion, this kind of severe distortion of the octahedral coordination results in a Jahn–Teller-type splitting of the d orbitals, thus leading to an increase in the energy level of dz^2, d_{xz} and d_{yz} orbitals. This suggests the orbital and spin distribution $(d_{xy})^1$ $(d_{xz}, d_{yz})^1$ $(dx^2 –y^2)$ $(dz2)^1$ leading to a total spin value of S = 5/2 (high spin). The more regular octahedral coordination of the Mn(4) atom [{Mn(4)}Se_6] suggests an octahedral splitting of $3d^5$ orbitals with spin distribution of (d_{xz}, d_{yz}, $d_{xy})^1$ (d_z^2, $d_x^2 – _y^2)^1$, which corresponds to a total spin value of S = 5/2 (high spin). The total number of spin, S = 5/2 for both Mn3 and Mn4 atoms, is consistent with the effective magnetic moment calculated from the magnetic-susceptibility data. The structure of $MnSb_2Se_4$ can therefore be regarded as layers A and B of magnetic chains alternating along the *c* = axis. The magnetic behavior of $MnSb_2Se_4$ therefore depends on the interactions between adjacent magnetic atoms within a single chain (intrachain) and/or the interchain interactions. The shortest distance between magnetic chains in adjacent magnetic layers is around 7.653 Å, and the intralayer separation between magnetic chains is around 6.832 Å (Figure VIII-2A). These distances are too long for direct or indirect magnetic exchange interactions between neighboring magnetic chains, thereby suggesting that $MnSb_2Se_4$ is a quasi1D magnetic system. Therefore, the magnetic behavior of the compound is controlled by the nature and magnitude of exchange interactions between adjacent magnetic atoms in [{Mn(1)}Se_6]∞ and [{Mn(2)}Se_6]∞ magnetic chains. However, Mn atoms within individual chains (along [010]) are 3.965 Å apart (Figure VIII-2B). This separation is too long for direct magnetic exchange interactions between the magnetic moments on neighboring Mn atoms. Therefore, adjacent Mn(1) and Mn(2) atoms are magnetically coupled by indirect exchange interactions through the bridging Se atoms. For instance, the observed Mn(1)–Se(2)–Mn(1) bond angle of 93.6° within the [{Mn(1)}Se_6]∞ chain

suggests antiferromagnetic or weak ferromagnetic coupling of spins localized on adjacent Mn(2) atoms. Within the $[\{Mn(2)\}Se_6]\infty$ chain, two Mn(1)–Se(4)–Mn(1) coupling paths with bond angles of 92.3 and 94.4° are possible, thereby indicating competition between AFM and FM ordering of spins localized on adjacent Mn(4) atoms (Figure VIII-2C). This magnetic frustration within the $[\{Mn(1)\}Se_6]\infty$ and $[\{Mn(2)\}Se_6]\infty$ chains are believed to be responsible for the observed broad downturn of the magnetic susceptibility at 20K as well as the frequency dependence of the peak (T_{max}) position and amplitude. Upon cooling the sample below 5K, the FM coupling presumably begins to dominate, thus leading to the observed increase in the DC magnetic susceptibility.

VIII-4-Optical and Charge Transport Properties

The diffuse reflectance infrared absorption spectrum of $MnSb_2Se_4$ was recorded at room temperature in the range 0.05–0.5eV. The band gap estimated from the absorption coefficient/scattering coefficient (α/S) ratio versus energy plot is about 0.32eV, which indicates that the compound is a narrow-band gap semiconductor at 300 K (Figure VIII-4B). The observed value of the energy gap is comparable to the optical band gap of $FeSb_2Se_4$ (Eg = 0.33eV)[25] and is consistent with the black color of the $MnSb_2Se_4$ crystals. The temperature dependence of the electrical resistivity (ρ) of $MnSb_2Se_4$ was measured from 100 to 300K (Figure VIII-4A). At room temperature, the electrical resistivity is approximately 8.9Ω.m and slightly increases with decreasing temperature down to about 230K. This trend is consistent with the semiconducting nature of the compound. The observed large value of the electrical resistivity of $MnSb_2Se_4$ at 300K presumably originates from the quasi-1D nature of the crystal structure in which individual $[\{Mn\}Se_6]\infty$ chains parallel to [010] are only weakly interconnected along [100] and [001] through long Sb–Se bonds to the 3D network (Figure VIII-2A). The resistivity rises rapidly with further decreases in the temperature, and below 180 K, it attained such high values (10 kΩ.m) that the noise precluded collection of the data (Figure VIII-4B). The rapid increase in the resistivity is similar to the one observed in $FeSb_2Se_4$[25]. From the Arrhenius plot (Figure VIII-4B, inset), we calculated the band gap value to be 0.52eV. This value is consistent with the observed optical band gap, thereby confirming again the semiconducting character of $MnSb_2Se_4$ at 300K. Figure VIII-4C shows the temperature dependence of the Seebeck coefficient of $MnSb_2Se_4$ from 200 to 300K. Positive values of the Seebeck coefficient were observed in the whole measured temperature range, thereby indicating that $MnSb_2Se_4$ is a p-type narrow-gap semiconductor. The

Seebeck data have progressively larger error bars as the temperature decreases due to the noise on the Seebeck voltage contacts associated with the rapid rise in electrical resistivity. The Seebeck coefficient at 300K is around $950\mu VK^{-1}$ and gradually increases with the decreasing temperature to a value of about $1050\mu VK^{-1}$ at 200 K. The temperature dependence of the total thermal conductivity of $MnSb_2Se_4$ is shown in Figure VII-4D. Because of the large electrical resistivity of $MnSb_2Se_4$ in the measured temperature range, the electronic contribution to the thermal conductivity ($\kappa_{elc.}$) is negligible. Therefore, the observed thermal conductivity values essentially correspond to the lattice contribution ($\kappa_{lat.}$). At 300K, the lattice thermal conductivity

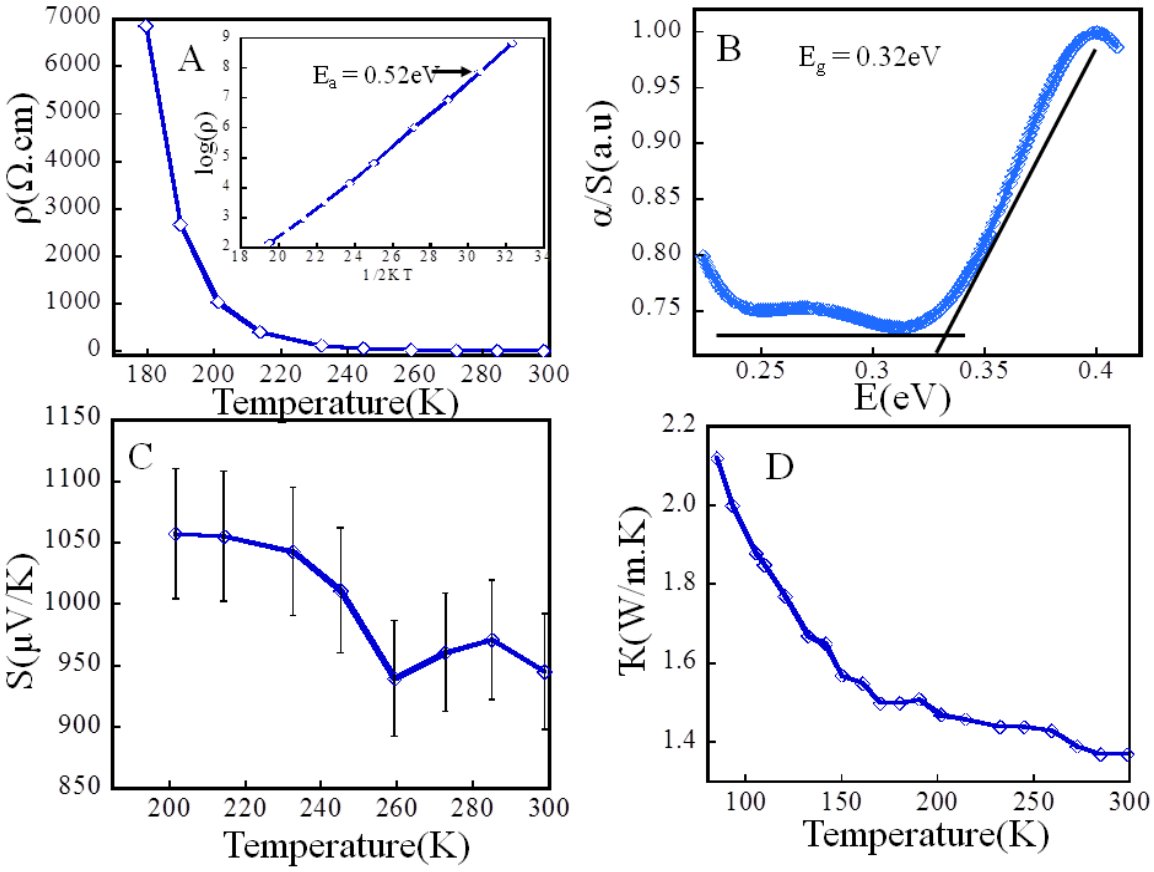

Figure VIII- 4: Temperature dependence of electronic and thermal charge transport of $MnSb_2Se_4$: (A) electrical resistivity; (C) Seebeck coefficient; (D) thermal conductivity. The sharp increase in the electrical resistivity around 230K is attributed to a semiconductor-to-insulator (SI) transition. The inset of (A) shows the plot of ln(ρ) versus $1/2k_BT$ from which the band gap of 0.52eV was estimated. (B) Room-temperature diffuse reflectance infrared spectrum of $MnSb_2Se_4$ showing a narrow optical band gap.

of $MnSb_2Se_4$ is 1.4W.m^{-1}.K^{-1} (Figure VIII-4D). This low value of the lattice thermal conductivity of $MnSb_2Se_4$ can be attributed to the combination of low crystal symmetry and complex structure and chemical composition with heavy elements such as Sb and Se. The lattice thermal conductivity of $MnSb_2Se_4$ gradually increases with decreasing temperature and a κ_{lat} value of 2.1W.m^{-1}.K^{-1} was measured at 90K. The observed increase in the lattice thermal conductivity with decreasing temperature is consistent with a gradual freezing of phonon umklapp processes.

VIII-5-Electronic Structure

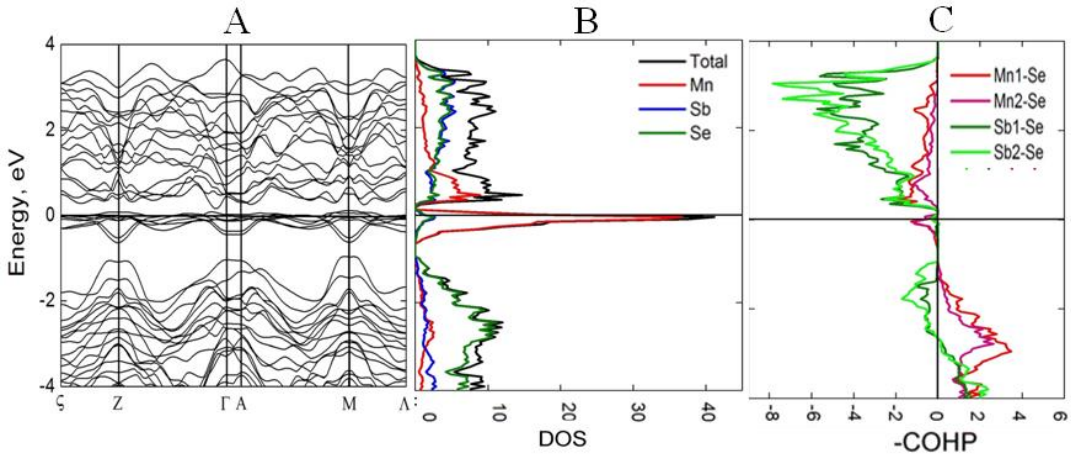

Figure VIII-5. (A) Electronic band structure of $MnSb_2Se_4$ near the Fermi energy showing a small energy gap of around 0.3eV. (B) Site-projected total density of states (DOS) and partial density of states for Mn, Sb, and Se atoms. (B) Crystal orbital Hamiltonian populations (COHP) for selected Mn(3)–Se, Mn(4)–Se, Sb(1)–Se, and Sb(2)–Se interactions.

Electronic band structure calculations of $MnSb_2Se_4$ show a small energy gap of around 0.3eV a narrow window around the Fermi level (E_F) (Figure VIII-5A). This value is consistent with the observed optical band gap as well as the activation energy near room temperature, thus further confirming the room-temperature semiconducting character of $MnSb_2Se_4$. The site-projected density of states (DOS) for one formula unit of nonmagnetic $MnSb_2Se_4$ (Figure VIII-5B), shows that the highest-occupied states cross the Fermi level at high density of states, which is attributed to Mn^{2+} t_{2g} states. The next occupied bands above E_F are formed by Mn^{2+} e_g states. The electron distribution of the d orbital could be t_{2g}^3 $(d_{xy}, d_{xz}, d_{yz})^1$ and e_g^2 $(d_x^2 - _y^2, d_z^2)^1$, thus confirming the

magnetic effective moment calculated from magnetic-susceptibility data. The large broad bands in the energy range from –4 to –1eV are dominated by bonding p states of Sb and Se, whereas the bottom of the conduction band is based mainly on empty Mn p orbitals. The analysis of bonding interactions between atoms in $MnSb_2Se_4$ by using the crystal orbital Hamiltonian population (COHP) method[62]showed that the major part of the valence band between –3 and –1eV is dominated by Mn–Se bonding interactions, whereas at the top of the valence band, Sb–Se and Mn–Se interactions dominate the antibonding interactions (Figure VII-5C). The Mn(3)–Se interactions contribute more strongly to the covalent bonding than Mn(4)–Se in the energy range of –3 to –1eV, and around the Fermi level both Mn(3)–Se and Mn(4)–Se equally contribute to the antibonding. Despite the significant antibonding interactions at E_F, the compound is stable because of the positive values of integrants, –ICOHP (Table VII-4), which predominantly emphasize the bonding character of orbitals below E_F. Above the Fermi level, all states are strongly antibonding, which suggests destabilization of the compound upon atomic substitutions by more electron-rich elements if the crystal structure of the phase remained the same.

Table VIII-4: –ICOHP for the Sb(1), Sb(2), Mn(3), and Mn(4) sites in $MnSb_2Se_4$.

Bond	No	Bond length	-ICOHP
Mn3-Se2	4	2.721(2)	1.26
Mn3-Se3	2	2.550(2)	1.86
Mn4-Se1	2	2.676(2)	1.81
Mn4-Se4	4	2.702(2)	1.53
Sb1-Se2	2	3.116(2)	0.21
Sb1-Se2	1	2.607(2)	2.32
Sb1-Se3	2	2.731(2)	1.64
Sb2-Se1	2	2.718(2)	1.77

Sb2-Se3	1	3.138(2)	0.22
Sb2-Se4	1	2.674(2)	1.88
Sb2-Se4	2	3.093(2)	0.32
Sb1-Se4	2	3.622(2)	0.01

Conclusion

A single phase of the monoclinic $MnSb_2Se_4$ phase was successfully synthesized by solid-state reaction of the elements at 773K and an accurate structural model was proposed by using single-crystal diffraction data. The compound crystallizes isostructurally with $FeSb_2Se_4$ [25] and exhibits Mn/Sb mixed occupancy at the Mn-rich M(2)(2*a*) site, as well as in all Sb-rich M(1) and M(2) positions. Charge-transport data, diffuse reflectance infrared spectroscopy, and electronic structure calculations revealed that $MnSb_2Se_4$ is a narrow-gap p-type semiconductor with E_g = 0.32eV and exhibits a sharp increase in the resistivity below 180K. The compound displays a low lattice thermal conductivity (ca. 1.4$W.m^{-1}.K^{-1}$ at 300K), melts congruently at 790 K, and is thermally stable up to 1000K. DC and AC magnetic-susceptibility measurements and the analysis of the geometrical parameters within the $[\{Mn\}Se_6]\infty$ single chains in light of the Goodenough–Kanamori rules[58-61] strongly suggest that $MnSb_2Se_4$ is not an ordinary antiferromagnet in which all the magnetic spins are antiparallel below T_N = 20K. The magnetism within individual chains in $MnSb_2Se_4$ is rather controlled by competing interactions

References

(1) Bente, E. A. J. M.; Hogervorst, W. *Z Phys D Atom Mol Cl* **1989**, *14*, 119.
(2) Bente, K.; Edenharter, A. *Z.Kristallogr.* **1989**, *31*, 186.
(3) Buerger, M. J.; Hahn, T. *Am Mineral* **1955**, *40*, 226.
(4) Djieutedjeu, H.; Poudeu, P. F. P.; Takas, N. J.; Makongo, J. P. A.; Rotaru, A.; Ranmohotti, K. G. S.; Anglin, C. J.; Spinu, L.; Wiley, J. B. *Angew Chem Int Edit* **2010**, *49*, 9977.
(5) Kurowski, D., University of Regensburg, Germany, 2003.
(6) Leone, P.; Doussier-Brochard, C.; Andre, G.; Moelo, Y. *Phys Chem Miner* **2008**, *35*, 201.
(7) Matar, S. F.; Weihrich, R.; Kurowski, D.; Pfitzner, A.; Eyert, V. *Phys Rev B* **2005**, *71*.
(8) Pfitzner, A.; Kurowski, D. *Z Kristallogr* **2000**, *215*, 373.
(9) Mumme, W. G.; Watts, J. A. *Acta Crystallogr B* **1980**, *36*, 1300.
(10) Leone, P.; Andre, G.; Doussier, C.; Moelo, Y. *J Magn Magn Mater* **2004**, *284*, 92.
(11) Matsushita, Y.; Ueda, Y. *Inorg Chem* **2003**, *42*, 7830.
(12) Matsushita, Y.; Ueda, Y. *Inorg Chem* **2006**, *45*, 2022.
(13) Leone, P.; Le Leuch, L. M.; Palvadeau, P.; Molinie, P.; Moelo, Y. *Solid State Sci* **2003**, *5*, 771.
(14) Lecker, A.; Kurowski, D.; Pfitzner, A. *Z Anorg Allg Chem* **2006**, *632*, 2144.
(15) Shannon, R. D. *Acta Crystallogr A* **1976**, *32*, 751.
(16) Mydosh, J. A. *Spin glasses: an experimental introduction*; Taylor & Franacis: London ; Washington, DC, 1993.
(17) Binder, K.; Young, A. P. *Rev Mod Phys* **1986**, *58*, 801.
(18) Fischer, K. H.; Hertz, J. A. *Spin glasses*; Cambridge University Press: Cambridge ; New York, NY, USA, 1991.
(19) Gingras, M. J. P.; Stager, C. V.; Gaulin, B. D.; Raju, N. P.; Greedan, J. E. *J Appl Phys* **1996**, *79*, 6170.
(20) Wang, P.; Stadnik, Z. M.; Zukrowski, J.; Cho, B. K.; Kim, J. Y. *Phys Rev B* **2010**, *82*.
(21) Goodenough, J. B. *Phys Rev* **1955**, *100*, 564.
(22) Goodenough, J. B. *J Phys Chem Solids* **1958**, *6*, 287.
(23) Goodenough, J. B.; Loeb, A. L. *Phys Rev* **1955**, *98*, 391.
(24) Kanamori, J. *J Phys Chem Solids* **1959**, *10*, 87.
(25) Dronskowski, R.; Blochl, P. E. *J Phys Chem-Us* **1993**, *97*, 8617.

Chapter IX

Carrier-Induced Switching from Antiferromagnetic to Ferromagnetic ordering in *p*-type $MnSb_{2-x}Sn_xSe_4$ Semiconductors

Introduction

There are currently widespread research activities in the fields of solid-state chemistry and solid-state physics focusing on the integration of semiconducting and magnetic functionalities within the same material and the manipulation of one property by the other [63-65]. Research efforts into the correlation between magnetism and transport properties over the past decades have focused on III-V and II-VI diluted magnetic semiconductors (DMS's) and diluted magnetic oxides (DMO's) [11,66-69]. The motivation for the choice of these material systems is dictated by the current structure of most electronics devices and the fact that doping these host materials with a transition metal (TM) element will not affect the processing and integration procedures. In addition, it was shown that such manipulation of the chemical composition of III-V, II-VI and oxide semiconductors leads to new materials with interesting magneto-optic, optoelectronic, nonlinear optic and photoelectric properties [48,70,71]. Long-range FM ordering in DMS and DMO compounds is believed to originate from exchange interactions between localized moments and spin polarized carriers (holes or electrons). However, the fabrication of practical devices such as information storage and processing units, light emitting diodes and detectors[66,68] based on these materials is severely hampered by their low Curie temperature (T_c). Understanding the mechanism of magnetic coupling in semiconductors is critically important to improving T_c values of DMS and DMOs above 300K. Besides III-V, II-VI and V-VI [72,73] DMSs and DMOs, magnetic semiconducting chalcogenides (MSC), such as EuS, EuSe and $CdCr_2Se_4$ have also been investigated [74-76]. DMSs, DMOs and MSCs are complex magnetic systems in the sense

thatseveral types of interactions are involved in the magnetic ordering. For instance, one must take into account contributions of electronic charge carriers (holes and electrons) in order to fully understand magnetic exchange interactions in such materials systems. Over the past two decades, significant advances have been made towards the fundamental understanding of the magnetism in III-V and II-VI semiconductors doped with Mn atoms. In these systems, the Mn atoms act both as an acceptor (providing holes) and as the magnetically active species (providing localized magnetic moments) in the semiconducting hosts. While it is widely accepted that holes in Mn-doped DMSs mediate the interactions between adjacent magnetic centers (Mn – Mn) in the host material to induce ferromagnetism, it is vigorously debated whether holes introduced when Mn substitutes for Ga in (Ga,Mn)As reside within the valence band of the host or form an impurity band within the band gap of the host material[23]. From the valence band concept, it was predicted that T_c increases monotonically with the Mn concentration and the hole density [8,77-82]. The alternative model, which assumes that the holes reside in a Mn derived impurity band, even for moderate or high Mn concentrations, also shows that T_c is related to the concentration of Mn and the hole density [67,83-87]. However, a more recent experimental study focusing on a simultaneous determination of the fraction of Mn atoms contributing to ferromagnetism and the hole density in (Ga,Mn)As suggested that the location of the Fermi level within the impurity band (i.e. the degree of hole localization), rather than the hole concentration determines T_c.[23] These contradictory reports underscore the difficulty to fully understand the correlations among electronic transport, magnetic ordering, and chemical composition in traditional Mn-doped DMSs. This is due to the fact that both the concentration of impurity states (holes) responsible for the electrical conduction, and the concentration of localized spins from the half-filled 3d Mn^{2+} shells responsible for the ferromagnetism in DMSs, are altered simultaneously when, for example, Mn ions substitute for Ga in (Mn,Ga)As. The complexity of the magnetism in DMSs, DMOs and MSCs is further increased by the fact that under external applied fields, spin-polarized electronic charge carriers can cluster into magnetic polarons (local short-range FM ordering of polarized itinerant spins) [88,89,15,90]. In such magnetic systems a discrepancy between the experimental and theoretical values of effective magnetic moment is generally observed. For example, Co- doped TiO_2 exhibits giant magnetic moments of $7.2\mu_B$/Co in Co^{2+}, while the value expected theoretically from the spin-only formula is $3\mu_B$ in a high spin state[91]. Therefore, to fully understand magnetic coupling in semiconductors, one must find a way to independently control

(1) the nature, concentrations and distribution of the magnetic ions (localized magnetic moments), and (2) the fraction of magnetic polarons in the material.

Low symmetry ternary and quaternary transition-metal chalcogenides have emerged as rich playgrounds for independent systematic investigations of electronic transport and magnetic exchange interactions in magnetic semiconductors and could enable fundamental understanding of correlations between both properties within a single crystal structure [1,25,30,48,70,71,92,93]. For instance, we have recently identified the homologous series of magnetic semiconductors with the general formula, $M_2Pn_4Sn_{N-3}Se_{N+5}$ (Pn = Sb, Bi; M = Mn, Fe; N ≥ 3) [1,25,70,92]. Members of this series of compounds adopt closely related structures formed by two distinct building units. In the crystal structure (Figure 1), two types of building units, denoted A and B alternate along [001]. The unit A is identical for all members of the homologous series and is built of paired rods of face-sharing monocapped trigonal prisms around Pn atoms alternating along the *a*-axis, with a single chain of edge-sharing octahedra around the magnetic M atoms. Various members of the series can be discriminated by the thickness of the NaCl-type building unit B separating adjacent units A, where the thickness of unit B is defined by the number N of edge-sharing octahedra running across its diagonal. Therefore, the composition and structure of various members of the $M_2Pn_4Sn_{N-3}Se_{N+5}$ (N ≥ 3) series can be derived for each value of N. The first member of the series with N = 3 corresponds to the fascinating class of ternary compounds MPn_2Q_4 (M = Fe, Mn; Pn = Sb, Bi; Q = S, Se). Our investigation of the crystal structure, magnetic properties and electronic transport properties of several compositions of the MPn_2Q_4 phases ($MnSb_2Se_4$ [92], $FeSb_2Se_4$ [25], $Mn_{1-x}Sn_xBi_2Se_4$ [1]) revealed that, despite the structural similarity of these phases, their magnetic behavior is defined by the nature of magnetic atoms within the $[M_nSe_{4n+2}]$ chains of edge-sharing octahedra (*magnetic subunit*). For instance, the dominant type of magnetic ordering in MPn_2Se_4 can be tuned from FM [25] to AFM [1,92] behaviors by altering the nature of the transition metal atoms within the $[M_nSe_{4n+2}]$ chain from Fe to Mn. Likewise, the dominant charge carrier type in MPn_2Se_4 can be manipulated by altering the composition of the $[Pn_2Se]$ network (*semiconducting subunit*) separating adjacent $[MSe_6]$ chains in the structure. For example, substituting Sb for Bi according to the Pn sites in MPn_2Se_4 induces drastic change in the conduction type from *p*-type for MSb_2Se_4 [92 25] to *n*-type for MBi_2Se_4 [1]. Recently, we showed that the dominant AFM ordering in $MnBi_2Se_4$ can be switched into weak FM interactions with T_c ~ 55K upon partial substitution of Mn by Sn within the magnetic subunit ($[M_nSe_{4n+2}]$ magnetic

chains) accordingly with the formula $Mn_{1-x}Sn_xBi_2Se_4$.[1] Here, we demonstrate that by altering the hole density within the semiconducting unit through Sb to Sn substitution, and without changing the concentration of Mn atoms within the magnetic subunit, the nature of dominant magnetic interaction in $MnSb_{2-x}Sn_xSe_4$ can be switched from the AFM ordering observed in the parent compound (x = 0) to FM ordering with $T_c \sim 56K$ for Sn-doped samples with $0.01 \leq x \leq 0.15$, followed by a reversal to AFM ordering for samples with higher Sn content. This surprising alteration in the magnetic behavior of $MnSb_{2-x}Sn_xSe_4$ compositions is rationalized within the context of the formation of various fractions of magnetic polarons due to the change in the hole density arising from the Sb to Sn substitutions within the semiconducting unit in the crystal structure of $MnSb_{2-x}Sn_xSe_4$.

IX-1-Experimental Section

IX-1-1-Powder X-ray Diffraction (PXRD)

X-ray powder diffraction (XRD) data were recorded on a Philips X'Pert system equipped with a curved graphite monochromator and Cu Kα radiation (λ = 1.5418 Å). Standard X-ray data were collected in a step-scanning mode with a 0.02° step width and 10s count time in the 2θ range of 10^o-120^o. The cell parameters were refined by the Rietveld method using the FullProf software package[94,95].

IX-1-2-Charge Transport Measurements

Electrical resistivity (*ρ)* and thermopower (*S*) were measured simultaneously from 300 K to 140 K. using (1) the standard four-probe method in a Quantum Design Physical Property Measurement System (PPMS) and (2) the four-probe longitudinal steady-state technique using a liquid ^{4}He cryostat. In the latter method, samples were mounted on the cryostat and protected from excessive radiation loss by two radiation shields. One end of the sample was attached to a heat sink by indium solder. The heat sink was the cold tip of the liquid helium cryostat, and the temperature was adjusted using a Lakeshore 340 temperature controller. Heat input to the sample was made via a small 350-Ω strain gauge heater attached to the free end of the sample using varnish. The heat flow injected by the heater developed a temperature difference ΔT between the two points along the length of the sample. Fine copper (Cu) wires were selected as Seebeck / resistive probes due to their small resistivity and thermopower.

IX-1-3-Magnetic Measurements

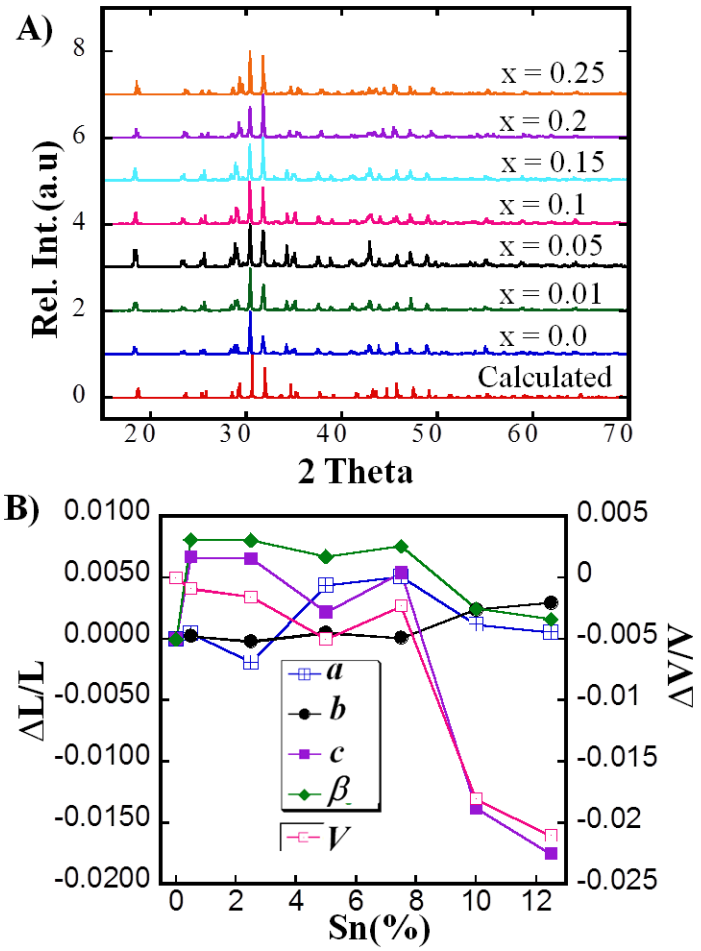

Figure-IX 1: **A)** X-ray diffraction pattern of $MnSb_{2-x}Sn_xSe_4$ compared with the theoretical pattern calculated from the single crystal structure refinement of $MnSb_2Se_4$. B) Relative change in the unit cell parameters and volume of $MnSb_{2-x}Sn_xSe_4$ as a function of Sn concentration.

DC and AC magnetic susceptibility measurements were performed on about 40 mg – 70 mg of polycrystalline $MnSb_{2-x}Sn_xSe_4$ powder using a Superconducting Quantum Interference Device (SQUID). DC susceptibility data in field cooled (FC) and zero field cooled (ZFC) modes were recorded over a temperature range from 2K to 300K with an applied magnetic field of 100 Oe. The AC susceptibility at different frequencies was collected on the same sample used for the DC measurements. The applied magnetic field used for the AC magnetic susceptibility was 0.1 Oe and data were collected within the temperature range between 5 K and 100 K. Field-dependent magnetization measurements were performed at 4 K on the samples with x = 0.05, 0.1 and 0.15 in applied magnetic fields up to 5 kOe.

IX-2-Synthesis and Structure

Polycrystalline powders of $MnSb_{2-x}Sn_xSe_4$ ($0 \leq x \leq 0.25$) were easily obtained from solid-state reaction of the elements in appropriate ratios. The single phase nature of the synthesized materials was confirmed by comparison of the experimental X-ray powder diffraction pattern of various compositions with the theoretical pattern calculated from the single crystal structure refinement data of the parent compound ($MnSb_2Se_4$). The excellent match between the experimental and theoretical patterns (Figure IX-1A) suggests that the synthesized $MnSb_{2-x}Sn_xSe_4$ phases are isostructural up to x = 0.25, which corresponds to the substitution of 12.5% Sb in the structure of $MnSb_2Se_4$ with Sn atoms. A plot of relative variations in the unit cell parameters of various $MnSb_{2-x}Sn_xSe_4$ ($0 \leq x \leq 0.25$) compositions refined using the X-ray diffraction patterns (Figure VIII-1B) shows that the *c*-axis initially expands by

Table IX-1: Cell parameters changes with Sn concentration

Sn Concentration	a(Å)	b(Å)	c(Å)	β(°)	V(Å^3)
0	13.2507	3.9638	15.3723	115.1594	734.905
0.01	13.2572	3.9647	15.4748	116.0931	734.255
0.05	13.2253	3.9830	15.4730	116.0871	733.746
0.10	13.3088	3.9658	15.4061	115.9346	731.235
0.15	13.3184	3.9642	15.5516	116.0314	731.211
0.20	13.2665	3.9734	15.1602	115.4437	721.635
0.25	13.2584	3.9755	15.1027	115.344	719.439

~0.5% for compositions with $0.01 \leq x \leq 0.15$ and contracts drastically with further increase in Sn content (See Table IX-1). A similar trend is observed for the change in the beta angle. However, the *a*-axis marginally expands with increasing Sn content, while the *b*-axis remains nearly constant. The observed anisotropic variations in the unit cell parameters with a stronger

perturbation of the *c*-axis resulted in a nearly constant unit cell volume up to 7.5% Sn substitution at Sb sites (x = 0.15) followed by a drastic ($\Delta V/V > 2\%$) contraction for higher Sn content. On one hand, the initial expansion of the *c*-axis can be explained by assuming a substitution of the small Sb^{3+} (ionic radius: 76 pm in six-fold coordination) ions by large Sn^{2+} (ionic radius: 93 pm in six-fold coordination [52,96]) ions in the structure of $MnSb_{2-x}Sn_xSe_4$. However, this cannot explain the sharp contraction of the *c*-axis observed for compositions with x > 0.15. In addition, a substitution between Sb^{3+} and Sn^{2+} should result in a gradual increase of the *c*-axis rather than the observed constant ~0.5% expansion for compositions with x ranging from 0.01 to 0.15. On the other hand, a substitution between Sb^{3+} (ionic radius: 76 pm in six-fold coordination) ions and a smaller Sn^{4+} (ionic radius: 69 pm in six-fold coordination[52,96]) should lead to a contraction in all unit cell parameters rather than the observed expansion of the *c*-axis and marginal increase in the *a*-axis. These contradictions suggest that the observed changes in the unit cell parameters are not solely due to the one-to-one substitution between Sb and Sn in the structure of $MnSb_{2-x}Sn_xSe_4$. Instead, one possible rationalization of the unusual trend in the variation of unit cell parameters can be obtained by taking into account the stereoactivity of the Sb electron "lone pair". In the crystal structure of $MnSb_2Se_4$ (Figure IX-1), the orientation of the Sb electron lone pair (along the *c*-axis) results in large separation between adjacent layers (broken bonds). If we consider the case of substitution between Sb^{3+} and Sn^{4+}, the anticipated contraction in the unit cell volume is presumably minimized by the stereoactivity of the Sb electron "lone pair" which opposes any attempt of the *c*-axis to contract. However, the stereoactivity of the Sb electron "lone pair" presumably vanishes for Sn content above 7.5% (x = 0.15), leading to a sharp contraction in the unit cell volume.

IX-3-Electronic transport properties

To probe the effect of Sn for Sb substitutions on the electronic transport properties of $MnSb_{2-x}Sn_xSe_4$ samples, we have measured the electrical conductivity and thermopower in the temperature range from 300 K to 140 K (Figure IX-3). Regardless of the Sn content, the electrical resistivity of various samples increases with decreasing temperature, suggesting intrinsic semiconducting behavior for all samples. However, a sharp increase in the slope is observed in the resistivity curves of various samples, and the onset temperature of such transitions increases from 200 K for x = 0 to 250 K for x = 0.15 (Figure IX-3A). For each composition, the electrical resistivity increases (within a narrow temperature window) by several orders of magnitude upon further cooling below the onset temperature and reaches values as high as 5×10^6 Ω . cm at 180 K for the composition with x = 0.25. Although the origin of the observed sudden increase in the electrical resistivity of $MnSb_{2-x}Sn_xSe_4$ compositions upon cooling is still unclear, a plausible explanation can be offered by taking into account interactions between spins of itinerant carriers (holes or electrons) and localized moments within the magnetic subunit. As the temperature decreases, magnetic exchange interactions between delocalized carriers (holes) and magnetic centers (Mn ions) presumably lead to the polarization of itinerant carrier-spins and a significant reduction of their mobility due to increased spin-scattering interactions. Alternatively, one can also envision the localization at low temperature of

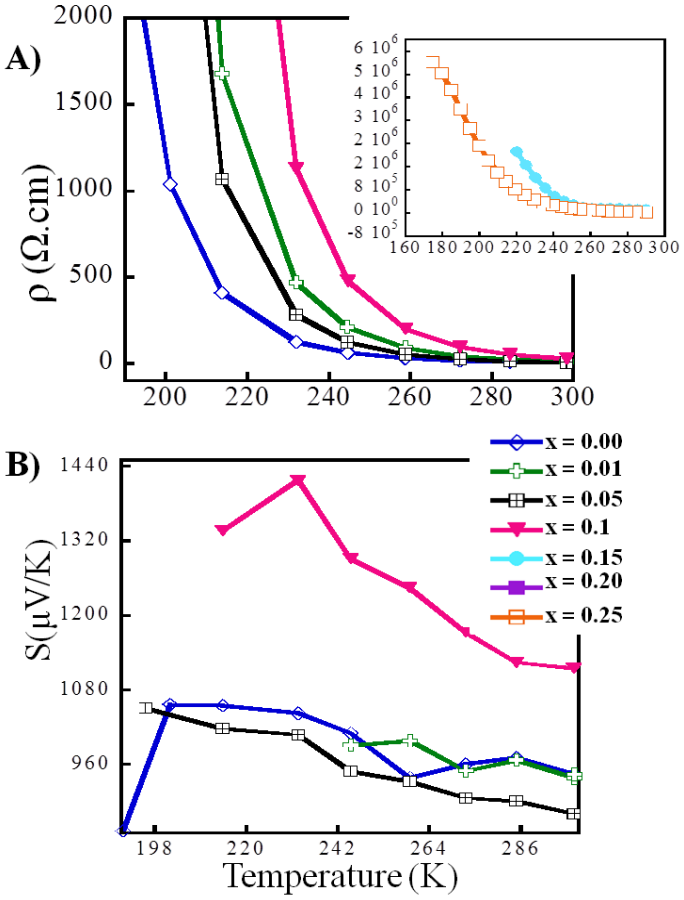

Figure-IX -2 : Temperature dependence of the electrical resistivity (A) and the Thermopower (B) of selected $MnSb_{2-x}Sn_xSe_4$ ($0 \le x \le 0.25$) compositions.

a significant fraction of spin-polarized itinerant holes due to strong AFM coupling with localized moments on magnetic centers (Mn ions) [17,97]. Both mechanisms (reduction of the carrier mobility or decrease in carrier density due to carrier localization) are consistent with the observed large increase in the electrical resistivity. The fits of the resistivity plots using the Arrhenius law suggest an increase in the electronic band gap of $MnSb_{2-x}Sn_xSe_4$ compositions from 0.52 eV for x = 0 to 0.63 eV for x = 0.1. These values along with the measured optical band gap of 0.32 eV for x = 0 indicate that $MnSb_{2-x}Sn_xSe_4$ compositions are narrow band gap semiconductors. In addition, the increase in the electronic band gap upon Sn doping is also consistent with the gradual increase in the onset temperature of the sharp increase in the resistivity curves.

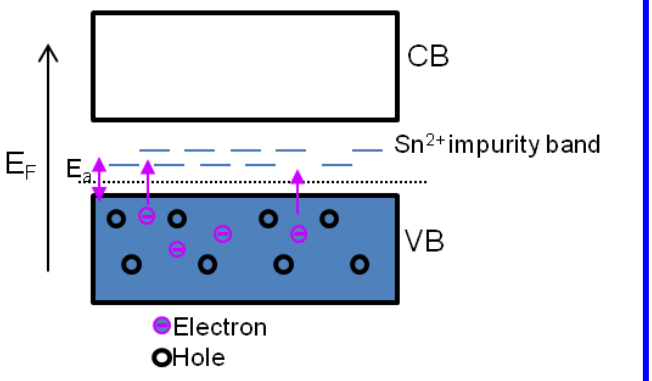

Figure-IX 3: Proposed band diagram for the understanding of electronic transport in $MnSb_{2-x}Sn_xSe_4$

Regardless of the temperature, the electrical resistivity of $MnSb_{2-x}Sn_xSe_4$ samples is surprisingly higher than that of the unsubstituted $MnSb_2Se_4$ phase. This general trend is contradictory to the increase in the hole density anticipated from the substitution of Sb^{3+} by Sn^{2+} and is more in agreement with a reduction in the overall hole density in the *p*-type $MnSb_2Se_4$ [92]. One possible explanation of the drop in hole density can be obtained by considering that Sn^{2+} ions substituting for Sb^{3+} formed impurity bands of acceptor states within the band gap of the parent compound rather than creating an additional hole within the valence band (VB) of $MnSb_2Se_4$. Within this band picture, a large excess of electrons is generated within the VB of the p-type $MnSb_2Se_4$ resulting in reduction of hole density at very low temperature through electron-hole compensation processes. Upon increasing the temperature, thermal excitation of excess electrons from the VB to the Sn^{2+} acceptor states within the band gap result in gradual increase in the hole density within the VB leading to sharp drop of the resistivity. However, the increase in the thermopower and the resistivity with increasing Sn content at a given temperature, suggest that thermal excitation (up to 300K) is not sufficient to promote all excess electrons generated within the VB of $MnSb_2Se_4$ to the Sn^{2+} impurity bands leading to a decrease in the overall hole density. One can therefore

speculate that upon increasing the Sn content, high concentration of acceptor states are generated at increasing higher energy within the band gap of $MnSb_2Se_4$ leading to an increase in the activation energy (Ea) necessary to promote excess electrons from the VB to the impurity band (Figure IX-3).

An alternatively, such decrease in the density of holes can be understood if one assumes that Sb^{3+} in the structure of $MnSb_{2-x}Sn_xSe_4$ is replaced by Sn^{4+}. Within this picture, the added Sn atoms act as donor impurities dumping extra electrons to the conduction band of the *p*-type $MnSb_{2-x}Sn_xSe_4$ semiconductor. However, a careful examination of the electrical resistivity curves of the various $MnSb_{2-x}Sn_xSe_4$ samples shows irregular change with increasing Sn concentration. For example, a marginal decrease in the resistivity is observed when the Sn content increases from x = 0.01 to x = 0.05 or from x = 0.15 to x = 0.25. Such irregularities in the electrical resistivity of $MnSb_{2-x}Sn_xSe_4$ samples suggest that the one-to-one substitution of Sb by Sn in the solid-state reaction leading to the formation of "$MnSb_{2-x}Sn_xSe_4$" follows two competing reaction paths (1), and (2), leading to the generation of both holes and electrons in the resulting sample:

$$Sb^{3+} \rightarrow Sn^{2+} + h^{\cdot} \qquad (1)$$

$$Sb^{3+} \rightarrow Sn^{4+} + e^{-} \qquad (2)$$

However, the observed higher resistivity of all Sn-doped samples when compared to $MnSb_2Se_4$ suggest that the reaction path (1) leading to the formation of Sn^{2+} impurity band within the band gap likely coexist with the reaction path (2) leading to the formation of Sn^{4+}. At 300K, the electrical resistivity increases from 9Ω .cm for the parent compound (x = 0) to 14Ω .cm and 35Ω .cm for x = 0.01 and x = 0.1, respectively. Further increasing the Sn content to x = 0.15 resulted in a sharper rise of the electrical resistivity to 1.4×10^5 Ω .cm at 300 K.

Figure IX-2B shows the temperature dependent thermopower plots of selected $MnSb_{2-x}Sn_xSe_4$ samples (x = 0, 0.01, 0.05 and 0.1). All samples show positive thermopower values indicating *p*-type semiconducting behavior in the measured temperature range. Regardless of temperature, the thermopower values remained nearly constant for Sn content up to x = 0.01, slightly decreased for the composition with x = 0.05, and drastically increased for the composition with x = 0.1. The Seebeck coefficient measurement of all samples with higher Sn concentrations failed due to the high electrical resistivity of these particular compositions. The

observed increase in the electrical resistivity and thermopower with increasing Sn substitution suggests that the one-to-one substitution of Sb by Sn in $MnSb_{2-x}Sn_xSe_4$ tends to reduce the overall density of holes in the parent structure through electron-hole compensation processes.

IX-4-Magnetic properties

To probe the effect of changes in the effective hole density arising from the Sn to Sb substitution on the magnetic behavior of the $MnSb_{2-x}Sn_xSe_4$ compounds, we measured the temperature dependence of both the ZFC and FC molar susceptibilities of several samples with different Sn concentrations under 100 Oe applied field (Figure IX-4A). In the crystal structure of the $MnSb_{2-x}Sn_xSe_4$ phases, the magnetic atoms (Mn) are essentially located within the magnetically quasi-isolated Mn_nSe_{4n+2} single chains of edge-sharing octahedra, which are 6.998(2) Å and 7.668(2) Å apart (Figure VIII-1). Therefore, the magnetic behavior of the $MnSb_{2-x}Sn_xSe_4$ phases is likely dominated by the intra-chain magnetic exchange interactions.

Table IX-2: Curie constant, Weiss constant and the effective magnetic moments extracted from the linear fits of the inverse susceptibility data of $MnSb_{2-x}Sn_xSe_4$.

Sn content (x)	Curie Constant (emu K mol^{-1})	Weiss Constant (K)	Effective Magnetic Moment (μ_B)
x= 0.0	5.48	–74	5.82
x=0.01	5.66	–41	6.73
x=0.05	5.03	–0.9	6.34
x=0.1	4.96	–8.8	6.30
x=0.15	4.01	1.2	5.66
x=0.20	5.67	–102	6.59
x=0.25	7.89	–99	7.94

Temperature dependent magnetic susceptibility data for the Sn-free composition ($MnSb_2Se_4$)[92] features a broad downturn at T_N = 20 K, suggesting AFM exchange interactions between localized spins on the nearest neighboring Mn atoms within individual Mn_nSe_{4n+2} single magnetic chains (Figure IX-4A). The linear fit of the inverse susceptibility between 120 K and 300 K using the Curie-Weiss law resulted in a negative Weiss constant θ = –74 K, and the

calculated effective magnetic moment of $\mu_{eff(calc)}$= 5.82μ_B (Table IX-2) was slightly smaller than the expected theoretical spin-only value of 5.92 μ_B for Mn^{2+} ($3d^5$) in the high-spin configuration. Upon Sn doping at the Sb sites in the structure of the $MnSb_{2-x}Sn_xSe_4$ phases, a marginal alteration in the magnitude of the molar susceptibilities is observed between 300 K and 56 K for various Sn concentrations. However, the magnetic susceptibilities for all samples gradually increase with decreasing temperature from 300 K to 56 K. Surprisingly, further cooling below 56 K revealed a drastic variation in the temperature dependent magnetic susceptibilities of Sn-doped samples. For instance, a noticeable increase in the magnitude of the magnetic susceptibility is observed below 56 K for the composition with x = 0.01 when compared to that of the Sn-free sample. A drastic increase in the magnitude of the susceptibility is observed for Sn concentrations ranging from x = 0.05 to x = 0.15, with the largest susceptibility values observed for the sample containing 2.5% Sn (x = 0.05). The sudden increase in the susceptibility values between 56 K and 40 K for the compositions with x = 0.01, 0.05, 0.1 and 0.15 is associated with the onset of local FM ordering in the samples. Below 40 K, the slope of the susceptibility curves drop suggesting a competition between the local FM ordering and the intrinsic AFM surperexchange interaction within the Mn_nSe_{4n+2} single magnetic chains (Figures IX-4A). Interestingly, the FM ordering observed in samples with low Sn concentrations ($0.01 \leq x \leq 0.15$) vanishes in samples with higher Sn content ($x > 0.15$) and a drastic drop in the susceptibility is observed below 56 K.

The temperature dependent inverse susceptibility data between 120 K and 300 K for all Sn-doped samples follow the Curie-Weiss law. The Weiss and Curie constants, as well as the effective magnetic moments extracted from the linear fits of the inverse susceptibility data, are shown in Table IX-2. Smaller Weiss constant values (compared to the Sn-free sample) and effective magnetic moments larger than the theoretical value of 5.92 μ_B expected from Mn^{2+} ions ($3d^5$) were observed for samples with x = 0.01, 0.05, 0.1 and 0.15 (Table IX-2).

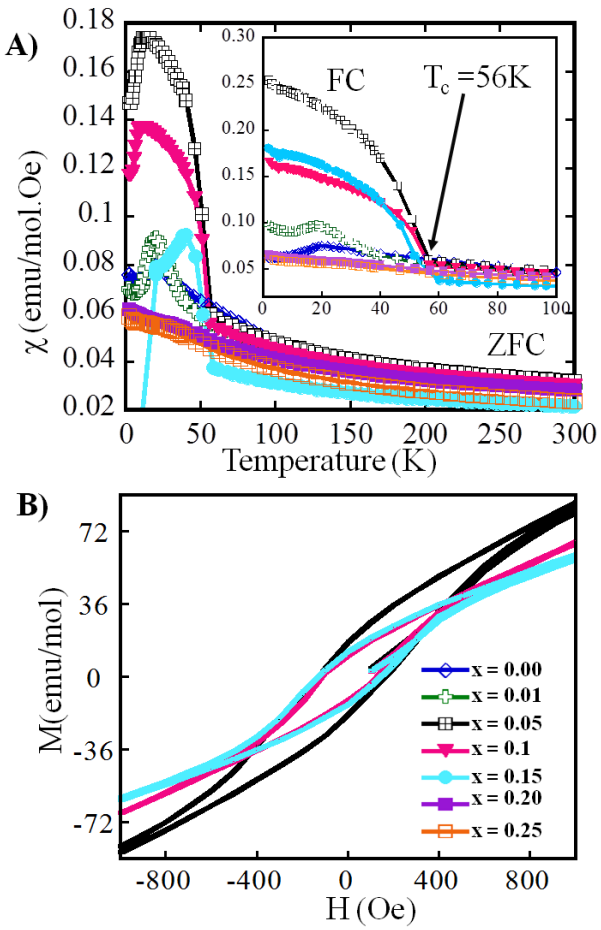

Figure-IX 4: A) Temperature dependence of the zero-field-cooled (ZFC) molar magnetic susceptibility of $MnSb_{2-x}Sn_xSe_4$ ($0 \leq x \leq 0.25$) measured under applied field of 100Oe. The inset is the corresponding field-cooled (FC) magnetic susceptibility within the temperature range 2K-100K. B) Field dependent magnetization at 4K of selected $MnSb_{2-x}Sn_xSe_4$ (x = 0.05; 0.1; 0.15) compositions showing broad hysteresis loops with a coercivity force of 150Oe.

Furthermore, isothermal field dependence of the magnetization performed at 4K in the 0-5 kOe range (Figure IX-4B) showed magnetic hysteresis with a coercive field, H_c = 150 Oe. However, saturation of the magnetization was not observed up to an applied field of 10 kOe. These results further confirmed that at the optimum Sn concentration, the $MnSb_{2-x}Sn_xSe_4$ phases retain a small FM character at low temperatures, despite the competing intrinsic intra-chain AFM interactions. Samples with Sn content above x = 0.15 showed larger negative Weiss constants and larger effective magnetic moments when compared to the pristine composition. This suggests that local FM ordering in these samples (x > 0.15) are likely dominated by the strong AFM exchange interactions within individual Mn_nSe_{4n+2} single magnetic chain.

To further probe the nature of the FM ordering in the $MnSb_{2-x}Sn_xSe_4$ phases (x = 0.01, 0.05, 0.15 and 0.25), we performed temperature dependent alternating current (AC) susceptibility at different frequencies under an applied field of 0.1 Oe. Figure IX-5 shows the temperature dependence of the in-phase part (χ') of the AC susceptibility of samples with different compositions under various frequencies. It was observed that the AC susceptibility (χ') for most samples (except the composition with x = 0.01) is frequency independent. For the composition with x = 0.01, χ' gradually increases with decreasing temperature and exhibits two distinct peaks at 76 K and 21 K (Figure IX-5A). The sharp peak observed around 76 K for this particular sample appears only when frequencies between 750 Hz and 1000 Hz are used and suggests the presence of a frustrated FM ordering presumably from spin polarized itinerant carriers. The peak around 21 K, however, can be associated with magnetic frustration arising from the competition between AFM ordering within individual Mn_nSe_{4n+2} single magnetic chains and weak FM ordering of spin-polarized itinerant carriers in the compound. For the compositions with x = 0.05 and x = 0.15, the shape of the temperature dependent in-phase susceptibility curves (Figure IX-5 B and C) are very similar to the corresponding ZFC DC susceptibility curves (Figure IX-5A). The sharp increase in the in-phase AC susceptibility observed at 56 K indicates onset of FM ordering in the samples (x = 0.05 and x = 0.15). However, the in-phase AC susceptibility curves feature a broad downturn between 45 K and 15 K, which is followed by a steeper drop in the susceptibility upon further cooling. The broad downturn in the AC susceptibility curves suggests a competition between the FM ordering observed at 56 K and the intrinsic AFM ordering within the Mn_nSe_{4n+2} single magnetic chains. Below 15 K, this competition is dominated by the intra-chain AFM ordering leading to a sharp drop in the magnetic susceptibility. For the composition with x = 0.15, a frequency independent and nearly linear increase in the in-phase AC susceptibility with decreasing temperature was observed (Figure IX-5D), suggesting the absence of any magnetic ordering at this composition. However, the large negative values of the Weiss constant (Table IX-2) suggest the presence of strong AFM interactions in $MnSb_{2-x}Sn_xSe_4$ compositions with Sn content greater than x = 0.15.

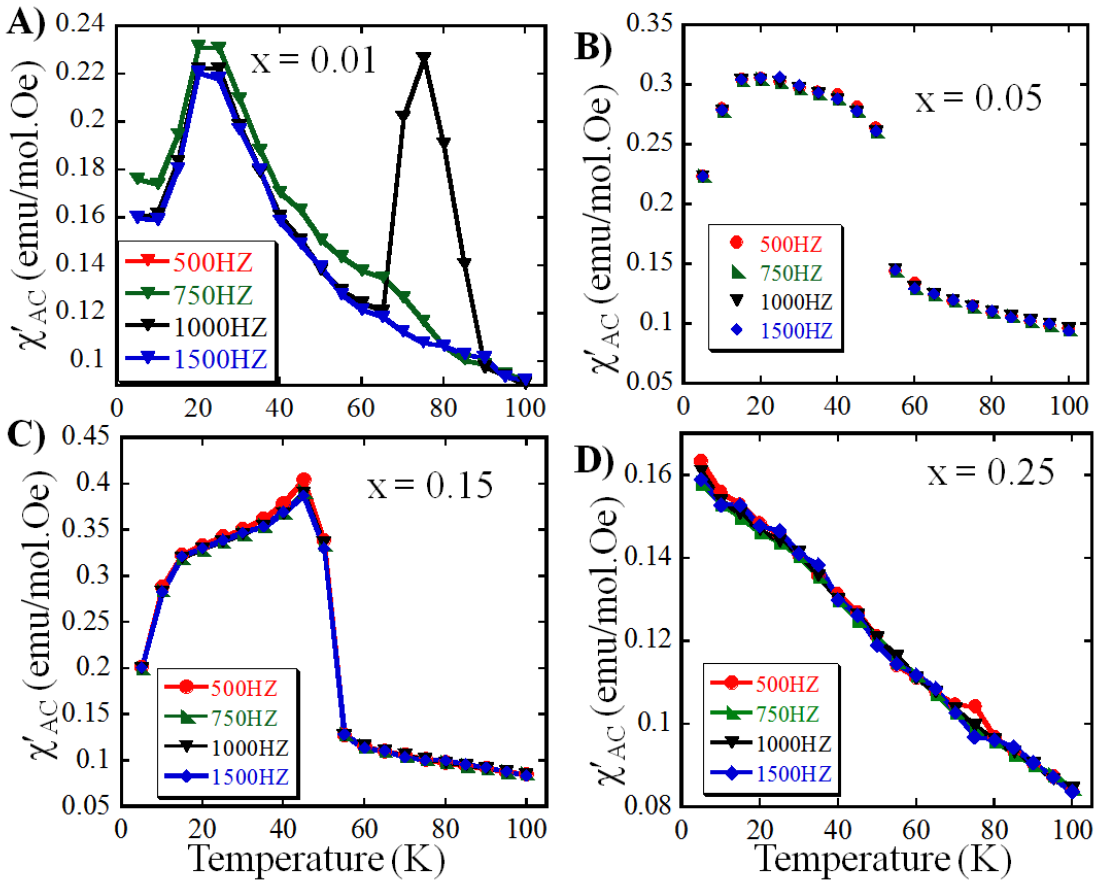

Figure-IX 5: Temperature dependence of the in phase component of the AC magnetic susceptibility for selected $MnSb_{2-x}Sn_xSe_4$ compositions measured at various frequencies (from 500 Hz to 1500 Hz) under an applied field of 0.1Oe. A): x = 0.01; B): x = 0.05; C): x = 0.15; D): x = 0.25.

The above magnetic data clearly indicate that the dominant magnetic ordering in various $MnSb_{2-x}Sn_xSe_4$ phases strongly depends on the fraction of Sn atoms in the compound. Starting from the AFM $MnSb_2Se_4$ phase, it was found that FM ordering with T_c = 56 K can be induced through partial isomorphic substitution of up to 7.5 % ($0.01 \leq x \leq 0.15$) Sn at Sb sites in the structure of $MnSb_2Se_4$. Interestingly, this FM ordering vanishes upon further increase of the Sn content above 7.5 %. Although the complete mechanism leading to the drastic changes that govern the magnetic ordering in $MnSb_{2-x}Sn_xSe_4$ is not fully understood, a plausible explanation of the observed data must take into account changes in the electronic transport properties within

this system upon isomorphic substitution of Sn at Sb sites. As stated above, the magnetism in the structure of the p-type semiconductor $MnSb_2Se_4$ is controlled by the magnetic interactions within the quasi-isolated magnetic subunits, Mn_nSe_{4n+2}, which consist of single chains formed by edge sharing octahedra of Se atoms around a Mn atom. Therefore, a Sn substitution at Sb sites in the $MnSb_{2-x}Sn_xSe_4$ phases is not expected to alter the dominant AFM magnetic exchange interactions between Mn ions within the Mn_nSe_{4n+2} magnetic subunits. However, an alteration of the electronic property (density and/or mobility of the majority charge carriers) is anticipated. The change in the electronic properties of $MnSb_{2-x}Sn_xSe_4$ is evident from the temperature dependent electrical resistivity and thermopower data (Figure IX-2). As discussed above, the substitution of Sb by Sn in $MnSb_2Se_4$ preferentially introduces additional electrons into the valence band of the p-type $MnSb_2Se_4$ system leading to a net reduction in the overall density of holes and an increase in the electrical resistivity. Furthermore, in the absence of an applied magnetic field, the large increase in the electrical resistivity (Figure IX-2A) as the temperature approaches the AFM ordering temperature was associated with (1) a sharp drop in hole mobility due to increased spin scattering arising from the interaction between localized magnetic moments on Mn ions and spins of itinerant holes and (2) a decrease in the effective hole density due to the freezing of extra free-electrons within the VB of $MnSb_2Se_4$ resulting in electron-hole compensation, and the localization of a small fraction of spin-polarized holes at sufficiently low temperatures. Within this picture, one can anticipate, under the application of an external magnetic field the formation of bound magnetic polarons (BMP) [17,98]. That is the clustering of a large number of spin-polarized itinerant holes around localized spin-polarized free-electrons or holes via AFM exchange interactions. The size of such BMPs grows with decreasing temperature, and the overlap of neighboring BMPs presumably results in parallel alignment (FM ordering) of spin polarized holes at the intersection of their magnetic field [17,98]. The above analysis is consistent with findings from dynamical mean field theory calculations, which showed that holes in FM $Ga_{1-x}Mn_xAs$ ($x = 0.03 – 0.07$) are likely just on the edge of being strongly localized [99]. The final size of BMPs and the magnitude of the magnetic moments originating from the interactions of neighboring BMPs are related to the fraction of spin-polarized itinerant holes, which in turn depends on the Sn content. At optimal Sn content ($0.01 \leq x \leq 0.15$), the magnetic moment from BMPs dominates the intrinsic AFM ordering within the magnetic subunits leading to the observed FM ordering. Within this optimal Sn concentration

range, the maximum susceptibility was observed for the composition with x = 0.05. Further increase in the Sn content resulted in lower susceptibility values due to the reduction in the effective density of spin-polarized itinerant holes. For compositions with higher Sn content (x > 0.15), the density of spin-polarized holes is significantly reduced due to a large drop in the density of holes. This presumably results in small and non-overlapping BMPs with predominantly AFM exchange interactions between them (Figure IX-4A).

Conclusion

In summary, we have systematically investigated the correlation between the electronic transport properties and the predominant magnetic ordering mechanism in *p*-type Sn-doped $MnSb_{2-x}Sn_xSe_4$ phases. We found that the partial substitution of Sb by Sn in the structure of $MnSb_2Se_4$ results in an increase in the electrical resistivity and thermopower, which is associated with a decrease in the overall density of holes. For optimum Sn concentration ($0.01 \leq x \leq 0.15$), a FM ordering with a Curie temperature T_c = 56 K appears in the samples. The maximum magnetic susceptibility below T_c in such FM samples is reached for the composition with x = 0.05, and the susceptibility gradually degrades with increasing Sn content. The FM ordering completely vanishes for compositions with Sn concentration exceeding x = 0.15. Interestingly, the Curie transition temperature remains constant within the composition range of FM ordering. This is consistent with a recent study of ferromagnetism in Mn-doped (Ga,Mn)As, which suggested that the T_c is controlled by the location of the Fermi level within the impurity band, rather than the hole concentration.[23]The observed remarkable alteration of the dominant magnetic ordering in $MnSb_{2-x}Sn_xSe_4$ phases from AFM to FM and back to AFM upon increasing Sn concentration is rationalized within the context of spin polarization and partial localization of itinerant holes, ultimately leading to the formation of BMPs at low temperatures. For optimum density of holes ($0.01 \leq x \leq 0.15$), neighboring BMPs overlap and interact with each other via shared spin-polarized holes. This interaction produces alignment of the polaron spins, and FM ordering occurs when sufficiently large polarons are formed and overlap. For compositions with high Sn content (x>0.15), the drastic decrease in the density of spin-polarized itinerant holes results in the formation of non-overlapping small BMPs with AFM ordering between them.

References

(1) Ranmohotti, K. G. S.; Djieutedjeu, H.; Poudeu, P. F. P. *J Am Chem Soc* **2012**, *134*, 14033.
(2) Story, T.; Gałązka, R. R.; Frankel, R. B.; Wolff, P. A. *Physical Review Letters* **1986**, *56*, 777.
(3) Chiba, D.; Fukami, S.; K., S.; N., I.; K., K.; T., O. *Nature Materials* **2011**, *10*, 853.
(4) Chiba, D.; Werpachowska, A.; Endo, M.; Nishitani, Y.; Matsukura, F.; Dietl, T.; Ohno, H. *Phys Rev Lett* **2010**, *104*.
(5) Akai, H. *Physical Review Letters* **1998**, *81*, 3002.
(6) Ando, K. *Science* **2006**, *312*, 1883.
(7) Chattopadhyay, A.; Das Sarma, S.; Millis, A. J. *Physical Review Letters* **2001**, *87*, 227202.
(8) Dietl, T.; Ohno, H.; Matsukura, F.; Cibert, J.; Ferrand, D. *Science* **2000**, *287*, 1019.
(9) Dietl, T. *Nat Mater* **2010**, *9*, 965.
(10) Cibert, J.; Kossacki, P.; Haury, A.; Ferrand, D.; Wasiela, A.; d'Aubigne, Y. M.; Arnoult, A.; Tatarenko, S.; Dietl, T. *J Cryst Growth* **1999**, *201*, 670.
(11) Coey, J. M. D.; Venkatesan, M.; Fitzgerald, C. B. *Nat Mater* **2005**, *4*, 173.
(12) Dietl, T.; Haury, A.; dAubigne, Y. M. *Phys Rev B* **1997**, *55*, R3347.
(13) Dietl, T.; Ohno, H. *Mater Today* **2006**, *9*, 18.
(14) Dietl, T.; Ohno, H.; Matsukura, F. *Phys Rev B* **2001**, *63*.
(15) Durst, A. C.; Bhatt, R. N.; Wolff, P. A. *Phys Rev B* **2002**, *65*.
(16) Ferrand, D.; Cibert, J.; Bourgognon, C.; Tatarenko, S.; Wasiela, A.; Fishman, G.; Bonanni, A.; Sitter, H.; Kolesnik, S.; Jaroszyski, J.; Barcz, A.; Dietl, T. *J Cryst Growth* **2000**, *214*, 387.
(17) Kaminski, A.; Das Sarma, S. *Phys Rev Lett* **2002**, *88*.
(18) Kundaliya, D. C.; Ogale, S. B.; Lofland, S. E.; Dhar, S.; Metting, C. J.; Shinde, S. R.; Ma, Z.; Varughese, B.; Ramanujachary, K. V.; Salamanca-Riba, L.; Venkatesan, T. *Nat Mater* **2004**, *3*, 709.
(19) Bader, S. D.; Parkin, S. S. P. *Annu Rev Conden Ma P* **2010**, *1*, 71.
(20) Fert, A.; George, J.-M.; Jaffres, H.; Mattana, R. *europhysics news* **2003**, 227.
(21) Jansen, R. *Nat Mater* **2012**, *11*, 400.
(22) *Concepts in Spin Electronics*; Sadamichi; Maekawa, Eds.; Oxford Science Publication: Oxford, 2006.
(23) Dobrowolska, M.; Tivakornsasithorn, K.; Liu, X.; Furdyna, J. K.; Berciu, M.; Yu, K. M.; Walukiewicz, W. *Nat Mater* **2012**, *11*, 444.
(24) Jungwirth, T.; Wang, K. Y.; Masek, J.; Edmonds, K. W.; Konig, J.; Sinova, J.; Polini, M.; Goncharuk, N. A.; MacDonald, A. H.; Sawicki, M.; Rushforth, A. W.; Campion, R. P.; Zhao, L. X.; Foxon, C. T.; Gallagher, B. L. *Phys Rev B* **2005**, *72*.
(25) Djieutedjeu, H.; Poudeu, P. F. P.; Takas, N. J.; Makongo, J. P. A.; Rotaru, A.; Ranmohotti, K. G. S.; Anglin, C. J.; Spinu, L.; Wiley, J. B. *Angew Chem Int Edit* **2010**, *49*, 9977.
(26) Macdonald, A. H.; Schiffer, P.; Samarth, N. *Nat Mater* **2005**, *4*, 195.
(27) Lee, S.; Hwang, S. J.; Lee, H. S.; Shon, Y.; U.Yuldashev, S.; Kim, D. Y. *Journal of Applied Physics* **2005**, *98*, 123905.
(28) Kanatzidis, M. G. *Semiconduct Semimet* **2001**, *69*, 51.
(29) Mrotzek, A.; Iordanidis, L.; Kanatzidis, M. G. *Inorg Chem* **2001**, *40*, 6204.
(30) Mrotzek, A.; Kanatzidis, M. G. *Accounts Chem Res* **2003**, *36*, 111.

(31) Tritt, T. M.; Subramanian, M. A. *MRS Bulletin* **2006**, *31*, 188.
(32) Lee, D. S.; Kim, T.-H.; Park, C.-H.; Chung, C.-Y.; Lim, Y. S.; Seo, W.-S.; Park, H.-H. *CrystEngComm* **2013**, *15*, 5532.
(33) Wright, D. A. *Nature* **1958**, *181*, 834.
(34) Dyck, J. S.; Hájek, P.; Lošťák, P.; Uher, C. *Physical Review B* **2002**, *65*, 115212.
(35) Zhou, Z.; Chien, Y.-J.; Uher, C. *Phys Rev B* **2006**, *74*, 224418.
(36) Dyck, J. S.; Drašar, Č.; Lošťák, P.; Uher, C. *Phys Rev B* **2005**, *71*, 115214.
(37) Kilanski, L.; Szymczak, R.; Dobrowolski, W.; Podgorni, A.; Avdonin, A.; Slynko, V. E.; Slynko, E. I. *Journal of Applied Physics* **2013**, *113*, 063702.
(38) Fukuma, Y.; Asada, H.; Arifuku, M.; Koyanagi, T. *Applied Physics Letters* **2002**, *80*, 1013.
(39) Bente, E. A. J. M.; Hogervorst, W. *Z Phys D Atom Mol Cl* **1989**, *14*, 119.
(40) Bente, K.; Edenharter, A. *Z.Kristallogr.* **1989**, *31*, 186.
(41) Buerger, M. J.; Hahn, T. *Am Mineral* **1955**, *40*, 226.
(42) Kurowski, D., University of Regensburg, Germany, 2003.
(43) Leone, P.; Doussier-Brochard, C.; Andre, G.; Moelo, Y. *Phys Chem Miner* **2008**, *35*, 201.
(44) Matar, S. F.; Weihrich, R.; Kurowski, D.; Pfitzner, A.; Eyert, V. *Phys Rev B* **2005**, *71*.
(45) Pfitzner, A.; Kurowski, D. *Z Kristallogr* **2000**, *215*, 373.
(46) Mumme, W. G.; Watts, J. A. *Acta Crystallogr B* **1980**, *36*, 1300.
(47) Leone, P.; Andre, G.; Doussier, C.; Moelo, Y. *J Magn Magn Mater* **2004**, *284*, 92.
(48) Matsushita, Y.; Ueda, Y. *Inorg Chem* **2003**, *42*, 7830.
(49) Matsushita, Y.; Ueda, Y. *Inorg Chem* **2006**, *45*, 2022.
(50) Leone, P.; Le Leuch, L. M.; Palvadeau, P.; Molinie, P.; Moelo, Y. *Solid State Sci* **2003**, *5*,771.
(51) Lecker, A.; Kurowski, D.; Pfitzner, A. *Z Anorg Allg Chem* **2006**, *632*, 2144.
(52) Shannon, R. D. *Acta Crystallogr A* **1976**, *32*, 751.
(53) Mydosh, J. A. *Spin glasses: an experimental introduction*; Taylor & Franacis: London ; Washington, DC, 1993.
(54) Binder, K.; Young, A. P. *Rev Mod Phys* **1986**, *58*, 801.
(55) Fischer, K. H.; Hertz, J. A. *Spin glasses*; Cambridge University Press: Cambridge ; New York, NY, USA, 1991.
(56) Gingras, M. J. P.; Stager, C. V.; Gaulin, B. D.; Raju, N. P.; Greedan, J. E. *J Appl Phys* **1996**, *79*, 6170.
(57) Wang, P.; Stadnik, Z. M.; Zukrowski, J.; Cho, B. K.; Kim, J. Y. *Phys Rev B* **2010**, *82*.
(58) Goodenough, J. B. *Phys Rev* **1955**, *100*, 564.
(59) Goodenough, J. B. *J Phys Chem Solids* **1958**, *6*, 287.
(60) Goodenough, J. B.; Loeb, A. L. *Phys Rev* **1955**, *98*, 391.
(61) Kanamori, J. *J Phys Chem Solids* **1959**, *10*, 87.
(62) Dronskowski, R.; Blochl, P. E. *J Phys Chem-Us* **1993**, *97*, 8617.
(63) Cadenas, R.; Perez, F. V.; Quintero, M.; Quintero, E.; Tovar, R.; Morocoima, M.;Gonzalez, J.; Bocaranda, P.; Ruiz, J.; Broto, J. M.; Rakoto, H. Physica B 2007, 389, 302.
(64) Nagaev, E. L. *Colossal Magnetoresistance and Phase seperation in Magnetic Semicondutors*; Imperial college Press, 2002.
(65) Quintero, E.; Quintero, M.; Morocoima, M.; Bocaranda, P. *J Appl Phys* **2007**, *102*.
(66) Matsumoto, Y. *Science* **2001**, *294*, 1003.

(67) Berciu, M.; Bhatt, R. N. *Phys Rev Lett* **2001**, *87*.
(68) Litvinov, V. I.; Dugaev, V. K. *Phys Rev Lett* **2001**, *86*, 5593.
(69) Venkatesan, M.; Fitzgerald, C. B.; Lunney, J. G.; Coey, J. M. D. *Phys Rev Lett* **2004**, *93*.
(70) Anglin, C.; Takas, N.; Callejas, J.; Poudeu, P. F. P. *J Solid State Chem* **2010**, *183*, 1529.(71) Poudeu, P. F. P.; Takas, N.; Anglin, C.; Eastwood, J.; Rivera, A. *J Am Chem Soc* **2010**, *132*, 5751.
(72) Zhou, Z. H.; Chien, Y. J.; Uher, C. *Phys Rev B* **2006**, *74*, 224418.
(73) Zhou, Z. H.; Chien, Y. J.; Uher, C. *Appl Phys Lett* **2005**, *87*, 112503.
(74) Goncharenko, I. N.; Mirebeau, I. *Phys Rev Lett* **1998**, *80*, 1082.
(75) Moodera, J. S.; Meservey, R.; Hao, X. *Phys Rev Lett* **1993**, *70*, 853.
(76) Sanford, N.; Davies, R. W.; Lempicki, A.; Miniscalco, W. J.; Nettel, S. J. *Phys Rev Lett* **1983**, *50*, 1803.
(77) Nishitani, Y.; Chiba, D.; Endo, M.; Sawicki, M.; Matsukura, F.; Dietl, T.; Ohno, H. *Phys Rev B* **2010**, *81*.
(78) Jungwirth, T.; Konig, J.; Sinova, J.; Kucera, J.; MacDonald, A. H. *Phys Rev B* **2002**, *66*.
(79) Neumaier, D.; Turek, M.; Wurstbauer, U.; Vogl, A.; Utz, M.; Wegscheider, W.; Weiss, D. *Phys Rev Lett* **2009**, *103*.
(80) Jungwirth, T.; Sinova, J.; MacDonald, A. H.; Gallagher, B. L.; Novak, V.; Edmonds, K. W.; Rushforth, A. W.; Campion, R. P.; Foxon, C. T.; Eaves, L.; Olejnik, E.; Masek, J.; Yang, S. R. E.; Wunderlich, J.; Gould, C.; Molenkamp, L. W.; Dietl, T.; Ohno, H. *Phys Rev B* **2007**, *76*.
(81) Richardella, A.; Roushan, P.; Mack, S.; Zhou, B.; Huse, D. A.; Awschalom, D. D.; Yazdani, A. *Science* **2010**, *327*, 665.
(82) Sawicki, M.; Chiba, D.; Korbecka, A.; Nishitani, Y.; Majewski, J. A.; Matsukura, F.; Dietl, T.; Ohno, H. *Nat Phys* **2010**, *6*, 22.
(83) Rokhinson, L. P.; Lyanda-Geller, Y.; Ge, Z.; Shen, S.; Liu, X.; Dobrowolska, M.; Furdyna, J. K. *Phys Rev B* **2007**, *76*.
(84) Mayer, M. A.; Stone, P. R.; Miller, N.; Smith, H. M.; Dubon, O. D.; Haller, E. E.; Yu, K. M.; Walukiewicz, W.; Liu, X.; Furdyna, J. K. *Phys Rev B* **2010**, *81*.
(85) Alberi, K.; Yu, K. M.; Stone, P. R.; Dubon, O. D.; Walukiewicz, W.; Wojtowicz, T.; Liu, X.; Furdyna, J. K. *Phys Rev B* **2008**, *78*.
(86) Erwin, S. C.; Petukhov, A. G. *Phys Rev Lett* **2002**, *89*.
(87) Mahadevan, P.; Zunger, A. *Appl Phys Lett* **2004**, *85*, 2860.(88) Heikes, R. R.; Chen, C. W. *Physics* **1964**, *1*, 159.

89) Li, H. F.; Xiao, Y. G.; Schmitz, B.; Persson, J.; Schmidt, W.; Meuffels, P.; Roth, G.; Bruckel, T. *Sci Rep-Uk* **2012**, *2*, 1.
(90) *Nanomagnetism and Spintronics*; Nasirpouri, F.; Nogoret, A., Eds.; Word Scientific Publishing Co.Pte.Ltd: Singapore, 2009.
(91) Pan, F.; Song, C.; Liu, X. J.; Yang, Y. C.; Zeng, F. *Mat Sci Eng R* **2008**, *62*, 1.
(92) Djieutedjeu, H.; Makongo, J. P. A.; Rotaru, A.; Palasyuk, A.; Takas, N. J.; Zhou, X. Y.; Ranmohotti, K. G. S.; Spinu, L.; Uher, C.; Poudeu, P. F. P. *European Journal of Inorganic Chemistry* **2011**, 3969.
(93) Poudeu, P. F. P.; Djieutedjeu, H.; Sahoo, P. *Z Anorg Allg Chem* **2012**, *638*, 2549.
(94) Rodriguez-Carvajal, J. *Physica B* **1993**, *192*, 55.
(95) Rodriguez-Carvajal, J. *Newsletter* **2001**, *26*, 12.
(96) Shannon, R. D.; Prewitt, C. T. *Acta Crystall B-Stru* **1969**, *B 25*, 925.
(97) Berciu, M.; Bhatt, R. N. *Phys Rev Lett* **2001**, *87*, 107203.
(98) Wolff, P. A.; Bhatt, R. N.; Durst, A. C. *J Appl Phys* **1996**, *79*, 5196.
(99) Chattopadhyay, A.; Das Sarma, S.; Millis, A. J. *Phys Rev Lett* **2001**, *87*.

Chapter X

General Conclusions and Future works

This dissertation work is to chemically design and synthesize new ferromagnetic semiconductor with low band gap and high Curie temperature. Our hypothesis was to design using bottom-up approach, a simple system embedding well ordered active magnetic center within the semiconducting framework based on chalcogenide chemistry insight. We successfully synthesized several systems with various magnetic and transport properties. In this dissertation we have reported the crystal structure and effect of thermal processing on the structure, magnetic properties, electrical properties, magneto transport and some thermoelectric properties of $FeSb_2Se_4$ and $MnSb_2Se_4$ which were found to be the simplest system in term of structure and number of atoms within the crystallographic unit cell.

$FeSb_2Se_4$ is reported as the new chemical compound displaying very high ferromagnetic ordering temperature in low band gap semiconducting framework with a remarkable interplay between reversible magnetic ordering phenomena and semiconductor-to-insulator (SI) transition upon cooling down to 120K. The observed cooperative magnetic and SI transitions in $FeSb_2Se_4$ are driven by local isostructural distortions arising from the preferential lattice contraction within the *ab* plane. Upon heating this material from 300K to 350K, a striking change along the *a*-axis of the crystal structure was observed. The *a*-axis drastically expands from 13.083(3)Å at 300K to 38.243(8)Å at 350K, while the β angle slightly drops from 114.78^{o}(300K) to $111.21(3)^{o}$(350K). Further heating the same material up to 400K results to in a change of *a*-axis to 27.543(6)Å and *c*-axis to 26.22(5)Å while β sharply decreases to $90.72(3)^{o}$. In addition the space group switches

from *C* 2 /*m* at 350K to *C* 1/*c* 1. These structural phase-changes are associated with the magnetic phase transitions observed at 323K and 450K, respectively. We anticipate that such structure-property relation is governed by the lone pair activity connecting A/B layer structure of this compound. The cooperative transition in this compound, to our knowledge, has no precedent in pure inorganic materials and represents a significant increase in the level of complexity with respect to known phase transitions. The neutron diffraction data and the Arrott`s plots revealed ferromagnetic ordering up to 600K. This ferromagnetic behavior was found to originate from long range exchange interaction via localized carrier forming bound magnetic polarons at low temperature and spin-polarized electrons at high temperature. We have texted the sensitivity of $FeSb_2Se_4$ to impurities and the effect of these impurities on its magnetic and transport properties. We started by doping this material with Sn and generated a series of compositions with general formula $FeSb_{2-x}Sn_xSe_4$ ($0 \leq x \leq 0.25$). All composition using this manipulation adopt the $FeSb_2Se_4$ structure. The magnetic and electrical properties show strongly alteration with increasing concentration of Sn. In fact, upon doping with Sn, all magnetic parameters such as the magnetization saturation, coercivity and remanence were altered while the material switches from semiconductor to metallic like behavior with increasing amount of Sn. Further investigation using X-ray photoelectron spectroscopy revealed that adding Sn into $FeSb_2Se_4$ induced the oxidation of Fe and Sb in $FeSb_2Se_4$ from Fe^{2+} to Fe^{3+} and Sb^{3+} to Sb^{5+}. This is consistent with the change from semiconductor to metallic behavior with increasing concentration of Sn. The loss of structurally induced transitions at 130K, 321K and 440K with increasing concentration confirm the effect and role of Sb lone pair in the process of structurally driven properties in $FeSb_2Se_4$. Long range exchange interaction persisted with increasing amount of Sn as suggested the field dependent magnetization of the highest doped composition which showed hysteresis up to 600K. X-ray photoelectron spectroscopy confirmed that the long range exchange interaction is the results of spin polarized hole or electron at impurities band edge of $FeSb_2Se_4$.

Although $FeSb_2Se_4$ showed interesting magnetic properties and strong spin dependent transport, the very low electrical conductivity of this material could limit its application. We attempt to solve this issue by either doped the parent compound with Te or proceed to the substitution of Se with Te to generated two series of materials: $FeSb_2Se_{4-x}Te_x$($0 \leq x \leq 0.1$) and $FeSb_2Se_{4-x}Te_x$ ($1 \leq x \leq 4$). Although the doping process conserved magnetic feature compared to the Te free

composition, the electrical conductivity were not significantly enhanced and decreases with increasing concentration of Te. Upon substitution of Se with Te, the structure deviated from monoclinic to the high tetragonal crystal symmetry. However, electrical and magnetic properties were significantly altered with striking enhancement of the electrical conductivity with Se free sample. Both series shows spin dependent transport phenomena and exhibit increasing magnetization with increasing amount of Te above room temperature.

$MnSb_2Se_4$ is an antiferromagnetic semiconductor with Neel temperature of 21K and Curie-Weiss constant of -73K. The effective magnetic moment of $5.93\mu_B$ observed in this compound suggests the presence of manganese in the oxidation Mn^{2+}. This compound is isostructural with $FeSb_2Se_4$ exhibit spin glass magnetic disorder as result of competing FM and AFM exchange interaction in the magnetic chains along the *b*-axis of the crystal structure. We found that the

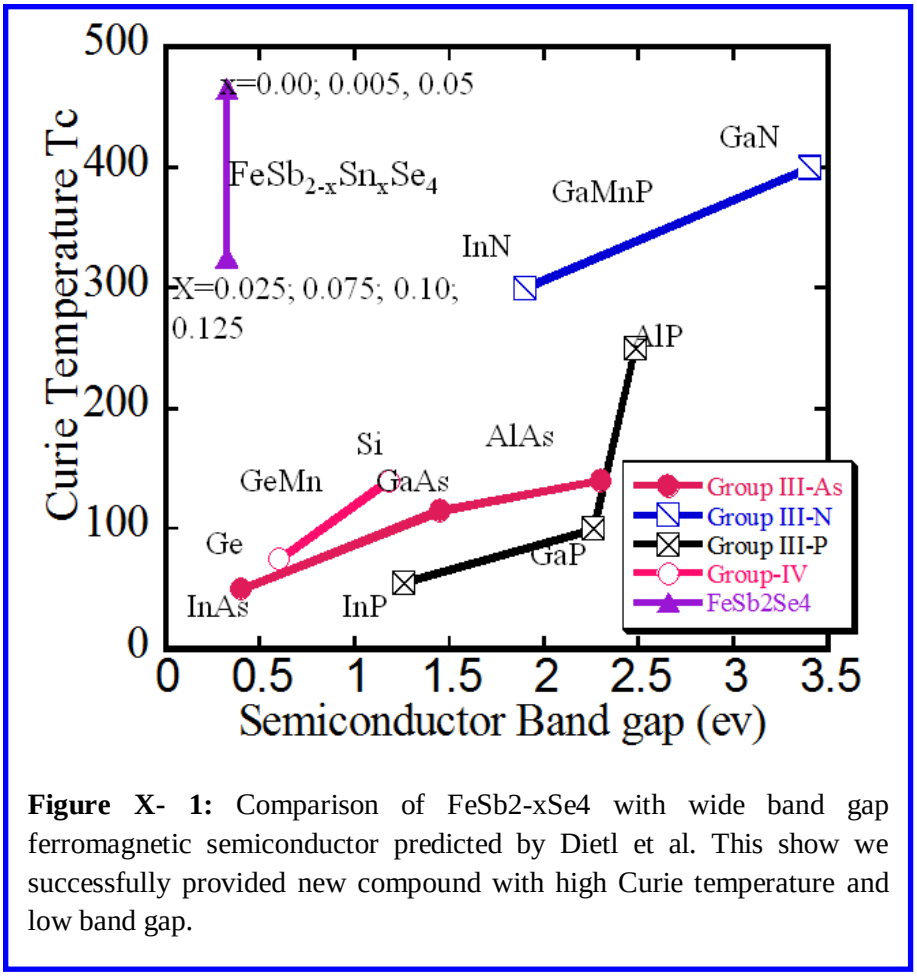

Figure X- 1: Comparison of FeSb2-xSe4 with wide band gap ferromagnetic semiconductor predicted by Dietl et al. This show we successfully provided new compound with high Curie temperature and low band gap.

partial substitution of Sb by Sn in the structure of $MnSb_2Se_4$ results in an increase in the electrical resistivity and thermopower, which is associated with a decrease in the overall density of holes. For optimum Sn concentration ($0.01 \leq x \leq 0.15$), a FM ordering with a Curie temperature $T_c = 56$ K appears in the samples. The maximum magnetic susceptibility below T_c in such FM samples is reached for the composition with $x = 0.05$, and the susceptibility gradually degrades with increasing Sn content. The FM ordering completely vanishes for compositions with Sn concentration exceeding $x = 0.15$. Interestingly, the Curie transition temperature remains constant within the composition range of FM ordering. This is consistent with a recent study of ferromagnetism in Mn-doped (Ga,Mn)As, which suggested that the T_c is controlled by the location of the Fermi level within the impurity band, rather than the hole concentration. The observed remarkable alteration of the dominant magnetic ordering in $MnSb_{2-x}Sn_xSe_4$ phases from AFM to FM and back to AFM upon increasing Sn concentration is rationalized within the context of spin polarization and partial localization of itinerant holes, ultimately leading to the formation of BMPs at low temperatures. For optimum density of holes ($0.01 \leq x \leq 0.15$), neighboring BMPs overlap and interact with each other via shared spin-polarized holes. This interaction produces alignment of the polaron spins, and FM ordering occurs when sufficiently large polarons are formed and overlap.

This work demonstrates that a single spintronics material can combine both low band gap and high Curie ferromagnetic temperature (**Figure X**). The requirements of large T_c, small band gap and conductance matching are better realized in the $FeSb_{2-x}Sn_xSe_4$ and $FeSb_2Se_{4-x}Te_x$ material system. Therefore these material and mainly $FeSb_2Se_4$ are anticipated as template for understanding of band structure of magnetic semiconductor with high Curie temperature and low band gap. This will open field bang gap engineering of commercial semiconductor when doping them with transition metal such as Mn, Fe, Co and Ni. Therefore, our recommendations in the future direction of spintronics studies are:

To experimentally and theoretically investigate the band structure of $FeSb_2Se_4$ and other ferromagnetic ternary chalcogenides with high Curie temperature. In addition to this extend the studies on the magnetic semiconductor with low Curie temperature and system with antiferromagnetic behavior. This allow to systematically understand the correlation between the

Fermi level, spin of the magnetic moment, the impurities and band structure organization and effect in the magnetic and semiconducting behavior.

To initiate the growth of large crystals for anisotropy investigation of various properties present in the $MnSb_2Se_4$, $FeSb_2Se_4$ and $FeSb_2Se_{4-x}Te_{x.}$ This will enable the knowledge of the favorable direction when embedding this system into devices. Furthermore development of the n-type analogue of $FeSb_2Se_4$ which is under process in our group will enable devices with alternated of n-p-type ferromagnetic semiconductor.

To investigate the correlation between the spintronics and thermoelectric properties in $FeSb_2Se_{4-x}Te_x$ and the effect of effect thermoelectric properties optimization on the magnetic behavior of the sample.

To explore other chalcogenide materials using the same approach as used to design $FeSb_2Se_4$ and $MnSb_2Se_4$ system and if possible extend it to rare earth transition metal.

Annexes:

Tables of geometrical information

Annex I: $MnSb_2Se_4$

Atomic parameters							
Atom	**Ox.**	**Wyck.**	**Site**	**S.O.F.**	**x/a**	**y/b**	**z/c**
Sb1		4i	m	0.976	0.35536(5)	0	0.12546(5)
Mn1		4i	m	0.024	0.35536(5)	0	0.12546(5)
Sb2		4i	m		0.72640(6)	-1.00000	0.36659(5)
Mn3		2a	2/m	0.721	1/2	-1/2	0
Sb3		2a	2/m	0.279	1/2	-1/2	0
Mn4		2d	2/m		1/2	-1.00000	1/2
Se1		4i	m		0.61423(7)	-1/2	0.45758(7)
Se2		4i	m		0.51242(8)	-1/2	0.17998(8)
Se3		4i	m		0.84441(8)	-1.50000	0.32763(7)
Se4		4i	m		0.15481(8)	-1/2	0.05320(7)

Selected geometric informations			
Atoms 1,2	**d 1,2 [Å]**	**Atoms 1,2**	**d 1,2 [Å]**
Sb1|Mn1—Se4^{i}	2.6655(13)	Mn4—Se3^{viii}	2.5490(14)
Sb1|Mn1—Se2	2.7162(10)	Mn4—Se3^{ix}	2.5490(14)
Sb1|Mn1—Se2^{ii}	2.7162(10)	Mn4—Se1	2.7167(7)
Sb2—Se1^{iii}	2.6032(15)	Mn4—Se1^{x}	2.7167(7)
Sb2—Se3	2.7246(9)	Mn4—Se1^{xi}	2.7167(7)
Sb2—Se3^{ii}	2.7246(9)	Mn4—Se1^{xii}	2.7167(7)
Mn3|Sb3—Se2^{iv}	2.6743(12)	Se1—Sb2^{iii}	2.6032(16)
Mn3|Sb3—Se2	2.6743(12)	Se1—Mn4^{ii}	2.7167(7)
Mn3|Sb3—Se4^{v}	2.6981(8)	Se2—Sb1|Mn1^{xii}	2.7162(10)
Mn3|Sb3—Se4^{vi}	2.6981(8)	Se2—Sb1|Mn1^{xii}	2.7162(10)
Mn3|Sb3—Se4^{i}	2.6981(8)	Se3—Mn4^{vii}	2.5489(14)
Mn3|Sb3—Se4^{vii}	2.6981(8)	Se3—Sb2^{xii}	2.7246(9)

Mn3|Sb3—Se2^{iv}	2.6743(12)	Se4—Sb1|Mn1^{i}	2.6655(13)
Mn3|Sb3—Se2	2.6743(12)	Se4—Sb1|Mn1^{i}	2.6655(13)
Mn3|Sb3—Se4^{v}	2.6981(8)	Se4—Mn3|Sb3^{xiii}	2.6982(8)
Mn3|Sb3—Se4^{vi}	2.6981(8)	Se4—Mn3|Sb3^{xiii}	2.6982(8)
Mn3|Sb3—Se4^{i}	2.6981(8)	Se4—Mn3|Sb3^{ix}	2.6982(8)
Mn3|Sb3—Se4^{vii}	2.6981(8)	Se4—Mn3|Sb3^{ix}	2.6982(8)

Atoms 1,2,3	Angle 1,2,3 [°]	Atoms 1,2,3	Angle 1,2,3 [°]
Se4^{i}—Sb1|Mn1—Se2	90.93(4)	Se1—Mn4—Se1^{x}	180.000
Se4^{i}—Sb1|Mn1—Se2^{ii}	90.93(4)	Se3^{viii}—Mn4—Se1^{xi}	91.98(3)
Se2—Sb1|Mn1—Se2^{ii}	93.58(4)	Se3^{ix}—Mn4—Se1^{xi}	88.02(3)
Se1^{iii}—Sb2—Se3	86.77(3)	Se1—Mn4—Se1^{xi}	86.44(3)
Se1^{iii}—Sb2—Se3^{ii}	86.77(3)	Se1^{x}—Mn4—Se1^{xi}	93.56(3)
Se3—Sb2—Se3^{ii}	93.21(4)	Se3^{viii}—Mn4—Se1^{xii}	88.02(3)
Se2^{iv}—Mn3|Sb3—Se2	180.000	Se3^{ix}—Mn4—Se1^{xii}	91.98(3)
Se2^{iv}—Mn3|Sb3—Se4^{v}	88.86(3)	Se1—Mn4—Se1^{xii}	93.56(3)
Se2—Mn3|Sb3—Se4^{v}	91.14(3)	Se1^{x}—Mn4—Se1^{xii}	86.44(3)
Se2^{iv}—Mn3|Sb3—Se4^{vi}	91.14(3)	Se1^{xi}—Mn4—Se1^{xii}	180.00(4)
Se2—Mn3|Sb3—Se4^{vi}	88.86(3)	Sb2^{iii}—Se1—Mn4	92.10(3)
Se4^{v}—Mn3|Sb3—Se4^{vi}	180.000	Sb2^{iii}—Se1—Mn4^{ii}	92.10(3)
Se2^{iv}—Mn3|Sb3—Se4^{i}	88.86(3)	Mn4—Se1—Mn4^{ii}	93.56(3)
Se2—Mn3|Sb3—Se4^{i}	91.14(3)	Mn3|Sb3—Se2—Mn3|Sb3	0.000
Se4^{v}—Mn3|Sb3—Se4^{i}	94.40(4)	Mn3|Sb3—Se2—Sb1|Mn1	88.68(4)
Se4^{vi}—Mn3|Sb3—Se4^{i}	85.60(4)	Mn3|Sb3—Se2—Sb1|Mn1	88.68(4)
Se2^{iv}—Mn3|Sb3—Se4^{vii}	91.14(3)	Mn3|Sb3—Se2—Sb1|Mn1^{xii}	88.68(4)
Se2—Mn3|Sb3—Se4^{vii}	88.86(3)	Mn3|Sb3—Se2—Sb1|Mn1^{xii}	88.68(4)
Se4^{v}—Mn3|Sb3—Se4^{vii}	85.60(4)	Sb1|Mn1—Se2—Sb1|Mn1^{xii}	93.58(4)
Se4^{vi}—Mn3|Sb3—Se4^{vii}	94.40(4)	Mn3|Sb3—Se2—Sb1|Mn1^{xii}	88.68(4)
Se4^{i}—Mn3|Sb3—Se4^{vii}	180.00(4)	Mn3|Sb3—Se2—Sb1|Mn1^{xii}	88.68(4)
Se2^{iv}—Mn3|Sb3—Se2	180.000	Sb1|Mn1—Se2—Sb1|Mn1^{xii}	93.58(4)
Se2^{iv}—Mn3|Sb3—Se4^{v}	88.86(3)	Sb1|Mn1^{xii}—Se2—Sb1|Mn1^{xii}	0.00(3)

Se2—Mn3|Sb3—Se4^{v}	91.14(3)	Mn4^{vii}—Se3—Sb2^{xii}	93.11(3)
Se2^{iv}—Mn3|Sb3—Se4^{vi}	91.14(3)	Mn4^{vii}—Se3—Sb2	93.11(3)
Se2—Mn3|Sb3—Se4^{vi}	88.86(3)	Sb2^{xii}—Se3—Sb2	93.21(4)
Se4^{v}—Mn3|Sb3—Se4^{vi}	180.000	Sb1|Mn1^{i}—Se4—Sb1|Mn1^{i}	0.00(3)
Se2^{iv}—Mn3|Sb3—Se4^{i}	88.86(3)	Sb1|Mn1^{i}—Se4—Mn3|Sb3^{xiii}	89.25(3)
Se2—Mn3|Sb3—Se4^{i}	91.14(3)	Sb1|Mn1^{i}—Se4—Mn3|Sb3^{xiii}	89.25(3)
Se4^{v}—Mn3|Sb3—Se4^{i}	94.40(4)	Sb1|Mn1^{i}—Se4—Mn3|Sb3^{xiii}	89.25(3)
Se4^{vi}—Mn3|Sb3—Se4^{i}	85.60(4)	Sb1|Mn1^{i}—Se4—Mn3|Sb3^{xiii}	89.25(3)
Se2^{iv}—Mn3|Sb3—Se4^{vii}	91.14(3)	Mn3|Sb3^{xiii}—Se4—Mn3|Sb3^{xiii}	0.000
Se2—Mn3|Sb3—Se4^{vii}	88.86(3)	Sb1|Mn1^{i}—Se4—Mn3|Sb3^{ix}	89.25(3)
Se4^{v}—Mn3|Sb3—Se4^{vii}	85.60(4)	Sb1|Mn1^{i}—Se4—Mn3|Sb3^{ix}	89.25(3)
Se4^{vi}—Mn3|Sb3—Se4^{vii}	94.40(4)	Mn3|Sb3^{xiii}—Se4—Mn3|Sb3^{ix}	94.40(4)
Se4^{i}—Mn3|Sb3—Se4^{vii}	180.00(4)	Mn3|Sb3^{xiii}—Se4—Mn3|Sb3^{ix}	94.40(4)
Se3^{viii}—Mn4—Se3^{ix}	180.000	Sb1|Mn1^{i}—Se4—Mn3|Sb3^{ix}	89.25(3)
Se3^{viii}—Mn4—Se1	88.02(3)	Sb1|Mn1^{i}—Se4—Mn3|Sb3^{ix}	89.25(3)
Se3^{ix}—Mn4—Se1	91.98(3)	Mn3|Sb3^{xiii}—Se4—Mn3|Sb3^{ix}	94.40(4)
Se3^{viii}—Mn4—Se1^{x}	91.98(3)	Mn3|Sb3^{xiii}—Se4—Mn3|Sb3^{ix}	94.40(4)
Se3^{ix}—Mn4—Se1^{x}	88.02(3)	Mn3|Sb3^{ix}—Se4—Mn3|Sb3^{ix}	0.000

(i) 0.5-x, -0.5-y, -z; (ii) x, 1+y, z; (iii) 1.5-x, -1.5-y, 1-z; (iv) 1-x, -1-y, -z;
(v) 0.5-x, -1.5-y, -z; (vi) 0.5+x, 0.5+y, z; (vii) 0.5+x, -0.5+y, z; (viii) 1.5-x, -2.5-y, 1-z;
(ix) -0.5+x, 0.5+y, z; (x) 1-x, -2-y, 1-z; (xi) 1-x, -1-y, 1-z; (xii) x, -1+y, z;
(xiii) -0.5+x, -0.5+y, z.

Annex II: $FeSb_2Se_4$ at 120K

Atomic parameters

Atom	Ox.	Wyck.	Site	S.O.F.	x/a	y/b	z/c	U [Å^2]
Sb1		4i	m	0.9652	0.27368(3)	0	0.63363(3)	
Fe1		4i	m	0.0348	0.27368(3)	0	0.63363(3)	
Sb2		4i	m	0.963	0.35481(3)	0	0.12565(3)	
Fe2		4i	m	0.037	0.35481(3)	0	0.12565(3)	
Fe3		2d	2/m		0	1/2	1/2	

Sb4	2a	2/m	0.143	0	0	0
Fe4	2a	2/m	0.857	0	0	0
Se1	4i	m		0.01185(4)	0	0.18002(4)
Se2	4i	m		0.11446(4)	0	0.45789(4)
Se3	4i	m		0.34477(4)	0	0.32759(4)
Se4	4i	m		0.65467(4)	0	0.05346(4

Selected geometric informations			
Atoms 1,2	**d 1,2 [Å]**	**Atoms 1,2**	**d 1,2 [Å]**
Sb1|Fe1—Se2	2.5846(7)	Fe4|Sb4—Sb2|Fe2^{viii}	3.7841(3)
Sb1|Fe1—Se3^{i}	2.7262(4)	Fe4|Sb4—Sb2|Fe2^{viii}	3.7841(3)
Sb1|Fe1—Se3^{ii}	2.7262(4)	Se1—Sb2|Fe2^{vii}	2.7031(4)
Sb1|Fe1—Se2^{ii}	3.1232(5)	Se1—Sb2|Fe2^{vii}	2.7031(4)
Sb1|Fe1—Se2^{i}	3.1232(5)	Se1—Sb2|Fe2^{viii}	2.7031(4)
Sb1|Fe1—Se1^{ii}	3.5941(6)	Se1—Sb2|Fe2^{viii}	2.7031(4)
Sb1|Fe1—Se1^{i}	3.5941(6)	Se1—Sb1|Fe1^{ii}	3.5941(6)
Sb1|Fe1—Fe3^{iii}	3.8031(4)	Se1—Sb1|Fe1^{ii}	3.5941(6)
Sb2|Fe2—Se4^{iv}	2.6859(6)	Se2—Fe3^{iii}	2.7161(3)
Sb2|Fe2—Se1^{v}	2.7031(4)	Se2—Sb1|Fe1^{ii}	3.1231(5)
Sb2|Fe2—Se1^{vi}	2.7031(4)	Se2—Sb1|Fe1^{i}	3.1231(5)
Sb2|Fe2—Se4^{vii}	3.0697(5)	Se2—Sb1|Fe1^{ii}	3.1231(5)
Sb2|Fe2—Se4^{viii}	3.0697(5)	Se2—Sb1|Fe1^{i}	3.1231(5)
Sb2|Fe2—Se3	3.1449(6)	Se3—Fe3^{vi}	2.5311(6)
Sb2|Fe2—Fe4|Sb4^{v}	3.7842(4)	Se3—Sb1|Fe1^{i}	2.7263(4)
Sb2|Fe2—Fe4|Sb4^{vi}	3.7842(4)	Se3—Sb1|Fe1^{i}	2.7263(4)
Fe3—Se3^{ii}	2.5311(6)	Se3—Sb1|Fe1^{ii}	2.7263(4)
Fe3—Se3^{viii}	2.5311(6)	Se3—Sb1|Fe1^{ii}	2.7263(4)
Fe3—Se2	2.7161(3)	Se3—Se2^{ii}	3.6647(6)
Fe3—Se2^{ix}	2.7161(3)	Se4—Fe4|Sb4^{vi}	2.6843(4)
Fe3—Se2^{x}	2.7161(3)	Se4—Fe4|Sb4^{vi}	2.6843(4)
Fe3—Se2^{xi}	2.7161(3)	Se4—Fe4|Sb4^{v}	2.6843(4)
Fe4|Sb4—Se4^{xii}	2.6843(4)	Se4—Fe4|Sb4^{v}	2.6843(4)
Fe4|Sb4—Se4^{viii}	2.6843(4)	Se4—Sb2|Fe2^{iv}	2.6858(6)
Fe4|Sb4—Se4^{xiii}	2.6843(4)	Se4—Sb2|Fe2^{iv}	2.6858(6)
Fe4|Sb4—Se4^{vii}	2.6843(4)	Se4—Sb2|Fe2^{v}	3.0697(5)
Fe4|Sb4—Se1^{xiv}	2.6878(6)	Se4—Sb2|Fe2^{v}	3.0697(5)
Fe4|Sb4—Se1	2.6878(6)		
Atoms 1,2,3	**Angle 1,2,3 [°]**	**Atoms 1,2,3**	**Angle 1,2,3 [°]**
Se2—Sb1|Fe1—Se3^{i}	87.223(16)	Se4^{xii}—Fe4|Sb4—Sb2|Fe2^{viii}	93.75(1)
Se2—Sb1|Fe1—Se3^{ii}	87.223(16)	Se4^{viii}—Fe4|Sb4—Sb2|Fe2^{viii}	86.25(1)
Se3^{i}—Sb1|Fe1—Se3^{ii}	92.99(2)	Se4^{xiii}—Fe4|Sb4—Sb2|Fe2^{viii}	45.215(12)
Se2—Sb1|Fe1—Se2^{ii}	81.620(15)	Se4^{vii}—Fe4|Sb4—Sb2|Fe2^{viii}	134.785(12)
Se3^{i}—Sb1|Fe1—Se2^{ii}	166.956(19)	Se1^{xiv}—Fe4|Sb4—Sb2|Fe2^{viii}	134.418(10)

Se3^{ii}—Sb1|Fe1—Se2^{ii}	93.198(11)	Se1—Fe4|Sb4—Sb2|Fe2^{viii}	45.581(10)
Se2—Sb1|Fe1—Se2^{i}	81.620(15)	Sb2|Fe2^{viii}—Fe4|Sb4—Sb2|Fe2^{viii}	0.000(9)
Se3^{i}—Sb1|Fe1—Se2^{i}	93.198(11)	Fe4|Sb4—Se1—Sb2|Fe2^{vii}	89.167(18)
Se3^{ii}—Sb1|Fe1—Se2^{i}	166.956(19)	Fe4|Sb4—Se1—Sb2|Fe2^{vii}	89.167(18)
Se2^{ii}—Sb1|Fe1—Se2^{i}	78.562(15)	Sb2|Fe2^{vii}—Se1—Sb2|Fe2^{vii}	0.000(12)
Se2—Sb1|Fe1—Se1^{ii}	145.142(9)	Fe4|Sb4—Se1—Sb2|Fe2^{viii}	89.167(17)
Se3^{i}—Sb1|Fe1—Se1^{ii}	123.034(19)	Sb2|Fe2^{vii}—Se1—Sb2|Fe2^{viii}	94.03(2)
Se3^{ii}—Sb1|Fe1—Se1^{ii}	75.349(14)	Sb2|Fe2^{vii}—Se1—Sb2|Fe2^{viii}	94.03(2)
Se2^{ii}—Sb1|Fe1—Se1^{ii}	69.729(13)	Fe4|Sb4—Se1—Sb2|Fe2^{viii}	89.167(17)
Se2^{i}—Sb1|Fe1—Se1^{ii}	110.498(15)	Sb2|Fe2^{vii}—Se1—Sb2|Fe2^{viii}	94.03(2)
Se2—Sb1|Fe1—Se1^{i}	145.142(9)	Sb2|Fe2^{vii}—Se1—Sb2|Fe2^{viii}	94.03(2)
Se3^{i}—Sb1|Fe1—Se1^{i}	75.349(14)	Sb2|Fe2^{viii}—Se1—Sb2|Fe2^{viii}	0.000(12)
Se3^{ii}—Sb1|Fe1—Se1^{i}	123.034(19)	Fe4|Sb4—Se1—Sb1|Fe1^{ii}	119.399(16)
Se2^{ii}—Sb1|Fe1—Se1^{i}	110.498(15)	Sb2|Fe2^{vii}—Se1—Sb1|Fe1^{ii}	150.47(2)
Se2^{i}—Sb1|Fe1—Se1^{i}	69.729(13)	Sb2|Fe2^{vii}—Se1—Sb1|Fe1^{ii}	150.47(2)
Se1^{ii}—Sb1|Fe1—Se1^{i}	66.756(13)	Sb2|Fe2^{viii}—Se1—Sb1|Fe1^{ii}	93.737(12)
Se2—Sb1|Fe1—Fe3^{iii}	45.552(10)	Sb2|Fe2^{viii}—Se1—Sb1|Fe1^{ii}	93.737(12)
Se3^{i}—Sb1|Fe1—Fe3^{iii}	41.671(12)	Fe4|Sb4—Se1—Sb1|Fe1^{ii}	119.399(16)
Se3^{ii}—Sb1|Fe1—Fe3^{iii}	90.415(13)	Sb2|Fe2^{vii}—Se1—Sb1|Fe1^{ii}	150.47(2)
Se2^{ii}—Sb1|Fe1—Fe3^{iii}	126.799(15)	Sb2|Fe2^{vii}—Se1—Sb1|Fe1^{ii}	150.47(2)
Se2^{i}—Sb1|Fe1—Fe3^{iii}	86.598(9)	Sb2|Fe2^{viii}—Se1—Sb1|Fe1^{ii}	93.737(12)
Se1^{ii}—Sb1|Fe1—Fe3^{iii}	159.458(15)	Sb2|Fe2^{viii}—Se1—Sb1|Fe1^{ii}	93.737(12)
Se1^{i}—Sb1|Fe1—Fe3^{iii}	111.366(10)	Sb1|Fe1^{ii}—Se1—Sb1|Fe1^{ii}	0.000(11)
Se4^{iv}—Sb2|Fe2—Se1^{v}	90.429(18)	Sb1|Fe1—Se2—Fe3^{iii}	91.659(15)
Se4^{iv}—Sb2|Fe2—Se1^{vi}	90.429(18)	Sb1|Fe1—Se2—Fe3	91.659(15)
Se1^{v}—Sb2|Fe2—Se1^{vi}	94.03(2)	Fe3^{iii}—Se2—Fe3	93.439(15)
Se4^{iv}—Sb2|Fe2—Se4^{vii}	88.692(17)	Sb1|Fe1—Se2—Sb1|Fe1^{ii}	98.380(15)
Se1^{v}—Sb2|Fe2—Se4^{vii}	173.045(13)	Fe3^{iii}—Se2—Sb1|Fe1^{ii}	167.799(19)
Se1^{vi}—Sb2|Fe2—Se4^{vii}	92.879(12)	Fe3—Se2—Sb1|Fe1^{ii}	93.185(6)
Se4^{iv}—Sb2|Fe2—Se4^{viii}	88.692(17)	Sb1|Fe1—Se2—Sb1|Fe1^{i}	98.380(15)
Se1^{v}—Sb2|Fe2—Se4^{viii}	92.879(12)	Fe3^{iii}—Se2—Sb1|Fe1^{i}	93.185(6)
Se1^{vi}—Sb2|Fe2—Se4^{viii}	173.045(13)	Fe3—Se2—Sb1|Fe1^{i}	167.799(19)
Se4^{vii}—Sb2|Fe2—Se4^{viii}	80.204(15)	Sb1|Fe1^{ii}—Se2—Sb1|Fe1^{i}	78.563(15)
Se4^{iv}—Sb2|Fe2—Se3	175.48(2)	Sb1|Fe1—Se2—Sb1|Fe1^{ii}	98.380(15)
Se1^{v}—Sb2|Fe2—Se3	92.652(18)	Fe3^{iii}—Se2—Sb1|Fe1^{ii}	167.799(19)
Se1^{vi}—Sb2|Fe2—Se3	92.652(17)	Fe3—Se2—Sb1|Fe1^{ii}	93.185(6)
Se4^{vii}—Sb2|Fe2—Se3	87.850(17)	Sb1|Fe1^{ii}—Se2—Sb1|Fe1^{ii}	0.000(11)
Se4^{viii}—Sb2|Fe2—Se3	87.850(16)	Sb1|Fe1^{i}—Se2—Sb1|Fe1^{ii}	78.563(15)
Se4^{iv}—Sb2|Fe2—Fe4|Sb4^{v}	45.18(1)	Sb1|Fe1—Se2—Sb1|Fe1^{i}	98.380(15)
Se1^{v}—Sb2|Fe2—Fe4|Sb4^{v}	45.251(13)	Fe3^{iii}—Se2—Sb1|Fe1^{i}	93.185(6)
Se1^{vi}—Sb2|Fe2—Fe4|Sb4^{v}	93.467(14)	Fe3—Se2—Sb1|Fe1^{i}	167.799(19)
Se4^{vii}—Sb2|Fe2—Fe4|Sb4^{v}	133.413(15)	Sb1|Fe1^{ii}—Se2—Sb1|Fe1^{i}	78.563(15)
Se4^{viii}—Sb2|Fe2—Fe4|Sb4^{v}	90.806(10)	Sb1|Fe1^{i}—Se2—Sb1|Fe1^{i}	0.000(11)
Se3—Sb2|Fe2—Fe4|Sb4^{v}	137.774(10)	Sb1|Fe1^{ii}—Se2—Sb1|Fe1^{i}	78.563(15)

Se4^{iv}—Sb2|Fe2—Fe4|Sb4^{vi}	45.18(1)	Fe3^{vi}—Se3—Sb1|Fe1^{i}	92.594(16)
Se1^{v}—Sb2|Fe2—Fe4|Sb4^{vi}	93.467(14)	Fe3^{vi}—Se3—Sb1|Fe1^{i}	92.594(16)
Se1^{vi}—Sb2|Fe2—Fe4|Sb4^{vi}	45.251(13)	Sb1|Fe1^{i}—Se3—Sb1|Fe1^{i}	0.000(12)
Se4^{vii}—Sb2|Fe2—Fe4|Sb4^{vi}	90.806(10)	Fe3^{vi}—Se3—Sb1|Fe1^{ii}	92.593(16)
Se4^{viii}—Sb2|Fe2—Fe4|Sb4^{vi}	133.413(15)	Sb1|Fe1^{i}—Se3—Sb1|Fe1^{ii}	92.986(19)
Se3—Sb2|Fe2—Fe4|Sb4^{vi}	137.774(10)	Sb1|Fe1^{i}—Se3—Sb1|Fe1^{ii}	92.986(19)
Fe4|Sb4^{v}—Sb2|Fe2—Fe4|Sb4^{vi}	63.005(7)	Fe3^{vi}—Se3—Sb1|Fe1^{ii}	92.593(16)
Se3^{ii}—Fe3—Se3^{viii}	180.000	Sb1|Fe1^{i}—Se3—Sb1|Fe1^{ii}	92.986(19)
Se3^{ii}—Fe3—Se2	88.524(13)	Sb1|Fe1^{i}—Se3—Sb1|Fe1^{ii}	92.986(19)
Se3^{viii}—Fe3—Se2	91.476(13)	Sb1|Fe1^{ii}—Se3—Sb1|Fe1^{ii}	0.000(16)
Se3^{ii}—Fe3—Se2^{ix}	91.476(13)	Fe3^{vi}—Se3—Sb2|Fe2	131.85(2)
Se3^{viii}—Fe3—Se2^{ix}	88.524(13)	Sb1|Fe1^{i}—Se3—Sb2|Fe2	118.788(16)
Se2—Fe3—Se2^{ix}	86.561(15)	Sb1|Fe1^{i}—Se3—Sb2|Fe2	118.788(16)
Se3^{ii}—Fe3—Se2^{x}	88.524(13)	Sb1|Fe1^{ii}—Se3—Sb2|Fe2	118.788(16)
Se3^{viii}—Fe3—Se2^{x}	91.476(13)	Sb1|Fe1^{ii}—Se3—Sb2|Fe2	118.788(16)
Se2—Fe3—Se2^{x}	93.439(15)	Fe3^{vi}—Se3—Se2^{ii}	47.81(1)
Se2^{ix}—Fe3—Se2^{x}	180.000	Sb1|Fe1^{i}—Se3—Se2^{ii}	94.182(17)
Se3^{ii}—Fe3—Se2^{xi}	91.476(13)	Sb1|Fe1^{i}—Se3—Se2^{ii}	94.182(17)
Se3^{viii}—Fe3—Se2^{xi}	88.524(13)	Sb1|Fe1^{ii}—Se3—Se2^{ii}	44.784(13)
Se2—Fe3—Se2^{xi}	180.000(16)	Sb1|Fe1^{ii}—Se3—Se2^{ii}	44.784(13)
Se2^{ix}—Fe3—Se2^{xi}	93.438(15)	Sb2|Fe2—Se3—Se2^{ii}	145.720(8)
Se2^{x}—Fe3—Se2^{xi}	86.562(15)	Fe4|Sb4^{vi}—Se4—Fe4|Sb4^{vi}	0.000
Se3^{ii}—Fe3—Sb1|Fe1	45.734(11)	Fe4|Sb4^{vi}—Se4—Fe4|Sb4^{v}	94.892(16)
Se3^{viii}—Fe3—Sb1|Fe1	134.266(11)	Fe4|Sb4^{vi}—Se4—Fe4|Sb4^{v}	94.892(16)
Se2—Fe3—Sb1|Fe1	42.790(12)	Fe4|Sb4^{vi}—Se4—Fe4|Sb4^{v}	94.892(16)
Se2^{ix}—Fe3—Sb1|Fe1	88.672(10)	Fe4|Sb4^{vi}—Se4—Fe4|Sb4^{v}	94.892(16)
Se2^{x}—Fe3—Sb1|Fe1	91.328(10)	Fe4|Sb4^{v}—Se4—Fe4|Sb4^{v}	0.000
Se2^{xi}—Fe3—Sb1|Fe1	137.210(12)	Fe4|Sb4^{vi}—Se4—Sb2|Fe2^{iv}	89.605(16)
Se4^{xii}—Fe4|Sb4—Se4^{viii}	180.000(18)	Fe4|Sb4^{vi}—Se4—Sb2|Fe2^{iv}	89.605(16)
Se4^{xii}—Fe4|Sb4—Se4^{xiii}	94.893(16)	Fe4|Sb4^{v}—Se4—Sb2|Fe2^{iv}	89.605(16)
Se4^{viii}—Fe4|Sb4—Se4^{xiii}	85.107(16)	Fe4|Sb4^{v}—Se4—Sb2|Fe2^{iv}	89.605(16)
Se4^{xii}—Fe4|Sb4—Se4^{vii}	85.107(16)	Fe4|Sb4^{vi}—Se4—Sb2|Fe2^{iv}	89.605(16)
Se4^{viii}—Fe4|Sb4—Se4^{vii}	94.893(16)	Fe4|Sb4^{vi}—Se4—Sb2|Fe2^{iv}	89.605(16)
Se4^{xiii}—Fe4|Sb4—Se4^{vii}	180.00(2)	Fe4|Sb4^{v}—Se4—Sb2|Fe2^{iv}	89.605(16)
Se4^{xii}—Fe4|Sb4—Se1^{xiv}	89.205(15)	Fe4|Sb4^{v}—Se4—Sb2|Fe2^{iv}	89.605(16)
Se4^{viii}—Fe4|Sb4—Se1^{xiv}	90.795(15)	Sb2|Fe2^{iv}—Se4—Sb2|Fe2^{iv}	0.000(14)
Se4^{xiii}—Fe4|Sb4—Se1^{xiv}	89.205(15)	Fe4|Sb4^{vi}—Se4—Sb2|Fe2^{v}	172.611(14)
Se4^{vii}—Fe4|Sb4—Se1^{xiv}	90.795(15)	Fe4|Sb4^{vi}—Se4—Sb2|Fe2^{v}	172.611(14)
Se4^{xii}—Fe4|Sb4—Se1	90.795(15)	Fe4|Sb4^{v}—Se4—Sb2|Fe2^{v}	92.446(7)
Se4^{viii}—Fe4|Sb4—Se1	89.205(15)	Fe4|Sb4^{v}—Se4—Sb2|Fe2^{v}	92.446(7)
Se4^{xiii}—Fe4|Sb4—Se1	90.795(15)	Sb2|Fe2^{iv}—Se4—Sb2|Fe2^{v}	91.308(17)
Se4^{vii}—Fe4|Sb4—Se1	89.205(15)	Sb2|Fe2^{iv}—Se4—Sb2|Fe2^{v}	91.308(17)
Se1^{xiv}—Fe4|Sb4—Se1	180.000	Fe4|Sb4^{vi}—Se4—Sb2|Fe2^{v}	172.611(14)
Se4^{xii}—Fe4|Sb4—Sb2|Fe2^{viii}	93.75(1)	Fe4|Sb4^{vi}—Se4—Sb2|Fe2^{v}	172.611(14)

Se4^{viii}—Fe4|Sb4—Sb2|Fe2^{viii}	86.25(1)	Fe4|Sb4^{v}—Se4—Sb2|Fe2^{v}	92.446(7)
Se4^{xiii}—Fe4|Sb4—Sb2|Fe2^{viii}	45.215(12)	Fe4|Sb4^{v}—Se4—Sb2|Fe2^{v}	92.446(7)
Se4^{vii}—Fe4|Sb4—Sb2|Fe2^{viii}	134.785(12)	Sb2|Fe2^{iv}—Se4—Sb2|Fe2^{v}	91.308(17)
Se1^{xiv}—Fe4|Sb4—Sb2|Fe2^{viii}	134.418(10)	Sb2|Fe2^{iv}—Se4—Sb2|Fe2^{v}	91.308(17)
Se1—Fe4|Sb4—Sb2|Fe2^{viii}	45.581(10)	Sb2|Fe2^{v}—Se4—Sb2|Fe2^{v}	0.00(1)

(i) 0.5-x, -0.5-y, 1-z; (ii) 0.5-x, 0.5-y, 1-z; (iii) x, -1+y, z; (iv) 1-x, -y, -z;
(v) 0.5+x, 0.5+y, z; (vi) 0.5+x, -0.5+y, z; (vii) -0.5+x, -0.5+y, z; (viii) -0.5+x, 0.5+y, z;
(ix) -x, -y, 1-z; (x) x, 1+y, z; (xi) -x, 1-y, 1-z; (xii) 0.5-x, -0.5-y, -z;
(xiii) 0.5-x, 0.5-y, -z; (xiv) -x, -y, -z.

Annex III : FeSb2Se4 (300K)

Atomic parameters							
Atom		**Ox.**	**Wyck.**	**Site**	**S.O.F.**	**x/a**	**y/b**	**z/c**
Sb1	3	4i	m	0.9581	0.27358(5)	0	0.63349(5)	
Fe1	2	4i	m	0.0419	0.27358(5)	0	0.63349(5)	
Sb2	3	4i	m	0.964	0.35477(6)	0	0.12596(5)	
Fe2	2	4i	m	0.036	0.35477(6)	0	0.12596(5)	
Fe3	2	2d	2/m		0	1/2	1/2	
Sb3	3	2a	2/m	0.157	0	0	0	
Fe4	2	2a	2/m	0.843	0	0	0	
Se1	-2	4i	m		0.01165(8)	0	0.18038(7)	
Se2	-2	4i	m		0.11446(7)	0	0.45747(6)	
Se3	-2	4i	m		0.34488(8)	0	0.32747(7)	
Se4	-2	4i	m		0.65512(7)	0	0.05397(7)	

Selected geometric informations			
Atoms 1,2	**d 1,2 [Å]**	**Atoms 1,2**	**d 1,2 [Å]**
Sb1|Fe1—Se2	2.6032(15)	Fe4|Sb4—Se4^{vii}	2.7041(8)
Sb1|Fe1—Se3^{i}	2.7312(9)	Fe4|Sb4—Sb2|Fe2^{xiv}	3.7772(9)
Sb1|Fe1—Se3^{ii}	2.7312(9)	Fe4|Sb4—Sb2|Fe2^{viii}	3.7772(9)
Sb1|Fe1—Se2^{ii}	3.1134(10)	Se1—Sb2|Fe2^{vii}	2.7183(9)
Sb1|Fe1—Se2^{i}	3.1134(10)	Se1—Sb2|Fe2^{vii}	2.7183(9)
Sb1|Fe1—Se1^{ii}	3.6198(14)	Se1—Sb2|Fe2^{viii}	2.7183(9)
Sb1|Fe1—Se1^{i}	3.6198(14)	Se1—Sb2|Fe2^{viii}	2.7183(9)
Sb1|Fe1—Fe3^{iii}	3.8346(12)	Se1—Sb1|Fe1^{ii}	3.6197(14)
Sb2|Fe2—Se4^{iv}	2.6813(13)	Se1—Sb1|Fe1^{ii}	3.6197(14)

Sb2|Fe2—Se1^{v}	2.7183(9)	Se2—Fe3^{iii}	2.7214(7)
Sb2|Fe2—Se1^{vi}	2.7183(9)	Se2—Sb1|Fe1^{ii}	3.1134(10)
Sb2|Fe2—Se4^{vii}	3.0867(10)	Se2—Sb1|Fe1^{ii}	3.1134(10)
Sb2|Fe2—Se4^{viii}	3.0867(10)	Se2—Sb1|Fe1^{i}	3.1134(10)
Sb2|Fe2—Se3	3.1181(12)	Se2—Sb1|Fe1^{i}	3.1134(10)
Sb2|Fe2—Fe4|Sb4^{v}	3.7772(9)	Se3—Fe3^{vi}	2.5475(14)
Sb2|Fe2—Fe4|Sb4^{vi}	3.7772(9)	Se3—Sb1|Fe1^{i}	2.7311(9)
Fe3—Se3^{ii}	2.5475(14)	Se3—Sb1|Fe1^{i}	2.7311(9)
Fe3—Se3^{viii}	2.5475(14)	Se3—Sb1|Fe1^{ii}	2.7311(9)
Fe3—Se2^{ix}	2.7214(7)	Se3—Sb1|Fe1^{ii}	2.7311(9)
Fe3—Se2^{x}	2.7214(7)	Se3—Se2^{ii}	3.6638(12)
Fe3—Se2^{xi}	2.7214(7)	Se4—Sb2|Fe2^{iv}	2.6813(13)
Fe3—Se2	2.7214(7)	Se4—Sb2|Fe2^{iv}	2.6813(13)
Fe3—Sb1|Fe1^{ix}	3.8346(12)	Se4—Fe4|Sb4^{vi}	2.7041(8)
Fe3—Sb1|Fe1^{x}	3.8346(12)	Se4—Fe4|Sb4^{vi}	2.7041(8)
Fe4|Sb4—Se1^{xii}	2.6794(12)	Se4—Fe4|Sb4^{v}	2.7041(8)
Fe4|Sb4—Se1	2.6795(12)	Se4—Fe4|Sb4^{v}	2.7041(8)
Fe4|Sb4—Se4^{xiii}	2.7041(8)	Se4—Sb2|Fe2^{v}	3.0867(10)
Fe4|Sb4—Se4^{viii}	2.7041(8)	Se4—Sb2|Fe2^{v}	3.0867(10)
Fe4|Sb4—Se4^{xiv}	2.7041(8)		

Atoms 1,2,3	Angle 1,2,3 [°]	Atoms 1,2,3	Angle 1,2,3 [°]
Se2—Sb1|Fe1—Se3^{i}	86.73(3)	Se4^{viii}—Fe4|Sb4—Sb2|Fe2^{xiv}	45.22(2)
Se2—Sb1|Fe1—Se3^{ii}	86.73(3)	Se4^{xiv}—Fe4|Sb4—Sb2|Fe2^{xiv}	86.22(2)
Se3^{i}—Sb1|Fe1—Se3^{ii}	93.15(4)	Se4^{vii}—Fe4|Sb4—Sb2|Fe2^{xiv}	93.78(2)
Se2—Sb1|Fe1—Se2^{ii}	82.26(3)	Se1^{xii}—Fe4|Sb4—Sb2|Fe2^{viii}	133.99(2)
Se3^{i}—Sb1|Fe1—Se2^{ii}	167.14(3)	Se1—Fe4|Sb4—Sb2|Fe2^{viii}	46.01(2)
Se3^{ii}—Sb1|Fe1—Se2^{ii}	92.84(3)	Se4^{xiii}—Fe4|Sb4—Sb2|Fe2^{viii}	93.78(2)
Se2—Sb1|Fe1—Se2^{i}	82.26(3)	Se4^{viii}—Fe4|Sb4—Sb2|Fe2^{viii}	86.22(2)
Se3^{i}—Sb1|Fe1—Se2^{i}	92.84(3)	Se4^{xiv}—Fe4|Sb4—Sb2|Fe2^{viii}	45.22(2)
Se3^{ii}—Sb1|Fe1—Se2^{i}	167.14(3)	Se4^{vii}—Fe4|Sb4—Sb2|Fe2^{viii}	134.78(2)
Se2^{ii}—Sb1|Fe1—Se2^{i}	79.15(3)	Sb2|Fe2^{xiv}—Fe4|Sb4—Sb2|Fe2^{viii}	116.645(19)
Se2—Sb1|Fe1—Se1^{ii}	145.261(19)	Fe4|Sb4—Se1—Sb2|Fe2^{vii}	88.81(4)
Se3^{i}—Sb1|Fe1—Se1^{ii}	123.50(3)	Fe4|Sb4—Se1—Sb2|Fe2^{vii}	88.81(4)
Se3^{ii}—Sb1|Fe1—Se1^{ii}	75.88(3)	Sb2|Fe2^{vii}—Se1—Sb2|Fe2^{vii}	0.00(5)
Se2^{ii}—Sb1|Fe1—Se1^{ii}	69.08(3)	Fe4|Sb4—Se1—Sb2|Fe2^{viii}	88.81(4)
Se2^{i}—Sb1|Fe1—Se1^{ii}	109.95(3)	Sb2|Fe2^{vii}—Se1—Sb2|Fe2^{viii}	93.72(4)
Se2—Sb1|Fe1—Se1^{i}	145.26(2)	Sb2|Fe2^{vii}—Se1—Sb2|Fe2^{viii}	93.72(4)
Se3^{i}—Sb1|Fe1—Se1^{i}	75.88(3)	Fe4|Sb4—Se1—Sb2|Fe2^{viii}	88.81(4)
Se3^{ii}—Sb1|Fe1—Se1^{i}	123.50(3)	Sb2|Fe2^{vii}—Se1—Sb2|Fe2^{viii}	93.72(4)
Se2^{ii}—Sb1|Fe1—Se1^{i}	109.95(3)	Sb2|Fe2^{vii}—Se1—Sb2|Fe2^{viii}	93.72(4)
Se2^{i}—Sb1|Fe1—Se1^{i}	69.08(3)	Sb2|Fe2^{viii}—Se1—Sb2|Fe2^{viii}	0.00(2)
Se1^{ii}—Sb1|Fe1—Se1^{i}	66.46(3)	Fe4|Sb4—Se1—Sb1|Fe1^{ii}	119.29(3)
Se2—Sb1|Fe1—Fe3^{iii}	45.17(2)	Sb2|Fe2^{vii}—Se1—Sb1|Fe1^{ii}	150.90(4)
Se3^{i}—Sb1|Fe1—Fe3^{iii}	41.56(2)	Sb2|Fe2^{vii}—Se1—Sb1|Fe1^{ii}	150.90(4)

Se3^{ii}—Sb1|Fe1—Fe3^{iii}	90.18(3)	Sb2|Fe2^{viii}—Se1—Sb1|Fe1^{ii}	94.24(3)
Se2^{ii}—Sb1|Fe1—Fe3^{iii}	127.07(3)	Sb2|Fe2^{viii}—Se1—Sb1|Fe1^{ii}	94.24(3)
Se2^{i}—Sb1|Fe1—Fe3^{iii}	86.77(2)	Fe4|Sb4—Se1—Sb1|Fe1^{ii}	119.29(3)
Se1^{ii}—Sb1|Fe1—Fe3^{iii}	159.82(3)	Sb2|Fe2^{vii}—Se1—Sb1|Fe1^{ii}	150.90(4)
Se1^{i}—Sb1|Fe1—Fe3^{iii}	111.82(3)	Sb2|Fe2^{vii}—Se1—Sb1|Fe1^{ii}	150.90(4)
Se4^{iv}—Sb2|Fe2—Se1^{v}	90.88(4)	Sb2|Fe2^{viii}—Se1—Sb1|Fe1^{ii}	94.24(3)
Se4^{iv}—Sb2|Fe2—Se1^{vi}	90.88(4)	Sb2|Fe2^{viii}—Se1—Sb1|Fe1^{ii}	94.24(3)
Se1^{v}—Sb2|Fe2—Se1^{vi}	93.72(4)	Sb1|Fe1^{ii}—Se1—Sb1|Fe1^{ii}	0.00(2)
Se4^{iv}—Sb2|Fe2—Se4^{vii}	88.24(4)	Sb1|Fe1—Se2—Fe3^{iii}	92.11(3)
Se1^{v}—Sb2|Fe2—Se4^{vii}	173.09(3)	Sb1|Fe1—Se2—Fe3	92.11(3)
Se1^{vi}—Sb2|Fe2—Se4^{vii}	93.15(3)	Fe3^{iii}—Se2—Fe3	93.58(3)
Se4^{iv}—Sb2|Fe2—Se4^{viii}	88.24(4)	Sb1|Fe1—Se2—Sb1|Fe1^{ii}	97.74(3)
Se1^{v}—Sb2|Fe2—Se4^{viii}	93.15(3)	Fe3^{iii}—Se2—Sb1|Fe1^{ii}	168.03(3)
Se1^{vi}—Sb2|Fe2—Se4^{viii}	173.09(3)	Fe3—Se2—Sb1|Fe1^{ii}	92.839(19)
Se4^{vii}—Sb2|Fe2—Se4^{viii}	79.97(3)	Sb1|Fe1—Se2—Sb1|Fe1^{ii}	97.74(3)
Se4^{iv}—Sb2|Fe2—Se3	175.34(4)	Fe3^{iii}—Se2—Sb1|Fe1^{ii}	168.03(3)
Se1^{v}—Sb2|Fe2—Se3	92.30(4)	Fe3—Se2—Sb1|Fe1^{ii}	92.839(19)
Se1^{vi}—Sb2|Fe2—Se3	92.30(4)	Sb1|Fe1^{ii}—Se2—Sb1|Fe1^{ii}	0.00(2)
Se4^{vii}—Sb2|Fe2—Se3	88.19(4)	Sb1|Fe1—Se2—Sb1|Fe1^{i}	97.74(3)
Se4^{viii}—Sb2|Fe2—Se3	88.19(4)	Fe3^{iii}—Se2—Sb1|Fe1^{i}	92.839(19)
Se4^{iv}—Sb2|Fe2—Fe4|Sb4^{v}	45.71(2)	Fe3—Se2—Sb1|Fe1^{i}	168.03(3)
Se1^{v}—Sb2|Fe2—Fe4|Sb4^{v}	45.17(3)	Sb1|Fe1^{ii}—Se2—Sb1|Fe1^{i}	79.15(3)
Se1^{vi}—Sb2|Fe2—Fe4|Sb4^{v}	93.52(3)	Sb1|Fe1^{ii}—Se2—Sb1|Fe1^{i}	79.15(3)
Se4^{vii}—Sb2|Fe2—Fe4|Sb4^{v}	133.50(3)	Sb1|Fe1—Se2—Sb1|Fe1^{i}	97.74(3)
Se4^{viii}—Sb2|Fe2—Fe4|Sb4^{v}	90.77(2)	Fe3^{iii}—Se2—Sb1|Fe1^{i}	92.839(19)
Se3—Sb2|Fe2—Fe4|Sb4^{v}	137.35(2)	Fe3—Se2—Sb1|Fe1^{i}	168.03(3)
Se4^{iv}—Sb2|Fe2—Fe4|Sb4^{vi}	45.71(2)	Sb1|Fe1^{ii}—Se2—Sb1|Fe1^{i}	79.15(3)
Se1^{v}—Sb2|Fe2—Fe4|Sb4^{vi}	93.52(3)	Sb1|Fe1^{ii}—Se2—Sb1|Fe1^{i}	79.15(3)
Se1^{vi}—Sb2|Fe2—Fe4|Sb4^{vi}	45.17(3)	Sb1|Fe1^{i}—Se2—Sb1|Fe1^{i}	0.00(2)
Se4^{vii}—Sb2|Fe2—Fe4|Sb4^{vi}	90.77(2)	Fe3^{vi}—Se3—Sb1|Fe1^{i}	93.11(3)
Se4^{viii}—Sb2|Fe2—Fe4|Sb4^{vi}	133.50(3)	Fe3^{vi}—Se3—Sb1|Fe1^{i}	93.11(3)
Se3—Sb2|Fe2—Fe4|Sb4^{vi}	137.35(2)	Sb1|Fe1^{i}—Se3—Sb1|Fe1^{i}	0.00(2)
Fe4|Sb4^{v}—Sb2|Fe2—Fe4|Sb4^{vi}	63.355(19)	Fe3^{vi}—Se3—Sb1|Fe1^{ii}	93.11(3)
Se3^{ii}—Fe3—Se3^{viii}	180.000	Sb1|Fe1^{i}—Se3—Sb1|Fe1^{ii}	93.15(4)
Se3^{ii}—Fe3—Se2^{ix}	91.95(3)	Sb1|Fe1^{i}—Se3—Sb1|Fe1^{ii}	93.15(4)
Se3^{viii}—Fe3—Se2^{ix}	88.05(3)	Fe3^{vi}—Se3—Sb1|Fe1^{ii}	93.11(3)
Se3^{ii}—Fe3—Se2^{x}	88.05(3)	Sb1|Fe1^{i}—Se3—Sb1|Fe1^{ii}	93.15(4)
Se3^{viii}—Fe3—Se2^{x}	91.95(3)	Sb1|Fe1^{i}—Se3—Sb1|Fe1^{ii}	93.15(4)
Se2^{ix}—Fe3—Se2^{x}	180.000	Sb1|Fe1^{ii}—Se3—Sb1|Fe1^{ii}	0.00(3)
Se3^{ii}—Fe3—Se2^{xi}	91.95(3)	Fe3^{vi}—Se3—Sb2|Fe2	131.69(4)
Se3^{viii}—Fe3—Se2^{xi}	88.05(3)	Sb1|Fe1^{i}—Se3—Sb2|Fe2	118.40(3)
Se2^{ix}—Fe3—Se2^{xi}	93.58(3)	Sb1|Fe1^{i}—Se3—Sb2|Fe2	118.40(3)
Se2^{x}—Fe3—Se2^{xi}	86.42(3)	Sb1|Fe1^{ii}—Se3—Sb2|Fe2	118.40(3)
Se3^{ii}—Fe3—Se2	88.05(3)	Sb1|Fe1^{ii}—Se3—Sb2|Fe2	118.40(3)

Se3^{viii}—Fe3—Se2	91.95(3)	Fe3^{vi}—Se3—Se2^{ii}	47.93(2)
Se2^{ix}—Fe3—Se2	86.42(3)	Sb1|Fe1^{i}—Se3—Se2^{ii}	94.68(3)
Se2^{x}—Fe3—Se2	93.58(3)	Sb1|Fe1^{i}—Se3—Se2^{ii}	94.68(3)
Se2^{xi}—Fe3—Se2	180.000	Sb1|Fe1^{ii}—Se3—Se2^{ii}	45.18(3)
Se3^{ii}—Fe3—Sb1|Fe1^{ix}	134.67(3)	Sb1|Fe1^{ii}—Se3—Se2^{ii}	45.18(3)
Se3^{viii}—Fe3—Sb1|Fe1^{ix}	45.33(3)	Sb2|Fe2—Se3—Se2^{ii}	145.580(17)
Se2^{ix}—Fe3—Sb1|Fe1^{ix}	42.72(2)	Sb2|Fe2^{iv}—Se4—Sb2|Fe2^{iv}	0.00(3)
Se2^{x}—Fe3—Sb1|Fe1^{ix}	137.28(2)	Sb2|Fe2^{iv}—Se4—Fe4|Sb4^{vi}	89.07(3)
Se2^{xi}—Fe3—Sb1|Fe1^{ix}	91.11(2)	Sb2|Fe2^{iv}—Se4—Fe4|Sb4^{vi}	89.07(3)
Se2—Fe3—Sb1|Fe1^{ix}	88.89(2)	Sb2|Fe2^{iv}—Se4—Fe4|Sb4^{vi}	89.07(3)
Se3^{ii}—Fe3—Sb1|Fe1^{x}	45.33(3)	Sb2|Fe2^{iv}—Se4—Fe4|Sb4^{vi}	89.07(3)
Se3^{viii}—Fe3—Sb1|Fe1^{x}	134.67(3)	Fe4|Sb4^{vi}—Se4—Fe4|Sb4^{vi}	0.000
Se2^{ix}—Fe3—Sb1|Fe1^{x}	137.28(2)	Sb2|Fe2^{iv}—Se4—Fe4|Sb4^{v}	89.07(3)
Se2^{x}—Fe3—Sb1|Fe1^{x}	42.72(2)	Sb2|Fe2^{iv}—Se4—Fe4|Sb4^{v}	89.07(3)
Se2^{xi}—Fe3—Sb1|Fe1^{x}	88.89(2)	Fe4|Sb4^{vi}—Se4—Fe4|Sb4^{v}	94.37(3)
Se2—Fe3—Sb1|Fe1^{x}	91.11(2)	Fe4|Sb4^{vi}—Se4—Fe4|Sb4^{v}	94.37(3)
Sb1|Fe1^{ix}—Fe3—Sb1|Fe1^{x}	180.000(15)	Sb2|Fe2^{iv}—Se4—Fe4|Sb4^{v}	89.07(3)
Se1^{xii}—Fe4|Sb4—Se1	180.000	Sb2|Fe2^{iv}—Se4—Fe4|Sb4^{v}	89.07(3)
Se1^{xii}—Fe4|Sb4—Se4^{xiii}	88.77(3)	Fe4|Sb4^{vi}—Se4—Fe4|Sb4^{v}	94.37(3)
Se1—Fe4|Sb4—Se4^{xiii}	91.23(3)	Fe4|Sb4^{vi}—Se4—Fe4|Sb4^{v}	94.37(3)
Se1^{xii}—Fe4|Sb4—Se4^{viii}	91.23(3)	Fe4|Sb4^{v}—Se4—Fe4|Sb4^{v}	0.000
Se1—Fe4|Sb4—Se4^{viii}	88.77(3)	Sb2|Fe2^{iv}—Se4—Sb2|Fe2^{v}	91.76(4)
Se4^{xiii}—Fe4|Sb4—Se4^{viii}	180.00(3)	Sb2|Fe2^{iv}—Se4—Sb2|Fe2^{v}	91.76(4)
Se1^{xii}—Fe4|Sb4—Se4^{xiv}	88.77(3)	Fe4|Sb4^{vi}—Se4—Sb2|Fe2^{v}	172.77(3)
Se1—Fe4|Sb4—Se4^{xiv}	91.23(3)	Fe4|Sb4^{vi}—Se4—Sb2|Fe2^{v}	172.77(3)
Se4^{xiii}—Fe4|Sb4—Se4^{xiv}	94.37(3)	Fe4|Sb4^{v}—Se4—Sb2|Fe2^{v}	92.83(2)
Se4^{viii}—Fe4|Sb4—Se4^{xiv}	85.63(3)	Fe4|Sb4^{v}—Se4—Sb2|Fe2^{v}	92.83(2)
Se1^{xii}—Fe4|Sb4—Se4^{vii}	91.23(3)	Sb2|Fe2^{iv}—Se4—Sb2|Fe2^{v}	91.76(4)
Se1—Fe4|Sb4—Se4^{vii}	88.77(3)	Sb2|Fe2^{iv}—Se4—Sb2|Fe2^{v}	91.76(4)
Se4^{xiii}—Fe4|Sb4—Se4^{vii}	85.63(3)	Fe4|Sb4^{vi}—Se4—Sb2|Fe2^{v}	172.77(3)
Se4^{viii}—Fe4|Sb4—Se4^{vii}	94.37(3)	Fe4|Sb4^{vi}—Se4—Sb2|Fe2^{v}	172.77(3)
Se4^{xiv}—Fe4|Sb4—Se4^{vii}	180.00(4)	Fe4|Sb4^{v}—Se4—Sb2|Fe2^{v}	92.83(2)
Se1^{xii}—Fe4|Sb4—Sb2|Fe2^{xiv}	46.01(2)	Fe4|Sb4^{v}—Se4—Sb2|Fe2^{v}	92.83(2)
Se1—Fe4|Sb4—Sb2|Fe2^{xiv}	133.99(2)	Sb2|Fe2^{v}—Se4—Sb2|Fe2^{v}	0.00(2)
Se4^{xiii}—Fe4|Sb4—Sb2|Fe2^{xiv}	134.78(2)		

(i) 0.5-x, -0.5-y, 1-z; (ii) 0.5-x, 0.5-y, 1-z; (iii) x, -1+y, z; (iv) 1-x, -y, -z;
(v) 0.5+x, 0.5+y, z; (vi) 0.5+x, -0.5+y, z; (vii) -0.5+x, -0.5+y, z; (viii) -0.5+x, 0.5+y, z;
(ix) -x, -y, 1-z; (x) x, 1+y, z; (xi) -x, 1-y, 1-z; (xii) -x, -y, -z;
(xiii) 0.5-x, -0.5-y, -z; (xiv) 0.5-x, 0.5-y, -z.

Annex IV:$Fe_{0.87}Sb_2Sn_{0.13}Se_4$ (120K)

Atomic parameters							
Atom	**Ox.**	**Wyck.**	**Site**	**S.O.F.**	**x/a**	**y/b**	**z/c**
Sb1		4i	m		0.14662(3)	0	0.37407(2)
Sb2		4i	m		0.27489(3)	1/2	0.13540(2)
Fe1		2d	2/m	0.741	0	1/2	1/2
Sn1		2d	2/m	0.259	0	1/2	1/2
Fe2		2a	2/m		1/2	1/2	0
Se1		4i	m		0.38532(4)	0	0.04084(3)
Se2		4i	m		-0.01015(4)	1/2	0.32010(3)
Se3		4i	m		0.15387(4)	0	0.55440(3)
Se4		4i	m		0.15487(4)	0	0.17353(3)

Selected geometric informations			
Atoms 1,2	**d 1,2 [Å]**	**Atoms 1,2**	**d 1,2 [Å]**
Sb1—Se3	2.6977(7)	Fe2—Se4^{ii}	2.5633(12)
Sb1—Se2^{i}	2.7149(6)	Fe2—Se1	2.7042(5)
Sb1—Se2	2.7149(6)	Fe2—Se1^{vii}	2.7043(5)
Sb2—Se1^{ii}	2.6172(12)	Fe2—Se1^{viii}	2.7043(5)
Sb2—Se4	2.7310(5)	Fe2—Se1^{iii}	2.7043(5)
Sb2—Se4^{iii}	2.7311(5)	Se1—Sb2^{ii}	2.6172(12)
Fe1|Sn1—Se2	2.6768(7)	Se1—Fe2^{i}	2.7042(5)
Fe1|Sn1—Se2^{iv}	2.6768(7)	Se2—Sb1^{iii}	2.7149(6)
Fe1|Sn1—Se3^{v}	2.6913(6)	Se3—Fe1|Sn1^{i}	2.6913(6)
Fe1|Sn1—Se3^{iv}	2.6913(6)	Se3—Fe1|Sn1^{i}	2.6913(6)
Fe1|Sn1—Se3	2.6913(6)	Se4—Fe2^{ix}	2.5633(12)
Fe1|Sn1—Se3^{iii}	2.6913(6)	Se4—Sb2^{i}	2.7310(5)
Fe2—Se4^{vi}	2.5633(12)		
Atoms 1,2,3	**Angle 1,2,3 [°]**	**Atoms 1,2,3**	**Angle 1,2,3 [°]**
Se3—Sb1—Se2^{i}	90.53(3)	Se1—Fe2—Se1^{vii}	180.000
Se3—Sb1—Se2	90.53(3)	Se4^{vi}—Fe2—Se1^{viii}	87.796(19)
Se2^{i}—Sb1—Se2	93.65(3)	Se4^{ii}—Fe2—Se1^{viii}	92.204(19)
Se1^{ii}—Sb2—Se4	86.16(2)	Se1—Fe2—Se1^{viii}	85.86(2)
Se1^{ii}—Sb2—Se4^{iii}	86.16(2)	Se1^{vii}—Fe2—Se1^{viii}	94.14(2)
Se4—Sb2—Se4^{iii}	92.93(2)	Se4^{vi}—Fe2—Se1^{iii}	92.204(19)
Se2—Fe1|Sn1—Se2^{iv}	180.000	Se4^{ii}—Fe2—Se1^{iii}	87.796(19)
Se2—Fe1|Sn1—Se3^{v}	88.51(2)	Se1—Fe2—Se1^{iii}	94.14(2)
Se2^{iv}—Fe1|Sn1—Se3^{v}	91.49(2)	Se1^{vii}—Fe2—Se1^{iii}	85.86(2)
Se2—Fe1|Sn1—Se3^{iv}	88.51(2)	Se1^{viii}—Fe2—Se1^{iii}	180.000(1)
Se2^{iv}—Fe1|Sn1—Se3^{iv}	91.49(2)	Sb2^{ii}—Se1—Fe2^{i}	92.733(18)
Se3^{v}—Fe1|Sn1—Se3^{iv}	94.73(3)	Sb2^{ii}—Se1—Fe2	92.733(19)
Se2—Fe1|Sn1—Se3	91.49(2)	Fe2^{i}—Se1—Fe2	94.14(2)
Se2^{iv}—Fe1|Sn1—Se3	88.51(2)	Fe1|Sn1—Se2—Sb1^{iii}	88.96(3)
Se3^{v}—Fe1|Sn1—Se3	85.27(3)	Fe1|Sn1—Se2—Sb1	88.96(3)

Se3^{iv}—Fe1|Sn1—Se3	179.999(2)	Sb1^{iii}—Se2—Sb1	93.65(3)
Se2—Fe1|Sn1—Se3^{iii}	91.49(2)	Fe1|Sn1—Se3—Fe1|Sn1^{i}	94.73(3)
Se2^{iv}—Fe1|Sn1—Se3^{iii}	88.51(2)	Fe1|Sn1—Se3—Fe1|Sn1^{i}	94.73(3)
Se3^{v}—Fe1|Sn1—Se3^{iii}	179.999(1)	Fe1|Sn1^{i}—Se3—Fe1|Sn1^{i}	0.000
Se3^{iv}—Fe1|Sn1—Se3^{iii}	85.27(3)	Fe1|Sn1—Se3—Sb1	89.02(2)
Se3—Fe1|Sn1—Se3^{iii}	94.73(3)	Fe1|Sn1^{i}—Se3—Sb1	89.02(3)
Se4^{vi}—Fe2—Se4^{ii}	180.000	Fe1|Sn1^{i}—Se3—Sb1	89.02(3)
Se4^{vi}—Fe2—Se1	92.205(18)	Fe2^{ix}—Se4—Sb2^{i}	93.31(2)
Se4^{ii}—Fe2—Se1	87.795(19)	Fe2^{ix}—Se4—Sb2	93.31(2)
Se4^{vi}—Fe2—Se1^{vii}	87.796(18)	Sb2^{i}—Se4—Sb2	92.94(2)
Se4^{ii}—Fe2—Se1^{vii}	92.204(18)		

(i) x, -1+y, z; (ii) 0.5-x, 0.5-y, -z; (iii) x, 1+y, z; (iv) -x, 1-y, 1-z;
(v) -x, -y, 1-z; (vi) 0.5+x, 0.5+y, z; (vii) 1-x, 1-y, -z; (viii) 1-x, -y, -z;
(ix) -0.5+x, -0.5+y, z.

Annex V:$Fe_{0.87}Sb_2Sn_{0.13}Se_4$ (300K)

Atomic parameters						
Atom	**Ox.**	**Wyck.**	**Site**	**S.O.F.**	**x/a**	**y/b**	**z/c**
Sb1		4i	m		0.35344(3)	0	0.12629(2)
Sb2		4i	m		0.22522(3)	1/2	0.36477(3)
Se3		4i	m		0.11483(4)	0	0.45874(3)
Fe4		2a	2/m	0.734	0	0	0
Sn4		2a	2/m	0.266	0	0	0
Se5		4i	m		0.15438(4)	1/2	0.05500(4)
Se6		4i	m		0.50987(4)	1/2	0.18026(4)
Se7		4i	m		0.34506(4)	0	0.32642(4)
Fe8		2d	2/m		0	1/2	1/2

Selected geometric informations			
Atoms 1,2	**d 1,2 [Å]**	**Atoms 1,2**	**d 1,2 [Å]**
Sb1—Se5^{i}	2.7092(8)	Se5—Fe4|Sn4^{iv}	2.7033(6)
Sb1—Se6	2.7201(6)	Se5—Fe4|Sn4^{iv}	2.7033(6)
Sb1—Se6^{ii}	2.7201(6)	Se5—Sb1^{i}	2.7091(8)
Sb2—Se3^{iii}	2.6177(12)	Se6—Fe4|Sn4^{viii}	2.6831(8)
Sb2—Se7^{iv}	2.7397(6)	Se6—Fe4|Sn4^{viii}	2.6831(8)
Sb2—Se7	2.7398(6)	Se6—Sb1^{iv}	2.7201(6)

Se3—Sb2^{iii}	2.6176(12)	Se7—Fe8^{ix}	2.5631(12)
Se3—Fe8^{ii}	2.7169(5)	Se7—Sb2^{ii}	2.7397(6)
Se3—Fe8	2.7169(5)	Fe8—Se7^{iii}	2.5631(12)
Fe4|Sn4—Se6^{i}	2.6831(8)	Fe8—Se7^{x}	2.5631(12)
Fe4|Sn4—Se6^{v}	2.6831(8)	Fe8—Se3^{iv}	2.7169(5)
Fe4|Sn4—Se5^{vi}	2.7033(6)	Fe8—Se3^{xi}	2.7169(5)
Fe4|Sn4—Se5^{ii}	2.7033(6)	Fe8—Se3^{xii}	2.7169(5)
Fe4|Sn4—Se5^{vii}	2.7033(6)	Fe8—Fe8^{iv}	3.9723(8)
Fe4|Sn4—Se5	2.7033(6)	Fe4|Sn4—Fe4|Sn4^{iv}	3.9723(8)
Atoms 1,2,3	**Angle 1,2,3 [°]**	**Atoms 1,2,3**	**Angle 1,2,3 [°]**
Se5^{i}—Sb1—Se6	90.52(3)	Fe4|Sn4—Se5—Sb1^{i}	88.92(3)
Se5^{i}—Sb1—Se6^{ii}	90.52(3)	Fe4|Sn4^{iv}—Se5—Sb1^{i}	88.92(2)
Se6—Sb1—Se6^{ii}	93.80(3)	Fe4|Sn4^{iv}—Se5—Sb1^{i}	88.92(2)
Se3^{iii}—Sb2—Se7^{iv}	86.21(2)	Fe4|Sn4^{viii}—Se6—Fe4|Sn4^{viii}	0.000
Se3^{iii}—Sb2—Se7	86.21(2)	Fe4|Sn4^{viii}—Se6—Sb1^{iv}	89.11(3)
Se7^{iv}—Sb2—Se7	92.93(2)	Fe4|Sn4^{viii}—Se6—Sb1^{iv}	89.11(3)
Sb2^{iii}—Se3—Fe8^{ii}	92.67(2)	Fe4|Sn4^{viii}—Se6—Sb1	89.11(3)
Sb2^{iii}—Se3—Fe8	92.67(2)	Fe4|Sn4^{viii}—Se6—Sb1	89.11(3)
Fe8^{ii}—Se3—Fe8	93.95(2)	Sb1^{iv}—Se6—Sb1	93.80(3)
Se6^{i}—Fe4|Sn4—Se6^{v}	180.00(2)	Fe8^{ix}—Se7—Sb2^{ii}	93.35(2)
Se6^{i}—Fe4|Sn4—Se5^{vi}	88.56(2)	Fe8^{ix}—Se7—Sb2	93.35(2)
Se6^{v}—Fe4|Sn4—Se5^{vi}	91.44(2)	Sb2^{ii}—Se7—Sb2	92.93(2)
Se6^{i}—Fe4|Sn4—Se5^{ii}	91.44(2)	Se7^{iii}—Fe8—Se7^{x}	180.000
Se6^{v}—Fe4|Sn4—Se5^{ii}	88.56(2)	Se7^{iii}—Fe8—Se3^{iv}	87.771(19)
Se5^{vi}—Fe4|Sn4—Se5^{ii}	85.43(3)	Se7^{x}—Fe8—Se3^{iv}	92.229(19)
Se6^{i}—Fe4|Sn4—Se5^{vii}	88.56(2)	Se7^{iii}—Fe8—Se3^{xi}	92.229(19)
Se6^{v}—Fe4|Sn4—Se5^{vii}	91.44(2)	Se7^{x}—Fe8—Se3^{xi}	87.771(19)
Se5^{vi}—Fe4|Sn4—Se5^{vii}	94.57(3)	Se3^{iv}—Fe8—Se3^{xi}	180.000
Se5^{ii}—Fe4|Sn4—Se5^{vii}	180.000(17)	Se7^{iii}—Fe8—Se3^{xii}	92.229(19)
Se6^{i}—Fe4|Sn4—Se5	91.44(3)	Se7^{x}—Fe8—Se3^{xii}	87.771(19)
Se6^{v}—Fe4|Sn4—Se5	88.56(3)	Se3^{iv}—Fe8—Se3^{xii}	86.05(2)
Se5^{vi}—Fe4|Sn4—Se5	180.000	Se3^{xi}—Fe8—Se3^{xii}	93.95(2)
Se5^{ii}—Fe4|Sn4—Se5	94.57(3)	Se7^{iii}—Fe8—Se3	87.770(19)
Se5^{vii}—Fe4|Sn4—Se5	85.43(3)	Se7^{x}—Fe8—Se3	92.230(19)
Fe4|Sn4—Se5—Fe4|Sn4^{iv}	94.57(3)	Se3^{iv}—Fe8—Se3	93.95(2)
Fe4|Sn4—Se5—Fe4|Sn4^{iv}	94.57(3)	Se3^{xi}—Fe8—Se3	86.05(2)
Fe4|Sn4^{iv}—Se5—Fe4|Sn4^{iv}	0.000	Se3^{xii}—Fe8—Se3	180.000

(i) 0.5-x, 0.5-y, -z; (ii) x, -1+y, z; (iii) 0.5-x, 0.5-y, 1-z; (iv) x, 1+y, z;
(v) -0.5+x, -0.5+y, z; (vi) -x, -y, -z; (vii) -x, 1-y, -z; (viii) 0.5+x, 0.5+y, z;
(ix) 0.5+x, -0.5+y, z; (x) -0.5+x, 0.5+y, z; (xi) -x, -y, 1-z; (xii) -x, 1-y, 1-z.

Annex VI:$Fe_{0.87}Sb_2Sn_{0.13}Se_4$ (350K)

Atomic parameters							
Atom	**Ox.**	**Wyck.**	**Site**	**S.O.F.**	**x/a**	**y/b**	**z/c**
Sb2		4i	m		0.1206(2)	-1/2	-0.3877(6)
Sb3		4i	m		0.0501(2)	-1.00000	-0.2753(5)
Sb4		4i	m		0.2572(2)	-2.00000	-0.6280(5)
Sb5		4i	m		0.0747(2)	-1.00000	-0.7261(5)
Sb6		4i	m		0.0922(2)	1/2	0.0453(6)
Se2		4i	m		0.0384(3)	1/2	0.1157(8)
Se3		4i	m		0.1292(3)	-1.00000	-0.7897(8)
Se4		4i	m		0.0541(3)	-1.00000	-0.4488(7)
Se5		4i	m		0.1705(2)	0	-0.3414(8)
Se6		4i	m		0.1623(4)	0	0.0036(8)
Se7		4i	m		0.1160(4)	-1/2	-0.2123(8)
Se8		4i	m		-0.0016(3)	-1.50000	-0.3249(10)
Se9		4i	m		0.2160(3)	1/2	-0.1191(7)
Se10		4i	m		0.0510(3)	0	-0.0723(6)
Se11		4i	m		0.1141(3)	-1/2	-0.5967(9)
Se12		4i	m		0.2185(3)	-2.50000	-0.7347(7)
Fe3		2a	2/m		0	0	0
Fe4		4i	m		0.1642(5)	-1.50000	-0.6676(13)
Se1		4i	m		0.2054(3)	-2.00000	-0.5512(7)
Fe1		2d	2/m	0.47	0	-1.50000	-1/2
Sn1		2d	2/m	0.53	0	-1.50000	-1/2
Fe2		4i	m	0.83	0.1674(8)	0	-0.1687(16)
Sn2		4i	m	0.17	0.1674(8)	0	-0.1687(16)
Sb1		4i	m		0.2165(2)	1/2	0.0583(5)

Selected geometric informations			
Atoms 1,2	**d 1,2 [Å]**	**Atoms 1,2**	**d 1,2 [Å]**
Sb2—Se5^{i}	2.664(7)	Se7—Fe2|Sn2^{i}	2.70(2)
Sb2—Se5	2.664(7)	Se7—Fe2|Sn2^{i}	2.70(2)
Sb2—Se7	2.734(16)	Se7—Fe2|Sn2	2.70(2)
Sb3—Se4	2.693(13)	Se7—Sb3^{ii}	3.072(12)
Sb3—Se8	2.711(9)	Se8—Sn1|Fe1	2.684(14)
Sb3—Se8^{ii}	2.711(9)	Se8—Sb3^{i}	2.711(9)
Sb3—Se7^{i}	3.072(12)	Se9—Fe2|Sn2	2.637(18)
Sb3—Se7	3.072(12)	Se9—Fe2|Sn2^{ii}	2.637(18)
Sb3—Se10^{i}	3.073(12)	Se9—Fe2|Sn2^{ii}	2.637(18)
Sb4—Se1	2.642(14)	Se9—Sb1	2.687(11)
Sb4—Se12	2.650(8)	Se10—Fe3	2.560(9)

Sb4—Se12^{ii}	2.650(8)	Se10—Sb6^{i}	2.752(9)
Sb5—Se3	2.593(16)	Se10—Sb3^{ii}	3.073(12)
Sb5—Se11	2.815(10)	Se11—Fe4^{ii}	2.51(2)
Sb5—Se11^{i}	2.815(10)	Se11—Sb5^{ii}	2.815(10)
Sb5—Se2^{iii}	3.038(10)	Se12—Fe4^{i}	2.62(2)
Sb5—Se2^{iv}	3.038(10)	Se12—Sb4^{i}	2.650(8)
Sb6—Se2	2.637(16)	Fe3—Se10^{vii}	2.56(1)
Sb6—Se10	2.752(9)	Fe3—Se2^{vii}	2.705(7)
Sb6—Se10^{ii}	2.752(9)	Fe3—Se2^{viii}	2.705(7)
Se2—Fe3	2.705(7)	Fe3—Se2^{i}	2.705(7)
Se2—Fe3^{ii}	2.705(7)	Fe4—Se11^{i}	2.51(2)
Se2—Sb5^{v}	3.038(10)	Fe4—Se12^{ii}	2.62(2)
Se2—Sb5^{vi}	3.038(10)	Fe4—Se3^{i}	2.716(15)
Se3—Fe4	2.716(15)	Fe4—Se1^{ii}	2.743(15)
Se3—Fe4^{ii}	2.716(15)	Fe4—Se1	2.743(15)
Se4—Sn1|Fe1	2.767(6)	Se1—Fe4^{i}	2.743(15)
Se4—Sn1|Fe1^{ii}	2.767(6)	Sn1|Fe1—Se8^{ix}	2.684(14)
Se4—Sn1|Fe1^{ii}	2.767(6)	Sn1|Fe1—Se4^{i}	2.767(6)
Se5—Sb2^{ii}	2.664(7)	Sn1|Fe1—Se4^{ix}	2.767(6)
Se5—Fe2|Sn2	2.67(3)	Sn1|Fe1—Se4^{x}	2.767(6)
Se6—Fe2|Sn2	2.69(3)	Fe2|Sn2—Se9^{i}	2.637(18)
Se6—Sb1^{i}	2.772(10)	Fe2|Sn2—Se7^{ii}	2.70(2)
Se6—Sb1	2.772(10)	Sb1—Se6^{ii}	2.772(10)

Atoms 1,2,3	**Angle 1,2,3 [°]**	**Atoms 1,2,3**	**Angle 1,2,3 [°]**
Se5^{i}—Sb2—Se5	96.4(3)	Fe2|Sn2^{ii}—Se9—Sb1	92.0(6)
Se5^{i}—Sb2—Se7	92.1(4)	Fe2|Sn2^{ii}—Se9—Sb1	92.0(6)
Se5—Sb2—Se7	92.1(4)	Fe3—Se10—Sb6	93.8(3)
Se4—Sb3—Se8	91.3(4)	Fe3—Se10—Sb6^{i}	93.8(3)
Se4—Sb3—Se8^{ii}	91.3(4)	Sb6—Se10—Sb6^{i}	92.3(4)
Se8—Sb3—Se8^{ii}	94.2(4)	Fe3—Se10—Sb3^{ii}	134.3(4)
Se4—Sb3—Se7^{i}	88.6(3)	Sb6—Se10—Sb3^{ii}	116.5(3)
Se8—Sb3—Se7^{i}	92.6(2)	Sb6^{i}—Se10—Sb3^{ii}	116.5(3)
Se8^{ii}—Sb3—Se7^{i}	173.2(3)	Fe4^{ii}—Se11—Sb5	89.9(5)
Se4—Sb3—Se7	88.6(3)	Fe4^{ii}—Se11—Sb5^{ii}	89.9(5)
Se8—Sb3—Se7	173.2(3)	Sb5—Se11—Sb5^{ii}	89.7(4)
Se8^{ii}—Sb3—Se7	92.6(2)	Fe4^{i}—Se12—Sb4^{i}	96.2(4)
Se7^{i}—Sb3—Se7	80.5(4)	Fe4^{i}—Se12—Sb4	96.2(4)
Se4—Sb3—Se10^{i}	176.5(4)	Sb4^{i}—Se12—Sb4	97.0(4)
Se8—Sb3—Se10^{i}	91.1(4)	Se10—Fe3—Se10^{vii}	180.0(2)
Se8^{ii}—Sb3—Se10^{i}	91.1(4)	Se10—Fe3—Se2^{vii}	92.3(3)
Se7^{i}—Sb3—Se10^{i}	88.7(3)	Se10^{vii}—Fe3—Se2^{vii}	87.7(3)
Se7—Sb3—Se10^{i}	88.7(3)	Se10—Fe3—Se2^{viii}	92.3(3)
Se1—Sb4—Se12	85.8(4)	Se10^{vii}—Fe3—Se2^{viii}	87.7(3)
Se1—Sb4—Se12^{ii}	85.8(4)	Se2^{vii}—Fe3—Se2^{viii}	94.5(3)

Se12—Sb4—Se12^{ii}	97.0(4)	Se10—Fe3—Se2	87.7(3)
Se3—Sb5—Se11	87.8(4)	Se10^{vii}—Fe3—Se2	92.3(3)
Se3—Sb5—Se11^{i}	87.8(4)	Se2^{vii}—Fe3—Se2	179.997(1)
Se11—Sb5—Se11^{i}	89.7(4)	Se2^{viii}—Fe3—Se2	85.5(3)
Se3—Sb5—Se2^{iii}	84.4(3)	Se10—Fe3—Se2^{i}	87.7(3)
Se11—Sb5—Se2^{iii}	171.4(4)	Se10^{vii}—Fe3—Se2^{i}	92.3(3)
Se11^{i}—Sb5—Se2^{iii}	93.8(2)	Se2^{vii}—Fe3—Se2^{i}	85.5(3)
Se3—Sb5—Se2^{iv}	84.4(3)	Se2^{viii}—Fe3—Se2^{i}	179.996(1)
Se11—Sb5—Se2^{iv}	93.8(2)	Se2—Fe3—Se2^{i}	94.5(3)
Se11^{i}—Sb5—Se2^{iv}	171.4(4)	Se11^{i}—Fe4—Se12^{ii}	177.7(9)
Se2^{iii}—Sb5—Se2^{iv}	81.6(3)	Se11^{i}—Fe4—Se3	91.6(6)
Se2—Sb6—Se10	85.2(4)	Se12^{ii}—Fe4—Se3	89.9(6)
Se2—Sb6—Se10^{ii}	85.2(4)	Se11^{i}—Fe4—Se3^{i}	91.6(6)
Se10—Sb6—Se10^{ii}	92.3(4)	Se12^{ii}—Fe4—Se3^{i}	89.9(6)
Sb6—Se2—Fe3	93.2(3)	Se3—Fe4—Se3^{i}	94.0(7)
Sb6—Se2—Fe3^{ii}	93.2(3)	Se11^{i}—Fe4—Se1^{ii}	94.1(6)
Fe3—Se2—Fe3^{ii}	94.5(3)	Se12^{ii}—Fe4—Se1^{ii}	84.4(6)
Sb6—Se2—Sb5^{v}	97.0(4)	Se3—Fe4—Se1^{ii}	86.36(19)
Fe3—Se2—Sb5^{v}	168.1(5)	Se3^{i}—Fe4—Se1^{ii}	174.3(9)
Fe3^{ii}—Se2—Sb5^{v}	91.09(10)	Se11^{i}—Fe4—Se1	94.1(6)
Sb6—Se2—Sb5^{vi}	97.0(4)	Se12^{ii}—Fe4—Se1	84.4(6)
Fe3—Se2—Sb5^{vi}	91.09(10)	Se3—Fe4—Se1	174.3(9)
Fe3^{ii}—Se2—Sb5^{vi}	168.1(5)	Se3^{i}—Fe4—Se1	86.36(19)
Sb5^{v}—Se2—Sb5^{vi}	81.6(3)	Se1^{ii}—Fe4—Se1	92.7(7)
Sb5—Se3—Fe4	90.5(5)	Sb4—Se1—Fe4^{i}	93.5(5)
Sb5—Se3—Fe4^{ii}	90.5(5)	Sb4—Se1—Fe4	93.5(5)
Fe4—Se3—Fe4^{ii}	94.0(7)	Fe4^{i}—Se1—Fe4	92.7(7)
Sb3—Se4—Sn1|Fe1	88.5(3)	Se8^{ix}—Sn1|Fe1—Se8	179.999(1)
Sb3—Se4—Sn1|Fe1^{ii}	88.5(3)	Se8^{ix}—Sn1|Fe1—Se4^{i}	89.7(3)
Sn1|Fe1—Se4—Sn1|Fe1^{ii}	91.7(3)	Se8—Sn1|Fe1—Se4^{i}	90.3(3)
Sb3—Se4—Sn1|Fe1^{ii}	88.5(3)	Se8^{ix}—Sn1|Fe1—Se4	89.7(3)
Sn1|Fe1—Se4—Sn1|Fe1^{ii}	91.7(3)	Se8—Sn1|Fe1—Se4	90.3(3)
Sn1|Fe1^{ii}—Se4—Sn1|Fe1^{ii}	0.000	Se4^{i}—Sn1|Fe1—Se4	91.7(3)
Sb2^{ii}—Se5—Sb2	96.4(3)	Se8^{ix}—Sn1|Fe1—Se4^{ix}	90.3(3)
Sb2^{ii}—Se5—Fe2|Sn2	88.7(5)	Se8—Sn1|Fe1—Se4^{ix}	89.7(3)
Sb2—Se5—Fe2|Sn2	88.7(5)	Se4^{i}—Sn1|Fe1—Se4^{ix}	88.3(3)
Fe2|Sn2—Se6—Sb1^{i}	88.9(5)	Se4—Sn1|Fe1—Se4^{ix}	180.0(3)
Fe2|Sn2—Se6—Sb1	88.9(5)	Se8^{ix}—Sn1|Fe1—Se4^{x}	90.3(3)
Sb1^{i}—Se6—Sb1	91.5(4)	Se8—Sn1|Fe1—Se4^{x}	89.7(3)
Fe2|Sn2^{i}—Se7—Fe2|Sn2^{i}	0.0(13)	Se4^{i}—Sn1|Fe1—Se4^{x}	180.000
Fe2|Sn2^{i}—Se7—Fe2|Sn2	94.6(9)	Se4—Sn1|Fe1—Se4^{x}	88.3(3)
Fe2|Sn2^{i}—Se7—Fe2|Sn2	94.6(9)	Se4^{ix}—Sn1|Fe1—Se4^{x}	91.7(3)
Fe2|Sn2^{i}—Se7—Sb2	86.5(7)	Se9—Fe2|Sn2—Se9^{i}	97.7(9)
Fe2|Sn2^{i}—Se7—Sb2	86.5(7)	Se9—Fe2|Sn2—Se5	90.1(8)

Fe2|Sn2—Se7—Sb2	86.5(7)	Se9^{i}—Fe2|Sn2—Se5	90.1(8)
Fe2|Sn2^{i}—Se7—Sb3	92.4(5)	Se9—Fe2|Sn2—Se6	90.8(6)
Fe2|Sn2^{i}—Se7—Sb3	92.4(5)	Se9^{i}—Fe2|Sn2—Se6	90.8(6)
Fe2|Sn2—Se7—Sb3	172.7(5)	Se5—Fe2|Sn2—Se6	178.5(12)
Sb2—Se7—Sb3	91.8(3)	Se9—Fe2|Sn2—Se7	176.8(13)
Fe2|Sn2^{i}—Se7—Sb3^{ii}	172.7(5)	Se9^{i}—Fe2|Sn2—Se7	83.79(19)
Fe2|Sn2^{i}—Se7—Sb3^{ii}	172.7(5)	Se5—Fe2|Sn2—Se7	92.7(7)
Fe2|Sn2—Se7—Sb3^{ii}	92.4(5)	Se6—Fe2|Sn2—Se7	86.3(8)
Sb2—Se7—Sb3^{ii}	91.8(3)	Se9—Fe2|Sn2—Se7^{ii}	83.79(19)
Sb3—Se7—Sb3^{ii}	80.5(4)	Se9^{i}—Fe2|Sn2—Se7^{ii}	176.8(13)
Sn1|Fe1—Se8—Sb3^{i}	89.9(4)	Se5—Fe2|Sn2—Se7^{ii}	92.7(7)
Sn1|Fe1—Se8—Sb3	89.9(4)	Se6—Fe2|Sn2—Se7^{ii}	86.3(8)
Sb3^{i}—Se8—Sb3	94.2(4)	Se7—Fe2|Sn2—Se7^{ii}	94.6(9)
Fe2|Sn2—Se9—Fe2|Sn2^{ii}	97.7(9)	Se9—Sb1—Se6	88.1(3)
Fe2|Sn2—Se9—Fe2|Sn2^{ii}	97.7(9)	Se9—Sb1—Se6^{ii}	88.1(3)
Fe2|Sn2^{ii}—Se9—Fe2|Sn2^{ii}	0.(1)	Se6—Sb1—Se6^{ii}	91.5(4)
Fe2|Sn2—Se9—Sb1	92.0(6)		

(i) x, -1+y, z; (ii) x, 1+y, z; (iii) x, -2+y, -1+z; (iv) x, -1+y, -1+z;
(v) x, 2+y, 1+z; (vi) x, 1+y, 1+z; (vii) -x, -y, -z; (viii) -x, 1-y, -z;
(ix) -x, -3-y, -1-z; (x) -x, -2-y, -1-z.

Annex:V : 400K

Atomic parameters							
Atom	**Ox.**	**Wyck.**	**Site**	**S.O.F.**	**x/a**	**y/b**	**z/c**
Sb1		8f	1		0.18694(6)	1.0058(4)	0.27023(5)
Sb2		8f	1		0.18679(4)	1.4962(3)	0.02030(4)
Sb3		8f	1		-0.06753(5)	0.5006(4)	-0.14646(5)
Sb4		8f	1		0.06758(5)	1.0009(4)	-0.10357(5)
Fe5		8f	1	0.78	0.25028(9)	1.9795(5)	0.12872(6)
Sn5		8f	1	0.22	0.25028(9)	1.9795(5)	0.12872(6)
Fe6		4e	2		0	0.9999(12)	-1/4
Fe7		4b	-1		0	1.50000	0
Se8		8f	1		0.02075(7)	0.4998(6)	-0.18232(6)
Se9		8f	1		-0.02070(7)	1.0005(6)	-0.06778(6)
Se10		8f	1		0.22311(7)	1.5037(6)	0.18861(6)
Se11		8f	1		0.27799(7)	1.5111(6)	0.06154(6)
Se12		8f	1		0.16023(7)	1.5021(6)	0.33503(7)
Se13		8f	1		0.15947(8)	1.9914(6)	0.08498(7)
Se14		8f	1		-0.08633(7)	1.0055(6)	-0.21588(7)
Se15		8f	1		0.08739(7)	1.4979(6)	-0.03429(7)

Selected geometric informations			
Atoms 1,2	**d 1,2 [Å]**	**Atoms 1,2**	**d 1,2 [Å]**
Sb1—Se3	2.715(3)	Fe3—Se1^{i}	2.717(4)
Sb1—Se5^{i}	2.722(4)	Fe3—Se1^{vi}	2.717(4)
Sb1—Se5	2.738(4)	Fe3—Se1	2.728(4)
Sb2—Se4	2.711(3)	Fe3—Se1^{v}	2.728(4)
Sb2—Se6^{ii}	2.718(5)	Se1—Fe3^{ii}	2.717(4)
Sb2—Se6	2.720(5)	Se2—Sb4^{ii}	2.604(3)
Sb3—Se1	2.630(3)	Se2—Fe2^{ii}	2.715(8)
Sb3—Se7^{ii}	2.747(5)	Se3—Fe1|Sn1^{i}	2.713(6)
Sb3—Se7	2.749(4)	Se3—Fe1|Sn1^{i}	2.713(6)
Sb4—Se2^{i}	2.604(3)	Se4—Fe1|Sn1^{i}	2.703(6)
Sb4—Se8	2.740(4)	Se4—Fe1|Sn1^{i}	2.703(6)
Sb4—Se8^{i}	2.744(4)	Se5—Sb1^{ii}	2.722(4)
Fe1|Sn1—Se6^{ii}	2.677(5)	Se6—Fe1|Sn1^{i}	2.677(5)
Fe1|Sn1—Se5	2.696(5)	Se6—Fe1|Sn1^{i}	2.677(5)
Fe1|Sn1—Se4^{ii}	2.703(6)	Se6—Sb2^{i}	2.718(5)
Fe1|Sn1—Se3	2.709(6)	Se7—Sb3^{i}	2.747(5)
Fe1|Sn1—Se4	2.713(6)	Se8—Sb4^{ii}	2.744(4)
Fe1|Sn1—Se3^{ii}	2.713(6)	Fe3—Fe3^{vii}	13.9145(30)
Fe2—Se8^{iii}	2.564(2)	Fe3—Fe3^{viii}	13.9145(30)
Fe2—Se8	2.564(2)	Fe1|Sn1—Fe1|Sn1^{ix}	6.8647(55)
Fe2—Se2^{i}	2.715(8)	Fe1|Sn1—Fe1|Sn1^{x}	6.8647(55)
Fe2—Se2^{iv}	2.715(8)	Fe2—Fe3^{xi}	6.8493(26)
Fe2—Se2	2.734(8)	Fe1|Sn1—Fe3^{xii}	7.8313(44)
Fe2—Se2^{iii}	2.734(8)	Fe1|Sn1—Fe2^{ii}	7.8582(48)
Fe3—Se7	2.561(2)	Fe2—Fe3^{vi}	6.8516(26)
Fe3—Se7^{v}	2.561(2)	Fe2—Fe3^{xiii}	6.8516(26)

Atoms 1,2,3	**Angle 1,2,3 [°]**	**Atoms 1,2,3**	**Angle 1,2,3 [°]**
Se3—Sb1—Se5^{i}	90.39(11)	Se7—Fe3—Se1^{vi}	92.16(10)
Se3—Sb1—Se5	90.11(10)	Se7^{v}—Fe3—Se1^{vi}	87.83(10)
Se5^{i}—Sb1—Se5	93.59(8)	Se1^{i}—Fe3—Se1^{vi}	180.000
Se4—Sb2—Se6^{ii}	90.83(12)	Se7—Fe3—Se1	87.89(10)
Se4—Sb2—Se6	90.69(12)	Se7^{v}—Fe3—Se1	92.11(10)
Se6^{ii}—Sb2—Se6	94.08(9)	Se1^{i}—Fe3—Se1	93.93(6)
Se1—Sb3—Se7^{ii}	85.85(12)	Se1^{vi}—Fe3—Se1	86.07(6)
Se1—Sb3—Se7	86.08(11)	Se7—Fe3—Se1^{v}	92.11(10)
Se7^{ii}—Sb3—Se7	92.80(9)	Se7^{v}—Fe3—Se1^{v}	87.89(10)
Se2^{i}—Sb4—Se8	86.29(11)	Se1^{i}—Fe3—Se1^{v}	86.07(6)

Se2^{i}—Sb4—Se8^{i}	86.60(11)	Se1^{vi}—Fe3—Se1^{v}	93.93(6)
Se8—Sb4—Se8^{i}	93.07(9)	Se1—Fe3—Se1^{v}	180.000(1)
Se6^{ii}—Fe1|Sn1—Se5	179.9(2)	Sb3—Se1—Fe3^{ii}	92.74(11)
Se6^{ii}—Fe1|Sn1—Se4^{ii}	91.80(16)	Sb3—Se1—Fe3	92.49(11)
Se5—Fe1|Sn1—Se4^{ii}	88.11(15)	Fe3^{ii}—Se1—Fe3	93.93(6)
Se6^{ii}—Fe1|Sn1—Se3	88.95(15)	Sb4^{ii}—Se2—Fe2^{ii}	92.88(11)
Se5—Fe1|Sn1—Se3	91.14(16)	Sb4^{ii}—Se2—Fe2	92.55(11)
Se4^{ii}—Fe1|Sn1—Se3	179.25(19)	Fe2^{ii}—Se2—Fe2	93.83(7)
Se6^{ii}—Fe1|Sn1—Se4	91.68(16)	Fe1|Sn1—Se3—Fe1|Sn1^{i}	94.44(13)
Se5—Fe1|Sn1—Se4	88.28(15)	Fe1|Sn1—Se3—Fe1|Sn1^{i}	94.44(13)
Se4^{ii}—Fe1|Sn1—Se4	94.59(13)	Fe1|Sn1^{i}—Se3—Fe1|Sn1^{i}	0.0(2)
Se3—Fe1|Sn1—Se4	85.42(17)	Fe1|Sn1—Se3—Sb1	89.48(13)
Se6^{ii}—Fe1|Sn1—Se3^{ii}	89.05(16)	Fe1|Sn1^{i}—Se3—Sb1	89.20(13)
Se5—Fe1|Sn1—Se3^{ii}	90.98(16)	Fe1|Sn1^{i}—Se3—Sb1	89.20(13)
Se4^{ii}—Fe1|Sn1—Se3^{ii}	85.54(17)	Fe1|Sn1^{i}—Se4—Fe1|Sn1^{i}	0.00(19)
Se3—Fe1|Sn1—Se3^{ii}	94.44(13)	Fe1|Sn1^{i}—Se4—Sb2	88.58(13)
Se4—Fe1|Sn1—Se3^{ii}	179.25(19)	Fe1|Sn1^{i}—Se4—Sb2	88.58(13)
Se8^{iii}—Fe2—Se8	180.0(5)	Fe1|Sn1^{i}—Se4—Fe1|Sn1	94.59(13)
Se8^{iii}—Fe2—Se2^{i}	92.41(19)	Fe1|Sn1^{i}—Se4—Fe1|Sn1	94.59(13)
Se8—Fe2—Se2^{i}	87.62(18)	Sb2—Se4—Fe1|Sn1	88.45(13)
Se8^{iii}—Fe2—Se2^{iv}	87.62(18)	Fe1|Sn1—Se5—Sb1^{ii}	89.42(13)
Se8—Fe2—Se2^{iv}	92.40(19)	Fe1|Sn1—Se5—Sb1	89.27(13)
Se2^{i}—Fe2—Se2^{iv}	86.6(3)	Sb1^{ii}—Se5—Sb1	93.59(8)
Se8^{iii}—Fe2—Se2	92.37(19)	Fe1|Sn1^{i}—Se6—Fe1|Sn1^{i}	0.0(3)
Se8—Fe2—Se2	87.61(18)	Fe1|Sn1^{i}—Se6—Sb2^{i}	89.03(14)
Se2^{i}—Fe2—Se2	93.83(7)	Fe1|Sn1^{i}—Se6—Sb2^{i}	89.03(14)
Se2^{iv}—Fe2—Se2	179.6(3)	Fe1|Sn1^{i}—Se6—Sb2	88.93(14)
Se8^{iii}—Fe2—Se2^{iii}	87.61(18)	Fe1|Sn1^{i}—Se6—Sb2	88.93(14)
Se8—Fe2—Se2^{iii}	92.37(19)	Sb2^{i}—Se6—Sb2	94.08(9)
Se2^{i}—Fe2—Se2^{iii}	179.6(3)	Fe3—Se7—Sb3^{i}	93.57(11)
Se2^{iv}—Fe2—Se2^{iii}	93.83(7)	Fe3—Se7—Sb3	93.52(11)
Se2—Fe2—Se2^{iii}	85.8(3)	Sb3^{i}—Se7—Sb3	92.80(9)
Se7—Fe3—Se7^{v}	179.998(1)	Fe2—Se8—Sb4	93.21(19)
Se7—Fe3—Se1^{i}	87.83(10)	Fe2—Se8—Sb4^{ii}	93.23(19)
Se7^{v}—Fe3—Se1^{i}	92.17(10)	Sb4—Se8—Sb4^{ii}	93.07(9)

(i) x, -1+y, z; (ii) x, 1+y, z; (iii) -x, y, 0.5-z; (iv) -x, -1+y, 0.5-z;
(v) -x, -y, 1-z; (vi) -x, 1-y, 1-z; (vii) -0.5+x, 0.5+y, z; (viii) 0.5+x, -0.5+y, z;
(ix) 0.5-x, -0.5+y, 0.5-z; (x) 0.5-x, 0.5+y, 0.5-z; (xi) x, -y, -0.5+z; (xii) 0.5-x, 0.5-y, 1-z;
(xiii) x, 1-y, -0.5+z.